Material - Processing - Quality Relationships During the Consolidation of Out-of-Autoclave Prepregs

Timotei Centea

Doctor of Philosophy

Department of Mechanical Engineering

McGill University

Montreal,Quebec

2013-03-05

A thesis submitted to McGill University in partial fulfillment of the requirements of the degree of Doctor of Philosophy

ACKNOWLEDGEMENTS

I extend my deepest thanks to Prof. Pascal Hubert, my research supervisor, for the opportunities he provided, his constant support and his constructive guidance. His example of professionalism and personal involvement is one I will strive to emulate.

This project was made possible by the National Science and Engineering Research Council of Canada (NSERC); the Consortium for Research and Innovation in Aerospace in Quebec; Bell Helicopter; Bombardier; Delastek; the Center for Development of Composites in Quebec; the National Research Council's Institute for Aerospace Research and Advanced Manufacturing Technologies Centre; the University of British Columbia; Concordia University and McGill University. I thank all involved for the financial, material and intellectual support. My stay at McGill was also made possible by personal financial support from NSERC, the Fonds Quebecois de Recherche Nature et Technologies, and the Faculty of Engineering's J.M Bishop and Vadasz awards. I am very thankful for their generosity. At McGill, my closest collaborator was James Kratz, and my work greatly benefited from his expertise and many years of close collaboration. My graduate experience also owes greatly to the members of the Structures and Composites Materials Laboratory, not only colleagues but valued friends. Last, but not least, none of this would have been possible without my family's love and support.

Finally, I would like to thank the advisory and evaluation committee members for accepting to review this thesis, and for their time and input.

CONTRIBUTIONS OF THE AUTHOR

The author of this thesis has performed all the work presented therein, with the following exceptions.

Chapter 4: Benedetto Marelli, a fellow Ph.D. student in the Department of Mining, Metals and Materials, provided micro-CT training and aided in the initial scans of the MTM45-1/5HS prepreg.

Chapter 5: Stella-Marissa Hughes, an undergraduate summer research assistant supervised by the author, performed a portion of the sample polishing, image acquisition and image analysis on the fibre bed compaction samples.

Chapter 6: James Kratz, a fellow Ph.D. candidate in McGill's Structures and Composite Materials Laboratory, provided the resin viscosity data as part of a joint study; furthermore, he also contributed to the set-up of the instrumentation used in this study.

Chapter 6: Lessa Grunenfelder, a fellow Ph.D. student from the University of Southern California (Los Angeles, United States), provided data relating the glass transition temperature of the 5320 resin to its room temperature out-time.

Chapters 6 and 7: Finally, Tobin Chew, an undergraduate Honours Thesis student supervised by the author, performed the detailed design and contributed to the manufacturing of the consolidation fixture.

The author gratefully acknowledges these contributions.

ABSTRACT

Out-of-autoclave (OOA) prepreg processing is a new manufacturing method for high performance composites that seeks to reduce costs and increase production flexibility relative to traditional autoclave processing. OOA prepregs may be vacuum bag-only cured in conventional ovens to produce autoclave-quality parts with low void contents. To achieve such quality under vacuum consolidation, OOA prepregs feature dry areas that allow gas evacuation during the early stages of processing but must be subsequently infiltrated with resin. The present thesis describes a four-part investigation into the consolidation of such OOA prepregs, with particular emphasis on flow phenomena and flow-induced defects.

First, a novel X-ray computed microtomography approach was successfully used to determine the microstructure of a representative OOA prepreg and track its evolution during processing. The results showed that, initially, the prepreg consisted of dry, micro-porous fibre tow cores surrounded by resin-rich areas and macro-pores, and that two phenomena occurred during processing: the progressive collapse of these macro-pores due to air evacuation at room temperature, and the impregnation of the dry tows at elevated temperature.

Second, an analytical model for tow impregnation was developed for three OOA prepregs, and used in a parametric study to evaluate the effect of various material properties and process parameters. The results showed that tow

impregnation can successfully occur in a wide variety of cases, but that deviations from ideal situations may lead to incomplete tow impregnation and flow-induced micro-porosity.

Third, the effects of cure cycle and out-time on OOA prepreg consolidation were studied experimentally through material characterization, laminate manufacture and microstructural quality analysis. The results demonstrated that out-time had a detrimental effect on resin properties, process phenomena and tow micro-porosity, but that certain cure cycles mitigated or even eliminated such defects. These results were also compared to model predictions, which showed agreement with the observed trends and part quality at low out-times but under-predicted micro-void sizes at very high out-times.

Finally, the effects of four deficient consolidation cases (repeated debulks, reduced ambient pressure, reduced vacuum and restricted air evacuation) were studied experimentally by laminate manufacture and final quality evaluation. The results established that reduced ambient pressure, reduced vacuum and restricted air evacuation had specific detrimental effects on consolidation phenomena and on macro- and micro-porosity within the final part, and clarified the allowable extent of such deviations for successful part manufacture

Overall, the thesis contributed to the knowledge on OOA prepreg processing in several ways. First, the key consolidation phenomena that occur during OOA prepreg consolidation were identified. Second, the effect of several material properties, process parameters and deviations from ideal conditions were evaluated to aid process optimization and define the allowable

process windows for successful part manufacture. Finally, a new set of experimental and modelling tools were proposed to aid material characterization, process analysis and quality prediction.

ABRÉGÉ

La mise-en-forme de pré-imprégnés hors-de-l'autoclave est une nouvelle méthode de fabrication pour les composites haute-performance qui cherche à réduire les coûts et à augmenter la flexibilité par rapport à la fabrication traditionnelle par l'autoclave. Les pré-imprégnés hors-de-l'autoclave peuvent être mis en forme sous un simple sac à vide, dans un four conventionnel. Pour limiter la porosité lors d'une consolidation sous vide seulement, ces matériaux comportent des zones sèches qui permettent l'évacuation de gaz au début de la mise-en-forme et qui doivent ensuite être infiltrées par de la résine. Cette thèse présente une invéstigation en quatre parties de la consolidation de tels pré-imprégnés hors-de-l'autoclave, avec une emphase particulière sur le phénomène d'écoulement et les défauts induits par l'écoulement.

En premier lieu, une nouvelle approche basée sur la microtomographie par rayons X a été utilisée avec succès pour déterminer la microstructure initiale d'un pré-imprégné hors-de-l'autoclave typique et pour suivre son évolution pendant la mise-en-forme. Les résultats ont démontré que, initialement, le pré-imprégné était constitué de noyaux de faisceaux de fibres entourés de zones riches en résine et de macro-pores, et que deux phénomènes ont prit place pendant la mise-en-forme: la disparition progressive des macro-pores due à l'évacuation des gaz à température ambiante, et l'imprégnation des faisceaux à températures élevées.

En deuxième lieu, un modèle analytique décrivant l'imprégnation des faisceaux à été développé pour trois pré-imprégnés hors-de-l'autoclave, et utilisé

pour une étude paramétrique afin d'évaluer l'effet de plusieurs propriétés des matériaux et paramètres de mise-en-forme. Les résultats ont démontré que l'imprégnation des faisceaux peut avoir lieu dans la majorité des cas, mais que des déviations des situations idéales peuvent causer une imprégnation incomplète et de la microporosité induite par l'écoulement.

Ensuite, les effets du cycle de température et du temps d'exposition des pré-imprégnés aux conditions ambiantes sur la consolidation ont été étudiés par l'entremise de la caractérisation des matériaux, de la fabrication de laminés et de l'analyse de leur microstructure. Les résultats ont démontré que le temps d'exposition aux conditions ambiantes a un effet néfaste sur les propriétés de la résine, sur les phénomènes prenant lieu durant la mise-en-forme et sur la micro-porosité dans les faisceaux des pièces fabriquées; toutefois, ils ont aussi démontré que certains cycles de température ont mitigé ou même éliminé ces défauts. Ces résultats ont aussi été comparés au prédictions du modèle, démontrant que ce dernier a capturé les tendances observées, mais qu'il a sous-prédit la taille des micro-porosités pour les cas d'exposition élevée aux conditions ambiantes.

Finalement, les effets de quatre cas de consolidation déficiente (l'application de vide répetée, la pression ambiante réduite, le vide réduit et l'évacuation d'air restreinte) ont été étudiés expérimentalement par la mise-en-forme de laminés et l'évaluation de leur qualité. Les résultats ont établi que la pression ambiante réduite, le vide réduit et l'évacuation d'air restreinte ont des éffets néfastes spécifiques sur les phénomènes de consolidation et sur la macro- et micro-porosité dans les pièces fabriquées, et clarifié l'ampleur permissible de telles déficiences pour des laminés d'une qualité acceptable.

Globalement, cette thèse a contribué à des plus amples connaissances et une meilleure compréhension de la mise-en-forme de pré-imprégnés hors-de-l'autoclave. Premièrement, les principaux phénomènes de consolidation prenant lieu pendant ce procédé ont été identifiés. Deuxièmement, les effets de plusieurs propriétés des matériaux, paramètres de mise-en-forme et déviations des conditions idéales ont été évalués afin d'aider à l'optimisation du procédé et de définir les fenêtres permissibles de variation pour une mise-en-forme réussie. Finalement, de nouvelles méthodes expérimentales et de modélisation ont été proposées pour aider la caractérisation des matériaux, l'analyse de procédés et la prédiction de qualité.

TABLE OF CONTENTS

LIST OF TABLES

LIST OF FIGURES

CHAPTER 1
Introduction

1.1 Introduction

The development of new aerospace structural materials is driven by two primary needs: to improve material performance in order to produce more capable, reliable and safe aircraft, and to reduce the monetary and environmental costs associated with their manufacture and operation.

Composite materials have the potential to address both these needs. Generally speaking, composites are engineered combinations of two or more materials whose combined performance exceeds that of the individual constituents. For aerospace primary and secondary structure applications, they most commonly consist of long, aligned carbon fibres embedded within an epoxy resin matrix.

Performance-wise, the carbon fibres reinforce the matrix, imparting high specific strength and stiffness as well as the ability to orient mechanical properties so as to address an expected set of loads. The epoxy maintains the part shape, protects the fibres from environmental degradation, transfers loads between them and resists interlaminar shear. Altogether, the composite improves on traditional metallic airframe materials by offering higher specific mechanical properties, fatigue and corrosion resistance, and design versatility [1].

Composites also offer a new paradigm for aircraft manufacture. Traditionally, large metallic aircraft structures such as fuselages and wing skins are built up from numerous smaller pieces using fasteners, and this assembly process can account for as much as 50 % of the total airframe cost [1]. Conversely, composites allow the creation of large, integrated parts, which dramatically reduce the number of joining operations and fasteners required, and can therefore lead to significant reductions in manufacturing time and expense.

Over the past decades, the use of carbon reinforced plastics in aerospace has increased dramatically, with the percent composite content of certain airframes reaching or exceeding 50 % by weight [2]; furthermore, other high performance industries are also following suit. However, such pervasive use comes into conflict with the limitations of traditional manufacturing methods.

Currently, most aerospace composite structures are manufactured using autoclaves. The composite material typically starts off as layers of "prepreg", or carbon fibre beds pre-impregnated with a catalyzed but uncured epoxy resin, which are stacked on a tool to form a laminate. As shown in Figure 1–1, this laminate is enclosed in a vacuum bag assembly and inserted into the autoclave. Then, the pressure within the bag is decreased from the ambient towards vacuum while the pressure within the autoclave is increased by up to a factor of six, and the temperature is raised to up to 200 °C. The pressure differential between bag and autoclave results in a consolidation pressure that compacts the laminate to the desired thickness and conforms it to the shape of the tool. Crucially, this high pressure also suppresses porosity, the main defect in composite parts, by wetting any remaining dry areas with resin

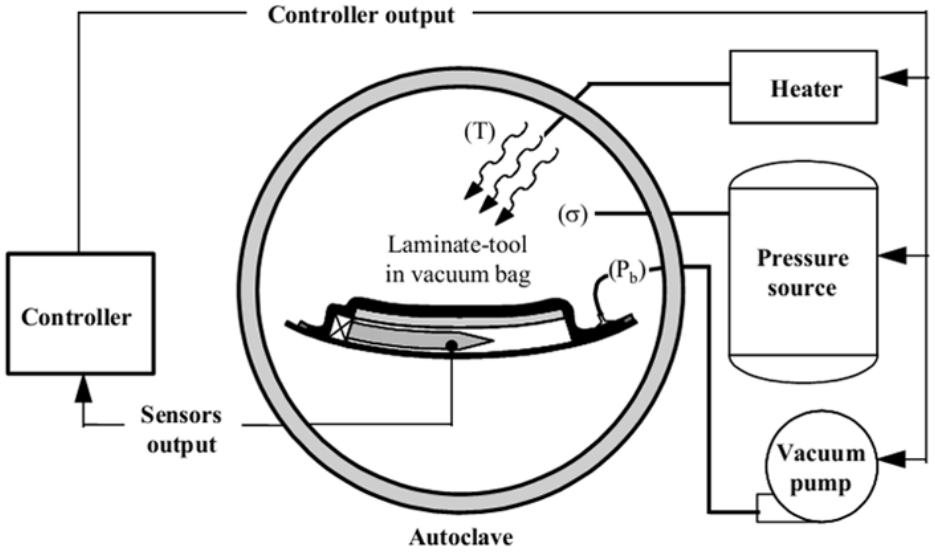

Figure 1–1: Schematic of autoclave processing [3].

and collapsing gas bubbles caused by volatiles down to an acceptable size. Simultaneously, the elevated temperature decreases the viscosity of the resin, allowing it to flow and completely impregnate the reinforcing fibre bed, and subsequently cures it, turning it from a viscous fluid into a stiff solid.

Autoclave processing is robust and well-understood; it consistently results in high quality parts, and therefore remains the benchmark for competing processes. However, autoclaves involve significant acquisition and operating costs. They also create an inflexible manufacturing environment, in which potential part designs are limited to the dimensions of available autoclaves, production rates are limited by autoclave scheduling, and large autoclaves must sometimes be inefficiently used for small parts. Given the current increase in composite usage, there is therefore significant interest in alternative

processes that allow the production of comparable quality parts outside of the autoclave.

1.2 Out-of-Autoclave Prepreg Processing

One such approach is out-of-autoclave (OOA) prepreg processing, which allows the manufacturing of autoclave-quality parts using vacuum bag-only (VBO) consolidation in conventional, unpressurized ovens rather than pressurized autoclaves.

Since vacuum bags rely on the pressure differential across the bag membrane, conventional ovens limit the available consolidation pressure to a maximum of approximately 101 325 Pa. Thus, the capacity to consolidate the laminate and, crucially, collapse voids is greatly reduced relative to the autoclave, and any gases present within the laminate must be removed to obtain low porosity parts.

To promote air evacuation, OOA prepregs feature partially impregnated microstructures that contain both dry areas and areas that contain excess resin. The dry areas are intended to act as relatively permeable "engineered vacuum channels" and allow gases present in the laminate to escape in the initial stages of processing. Then, under heated consolidation, resin from the resin-rich areas infiltrates the dry areas to produce a uniform and low-porosity microstructure [4, 5].

1.3 Problem Statement

These phenomena, which are illustrated schematically in Figure 1–2, add a significant level of complexity to OOA prepreg processing. They also add inherent risk, since porosity is intentionally introduced into the prepreg in order to prevent porosity in the final part. To further compound the challenge,

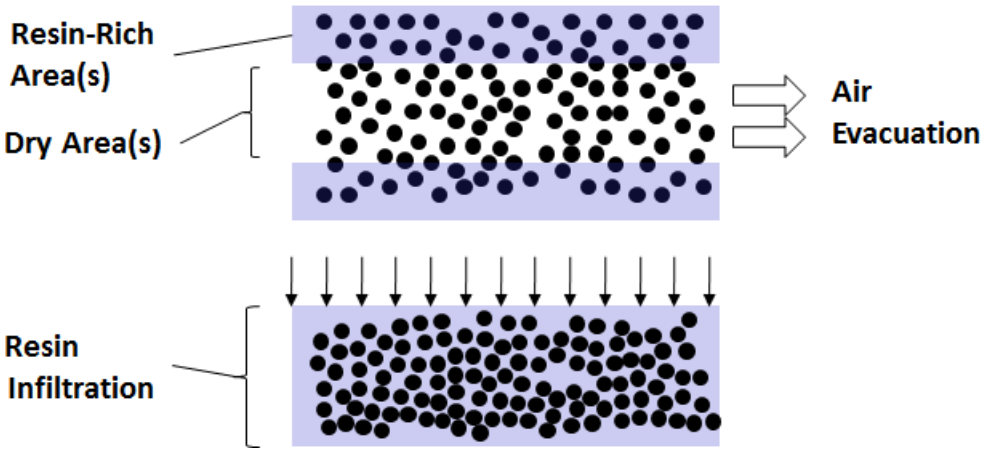

Figure 1–2: Schematic of OOA microstructural phenomena.

the flow aspects are likely to be highly dependent on several factors, including the properties of the constituent materials and the process parameters. They are also likely to be more sensitive to unintended variations in these factors than traditional autoclave processing, since the inherent safeguard of high pressure no longer exists. Thus, a thorough understanding of the relationship between material properties, process parameters, consolidation phenomena and final part quality is an essential first step towards assessing the potential of this manufacturing process.

1.4 Outline

The main body of this thesis progresses as follows. The present chapter introduces and motivates the topic. Chapter 2 reviews relevant theory and literature, and identifies areas where further study is needed. Chapter 3 outlines the specific objectives of the thesis and describes how each of the main chapters relates to them. Chapters 4 - 7 present the main findings of the thesis, while Chapter 8 summarizes its key contributions. In addition to

the main body, several appendices are also included to provide further details and supporting data.

CHAPTER 2
Theory and Literature Review

The present chapter first offers a concise review of relevant background theory and literature. Then, it assesses the state-of-the-art in out-of-autoclave prepreg processing and identifies areas where further study is required.

2.1 Manufacturing Processes for Aerospace Structural Composites

All high performance composites are manufactured using a combination of controlled temperature and pressure. However, the manner in which these process parameters are applied varies, and manufacturing methods for high performance structural composites may be divided into prepreg and liquid moulding processes.

2.1.1 Prepreg Processes

Prepreg processes, based on the use of fibre beds pre-impregnated with resin, include the traditional autoclave technique as well as variants such as OOA manufacturing. They generally consist of four manufacturing steps: prepregging, ply collation, vacuum bagging and cure.

Prepregging is the process by which the material supplier pre-impregnates a dry fibre bed with resin to form the prepreg. Most high performance prepregs are fabricated by "hot melt", which consists of applying the desired quantity of resin as a film to one or both sides of the fibre bed, and using heated compression rollers to achieve the desired degree of impregnation. Individual prepreg layers are usually between 0.1 mm and 1 mm thick,

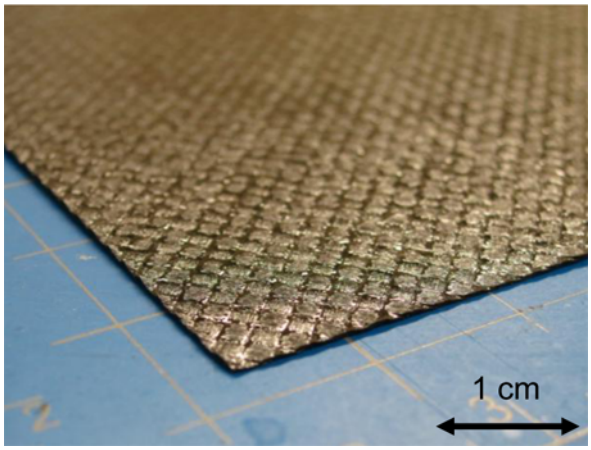

Figure 2–1: Photograph of a prepreg ply.

and contain approximately 30 % to 40 % resin by weight. A picture of a representative carbon fibre prepreg ply is shown in Figure 2–1. Although it has been suggested by a few authors that traditional autoclave prepregs may be partially impregnated [1, 6, 7], very little experimental characterization exists and most literature assumes that they are fully saturated with resin.

Ply collation consists of laying up multiple prepreg plies on a tool in a specific order and orientation to form a laminate. Lay-up generally takes place manually, but may be automated. If the prepreg layers are difficult to collate or conform to the shape of the tool, intermediate "debulking" steps in which vacuum consolidation is temporarily applied using a vacuum bag may be used to compact the layers. Several issues may arise during ply collation, including air entrapment between plies and room temperature resin polymerization (leading to undesirable property changes), both of which may be detrimental to final part quality [8].

Vacuum bagging consists of enclosing the laminate within an assembly of "consumables" designed to ensure adequate cure; a traditional autoclave

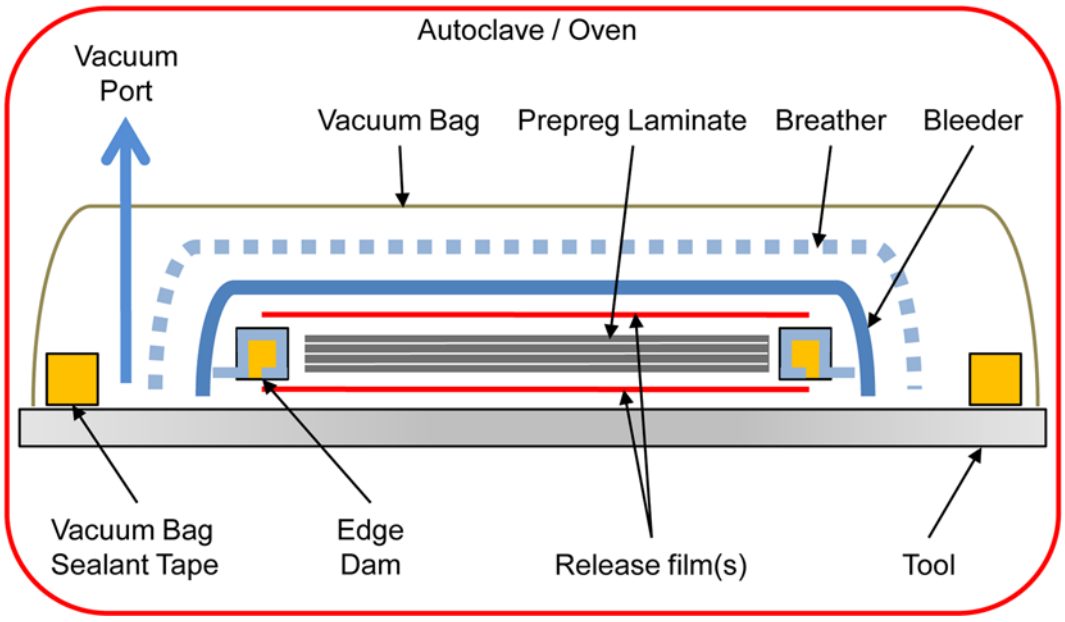

Figure 2–2: Schematic of a traditional autoclave layup.

example is shown in Figure 2–2. It consists of a metallic tool, coated with a release agent or covered in fluorinated ethylene propylene (FEP) release film to prevent resin adhesion; the laminate; a second release film, sometimes perforated to allow resin and/or gas transfer; bleeder and breather cloths that allow resin to seep out and pressure to equilibrate within the bag; edge bleeder dams that maintain the laminate in place while allowing resin to escape through the sides, and an impermeable vacuum bag (with vacuum port) that creates a pressure differential with the exterior [8]. The correct assembly of these consumables is critical; in particular, the quality of the vacuum bag seals is essential to ensure a pressure differential and avoid gas leaks into the bag.

Finally, the cure step is defined by temperature and pressure cycles, an example of which is shown in Figure 2–3. A traditional temperature cycle for

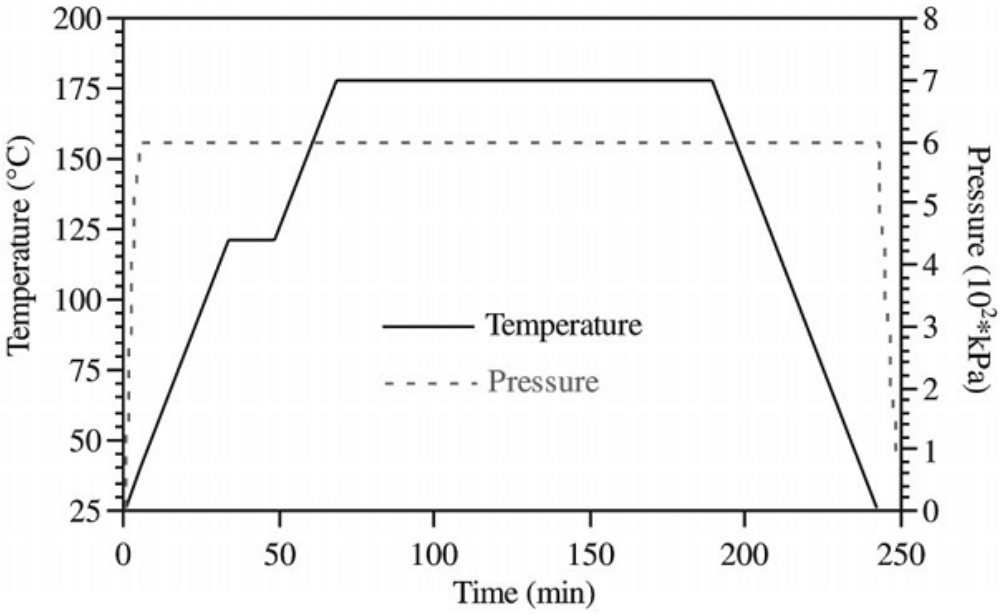

Figure 2–3: Schematic of a traditional autoclave cure cycle [8].

an aerospace epoxy consists of a combination of heating ramps ($0.5\,^{\circ}\mathrm{C\,min^{-1}}$ to $3\,^{\circ}\mathrm{C\,min^{-1}}$) and isothermal dwells ($121\,^{\circ}\mathrm{C}$ to $177\,^{\circ}\mathrm{C}$), with dwell times on the order of hours. The temperature profile is chosen so as to optimize the thermochemical properties of the resin during and after cure. The cooling ramp, while negligible for consolidation since it occurs after gelation, is known to influence residual stress formation [8]. In the case of autoclave processing, the pressure cycle usually consists of reduced pressure ($0\,\mathrm{Pa}$ to $101\,325\,\mathrm{Pa}$) within the bag and increased pressure ($101\,325\,\mathrm{Pa}$ to $607\,950\,\mathrm{Pa}$) within the autoclave. These pressures are chosen so as to ensure the proper flow, compaction and void control phenomena for a given material and part. Curing is the key stage of manufacturing, as it includes the thermochemical changes within the resin and the defect-governing consolidation phenomena within the laminate.

The extensive track record, consistency, robustness and accumulated understanding of autoclave processing have led to its status as the benchmark high performance composite process. However, its high acquisition and operating costs and restrictive nature have led to the development of alternate approaches. One such approach is liquid composite moulding, which has gained significant popularity in recent decades and is described in the following sub-section. Another, as mentioned in the introduction, is the OOA prepreg process that is the subject of this thesis.

2.1.2 Liquid Composite Moulding

Liquid composite moulding (LCM) processes forego the use of prepregs in favor of infiltrating an entirely dry fibre bed with neat (or unreinforced) resin. Such processes are well-suited for relatively small but complex parts, which may be difficult to lay up using prepreg, and for parts in which detail features, surface finish and dimensional stability are critical [9].

LCM refers to a broad spectrum of processes. On one side lie closed-mould techniques such as the common resin transfer moulding (Figure 2–4), in which a dry fibre "preform" is placed within a closed cavity and infiltrated with resin from a pressurized pot. One the other side lie open-mould processes like resin film infusion (Figure 2–5), in which a stack that includes dry fibre layers as well as a quantity of neat resin is cured within a vacuum bag in an autoclave or traditional oven. Between these two extremes lie several intermediate variations. Process parameters vary widely, but for high performance applications such as aerospace, pressures driving resin flow generally range from 101 325 Pa to 607 950 Pa and temperatures from 121 °C to 177 °C.

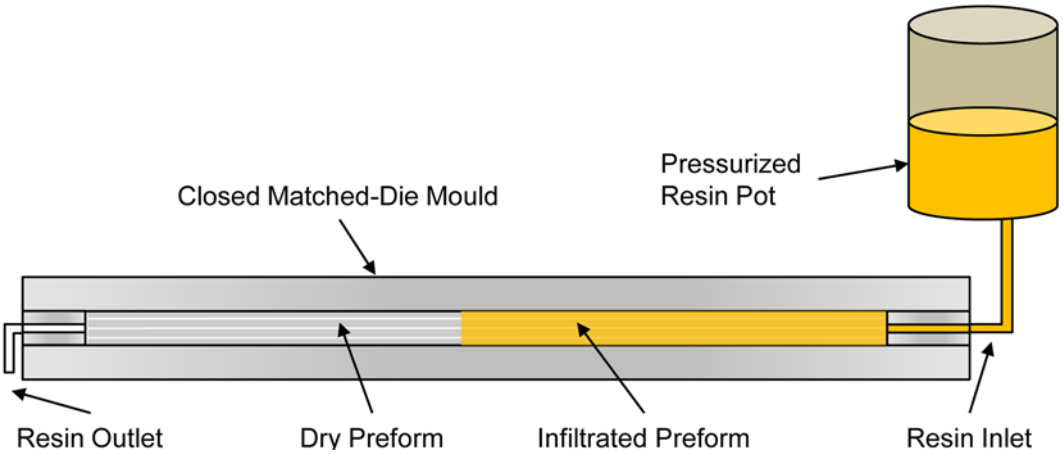

Figure 2–4: Schematic of the resin transfer moulding process.

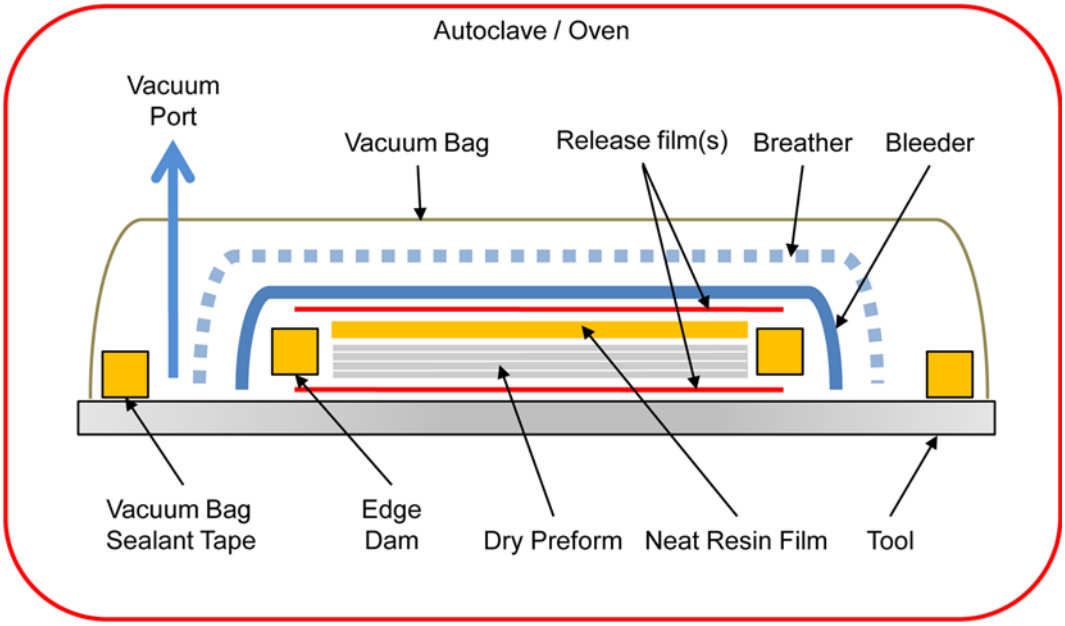

Figure 2–5: Schematic of the resin film infusion process.

While there are many differences between LCM and OOA prepreg processes, the presence of resin infiltration flows is a common thread. Thus, in further sections, relevant literature concerning LCM processes may also be mentioned.

2.2 Process Analysis Fundamentals

2.2.1 Resin Flow in Composites Processing

The techniques used to manufacture most aerospace structural composites are "porous media manufacturing processes" and involve resin infiltration into near-stationary porous preforms [10]. As explained by Michaud and Mortensen [11], for composite materials, the scale of individual pore network flow channels is much smaller than the scale of the overall flow field of interest. Hence, such infiltration may be described using a continuum mechanics approach, in which material properties are averaged within an appropriately-sized representative volume element (REV) containing all phases of interest; more extensive discussions of the assumptions, method and results of this volume averaging approach may be found in references [12–14]. Within this framework, and in light of the common assumptions of incompressible resin and individual fibres, the following governing laws are outlined by Michaud and Mortensen [11] for composites process analysis .

The mass conservation equations for the fibre bed and resin phases may be expressed as, respectively [11]:

$$\frac{\partial V_f}{\partial t} + \nabla \cdot (V_f \bar{v_f}) = 0 \tag{2.1}$$

$$\frac{\partial((1-V_f)S)}{\partial t} + \nabla \cdot ((1-V_f)S\bar{v_r}) = 0 \tag{2.2}$$

V_f is the fibre volume fraction within the REV, or the proportion of fibre volume to total REV volume. S is the saturation, or the ratio of resin volume to total pore volume. $\bar{v_f}$ is the average fibre velocity, or the average of all individual fibre velocity vectors, which may vary at different points within the REV. $\bar{v_r}$ is the average local velocity of the resin, or the average of individual velocity vectors, which may vary locally as the resin flows through the pores of the fibre bed medium within the REV.

The momentum equations may be expressed through Darcy's Law:

$$(1-V_f)S(\bar{v_r} - \bar{v_f}) = -\frac{\bar{\bar{K}}}{\mu}\nabla P \tag{2.3}$$

The quantity $(\bar{v_r} - \bar{v_f})$, the relative velocity of the resin phase with respect to the near-stationary fibre phase, is of primary interest when considering resin infiltration into a near-stationary preform. It is described in light of several variables: $\bar{\bar{K}}$, the permeability tensor of the preform, or a measure of its capacity to accommodate fluid flow; μ, the dynamic viscosity of the resin; and P, the pore pressure of the resin, or the average resin pressure within the fibre bed's pores, in the REV.

Darcy's Law is a specialization of the momentum balance equation, first proposed on the basis of soil science experiments by Henry Darcy around 1856 [15], and later more rigorously derived from the fundamental fluid flow equations (for example, in [16]). As per the latter, it is applicable to transient, multidimensional flows through anisotropic porous media provided the fluid

is Newtonian; the porous medium is homogeneous; long-range viscous effects are negligible (or the divergence of the volume-averaged viscous stress may be neglected due to the large length scale over which velocity changes); and inertial effects may be neglected when compared to the drag forces between fluid and medium. The latter conditions are associated with flows characterized by a Reynolds number smaller that approximately one [11], where the appropriate Reynolds number is given by Tucker and Dessenberger as [16]:

$$Re = \frac{\rho v d_p}{\mu} \tag{2.4}$$

ρ is the fluid density, v is the fluid velocity averaged over a cross-sectional area that includes both the pore space and the solid medium (or the specific discharge), μ is the fluid viscosity and d_p is a characteristic length representative of the dimension of the pore channels available to flow [16].

Since these assumptions are usually satisfied by the low velocity, "creeping" flows present during most epoxy matrix composite manufacturing, Darcy's Law offers a convenient and widely used means of describing such phenomena.

The stress equilibrium between fibres and resin is finally assumed to be shared between fibres and resin [11]:

$$\nabla \cdot \bar{\bar{\sigma}} - \nabla SP = 0 \tag{2.5}$$

$\bar{\bar{\sigma}}$ denotes the load carried by the preform divided by its area of application (which may consist of both fibres and resin) and is denoted the "effective stress" tensor; this approach is inspired by the soil consolidation work of Biot [17] and Terzaghi [18].

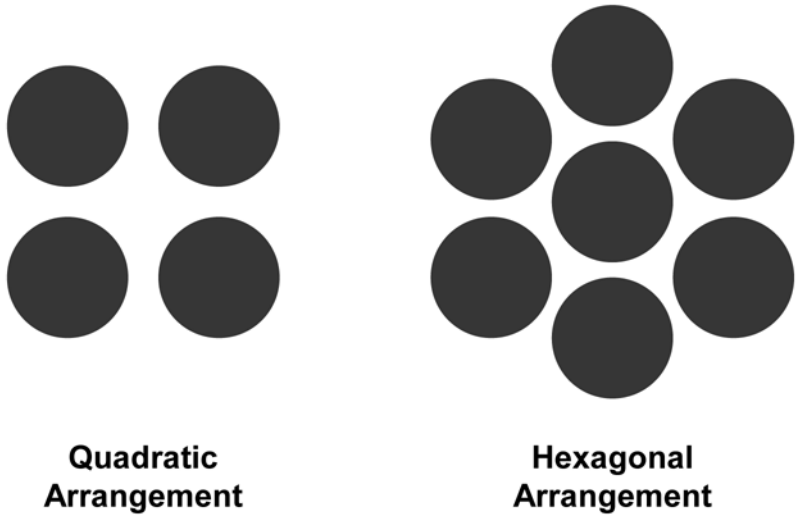

Figure 2–6: Schematic of idealized quadratic and hexagonal fibre packing arrangements.

This theoretical framework highlights that flow in composites processing is fundamentally dependent on the properties of the reinforcing fibre bed (V_f, $\bar{\bar{\sigma}}$ and $\bar{\bar{K}}$) and matrix resin (μ), and therefore on the process temperature and pressure, which may affect these properties.

2.2.2 Fibre Bed Properties

2.2.2.1 Morphology

The carbon reinforcements used in high performance aerospace applications are high aspect ratio fibres, whose diameter is approximately 7 µm and whose length may span the entire manufactured part. For ease of handling, these fibres are commonly combined, either by creating "tapes" of unidirectional fibres stitched with nylon threads in the transverse direction, or by bundling them into tows and weaving them into fabrics with various architectures [1].

Tows may consist of 3000 to 24 000 individual fibres (often denoted 3K to 24K), and their packing impacts the fibre volume fraction and, consequently, the porosity of the preform. Two idealized packing arrangements are commonly considered and shown in Figure 2–6: the quadratic and the hexagonal. The quadratic arrangement is the less dense of the two, allowing a maximum fibre volume fraction of $\pi/4$, or 78.5 %, while the hexagonal fibre arrangement permits a maximum theoretical volume fraction of $\pi/(2\sqrt{(}3))$, or 90.7 % [19]. In both cases, the fibres are assumed to be perfectly aligned. In reality, however, the fibres exhibit some waviness, either due to their manufacturing process or due to being woven, and their packing in the cross-section is to some degree random [20, 21].

In the case of fabric preforms, the carbon fibre tows are interlaced in a repeating pattern. Figure 2–7 shows an example of a plain weave (PW), and highlights the fact that fabrics are dual-scale structures, containing both micro-scale porosity (on the order of 1 µm to 10 µm) inside the tows, between the individual fibres, and macro-porosity (on the order of 10 µm to 1000 µm) between the tows [22]. Fabrics may therefore be said to have a higher "bulk factor", or proportion of pore content, than the more compact unidirectional tapes. Both tapes and fabrics are commonly described by their dry weight per unit area, or areal weight; common values range from $100\,\mathrm{g\,m^{-2}}$ to $500\,\mathrm{g\,m^{-2}}$.

2.2.2.2 Compaction

Since aerospace composites are generally thin and planar, they are most often compressed in the out-of-plane direction during processing. Therefore, the through-thickness stress-strain (or compaction) behaviour of the preform is an important factor and has been the subject of considerable research.

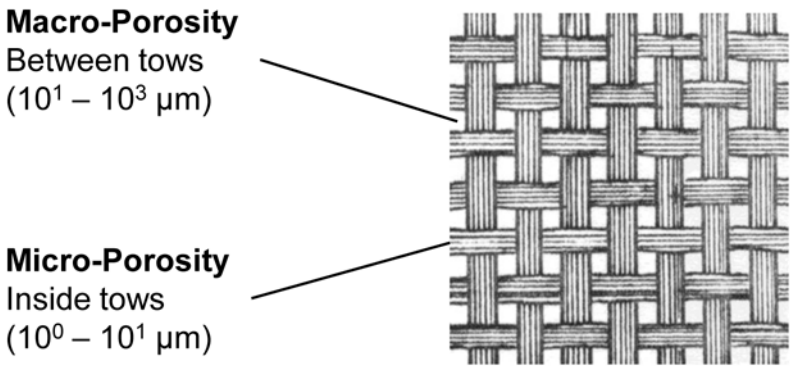

Figure 2–7: Schematic of a plain weave fabric (adapted from [1]).

Compaction measurements are generally performed using mechanical testing frames equipped with compression fixtures consisting of flat, well-aligned platens. A preform sample with the relevant layup is placed between the platens and compressed while the thickness and load are recorded. The fibre volume fraction and effective stress are then obtained from the measured data and sample geometry [11]. If the material of interest is a prepreg, and hence already impregnated with resin, a modified version of this technique proposed by Hubert and Poursartip [23] may be used. The approach consists of successive compression and constant thickness hold steps between heated platens; during compression, load is carried by both preform and resin, but the resin is allowed to seep out at constant thickness, eventually isolating the load-carrying contribution of the fibre bed.

The most influential early work is arguably that of Gutowski et al. [21,24], who performed experiments and modelling on the deformation behaviour of tows and unidirectional fibre beds, and emphasized that at the fibre level, this phenomenon is intimately linked to waviness and, hence, to an increasing number of contact points during compression. Many materials and conditions

were subsequently analyzed, and a detailed review of experimental data by Robitalle and Gauvin [25] highlights the following clearly identifiable facts. The dry fibre bed stacks exhibit non-linear stiffening behaviour on compression, due to increasing fibre-to-fibre contacts caused by fibre waviness. They also exhibit visco-elastic behaviour due to fibre re-arrangement and/or breakage, either through a slow decrease in thickness under constant applied pressure, a decrease in carried load at constant thickness, or a shift in the compaction curve on subsequent compression steps. Finally, the compaction behaviour may depend on numerous parameters, including preform morphology, number and orientation of layers, number of successive compression steps, compression speed, applied pressure (during relaxation), temperature (if certain types of binders or fibre coatings are present) and the presence of a lubricant.

Several compaction models exist in the literature seeking to relate the fibre volume fraction of the preform to the applied load in light of various assumptions. Some are mechanistic, based on beam bending theory, while other are phenomenological. Many make use, to some extent, of fitting parameters in order to be quickly applicable to a wide variety of commercial materials. The assumption of non-linear elastic (stiffening) behaviour is considered sufficient for prepreg processing [20]. Common models include those of Gutowski et al. [21], shown in Eq. 2.6, or those based on a power law, shown in Eq. 2.7 [11].

$$\sigma = A_s \frac{\sqrt{V_f/V_{f0}} - 1}{(\sqrt{V_{fa}/V_f} - 1)^4} \tag{2.6}$$

$$\sigma = A_s(V_f - V_{f0})^n \tag{2.7}$$

σ is the effective through-thickness stress carried by the fibre bed; V_f is, as defined before, the fibre volume fraction; A_s is a constant representing the stiffness and waviness of the fibres; V_{f0} is the fibre volume fraction in the uncompressed state and V_{fa} the maximum potential volume fraction. In addition, in Eq. 2.7, n is a power-law constant [11, 21]. One or more of A_s, V_{f0}, V_{fa} and n may be obtained by fitting the model to experimental data.

2.2.2.3 Permeability

The permeability of a medium is its capacity to accommodate fluid flow. Generally direction-dependent, it may be expressed as a second-order tensor. Furthermore, it is a function of the pore network morphology, and thus of the fibre volume fraction and arrangement in the preform.

The measurement of preform permeability is a key component of composites process analysis, and has been the subject of extensive discussion (a detailed review may be found in [26]). Generally speaking, the permeability in a specific direction may be obtained from steady-state or transient experiments using Darcy's Law [11]. However, several challenges remain, including the dual-scale nature of many preforms, which may lead to unsaturated flow; the difficulty of reconciling results obtained with model fluids (such as silicone oil) to resin flows and, most importantly, the many sources of variability and uncertainty, from those inherent to the preform materials to those brought on by the absence of standardized test procedures [27].

Permeabilities may also be estimated using several modelling approaches [11, 26]. One approach is based on soil mechanics and the concept of flow through capillaries, and models such as the Carman-Kozeny were initially extensively used. However, since the pore morphology of carbon fibre beds is different from that of soils, these equations are not rigorously applicable and may be inappropriate [20, 28]. A second approach approximates fibres as arrays of regularly spaced cylinders, and considers the flow around them in order to derive the resistance they induce, and hence the permeability. Analytical results include the Bruschke-Advani [29] and Gebart [19] models, which predict the permeability across and along said cylinders for known volume fraction, packing and geometry inputs. The Gebart equations for transverse permeability are shown below, where $K_{\perp,quad}$ is the transverse permeability for quadratic fibre packing, $K_{\perp,hex}$ is the transverse permeability for hexagonal fibre packing and R_{fib} is the fibre radius:

$$K_{\perp,quad} = \frac{16}{9\pi\sqrt{2}} \left[\sqrt{\frac{\pi/4}{V_f}} - 1 \right]^{5/2} R_{fib}^2 \tag{2.8}$$

$$K_{\perp,hex} = \frac{16}{9\pi\sqrt{6}} \left[\sqrt{\frac{\pi/(2\sqrt{3})}{V_f}} - 1 \right]^{5/2} R_{fib}^2 \tag{2.9}$$

While these models are convenient in their closed-form, they cannot capture the effect of variability in fibre size and packing arrangement, which has been shown to lead to reductions in actual permeability (for example, in [30, 31]). Furthermore, they are also mostly limited to single-scale porous media. Thus, a final approach to estimating permeability is computational

fluid dynamics, which may be applied to complex geometries and flow conditions, but which remains time- and resource-intensive [11].

2.2.3 Resin Properties

2.2.3.1 Degree of Cure

The epoxy resins commonly used in structural aerospace composites are thermosets. In their initial, uncured state, they are viscous fluids consisting of relatively small molecules called monomers and several additives, among which is a catalyst. This catalyst induces an irreversible chemical reaction called polymerization, or cure, which sees the monomers combine to form larger molecules and, eventually, a single cross-linked network that spans the entire material. For most high performance structural epoxies, cure occurs relatively slowly at ambient temperature, in order to allow for material handling and part preparation, but much faster at elevated temperatures. Polymerization is a finite process: the decreasing number of unchained molecules, along with the inhibiting presence of a physical network, are such that eventually no further cross-linking is possible and the material reaches a final, solid state. While high temperatures lead to faster cure, the cross-linking reaction is exothermic, and the energy released is denoted the "heat of reaction" [1,20].

The temperature profile, or cure cycle, imposed to a composite part is the primary input affecting resin behaviour. In this context, polymerization is therefore generally characterized by monitoring the time-history of the heat of reaction using differential scanning calorimeters (DSC) under a wide variety of temperature conditions [32]. The ratio of the heat of reaction released up to a time t, or $H(t)$, to the total heat of reaction, H_{tot}, may then be used to define a degree of cure α such that $0 < \alpha \leq 1$ [20]:

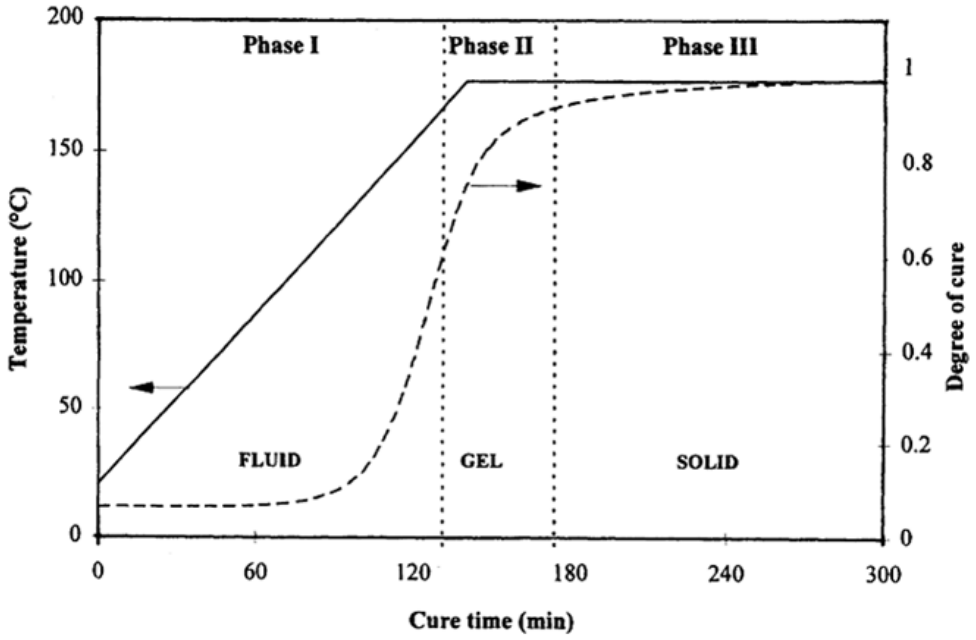

Figure 2–8: Graph of the evolution of the degree of cure α with time for a standard cure cycle [20].

$$\alpha(t) = \frac{H(t)}{H_{tot}} \tag{2.10}$$

The resin cure kinetics, or the evolution of α with time for a given cure cycle, may be divided into three phases, as shown in Figure 2–8. At the beginning of Phase I, the resin is a viscous fluid. Then, as the temperature increases from the ambient towards the target processing temperature, polymerization begins. Eventually, molecular cross-linking creates a network that spans the entire material domain, and the resin changes from a viscous fluid into a malleable, gelatinous solid. This marks the onset of Phase II, during which cross-linking continues, but at a decreasing rate, since molecular mobility is now increasingly constrained by the cross-linked network. The consistency of the resin after Phase I is dictated by a property called the

glass transition temperature, or T_g, which increases with α. As long as the glass transition temperature remains below the process temperature, the resin remains a gel. However, once cure is sufficiently advanced that the glass transition temperature exceeds the process temperature, the resin turns from a gel into a glassy solid. This moment, called vitrification, marks the beginning of Phase III, during which the rate of cure is drastically reduced by the now immobile cross-linked network. The end of Phase III sees the resin reach its ultimate degree of cure, ensuring the highest glass transition temperature and mechanical properties [20].

The rate of cure $d\alpha/dt$ is therefore influenced by both temperature and time, and several cure kinetics models accounting for these dependencies have been proposed. As summarized by Hubert and Poursartip [20], some are mechanistic, and based on the details of the chemical reactions involved, while others are semi-empirical, and rely on approximating the measured trends by fitting an equation with several constants to measured data. The latter approach is particularly favored with commercial materials, whose chemical compositions are usually proprietary and undisclosed [20, 32]. Common models include those based on nth order rate equations [32], the Kamal-Sourour model [33] and, more recently, versions of the model proposed by Cole et al. [34], which accounts for the shift to diffusion-controlled cure close to vitrification [35, 36].

2.2.3.2 Viscosity

The evolution of the resin viscosity μ primarily depends on the temperature and degree of cure. An increase in temperature leads to higher molecular mobility and therefore to lower viscosity, but also accelerates cure. Conversely,

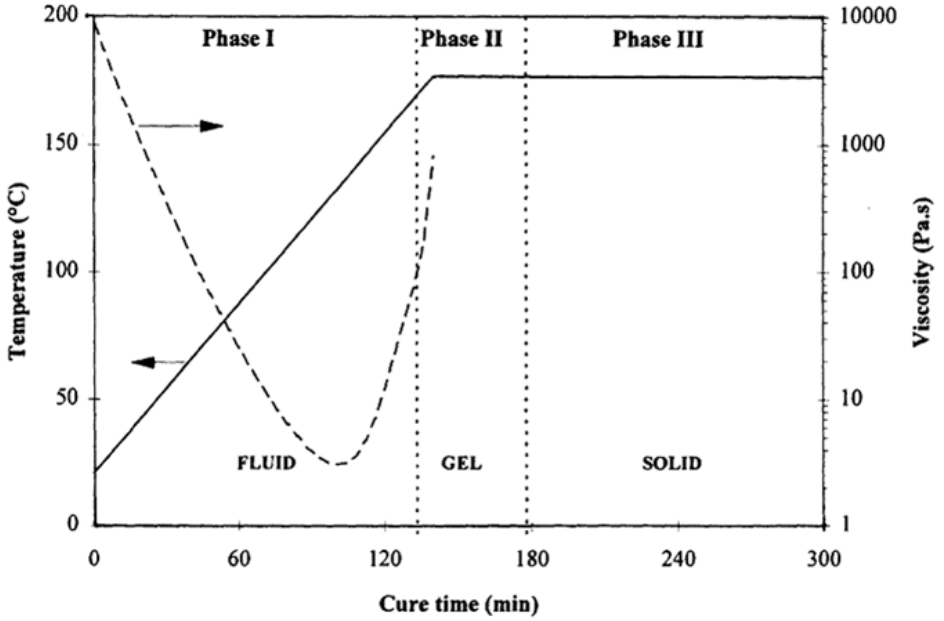

Figure 2–9: Graph of the evolution of the resin viscosity μ with time for a standard cure cycle [20]

an increase in degree of cure leads to longer molecular chains, and therefore to higher viscosity. The traditional effect of these two competing factors on resin viscosity is shown in Figure 2–9. Initially, as the temperature increases and the resin degree of cure is low, the thermal effect is predominant and the viscosity decreases. Then, as the degree of cure begins to increase more rapidly while the temperature approaches the isothermal dwell, the process becomes cure-driven and the viscosity begins to increase at an increasing rate until gelation [20].

For thermoset composite flow analysis, epoxies are assumed to exhibit Newtonian behaviour. As summarized by Hubert and Poursartip [20], two arguments have been used in the literature to justify this assumption. First, flow in high fibre volume fraction preforms is creeping, and is likely to involve

relatively low shear rates. Conversely, non-Newtonian behaviour is associated with relatively high shear rates [11]. Second, most infiltration flows occur in the early stages of the process cycle, while the resin degree of cure is low. During this time, the resin likely remains primarily a viscous fluid. Thus, deviations from shear rate-independent behaviour, which have been reported as the resin approaches the gel point and behaves increasingly like a solid (for example, [37]), are likely to be minimized. While the strict validity of this assumption may also depend on the formulation of individual resins, the Newtonian approach has been applied to many commercial systems, has led to a large body of characterization and flow analysis literature, and is likely reasonable.

Characterization efforts mirror those used to analyze the degree of cure. Experimentally, the resin viscosity is obtained using thermorheological tools such as parallel plate rheometers, which allow measurements under the dynamic and isothermal temperature conditions relevant to processing. Then, this data may be used to obtain the fitting constants of semi-empirical models. A common relationship is that suggested by Castro and Macosko [38], which relates the dynamic viscosity to the instantaneous temperature and degree of cure and has been commonly cited [32, 35, 36].

2.2.4 Void Formation in Composite Processing

The primary defects governed by consolidation phenomena are voids, or unfilled pores present within the microstructure. During processing, porosity may be gas-induced, caused by the presence of bubbles within the resin, or flow-induced, caused by incomplete wetting of the preform by the resin matrix.

Gas-induced porosity may arise due to many phenomena: volatiles released by the chemical polymerization reaction, moisture absorbed by the resin at ambient conditions and released as vapor during processing, and air entrapped during layup. These gases may be evacuated in the initial stages of processing if the laminate is permeable and vacuum is applied under the bag for a sufficient period of time; this evacuation process has also been described using Darcy's Law for flow in porous media [39]. If, however, volatiles do remain, they result in an air bubble within the resin and, potentially, in a void within the final part. While the resin is fluid, the bubble size is a function of the gas pressure within it, P_{void} and the resin pressure surrounding it, P_r, with the condition for void growth being:

$$P_{void} > P_r \tag{2.11}$$

Conversely, if $P_{void} < P_r$, the void will shrink. The void pressure is a function of many variables, including the nature of the gas within it and the process temperature. The resin pressure is a function of the applied pressure on the laminate and of flow and compaction phenomena [1]. The most commonly cited model for void growth is that of Kardos et al. [40], which considers temperature, pressure and moisture factors in the context of autoclave processing.

Flow-induced porosity (often referred to as "dry spots") may arise if areas of the preform remain unimpregnated due to incomplete infiltration caused by slow flow rates, premature resin gelation or excessive resin loss during consolidation. Such porosity may arise even in the absence of entrapped gases. The formation of such porosity may be predicted using resin flow models.

2.3 Methods for Analyzing Consolidation Flow Phenomena

Several methods have been used to study consolidation in composites processing. So far, most work has focused on autoclave prepregs or liquid composite moulding, and the considerable knowledge thus amassed has been reviewed in many texts (including books [1,10,28,41] and review articles [20]). The aim of this section is to identify possible approaches to analyze consolidation in view of their potential applicability to OOA prepreg manufacturing.

2.3.1 Experimental

Experimentally, flow and compaction during composites processing may be investigated using in-situ sensing or microstructural analysis.

2.3.1.1 In-Situ Sensing

In-situ sensing consists of using embedded sensors to obtain the time histories of measurable material properties, including temperature, resin pressure (and/or flowrate) and laminate thickness.

Temperature measurement is common, both for industrial process control and for research, and is recommended by material manufacturers [42]. Generally, thermocouples are embedded in the tool or in the part itself in order to detect any deviations from the desired cure cycle (such as thermal lag due to the mass of the tool, or temperature overshoots due to resin exotherms).

Resin pressure is commonly measured in LCM processes such as RTM using point probes embedded in the tool, and flowmeters may also be used to measure mass tranfer at inlet or outlet gates [9]. In LCM processes, flow is often assumed to occur only in-plane, and point measures thus offer valuable data about the flow front arrival and subsequent evolution of the resin pressure

behind it. Furthermore, this data can then be used for process control or matched to simulation predictions [9].

Resin cure data may also be obtained in-situ using frequency-dependent electromagnetic sensing (FDEMS); furthermore, FDEMS may also capture aspects of flow and mechanical properties. While such an approach is not prevalent, authors have suggested its use for process monitoring, control and optimization [43].

In prepreg processing, acquiring detailed, accurate and reliable data about the temporal and spatial variation of the resin pressure is more difficult [20]. Sensors located in the tool and their associated wiring must withstand autoclave temperatures and pressures and be integrated so as to measure the fluid pressure alone, without the contribution of the compressing fibre bed. Furthermore, pressure data at the tool surface may not provide full information about prepreg resin flow, which can occur in multiple dimensions, and localized devices (such as needle-tipped probes) may be needed. Despite these challenges, prepreg resin pressure measurements have been reported by several authors for flat, fully saturated laminates (for example, [44–46]).

In-situ tracking of laminate thickness can also be valuable for processes in which fibre bed compaction and resin flow are coupled. Such measurements have been reported based on linear variable differential transformer (LVDT) point sensors [47] or full-field stereophotogrammetry [48, 49].

2.3.1.2 Microstructural Observation

The most direct method of microstructural analysis is direct visual flow observation. For LCM flows, transparent mould walls (such as clear acrylic or glass for RTM or a vacuum bag for vacuum resin infusion processes) are

commonly seen in the literature (for example, [50–53]), and allow fairly easy observation. For prepregs, where fluid migration is internal and occurs over smaller length scales, direct observation is much more challenging, and requires "tagging" the resin with a visible marker and observing flow ex-situ, as in the study by Hubert [3].

More exotic methods have also been used to analyze flow. Poursartip et al. [54] used elemental analysis within a scanning electron microscope to measure resin content and track resin flow. Neacsu et al. [55] used a copper wire sensor system embedded in a large-scale representative model of a fibre tow to measure capillary-driven flow front arrival times. In a different study, Neacsu et al. [56] also visualized a similar capillary-driven water infiltration of a model fibre bundle using magnetic resonance imaging (MRI). Endruweit et al. [57, 58] also proposed and validated the MRI approach for tracking textile impregnation in conditions that were closer to processing. Finally, Thomas et al. [59, 60] used ultrasound to visualize the progressive infiltration of resin into a dry fibre layer in-situ.

Finally, analysis of cured laminates is commonly used to gain post-mortem information about flow and compaction phenomena. Direct observation of external features and optical microscopy of polished samples may be used to determine microstructural features such as the fibre volume fraction and the amount, distribution and morphology of defects such as porosity.

2.3.2 Modelling

Flow modelling may, for clarity, be broadly divided into two categories: those focusing on the resin bleed-based consolidation of saturated prepregs (generally developed to analyze autoclave processing) and those focusing on

the infiltration of dry fibre beds (generally developed for RTM and other LCM variants).

2.3.2.1 Prepreg (Autoclave) Models

When a consolidation pressure is applied to a flat laminate consisting of multiple layers of traditional (autoclave, saturated) prepreg, it is initially carried entirely by the resin. Then, resin begins to bleed out of the laminate through any boundaries that allow it (be they the laminate edges or the top surface) and the laminate thickness starts to decrease. Therefore, the fibre bed progressively compresses and carries an increasing portion of the applied load, reducing the resin pressure and, by extension, increasing the potential for void formation and growth. Consolidation ceases due to one of two causes: either the applied pressure is carried entirely by the fibre bed and the laminate thickness reaches equilibrium, or the resin gels. [1].

The outputs of interest during consolidation are, primarily, the fibre volume fraction within the laminate (or the thickness) and the resin pressure. The fibre volume fraction controls the mechanical properties and dimensional accuracy of the cured part; the resin pressure can be used to obtain the velocity field and is a critical porosity control mechanism. The primary inputs are the material properties of the fibres and resin and the process temperature and pressure.

The first notable consolidation model applicable to prepreg processing was developed by Loos and Springer in the early 1980s [61, 62]. Their model consists of four interacting components predicting thermochemical resin properties, resin flow, void growth and residual stress formation. The flow model, which is of particular interest, is based on Darcy's Law, decouples the in-plane

and out-of-plane flows and assumes that the prepreg plies are compacted sequentially from the top if only out-of-plane resin bleeding occurs. Hence, it is known as the "sequential compaction model". The authors compared predictions for temperature and resin mass loss with experimental data, and saw good agreement.

In the late 1980s and early 1990s, models applicable to autoclave prepregs were also developed by Gutowski et al. [21, 63] and Davé et al. [64–66] and further validated by Dudukovic et al. [67]. These similar models make use of the now-traditional assumption that the applied consolidation pressure is shared between the fibre bed effective stress and the resin pressure (previously presented as Equation 2.5); they have been shown to be more general formulations of the approach of Loos and Springer [68]. While some differences exist in their solution methods, these models also predict resin flow and fibre volume fraction data in light of input material properties and process parameters. Both models were compared to experiments on flat laminates, and showed good agreement with measured values.

Subsequent efforts focused on extending the above approach to more complicated features, mainly through its implementation into numerical codes. Finite element models developed by Young [69], Hubert et al. [70] and Li and Tucker [71], for example, allow the analysis of complex geometries involving angles and thickness tapers and the prediction of the effect of flow and compaction on geometric deviations (such as corner thinning or thickening).

2.3.2.2 Liquid Composite Moulding

In contrast to autoclave prepreg processing, LCM part manufacture involves massive resin infiltration into a dry fibre preform. Generally, the resin

enters the preform from one or more inlet points (or boundaries) and forms a flow front that advances towards one or more outlets. The difference between inlet and flow front pressures drives the flow front forward and, between these two boundaries, the resin pressure decreases in accordance with Darcy's Law.

The prediction of the flow front progression as a function of part geometry, temperature, pressure and constituent material properties is the key interest in LCM analysis. Once these flow dynamics are predicted, the time to full infiltration may be optimized and the presence of any remaining dry areas may be addressed.

LCM modelling efforts have been the subject of a great quantity of literature, and several detailed reviews of their evolution are available [10, 28]. Fundamentally, LCM flow modelling is based on formulating the governing equations for moving boundary flows in porous media and solving the resulting system either analytically (for simple geometries) or numerically (for more complex situations). Initial models were applicable to isothermal, saturated flows with constant fibre bed thickness and properties, which are appropriate for closed-mould, matched-die processes such as RTM. With time, however, they have been generalized to other LCM processes and have grown increasingly sophisticated. Many complex phenomena have been adressed, including coupling between resin pressure and fibre bed compaction (for LCM processes with one or more flexible boundaries); unsaturated flow (or flow occurring on two length and time scales due to dual-scale porosity networks in fabrics); the effect of capillary action (wetting); "racetracking", or preferential flow in gaps between the preform and mould walls; void formation; non-isothermal conditions, and resin cure [10].

In light of the partially impregnated nature of OOA prepregs, a particularly relevant issue is that of unsaturated flow, or flow in which the preform region behind the flow front is only partially impregnated with resin [72]. Such a situation may occur if the micro-pores within the tows fill with resin at a slower rate than the larger, surrounding macro-pores due their lower permeability, and can lead to entrapped air within the tows and porosity in the cured part. Several tow impregnation models may be found in the literature, either used to understand the physical relations governing tow impregnation or coupled into larger-scale LCM simulations (for example, Advani and Sozer [10], Chan and Morgan [73], Sadiq et al. [74] and Foley and Gillespie [75]).

2.4 Out-of-Autoclave Prepreg Processing

In contrast to autoclave and LCM processes, literature on OOA prepreg processing is scarce and dispersed around a number of different topics: general material and process descriptions; OOA resin properties; prepreg permeability and gas flow; void formation, and, finally, flow and compaction phenomena.

2.4.1 General Material and Process Descriptions

Thorfinnson and Biermann [6, 7] were the first to discuss the effect of prepreg formatting on process phenomena and final part quality. In the mid-1980s, they presented two experimental studies whose results show that partially impregnated prepregs allow the autoclave manufacture of high quality parts without the use of the time-consuming debulking steps traditionally used to remove air during the lay-up of thick laminates. They suggested that the relatively permeable network of dry zones present in such prepregs allows entrapped air and other volatiles to exit in the initial stages of autoclave processing.

Despite this suggestion, further discussion of prepreg formatting is limited until the 2000s, when, through a series of technical papers, material development teams presented a new generation of OOA prepregs and demonstrated the viability of vacuum bag-only processing for several part geometries [4, 5, 76–83].

Repecka and Boyd [4] and Ridgard [5] outline several features common to all OOA materials, and emphasize important characteristics of the layup, bagging and cure of OOA prepregs.

The key requirement for OOA processing of low porosity parts is the removal of air entrapped during lay-up, since the high autoclave pressures used to suppress void formation and growth are not accessible in vacuum bag-only cure [5].

To favor this removal, OOA prepregs are "breathable", featuring partially impregnated microstructures consisting of both resin-rich and dry areas. The latter, sometimes denoted as "engineered vacuum channels" or "eVaCs", are relatively permeable in the initial stages of processing and allow gas migration towards the laminate boundaries; then, they are infiltrated by resin to produce a void-free microstructure [4, 5].

To allow gases to escape from the laminate's dry areas into the bag, OOA bag assemblies must include permeable boundaries that connect the laminate to the breather cloth. For in-plane gas evacuation, these paths may take the form of dry fibreglass strands, cork or other "edge breathing" arrangements placed at the laminate edges. For through-thickness air evacuation, perforated release film is used to separate the top laminate surface from the breather [4,5].

The cure cycles used for OOA prepreg processing also feature three notable differences relative to autoclave processing. First, since maximizing air evacuation and consolidation pressure is essential, the quality of the vacuum in the bag is critical. A maximum bag pressure of 6500 Pa (usually specified as a minimum vacuum gauge reading of 28 in Hg) is generally recommended, and the importance of a leak-proof bag is emphasized [4, 5, 76, 84, 85]. Second, an initial room-temperature vacuum hold is recommended to evacuate gases entrapped during laminate lay-up [84, 85]. This hold may range from a few hours for small parts to more than 16 h for larger components. Third, OOA dwell temperatures generally range from 80 °C to 121 °C, and are therefore lower than the traditional 177 °C used for epoxy-based autoclave prepregs. This decrease achieves two aims: in conjunction with the resin formulation, it ensures a resin viscosity profile that allows enough time for air evacuation through the dry fibre regions but full prepreg impregnation before gelation [5], and it may also mitigate void growth by limiting the void gas pressure. However, OOA prepregs require an additional "post-cure" to maximize the resin's thermomechanical properties.

These process descriptions offer useful guidelines and suggest that successful OOA processing depends on several concurrent phenomena. However, they provide few details on the fundamental physics that may be involved during manufacture.

2.4.2 OOA Resin Properties

Kratz et al. [36] characterized the cure kinetics, viscosity and glass transition temperature behaviour of two common OOA epoxy matrix resins: Advanced Composite Group's MTM45-1 and Cytec Engineered Materials' Cycom 5320.

For the cure kinetics model, they combined the models proposed by Kamal and Sourour [33] and by Cole et al. [34] into the following expression:

$$\frac{d\alpha}{dt} = K_1\alpha^{m_1}(1-\alpha)^{n_1} + \frac{K_2\alpha^{m_2}(1-\alpha)^{n_2}}{1+\exp(D(\alpha-(\alpha_{C0}+\alpha_{CT}T)))} \tag{2.12}$$

where K_i is the Arrhenius temperature dependency:

$$K_i = A_i \exp(-E_{Ai}/(RT)) \tag{2.13}$$

For the viscosity model, they resorted to the model used by Khoun et al. [35], a modification of the model proposed by Castro and Macosko [38]:

$$\mu = \mu_1 + \mu_2 \left(\frac{\alpha_{gel}}{\alpha_{gel}-\alpha}\right)^{A+B\alpha+C\alpha^2} \tag{2.14}$$

where μ_i is the Arrhenius temperature dependency:

$$\mu_i = A_{\mu i} \exp(E_{\mu i}/(RT)) \tag{2.15}$$

For the glass transition temperature, they used the common DiBenedetto model [86]:

$$\frac{T_g - T_{g0}}{T_{g\infty} - T_{g0}} = \frac{\lambda\alpha}{1-(1-\lambda)\,\alpha} \tag{2.16}$$

In the above equations, R is the universal gas constant. In the cure kinetics model, E_{Ai} is the activation energy of the resin; D is a diffusion constant; α_{C0} is the critical degree of cure at absolute zero; α_{CT} accounts for the latter's increase with temperature; A_i, m_i and n_i are constants. In the viscosity model, $E_{\mu i}$ is the viscosity activation energy; α_{gel} is the degree of cure at gelation; and A, B, C and $A_{\mu i}$ are constants. In the glass transition temperature model, T_g is the glass transition temperature corresponding to a degree of cure α, $T_{g\infty}$ and T_{g0} are the glass transition temperatures of fully cured and uncured resin, respectively, and λ is a shape parameter used as a fitting constant. The numerical values of all constants for the MTM45-1 and 5320 resins are provided in [36]. These models may be used to predict the evolution of these properties for any temperature cycle.

The results presented by Kratz et al. [36] show that the time-temperature cycle has a significant impact on resin viscosity, suggesting that cure cycle selection is a critical step in OOA processing. In general, the authors suggest that, for these representative materials, a "flow time" at low viscosity (defined as below 100 Pa s in their study) of approximately 60 - 120 min (depending on dwell temperature) may be available for prepreg impregnation.

2.4.3 Gas Flow and Air Evacuation

The gas flow involved in OOA prepreg processing has been studied by several authors in the context of prepreg permeability, air evacuation and void formation.

Arafath et al. [39] developed a model for gas evacuation in prepregs applicable to OOA materials. The model, based on Darcy's Law and mass continuity equations, was combined with measured permeability values for

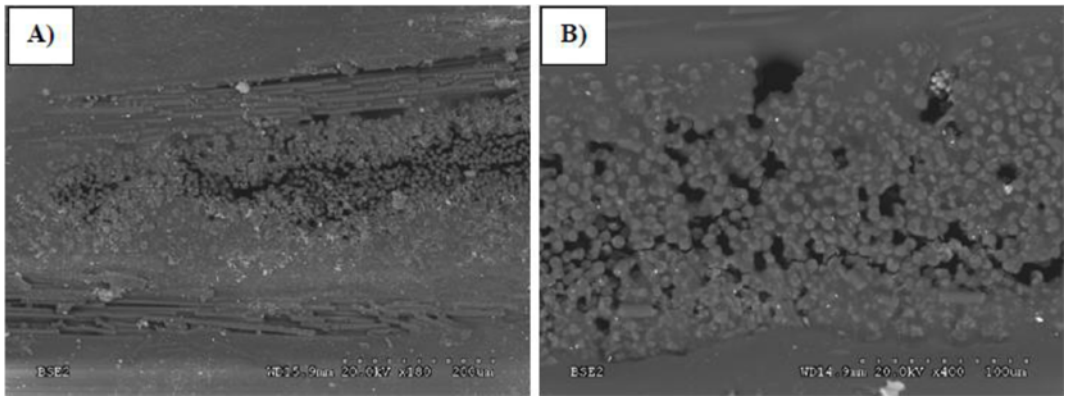

Figure 2–10: SEM micrographs showing micro-voids in an uncured MTM45-1/5HS laminate at two different magnification levels (A, B) [87].

a traditional autoclave prepreg and used to estimate the time required to evacuate a known mass fraction of air from a laminate. Their results showed that the time required to evacuate air varies linearly with permeability and quadratically with length, and logarithmically with mass fraction, and may quickly increase. For example, for the materials considered, evacuating 90 % of the air from a 1 m long laminate requires approximately 36 min, while doing the same for a 4 m part would require over 7 days.

Louis et al. [87] measured the permeability of an OOA prepreg based on MTM45-1 resin and an five-harness satin (5HS) fabric in the in-plane and through-thickness directions, under a variety of process-relevant conditions. Their results showed that the in-plane permeability is several orders of magnitude higher than the transverse, suggesting that in-plane air evacuation through edge breathing dams is the dominant gas extraction method. Furthermore, they also imaged the prepreg microstructure using scanning electron microscopy (SEM), and detected the presence of micro-porosity within the fabric's dry fibre tows (Figure 2–10).

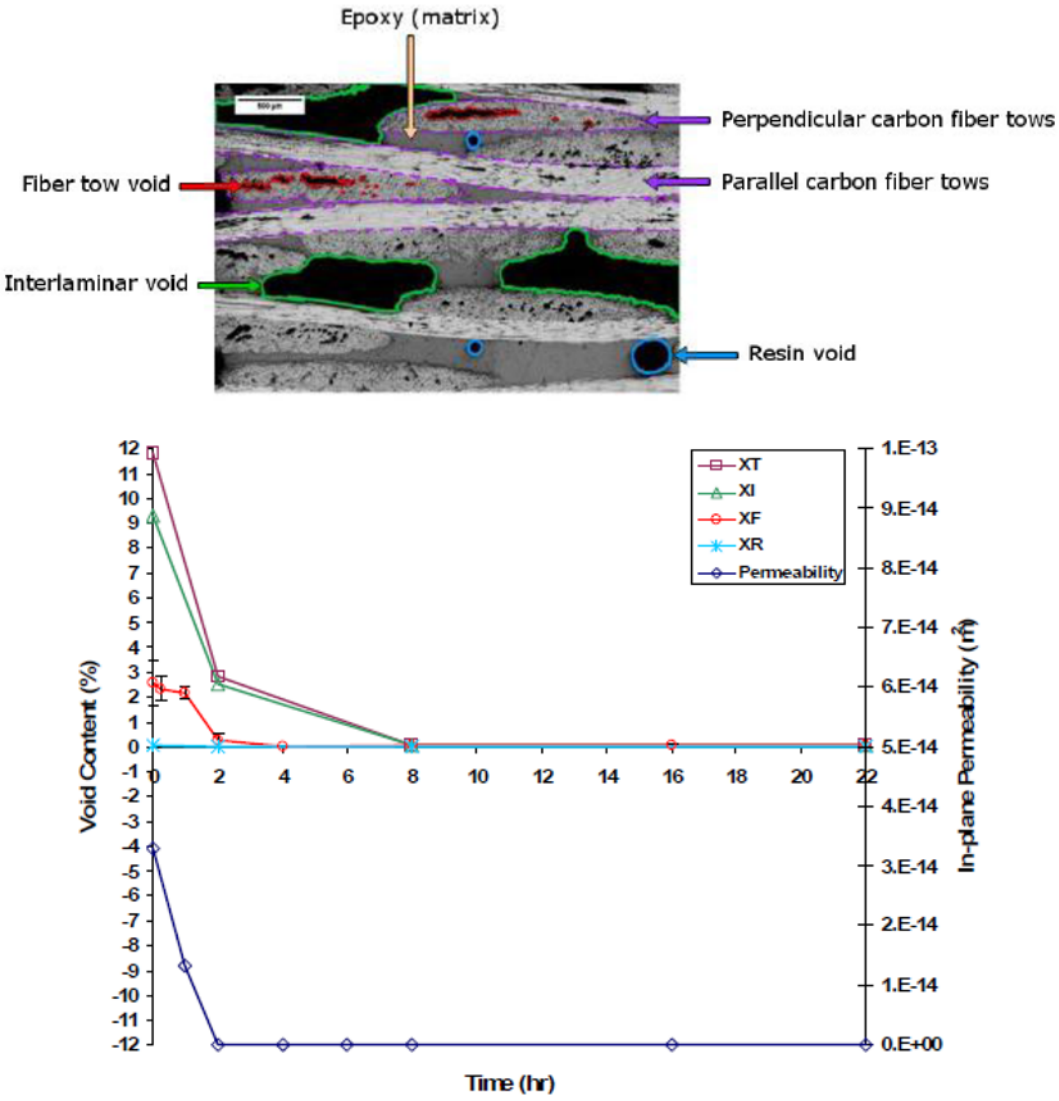

Figure 2–11: Optical micrograph showing examples of void morphology (top), and graph showing the evolution of total void content (XT), as composed of interlaminar voids (XI), fibre tow voids (XF) and resin voids (XR) as well as prepreg in-plane permeability over a benchmark cure cycle (bottom) [88].

Fahrang et al. [88] measured the evolution of the same prepreg's in-plane permeability during processing and compared it with the evolution of inter-laminar, resin and fibre tow voids, measured using optical microscopy. Their data showed that the material under analysis does indeed initially feature significant levels of all three pore morphologies, but that during processing, these levels decrease. It also demonstrated a correlation between the prepreg's in-plane permeability and the amount of fibre tow voids (shown in Figure 2–11). This observation thus supports the assumptions that air evacuation is favored by a partially dry fibre tow network.

Gas flow through OOA prepregs has also been investigated by Tavares et al. [89–93] and Kratz et al. [94–97] in the context of honeycomb sandwich structures. While the inclusion of a honeycomb core adds significant complexity, such studies have highlighted that composite facesheet properties such as fibre bed architecture, resin cure kinetics and rheology, and prepreg impregnation and permeability combine with process parameters such as the cure cycle to significantly impact the in-plane and transverse gas flows and the final part quality.

2.4.4 Void Formation

Void formation in OOA prepreg processing has also been considered. As previously mentioned, Fahrang et al. [88] investigated the evolution of porosity within a laminate for an MTM45-1/5HS prepreg and a single cure cycle, and detected both the gradual impregnation of dry fibre areas and the progressive disappearance of bubble-shaped, likely gas-induced voids due to air evacuation and hydrostatic resin pressure (Figure 2–11).

Hsiao et al. [98] and Kay and Fernlund [99] both investigated the effect of process parameters on macro-voids within MTM45-1/5HS laminates and determined that reduced vacuum levels, increased ambient moisture, larger part sizes, and shorter room-temperature vacuum hold times increase porosity.

Grunenfelder and Nutt [100] considered the specific impact of dissolved moisture on void formation for an OOA prepreg with MTM44-1 resin and a 2x2 twill carbon fabric. Their experiments showed that water absorbed by the resin may have adverse effects on resin cure kinetics and gel time, and result in bubble-like resin voids. Furthermore, a void formation model based on the same phenomena found good agreement with the measured trends.

Grunenfelder and Nutt [101, 102] also investigated the effects of room-temperature exposure on the resin, prepreg and laminate properties of an OOA material consisting of 5320 resin and a 5HS carbon fabric. They showed that such out-time may induce resin polymerization, decrease prepreg tack and cause increased porosity and reduced mechanical properties in the final part. Figure 2–12 shows optical micrographs of autoclave- and vacuum bag-only-cured laminates at three different out-time levels. Interestingly, the VBO laminates show porosity primarily inside the fibre tows, suggesting that the out-time-induced resin viscosity increase affected resin infiltration into these dry fibre areas.

Finally, void formation has also been researched in the context of complex shape parts by Brillant [103], Brillant and Hubert [104], and Cauberghs and Hubert [105], who considered the relationship between corner geometries, layup, consumable arrangement and part quality. Their key findings

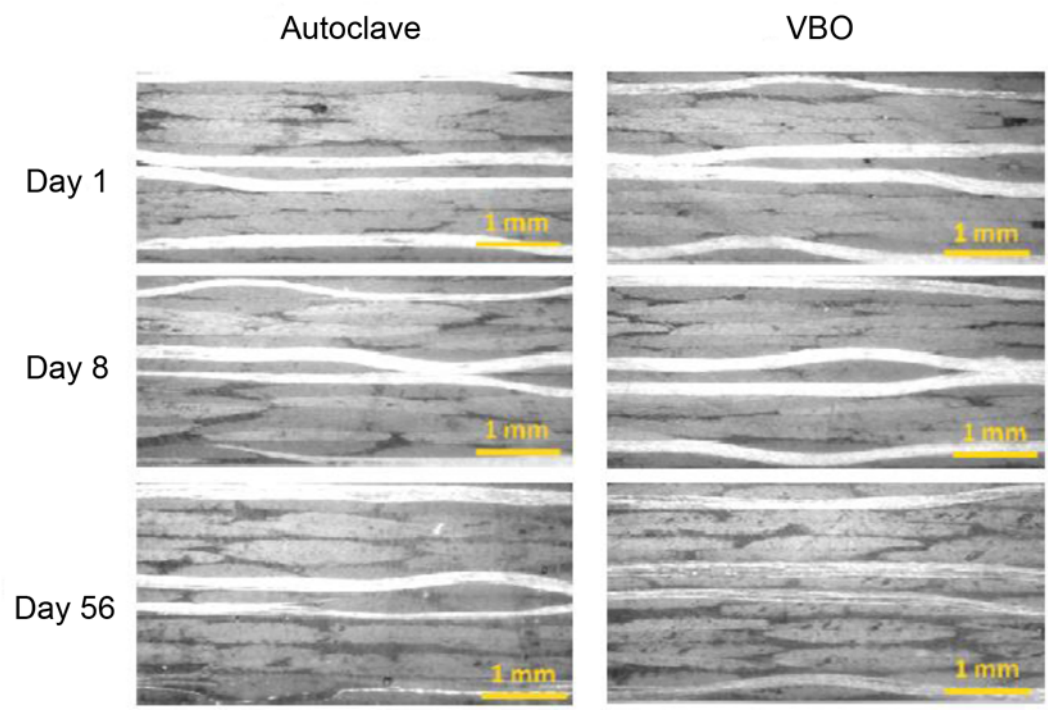

Figure 2–12: Optical micrographs showing an increase in porosity with increased out-time in autoclaved and vacuum-bag-only (VBO) cured laminates (adapted from [102]).

show that corners can feature significant voids and thickness deviations, particularly for tight radii, due to a combination of locally reduced consolidation pressure, prepreg bulk factor and consumable bridging, but that adjustments to laminate thickness and consumable arrangement may mitigate defects.

2.4.5 Flow and Compaction

Literature focusing on the fundamentals of flow and compaction in OOA prepregs is quite limited. Tavares et al. [90] measured and modelled the relationship between the progressive impregnation of an OOA prepreg honeycomb structure facesheet and its through-thickness permeability. However, the material used features resin applied in strips over portions the dry fibre bed, and

is therefore not representative of latest-generation OOA prepregs, which are formed using resin films applied to the entire surface of one or both sides of the reinforcement.

Thomas et al. [59,60] tracked the transverse flow of an OOA resin (Cytec Engineered Materials' 5215) into a dry carbon fibre layer using a vacuum bag immersed in a heated water tank and ultrasonic imaging. In addition to demonstrating the viability of ultrasound in measuring resin flow, their results suggest that for their materials and process conditions, transverse flow lasted between 10 min and 50 min and was dual-scale in nature, occurring first (and faster) within the macro-pore network around the tows and then infiltrating the fibre tow cores.

Wyscocki et al. [106] proposed a generic two-phase continuum theory for the flow and compaction of partially saturated porous media, implemented it into a finite element code, and considered the consolidation of an OOA prepreg hat stringer as a case study. While their approach is potentially powerful and offers the chance to consider coupled fibre bed compaction, macro-flow around the tows and micro-flow within them, the continuum approach neglects the specific geometry of the porous medium. Furthermore, the case study did not address the effect of process parameters such as pressure and cure cycle.

Fahrang et al. [88] confirmed the presence of progressive impregnation in OOA prepregs in a previously discussed study by observing the evolution of several types of porosity during cure. However, flow phenomena were not specifically considered, and the study did not evaluate the importance of material properties or process parameters.

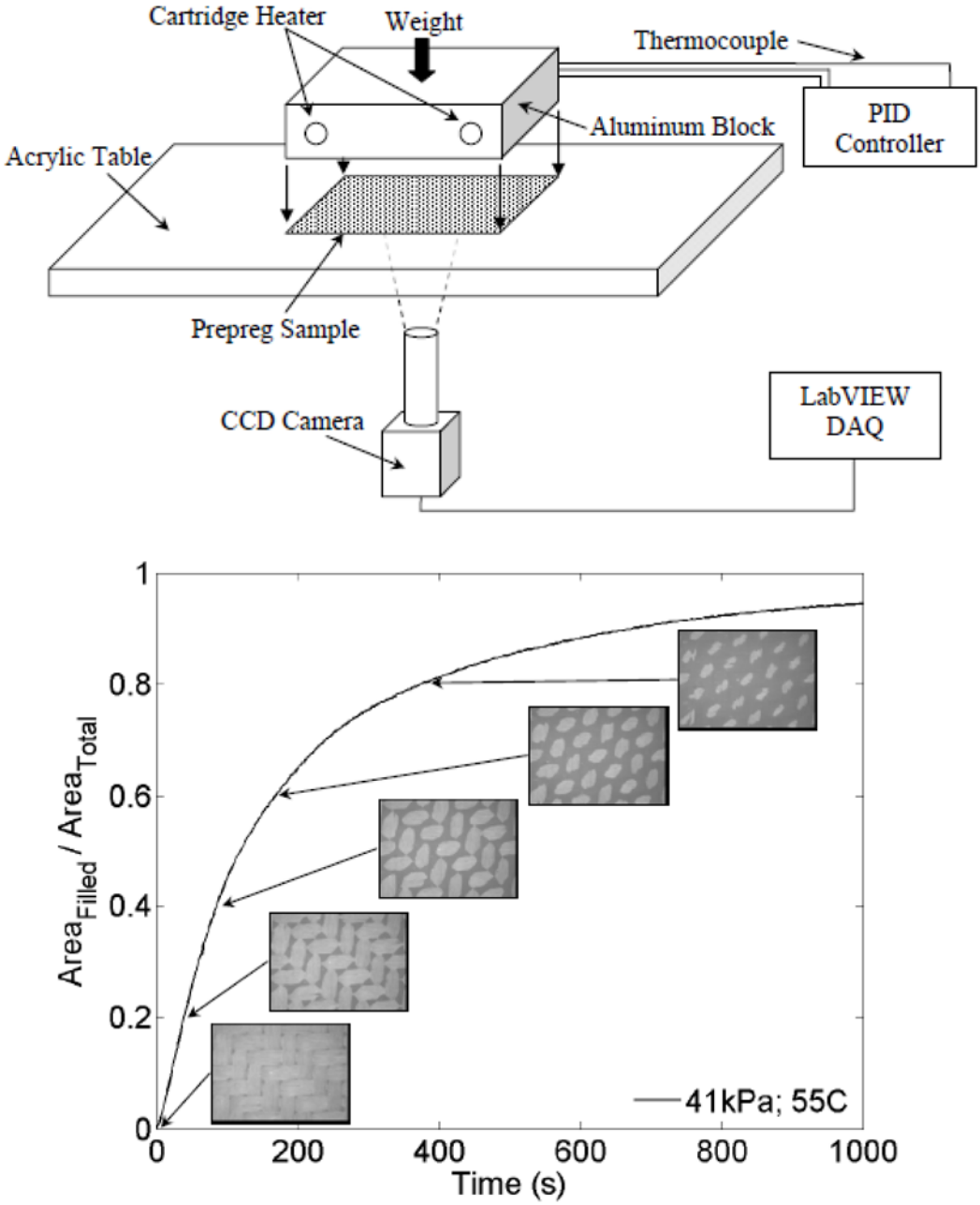

Figure 2–13: Schematic of the experimental apparatus used by Cender et al. to investigate through-thickness resin film infiltration into a dry fibre layer (top), and graph showing the evolution of preform infiltration with time (bottom) [107].

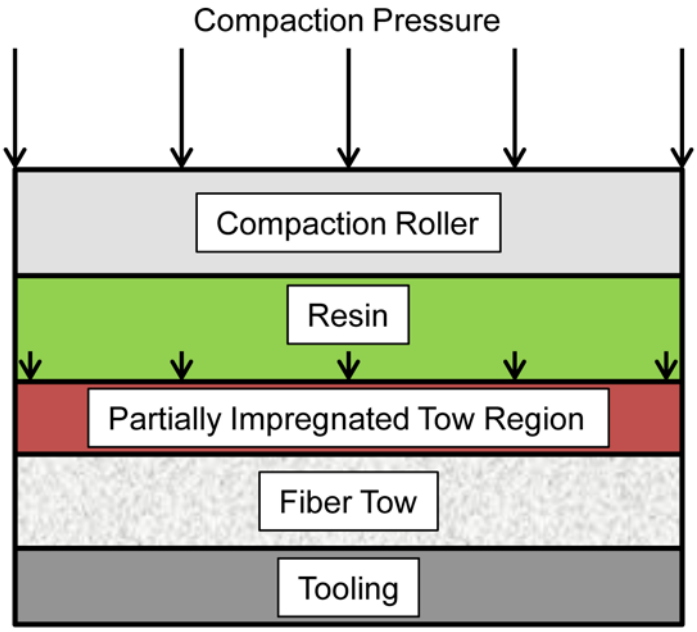

Figure 2–14: Schematic of the unit cell proposed by Gangloff et al. to model online partially impregnated prepreg consolidation during automated fibre placement (adapted from [108])

Cender et al. [107] investigated the infiltration of a resin film into a dry fibre preform. Experiments consisted of imposing temperature and pressure using a press-like apparatus (Figure 2–13), and quantifying fluid infiltration using image analysis of the preform's surface. Modelling consisted of a one-dimensional rectilinear application of Darcy's Law, cast so as to capture both macro-flow around the fabric tows and micro-flow within them. The approach clarified the flow dynamics and model predictions showed good agreement with the experimental data. However, the external flow tracking and unrepresentative process conditions make it difficult to draw conclusions about either the flow phenomena or the applicability to vacuum bag-only processing.

Finally, Gangloff et al. [108] presented a model for the partial impregnation of unidirectional tape that occurs during automated ply collation. The

model relies on the application of Darcy's Law to a rectilinear unit cell consisting of a resin film, partially impregnated tow region, dry tow region and tool (as shown in Figure 2–14), and depends on process parameters such as the tow head speed and pressure. The results showed that the percent reduction in the dry fibre region depends on the speed of collation of the tow and the applied pressure in a non-linear manner. However, while the model is versatile, the analysis was not extended to the full impregnation that occurs during processing and was not compared to experimental data.

2.5 Conclusions

The above review leads to several conclusions about the applicability of current composites processing knowledge to OOA prepregs, and about the gaps existing in the literature on OOA prepreg consolidation.

The existing frameworks used for composites process analysis are applicable, but scantily applied. The majority of published, fundamental knowledge on composites process analysis is relevant to OOA prepregs. Indeed, the constituent fibres and resin of such materials may be (and, in a limited number of cases, have been) characterized using known experiments and models, and the traditional frameworks for understanding and analyzing resin flow and void formation are applicable. However, these available tools have been infrequently used to expand the knowledge of OOA prepreg processing. Furthermore, available studies on the consolidation of such prepregs are generally limited to single materials and process conditions.

The microstructural evolution and key consolidation phenomena involved in OOA prepreg processing have not been systematically studied or fully understood. The partial impregnation of OOA

prepregs has been implied in some studies [4, 5, 77, 78] and shown, in a few others, to at least partly consist of micro-porosity between fibres [87, 88, 102]. However, the precise quantity, morphology, distribution and evolution of dry and resin-rich areas in commercially-available and commonly-used OOA prepregs has not been systematically determined. A more detailed description of the microstructural changes in OOA prepregs during processing is therefore a natural first step towards better understanding them.

The dependence of impregnation and defect formation phenomena on material properties and process parameters has not been studied. The flow and compaction phenomena that constitute the progressive impregnation of OOA prepregs are likely (and have been suggested) to depend on several material properties and process parameters, many of which may be controlled during part manufacture. However, limited knowledge is available on each factor's effect and importance, since essentially all studies are restricted to single materials (and thus fibre bed architectures and resins), temperature cure cycles and consolidation pressure conditions. Hence, a better understanding of these relationships is also required in order to optimize OOA processing.

Furthermore, some process inputs may also be subject to uncontrolled deviations from their ideal state. Given the reduced consolidation pressure (relative to the autoclave benchmark), it is reasonable to assume that OOA processing may benefit from fewer safeguards against defect formation. Some studies have considered individual deviations (such as moisture absorption [98–100], reduced vacuum and part size [98, 99], and out-time [102]), but have focused on one material and on void formation rather than overall

consolidation phenomena. Therefore, the sensitivity of OOA prepreg consolidation to potentially "deficient" conditions, and hence the robustness of the approach, should be further assessed in order to validate its viability.

Additional experimental and modelling tools are desirable. To achieve the above goals, a combination of experiments and modeling is necessary. Several experimental approaches for prepreg consolidation analysis have been identified. However, acquiring accurate, detailed and useful data remains a challenge, and the development of new characterization and process monitoring tools is of interest. Similarly, many flow models exist. However, autoclave models assume saturated prepregs, and are therefore unsuitable for OOA processing. Likewise, LCM models are generally geared towards predicting the large-scale infiltration for complex shape parts rather than flexible microstructural investigation and process evaluation. Hence, the development of a more direct, useful model that predicts OOA prepreg consolidation quality in light of the main process parameters and thus allows the identification of appropriate process windows is also desirable.

The above conclusions are summarized in Table 2–1 in terms of existing knowledge and the desirable expansion of knowledge.

Table 2–1: Existing knowledge and desired expansion of knowledge

Existing Knowledge	**1.** Fibre bed and resin behaviour **2.** Theory of resin flow in composites processing **3.** Theory of void formation in composites processing **4.** Methods for consolidation analysis in composites processing (from autoclave and LCM)
Expansion of Knowledge	**1.** OOA prepreg microstructure **2.** Effect of selectable material properties and process parameters on OOA prepreg consolidation, and potential for optimization **3.** Effect of process deviations on OOA prepreg consolidation, and process robustness **4.** New experimental methods and modelling tools for OOA prepreg consolidation analysis

CHAPTER 3
Thesis Objectives and Structure

3.1 Thesis Objectives

In light of the interest in OOA processing and the lack of detailed literature, the overall aim of this thesis is to gain a better understanding of the relationships between material properties, process parameters, physical phenomena and part quality that constitute OOA prepreg consolidation. To this effect, the following specific objectives are proposed:

1. Characterize the initial and evolving microstructure of OOA prepregs and identify the fundamental consolidation phenomena.
2. Evaluate, through complementary experiments and modelling, the effect of important material properties and process parameters on these consolidation phenomena, so as to guide process optimization.
3. Evaluate, through complementary experiments and modelling, the effect of the main potential deviations in material properties and process parameters on consolidation phenomena, and assess the process robustness.
4. Throughout the proposed research, develop new experimental methods and model(s) that address the gaps identified in the literature and aid in the analysis of OOA prepreg consolidation.

3.2 Thesis Structure

The above objectives are achieved through the research described in the following four chapters, which take a building-block approach:

- **Chapter 4** proposes and demonstrates a novel X-ray microtomography method to characterize the initial and evolving microstructure of OOA prepregs, and identifies the key consolidation phenomena: tow impregnation and void suppression.
- **Chapter 5** focuses on the development of a tow impregnation model for OOA prepregs and on its use in a parametric study that estimates the effect of several material properties and process parameters.
- **Chapter 6** investigates the effect of cure cycle and room temperature out-time on the consolidation of OOA prepreg laminates through a detailed experimental study, and identifies a predominant impact on tow impregnation.
- **Chapter 7** evaluates the effect of several deficient consolidation pressure conditions on the consolidation of OOA laminates through a detailed experimental study, and identifies specific consequences on both tow impregnation and void suppression.

The relationship between the thesis objectives and the above-listed chapters is shown in Figure 3–1.

3.3 Note on Materials

Several OOA prepregs are used within this thesis. They consist of two different epoxy resins and several carbon reinforcement architectures. The resins, Cytec Engineered Material's 5320 and Advanced Composite Group's MTM45-1, are two popular OOA systems, while the fibre beds span a wide

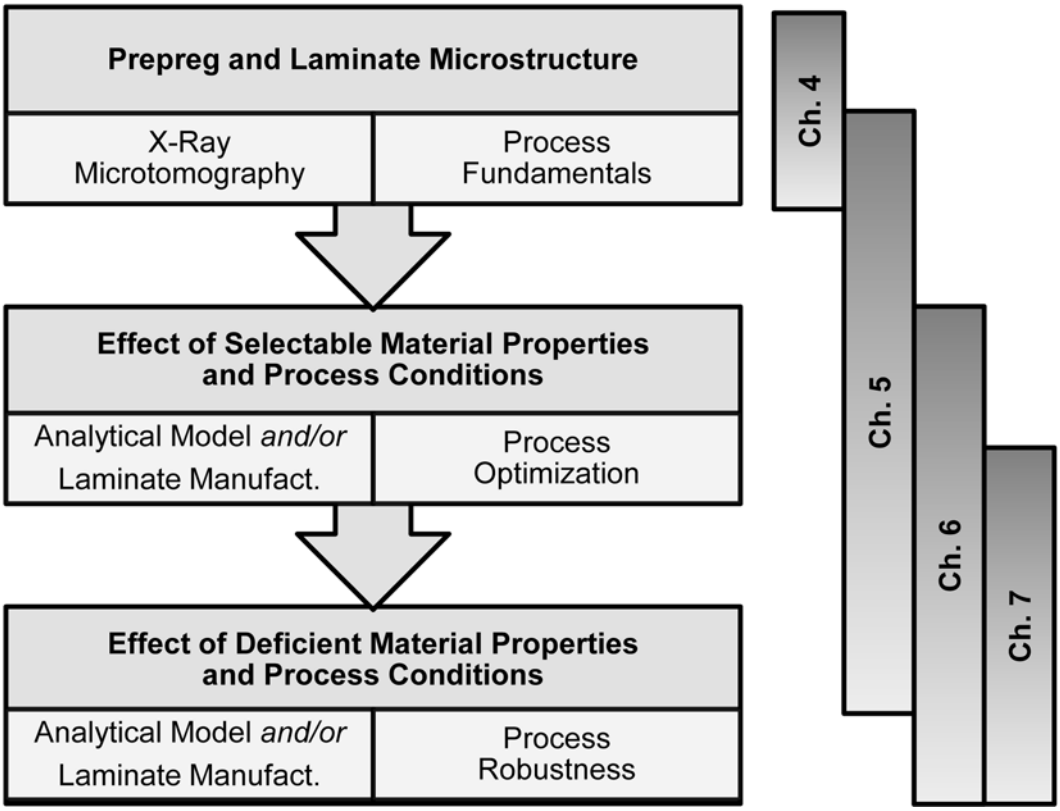

Figure 3–1: Flowchart outline of the thesis.

range of architectures, from woven fabrics to a unidirectional tape. Overall, these materials are representative of the novel class of prepregs they belong to, but also offer a variety of different properties within it.

Generally, prepregs were selected for a given study so as to vary one or more material properties of potential influence to the phenomena of interest in the study. In certain cases, material selection was also contingent on the availability of a given system at the time of the study.

CHAPTER 4
Microstructural Analysis of Out-of-Autoclave Prepregs by X-Ray Microtomography

4.1 Introduction

The manufacture of low porosity parts by OOA prepreg techniques relies on the evacuation of gases entrapped during prepregging, ply collation and vacuum bagging. To this effect, OOA prepregs are engineered to feature dry, relatively permeable areas that allow gas evacuation when vacuum is applied to the bag at the beginning of the cure cycle. These areas may consist of macro-porosity between plies and within the resin, or micro-porosity inside the fibre tows, between individual fibres. During heated consolidation, these spaces are progressively infiltrated by resin to produce an (ideally) uniform, void-free structure. A natural first step in analyzing OOA prepreg manufacturing is gaining a better understanding of the size, distribution and morphology of these dry areas within a representative OOA prepreg and, subsequently, of their evolution during processing.

4.1.1 Background

As explained in Chapter 2, several methods suitable for prepreg microstructure imaging exist, including visual observation under an optical microscope, scanning electron microscopy, ultrasound and magnetic resonance imaging (MRI). However, each of these techniques has distinct limitations.

Optical microscopy requires the prepreg sample to be embedded within mounting epoxy and highly polished, operations that may disturb the original

arrangement of the fibres and resin. Furthermore, since each sample section corresponds to a single, small, two-dimensional region and material state, the data acquired is limited. The latter limitation also applies to scanning electron microscopy.

Ultrasound offers several advantages over microscopy, including the capacity to scan samples within vacuum bags, in-situ; the potential to monitor flow as it progresses due to sampling rates on the order of minutes; and the ability to observe material changes through the thickness (as in [59, 60]). However, its spatial resolution remains too coarse relative to the diameter of individual fibres within the microstructure, and the through-thickness information it provides is projected rather than being truly three-dimensional.

MRI is capable of offering even faster sampling rates than those listed for ultrasound (as fast as 13 s, as per [56]) and may acquire fully three-dimensional data. However, in published studies, convenient "model" materials have often been used in place of actual fibres or resin due to the requirements of the technique (e.g., the resin matrix being replaced by corn syrup in [56, 58]). Furthermore, the reported spatial resolutions remain between 200 µm - 500 µm, or much higher than the diameter of individual fibres [56, 58]. Finally, the equipment required is exceedingly specialized, and not often available for materials science.

Therefore, there is a need for additional characterization tools that offer high spatial resolution and the ability to analyze samples at different stages of processing without requiring extensive and potentially damaging sample preparation.

4.1.2 X-Ray Microtomography

X-ray microtomography (or micro-CT) is an experimental technique that can provide density-based three-dimensional microstructural data. Micro-CT relies on X-ray attenuation, which may be described by [109]:

$$I = I_0 \exp\left(-\int \eta_{att,ave}(s) d\bar{s}\right) \tag{4.1}$$

I is the beam intensity at a given point, I_0 is the intensity of an unattenuated beam, $\eta_{att,ave}$ is the average linear attenuation coefficient within an incremental line element $d\bar{s}$ oriented along the direction of X-ray propagation. The linear attenuation coefficient $\eta_{att,ave}$ is related to the number of atoms encountered by the beam, and thus to a material's nature and density [109]. This fundamental fact, coupled with the measurement of X-ray intensity levels and geometric reconstruction algorithms, allows the non-destructive observation of different materials and phases within a microstructure.

A sample is placed on a rotating stage between an X-ray generator and a detector. For a specific exposure time, X-rays radiate from the generator, cross the sample while attenuating, and reach the detector to form a "shadow projection" containing information about the microstructure. The sample is then rotated a fractional amount, and a second shadow projection is obtained from a slightly offset perspective. An 180° rotation produces a projection set that is considered sufficiently complete, and which is reconstructed into parallel micro-slices using a mathematical algorithm that accounts for the point source and consequent cone-like geometry of the X-ray beam [110].

Modern micro-CT systems designed for experimental medicine and materials science offer many advantages. They inherently require no sample preparation other than trimming the sample to the required size. Furthermore, they offer very high spatial resolutions (up to 1 µm per pixel) as well as the capacity to obtain detailed three-dimensional data [110]. Micro-CT has recently been used in materials research to characterize woven fibre architectures and to inspect damage [111–115].

4.2 Objectives and Structure

The present chapter has two concurrent aims: to determine the initial and evolving microstructure of a representative OOA prepreg and, in the process, develop and demonstrate a micro-CT based method for prepreg microstructural analysis.

The proposed steps consist of processing laminates to different stages of a standard cure cycle, scanning laminate samples using micro-CT, and using the resulting X-ray micrographs to determine the key changes in prepreg microstructure.

4.3 Materials

The material chosen for this study is an OOA prepreg manufactured by the Advanced Composites Group (ACG). Its key properties are summarized in Table 4–1. The reinforcement consists of a common five harness satin (5HS) carbon fibre fabric. The resin matrix is ACG's MTM45-1 high performance toughened epoxy resin, whose cure kinetics and viscosity behaviour has been characterized by Kratz et al. [36]. From visual observation, it may be noted that the prepreg features resin films on both side of the fabric. This prepreg is denoted, from this point forward, as "MTM45-1/5HS".

Table 4–1: Properties of the MTM45-1/5HS prepreg.

Property	**MTM45-1/5HS**
Resin	MTM45-1
Resin Content	36 % wt.
Fibre Bed	CF2426A
Fibre Areal Weight	$375\,\mathrm{g\,m^{-2}}$

4.4 Procedures

4.4.1 Laminate Preparation

Laminates measuring approximately 10 cm by 15 cm were prepared according to OOA techniques. First, the plies were cut and collated according to a $[(0°/90°)_{(2,4)}]_s$ layup (while most laminates consisted of four plies, two consisted of eight plies due to early test trials). This layup, and hence the laminate thickness, was chosen so as to provide a sufficient material volume (and cross-sectional area) for analysis, but remain relatively transparent to X-rays and provide reasonable contrast in the final X-ray micrographs.

4.4.2 Laminate Partial Processing

For cure, the laminates were enclosed in a vacuum bag assembly consisting of a flat aluminum tool, a layer of tool-side release film and a layer of bag-side release film (both non-perforated), edge-breathing dams consisting of sealant tape wrapped in fibreglass cloth, breather cloth, a vacuum valve and a layer of vacuum bagging film held to the tool with sealant tape. A schematic of this consumable arrangement is shown in Figure 4–1.

The laminates were partially cured using a process cycle consisting of an hour-long vacuum hold at 25 °C (chosen on the basis of best-experience guidelines, since no specific times are provided in the MTM45-1 material

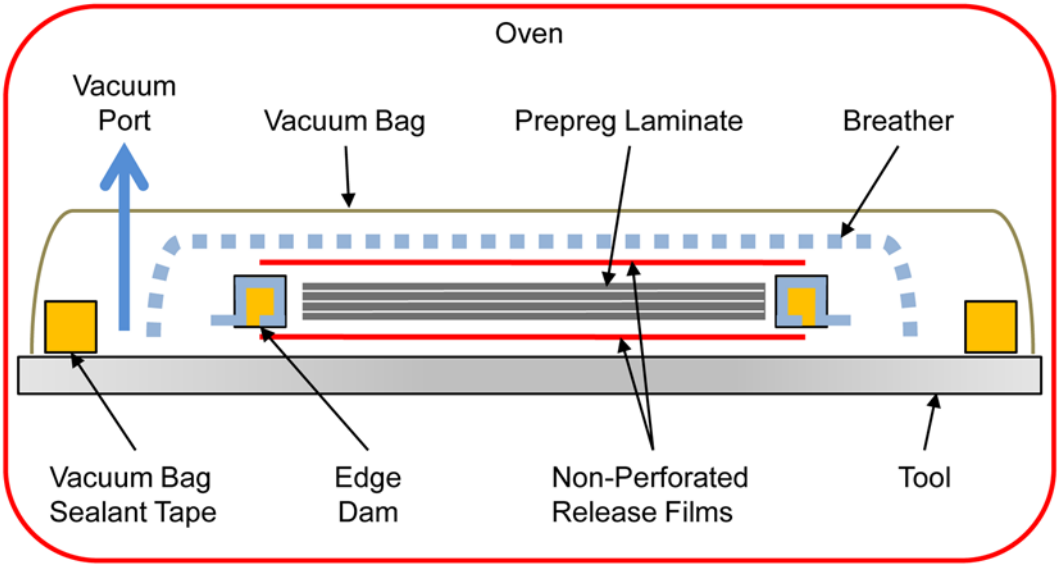

Figure 4–1: Schematic of the consumable arrangement used to manufacture the partially processed laminates.

data sheet [84]), a 2 °C min^{-1} ramp to 85 °C, and a 85 °C dwell. Laminates were partially processed to several different points within the cycle: 0 (unprocessed), 15, 30, 45 and 60 minutes, to investigate vacuum consolidation under room-temperature conditions; and 80, 93, 104, 110 and 180 minutes, to investigate consolidation under heated conditions. These laminates are numbered from 1 to 10, in order of increasing process time, and their processing is summarized in Table 4–2.

Cure occurred in a Thermal Product Solutions (TPS) Blue M convection oven. The wall-mounted Busch vacuum pumps used to evacuate the bags were able to draw sufficient vacuum for OOA prepreg processing (i.e. vacuum levels were below 5 kPa). The temperature profile common to all laminates was recorded using a type-K thermocouple (OMEGA TT-K-30-SLE (ROHS)),

Table 4–2: Laminates manufactured for micro-CT analysis.

#	Layers	Process Time	Process Conditions
1	4	0 min	None
2	4	15 min	Room temperature, vacuum
3	4	30 min	↓
4	4	45 min	
5	4	60 min	
6	4	80 min	Elevated temperature, vacuum
7	4	93 min	↓
8	8	104 min	
9	4	110 min	
10	8	180 min	

a digital acquisition system (National Instruments NI9213) and a computer equipped with LabView SignalExpress.

Once each laminate reached the desired processing stage, the vacuum bag assembly was removed from the oven, disconnected from the vacuum source and quickly cooled in a freezer. This cool-down is believed to have rapidly precluded resin flow, but not influenced any other aspect of the study.

4.4.3 Micro-CT

4.4.3.1 Scan

Two samples (A and B), nominally 15 mm by 15 mm, were cut from the center of each laminate. In addition, one sample (C) was cut from the 60 min and 180 min laminates for additional higher-resolution verification scans (described below).

Before the scan, each sample was fixed onto a copper mounting stand within a notched Styrofoam block held together with masking tape, and was thus firmly held with minimal pressure.

Figure 4–2: Photograph of the Skyscan 1172 High Resolution Micro-CT

The tomography system used for this study was Skyscan's 1172 High Resolution Micro-CT (Figure 4–2). The key scan parameters are shown in Table 4–3. The scan resolution is the spatial dimension of each pixel. The 7 µm/pixel value used for all A and B samples offers high resolvable detail (on the order of individual carbon fibre diameters and micro-porosity) as well as a field of view 27 mm wide, which allows reasonably-sized samples to be scanned. The 2 µm/pixel value for samples C was the highest attainable resolution for a reasonable field of view (5 mm). The image size defines the number of pixels in the detector's field of view; the maximum value of 4000 x 2096 pixels was chosen. The X-ray voltage and intensity were adjusted in light of the other parameters and the sample attenuation properties, mounting position and geometry to optimize contrast. Scan times were between 1 and 2 hours.

Table 4–3: Micro-CT scan parameters.

Parameters	Value
Filter	None
Resolution (samples A and B)	7 µm/pixel
Resolution (samples C)	2 µm/pixel
Image size	4000 x 2096 pixels
X-ray voltage	64 kV
X-ray intensity	154 µA

4.4.3.2 Reconstruction

Skyscan's NRecon software was used to reconstruct the raw output of the scan (or the shadow projections) into sets of parallel X-ray micrographs. All reconstruction setting were kept constant with the exception of the post-alignment, which was adjusted if needed for the best image quality. Reconstruction times were on the order of 5 h per sample.

A more extensive description of the experimental steps used during micro-CT scanning and reconstruction may be found in Appendix B.

4.5 Results and Discussion

4.5.1 Laminate Preparation and Partial Processing

The cure cycle temperatures and the predicted resin properties, calculated from Eq. (2.12) and Eq. (2.14), are shown in Figure 4–3. The temperature peaks at the end of the ramp are due to an oven set-point compensation to ensure the desired ramp rate. The predicted degree of cure of the resin exhibited only a slight increase over the total duration of the partial cure cycle, from $\alpha = 0.01$ to $\alpha = 0.03$. The predicted resin viscosity decreased from a room temperature value of approximately μ =16 700 Pa s to a minimum

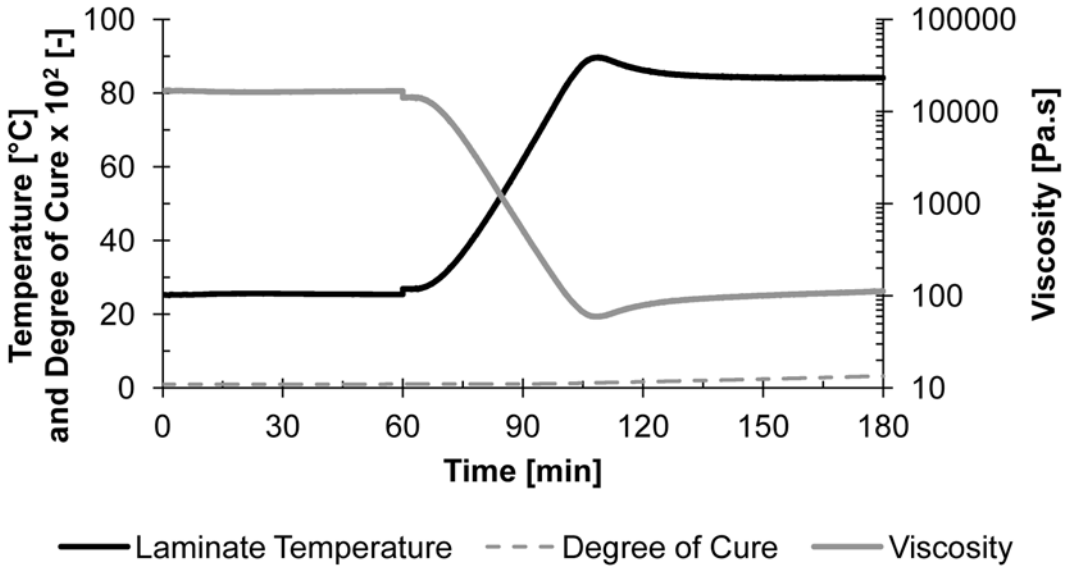

Figure 4–3: Graph of the laminate temperature and the resin degree of cure and viscosity during partial processing. The degree of cure values are multiplied by 10^2 for graphing purposes.

value of μ =59 Pa s (at the temperature peak). During the 85 °C isotherm, it exhibited a slight gradual increase to a final value of μ =113 Pa s at 180 min. Gelation, predicted to occur after approximately eight hours at the dwell temperature, was not reached. As the partial processing time increased, the laminates became progressively stiffer at room temperature (once removed from the vacuum bag assembly for sample sectioning), indicating resin cure and, potentially, a decreasing amount of relatively compliant dry fibre areas.

4.5.2 Micro-CT

4.5.2.1 Visualization

Representative X-ray micrographs for the 7 µm/pixel scans (samples A and B) are presented in Figure 4–4. By convention, brighter grayscale values denote denser areas. Voids, or areas of zero attenuation, tend towards black.

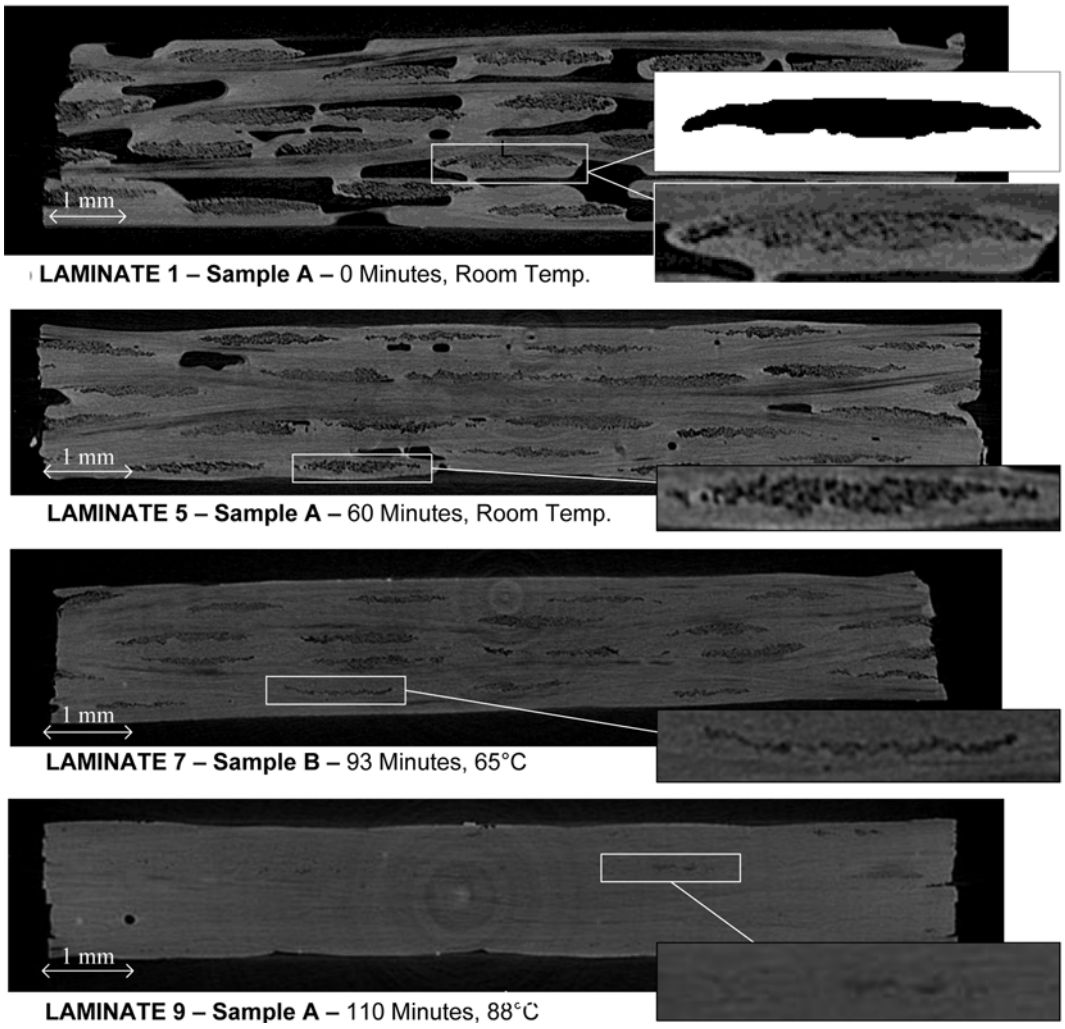

Figure 4–4: X-ray micrographs of partially processed laminates (samples A and B), with magnified insets. Brightness and contrast adjusted for visibility. The additional inset for Laminate 1 shows how the visible dry fibre tow area was measured.

Laminate 1, sample A (0 min) shows the initial, uncompacted state. Within each ply, the dark gray, ellipse-like shapes are dry, unimpregnated tow cores consisting, as seen in the magnified insert, of dense, bright fibres and dark micro-voids. These dry cores are surrounded by resin-rich regions, and the infiltration front delimiting the two is visible. Large gaps are present between plies due to air entrapped during laminate preparation. The various layers and their tows are not nested (since no consolidation pressure has yet been applied) and thus, the bulk factor of the laminate is very high.

Laminate 5, sample A (60 min) features significantly fewer inter-ply gaps due to compaction and ply adhesion during the hour-long room temperature vacuum hold. The dry fibre areas within individual fibre tows are also smaller after compaction but remain partially dry. These tows can now be clearly identified as the principal gas evacuation channels, since they offer continuous pathways through the laminate even after compaction; in contrast, inter-ply gaps are shown to be localized air pockets.

Laminate 7, sample B (93 min) and Laminate 9, sample A (110 min) show that once the process temperature increases, the fibre tows are remaining inter-ply gaps are progressively infiltrated. It is worth noting that infiltration occurs inwards from all sides, but that the flow front is non-uniform, likely due to local variations in fibre packing and transverse permeability. For the same reason, the degree of impregnation varies significantly between tows within the same sample; for example, in laminate 7, sample B, some tows are almost fully infiltrated while others have visible dry areas comparable to those of the 0 min and 60 min samples.

While the 7 µm/pixel offers large sample sizes and the ability to track impregnation for a large number of tows, it renders infiltrated regions "invisible." The tows are initially darker than surrounding resin because they consist of "bright" single fibres (density of $1.7\,\mathrm{g\,cm^{-3}}$, diameter of 7 µm) and black micro-void spaces around them. At a scan resolution of 7 µm/pixel, each pixel within a bundle may contain a portion of a single fibre and some surrounding void space, causing a "smearing" effect and resulting in a relatively dark gray shade within the X-ray micrograph. Similarly, as tows are impregnated with resin of comparable density ($1.2\,\mathrm{g\,cm^{-3}}$ [84]), the smearing results in a slightly brighter shade of gray.

The 2 µm/pixel scan resolution of the sample C scans reveals finer intra-tow details at the cost of much smaller sample sizes. Thus, these scans were used to confirm the interpretation of the 7 µm/pixel micrographs. In Figure 4–5, the tows from laminate 5, sample C (60 min) contain fibres and fibre agglomerations (bright circular areas) surrounded by dark void space, and the outline of the infiltration front is well-defined. In laminate 10, sample C (180 min), infiltration has occurred and the flow front no longer exists, but careful observation can distinguish tow boundaries, the outlines of fibre groups within the matrix and occasional micro-void spaces (which indicate that even after infiltration, some areas may remain locally unsaturated due to differences in flow).

The micro-CT data can also be visualized in three dimensions to observe macro-void distribution and morphology. Figure 4–6 shows renderings of the macro-voids (or inter-ply voids, shown in gray) inside laminates 1 (0 min), 5 (60 min) and 9 (110 min). The high bulk factor of the first laminate, due to

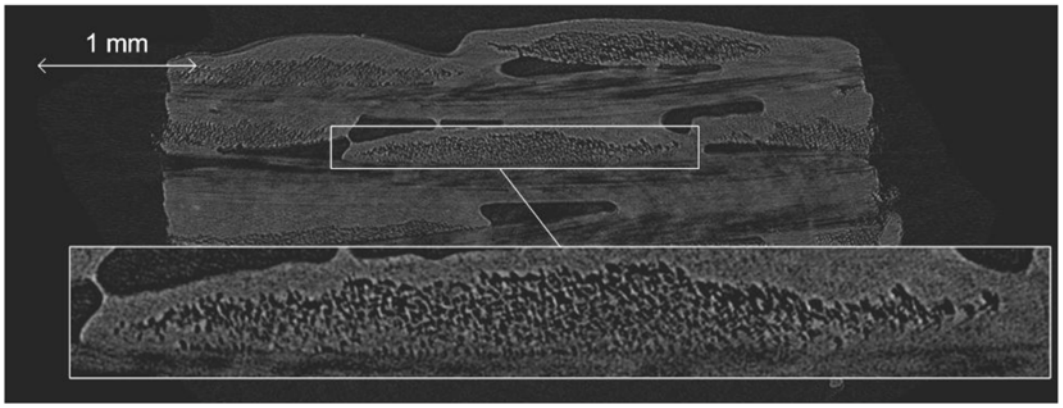

LAMINATE 5 – Sample C – 60 Minutes, Room Temp.

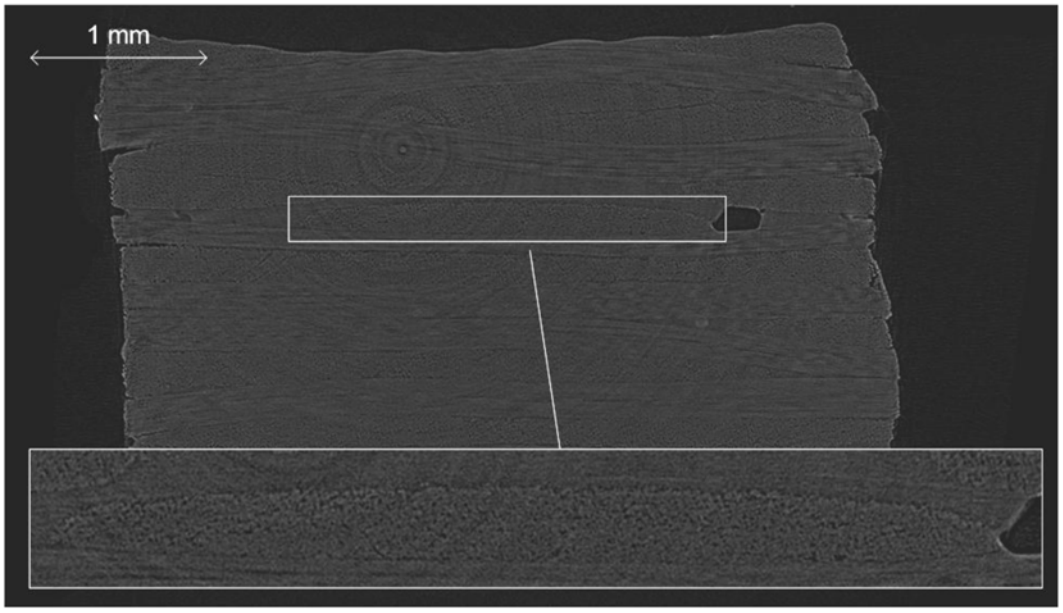

LAMINATE 10 – Sample C – 180 Minutes, 85 °C

Figure 4–5: X-ray micrographs of partially processed laminates (samples C) with magnified insets. Brightness and contrast adjusted for visibility.

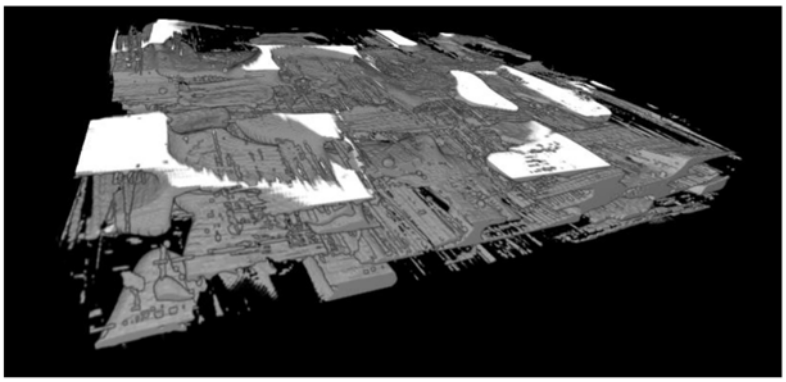

LAMINATE 1 – Sample A – 0 Minutes, Room Temp.

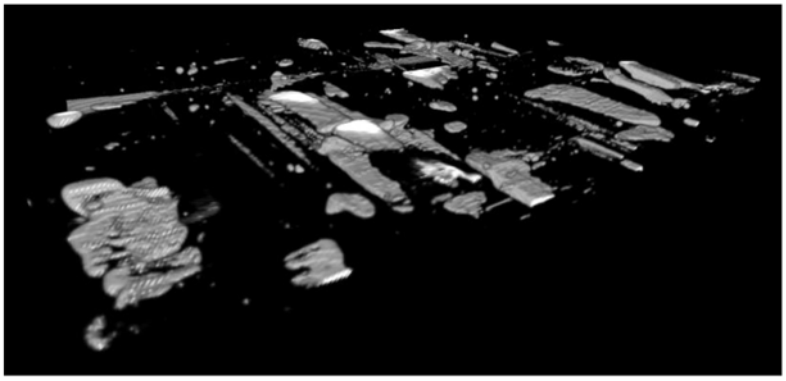

LAMINATE 5 – Sample A – 60 Minutes, Room Temp.

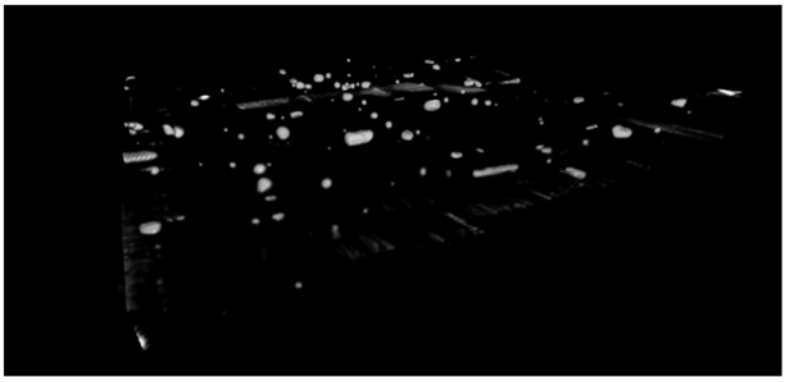

LAMINATE 9 – Sample A – 110 Minutes, 88 °C

Figure 4–6: Renderings, in three dimensions, of void content, distribution and morphology in partially processed laminates.

many flat inter-ply gaps, is visible. After an hour under room temperature vacuum consolidation, the number of gaps has decreased dramatically due to air evacuation and fibre bed compaction. After 110 min and resin flow under high temperatures, only a few isolated macro-voids remain. Their ellipsoid "bubble" shape, characteristic of voids in final cured parts, indicates that the local resin pressure may be insufficient to counter that of the entrapped, compressed gases within them.

4.5.2.2 Measurements

The extent of impregnation at each stage was quantified by measuring visible dry fibre tow areas A_f (or average unsaturated areas) from samples A and B. For each sample, a representative micro-slice was chosen at the center (to avoid edge effects due to sample preparation), and the visible dry fibre tow area of ten fibre tows was measured within the ImageJ software [116] using manual selection and thresholding (as shown in the inset in Figure 4–4) and averaged. Significant variability was noted between tows of the same sample, but averages from different samples of the same laminate were consistent.

The average ply thickness of each sample was also calculated by measuring the sample thickness and dividing by the number of layers. Note that during processing, a laminate's thickness may decrease due to both resin flow into void spaces (mass transport) and fibre bed compaction (strain); since the laminates were removed from vacuum conditions prior to scanning, some strain relaxation may have occurred.

Finally, the evolution of the macro-void content was quantified. Skyscan's CTan software was used to select a volume of interest containing the sample (but no surrounding void space), and to separate solid and void spaces through

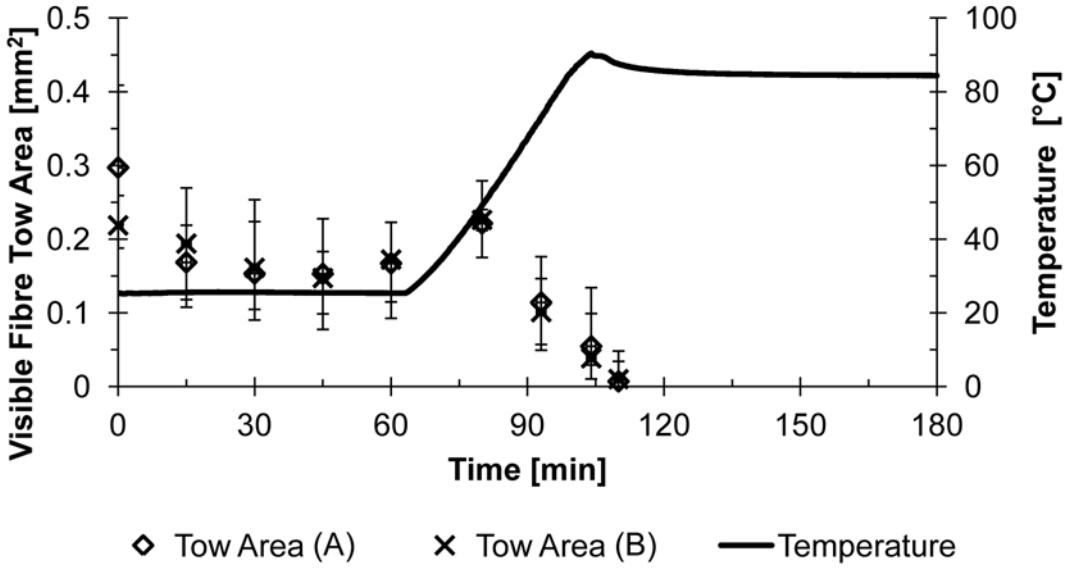

Figure 4–7: Graph of the evolution of the visible dry fibre tow area with processing. The two markers show the measured values for samples A and B taken from each partially processed laminate. The error bars show minimum and maximum measured values for each sample.

grayscale thresholding. The resultant binary images, composed of either white (solid) or black (void) pixels, were then exported into the ImageJ software and subjected to three algorithms (Despeckle, Remove Outliers and Median filter). The algorithms were used to remove both noise inherent to the X-ray process and any micro-voids present in the scan, since the infiltration of the latter was measured through visible dry fibre tow areas. Then, CTan's "3D Analysis" feature was used to obtain the percent volumes of solid and void within the volume of interest.

The measured data is shown in Figures 4–7 to 4–9 along with the cure cycle temperature. The unprocessed samples exhibit the largest visible dry fibre tows, average ply thicknesses and macro-porosity percentages. As soon as vacuum is applied, all three quantities decrease. During the room-temperature

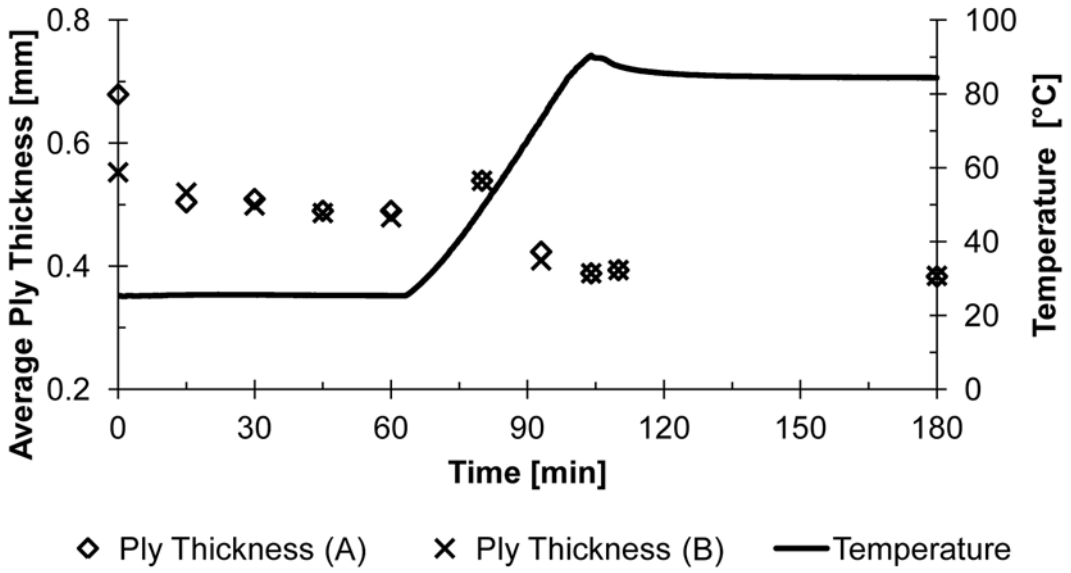

Figure 4–8: Graph of the evolution of the average ply thickness with processing. The two markers show the measured values for samples A and B taken from each partially processed laminate.

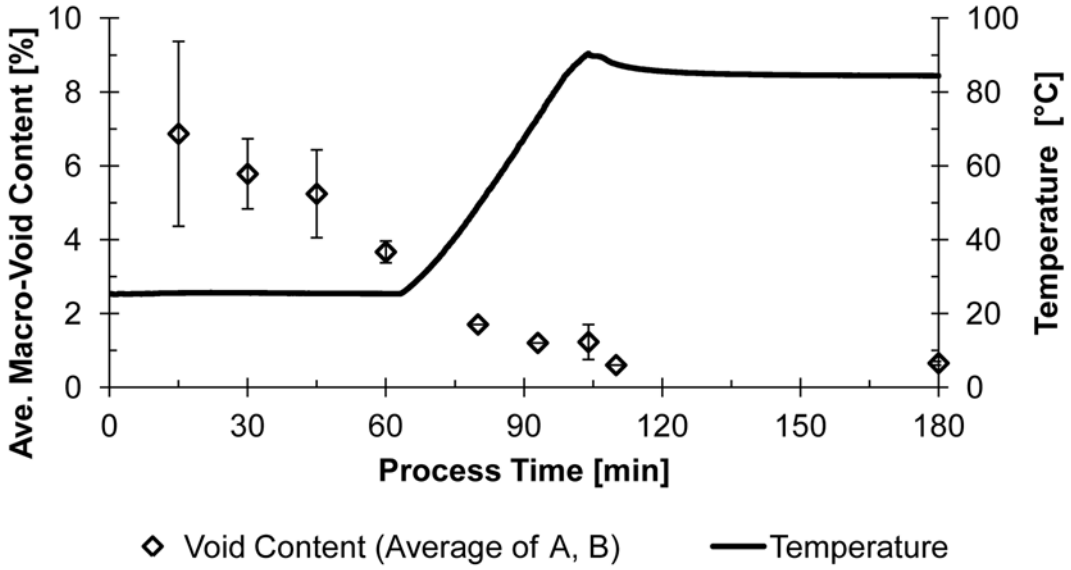

Figure 4–9: Graph of the evolution of the macro-porosity with processing. The markers show the average of the measured values for samples A and B taken from each partially processed laminate. Error bars show minimum and maximum measured values. Value at 0 min (16.9 %) omitted for clarity.

hold, the void content shows a steady and significant reduction (from 7 % to 4 %), while the average ply thickness exhibits a small but steady decrease and the visible dry fibre tow area undergoes only slight variations following initial compression. This indicates that air is evacuated and inter-ply gaps are being closed off due to ply adhesion, tow nesting and, potentially, some local resin migration.

Once the temperature is elevated and increases to past 60 °C, the visible fibre tow area begins to decrease in a consistent manner, indicating the onset of tow impregnation, and all three measured quantities see large reductions (the one-time increase in all three measurements at the 80 min sample may be an outlier due to material variability or an undetected experimental error). The onset of microstructural changes with elevated temperature suggests that the resin viscosity is the critical parameter controlling the start of tow infiltration. Impregnation continues until approximately 110 min at a relatively constant rate, for a total time of approximately 35 min. In contrast, the rates of decrease in porosity and average ply thickness slow down approximately 5 to 10 min beforehand. This difference highlights the effect of impregnation on the material's ability to "breathe." As resin progressively infiltrates the tows, their permeability decreases. Furthermore, since tow impregnation may not be fully uniform along the tow length, the pathways formed by the formerly dry cores may cease to be continuous to the laminate boundaries. Thus, gases remaining in the material, both inside and outside the tows, are increasingly difficult to evacuate; the stabilization of the macro-void content around 100 min suggests that little air flows out past that point. These conclusions are in agreement with the similar results by Fahrang et al. [88]. When the resin gels

(after approximately eight hours at 85 °C), the remaining air pockets become voids in the final cured part.

The final samples, from laminate 10 (180 min), exhibit no visible dry fibre tow areas, a macro-void content of 0.65 % and an average ply thickness of 0.384 mm (within 1.2 % of the cured ply thickness of 0.389 mm predicted by the material manufacturer [84]).

4.6 Conclusions

The present chapter had two aims: to identify the key aspects of consolidation for a representative OOA prepreg, and to demonstrate a new method for analyzing prepreg consolidation. To this effect, laminates based on MTM45-1/5HS prepreg were processed to different stages of a standard cure cycle, samples were scanned using micro-CT, and detailed microstructural data was obtained from the resulting X-ray micrographs. The conclusions and contributions of this study are the following.

1. **OOA prepreg consolidation consists of two key phenomena: tow impregnation and macro-void collapse.** The fibre tows initially feature dry cores that form a permeable vascular network, and are progressively filled by resin at elevated temperatures. Macro-voids, formed by gases entrapped in the fabric's interstitial macro-pores during layup, decrease in size as these gases are evacuated through the vascular network; however, once the tows are nearly saturated, gas evacuation ceases due to decreased tow permeability, and the macro-void content stabilizes. The remainder of this thesis will consider these consolidation phenomena in detail for several OOA prepregs, and evaluate their relationships with various material properties and process conditions.

2. **Micro-CT is a powerful tool for imaging and measuring prepreg microstructural features.** Its primary strengths are the ability to scan actual prepregs and laminates (as opposed to "model" materials) without extensive and potentially disruptive sample preparation, and to capture very high resolution three-dimensional data that may be used for detailed quantitative analysis. As such, it offers significant advantages over traditional methods such as optical microscopy, and allows it to complement and compare favorably to other novel characterization methods such as ultrasound and MRI. Its primary weaknesses are the ex-situ nature of the scan, which requires interrupting the process cycle, and the significant scan times and dataset sizes. However, these weaknesses may be overcome and, overall, pale in light of the wealth of information that may be obtained.

CHAPTER 5
Modelling the Effect of Material Properties and Process Parameters on Tow Impregnation in Out-of-Autoclave Prepregs

5.1 Introduction

In Chapter 4, tow impregnation was identified as a key consolidation phenomenon. The dynamics of this infiltration flow depend on the properties of the constituent materials and the manufacturing conditions, and are likely to impact part quality. Hence, a study of the effect of key material properties and process parameters on OOA prepreg tow impregnation is a logical next step towards understanding, evaluating and potentially optimizing this manufacturing method.

5.1.1 Background

As detailed in the literature review, tow impregnation has been addressed in a number of previous works, usually within the context of unsaturated flow in LCM processes (for example, [10, 73–75]). In such cases, flow commonly occurs under isothermal conditions and relatively high driving pressures.

Conversely, OOA prepreg impregnation may occur in non-isothermal conditions, such as during the initial temperature ramp, as well as during the isothermal dwell. This heat-up will induce changes in the resin viscosity of a magnitude not commonly seen in LCM, making cure cycle parameters important factors. Furthermore, while OOA resin viscosities can be significantly higher than those of common LCM systems during processing (on the order of 100 Pa s versus 0.1 Pa s), impregnation is driven by, at most, atmospheric

consolidation pressure. Variations in input factors may therefore lead to large differences in flow rates; in extremis, some conditions may potentially result in incomplete impregnation at gelation and flow-induced micro-voids.

Literature on flow phenomena in OOA prepregs is scarce. However, studies on resin properties, gas transfer and void formation have highlighted that OOA materials and processes are sensitive to variations in input parameters. Such sensitivity may be a concern. If tow impregnation occurs too quickly, the prepreg permeability may be prematurely reduced and air may remain entrapped within the laminate, leading to porosity (however, such a case may be precluded by a sufficiently long room temperature vacuum hold). Conversely, if tow impregnation is too slow, some tow porosity may still exist at resin gelation, and lead to pervasive micro-voids within the final part. However, such sensitivity may also provide an opportunity, since tow impregnation dynamics can offer an avenue for process optimization: all other issues being equal, faster tow infiltration may lead to faster manufacturing times. Overall, these property-processing-quality relationships require thorough understanding.

5.2 Objectives and Structure

The present study aims to assess the role of several factors on OOA tow impregnation and is accomplished in three steps. First, the micro-CT method proposed in Chapter 4 is used to analyze the tow impregnation dynamics of three commercially-available OOA prepregs. Second, a representative model for tow impregnation is developed. This flow model is based on Darcy's Law and assumes rigid circular tows, radial impregnation by a polymerizing resin and negligible gas entrapment phenomena. Third, the required model parameters, consisting of tow fibre volume fractions and geometry, resin cure

kinetics and viscosity profiles, pressure boundary conditions and tow permeabilities, are determined for each material. Finally, the developed models are used for a parametric study that evaluates, for each material, the effect of cure cycle (ramp rate and dwell temperature), resin initial degree of cure and consolidation pressure on tow impregnation and potential micro-void formation.

5.3 Materials

The OOA prepregs considered in this study are manufactured by Cytec Engineered Materials and the Advanced Composites Group (ACG). Their properties are summarized in Table 5–1. The Cytec prepregs consist of CYCOM 5320 toughened epoxy resin and two fibre architectures: a plain weave (PW) and an 8 harness satin (8HS). Both fabrics consist of 3K tows but the 8HS has a higher areal weight due to thicker, more tightly woven plies; by comparing their different behavior, the influence of fabric architecture may be explored. These Cytec prepregs are henceforth referred to as "5320/PW" and "5320/8HS". The ACG prepreg is the same MTM45-1/5HS material used in the previous chapter, and consists of a toughened epoxy resin and a 5HS fabric with larger 6K tows; comparing its behavior to the 5320-based resins will verify whether the observed trends are consistent across multiple material systems. It should be noted that the cure kinetics and viscosity of both resins were previously characterized by Kratz et al. [36], and may be predicted for any time-temperature cycle.

Table 5–1: Properties of the 5320/PW, 5320/8HS and MTM45-1/5HS prepregs.

Parameters	5320/PW	5320/8HS	MTM45-1/5HS
Resin	5320	5320	MTM45-1
Resin content	36 %	36 %	36 %
Out-life	21 days	21 days	21 days
Fabric	T650-3K PW	T650-3K 8HS	CF2426A
Areal weight	$195\,\mathrm{g\,cm^{-3}}$	$370\,\mathrm{g\,cm^{-3}}$	$375\,\mathrm{g\,cm^{-3}}$
Tow count	3k	3k	6k

5.4 Micro-Flow Characterization

5.4.1 Laminate Layup and Partial Processing

The tow impregnation dynamics of each material were obtained using the previously presented micro-CT characterization method, which consists of processing laminates to different stages of a benchmark cure cycle, interrupting the process to prevent further microstructural changes, and quantifying the degree of tow impregnation from X-ray micrographs.

For the MTM45-1/5HS prepreg, this data has already been obtained and presented in Chapter 4. Recall that the benchmark cycle used consisted of an hour-long vacuum hold at 25 °C (chosen on the basis of best-experience guidelines, since no specific times are provided in the material data sheet [84]), a $2\,^{\circ}\mathrm{C\,min^{-1}}$ ramp to 85 °C, and an 85 °C dwell. Laminates were partially processed to the following points: unprocessed; 15, 30, 45 and 60 minutes under room-temperature vacuum consolidation, and 80, 93, 104, 110 and 180 minutes under heated conditions. The laminates measured approximately 100 mm by 100 mm, and had layups of $[(0^{\circ}/90^{\circ})_2]_s$ and $[(0^{\circ}/90^{\circ})_4]_s$.

For the 5320/PW and 5320/8HS prepregs, the benchmark cycle consisted of a 16 h room temperature vacuum hold (chosen as the longest explicitly recommended hold in the manufacturer's data sheet [85]), a $1.21\,^{\circ}\mathrm{C\,min^{-1}}$ ramp to 93 °C and a hold at 93 °C (also chosen based on the manufacturer's data sheet [85]). Laminates were processed to five different stages of the cycle: unprocessed; after the 16 h room temperature vacuum hold, and after the same hold plus 20, 40 and 60 min. The laminates measured approximately 150 mm by 100 mm, with layups of $[(0^{\circ}/90^{\circ})_4]_s$ for the 5320/PW and $[(0^{\circ}/90^{\circ})_2]_s$ for the 5320/8HS.

Figure 5–1 shows the measured laminate temperature profiles along with the predicted resin degree of cure and viscosity for both materials and benchmark cure cycles. In both graphs, time $t = 0$ corresponds to the end of the room temperature vacuum hold. As detailed in the previous chapter, for the MTM45-1/5HS cycle, the predicted degree of cure increased from $\alpha = 0.01$ to $\alpha = 0.03$, while the predicted viscosity decreased from $\mu = 16\,700\,\mathrm{Pa\,s}$ at room-temperature to a minimum of $\mu = 59\,\mathrm{Pa\,s}$. For the 5320/PW and 5320/8HS cycle, the degree of cure increased from $\alpha = 0.01$ to $\alpha = 0.02$ while the viscosity decreased from $\mu = 50\,831\,\mathrm{Pa\,s}$ to a minimum of $\mu = 53\,\mathrm{Pa\,s}$. In both cases, resin gelation was predicted to occur several hours after the last partial processing point.

5.4.2 Micro-CT

The 5320-based prepregs were subjected to micro-CT scans using the technique presented in Chapter 4. Square samples measuring approximately 18 mm per side were cut from the center of each laminate and inserted in a Skyscan 1172 High Resolution Micro-CT. The scan resolution was 7 µm/pixel;

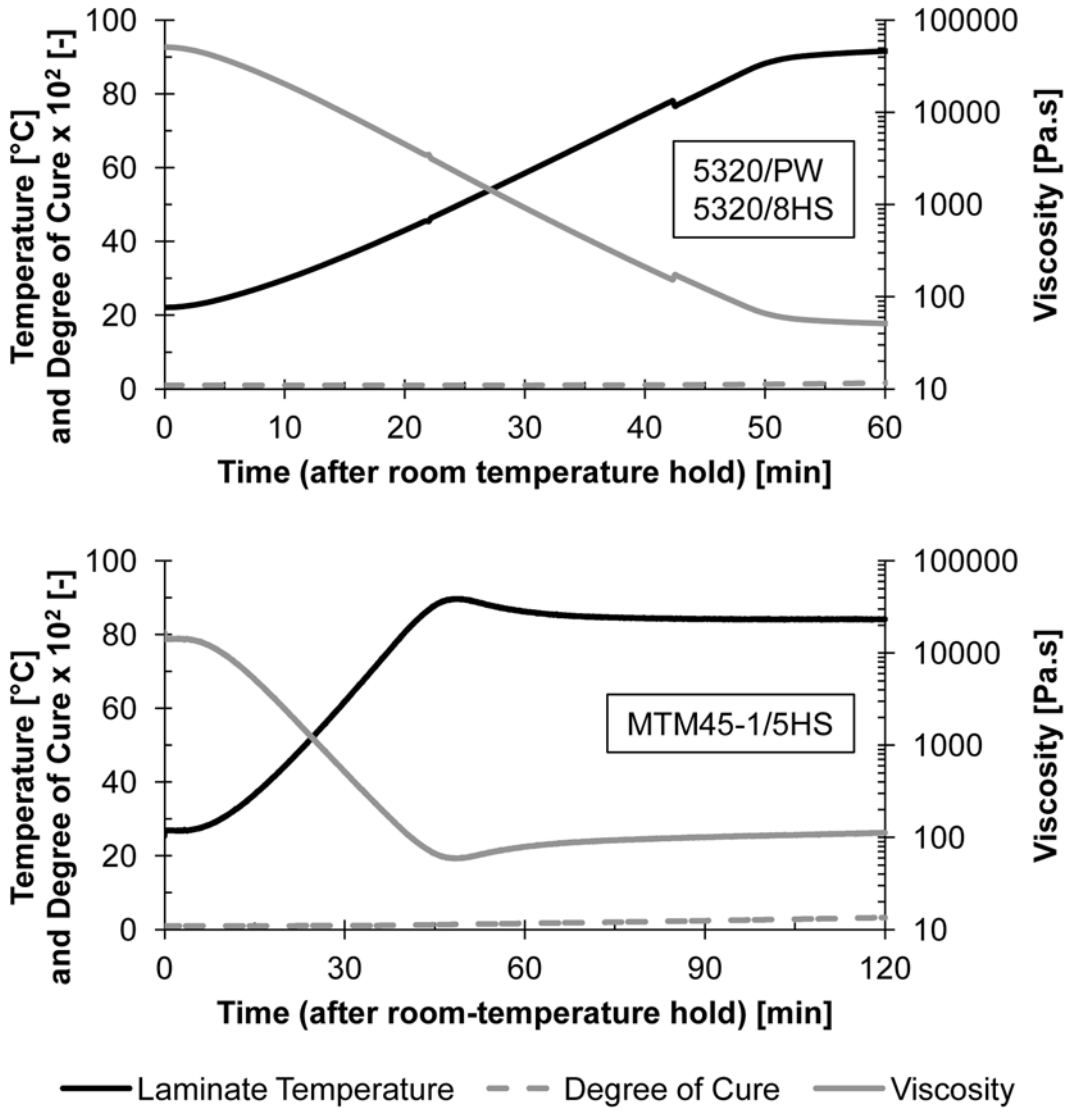

Figure 5–1: Graphs of the partial processing cycles for the 5320/PW and 5320/8HS prepregs (top), and the MTM45-1/5HS prepreg (bottom). The degree of cure values are multiplied by 10^2 for graphing purposes. Note that in both graphs, time $t = 0$ corresponds to the end of the room temperature vacuum hold.

the image size was 4000 x 2096 pixel; the X-ray voltage and intensity were 64 kV and 157 µA, respectively, and no filter was used.

Figure 5–2 shows portions of representative X-ray micrographs for all three materials, at two distinct stages of processing: after the room temperature vacuum hold, and between 30 min and 40 min into the elevated temperature cure. The dark ellipse-like shapes visible in the left-hand micrographs are, as explained before, dry tow areas consisting of carbon fibres and micro-voids. Their presence confirms that all three material are, initially, only partially impregnated and that, after the room temperature holds, the fibre tows remain dry. Their decreased size in the right-hand micrographs shows that they are subsequently infiltrated by resin. The dry areas of the 5320/PW are noticeably more elongated than those of the 5320/8HS, indicating differences in fabric morphology; those of the 5HS are about as thick as the 5320/8HS, but nearly twice as wide due to the larger tow count. The macro-voids seen in the right-hand micrograph of the 5320-based prepregs are delaminations brought on by absence of vacuum compaction, sample manipulation and the partially cured resin's loss of tack.

The evolution of the visible dry fibre area A_f was quantified using image analysis, according to the previously described procedure. For each sample, 20 dry tow areas were measured and averaged. Then, these areas were normalized by defining a degree of impregnation β as follows, where A_{tow} is the average cross-sectional area of the dry tows in the unprocessed samples:

$$\beta = 1 - \sqrt{\frac{A_f}{A_{tow}}} \tag{5.1}$$

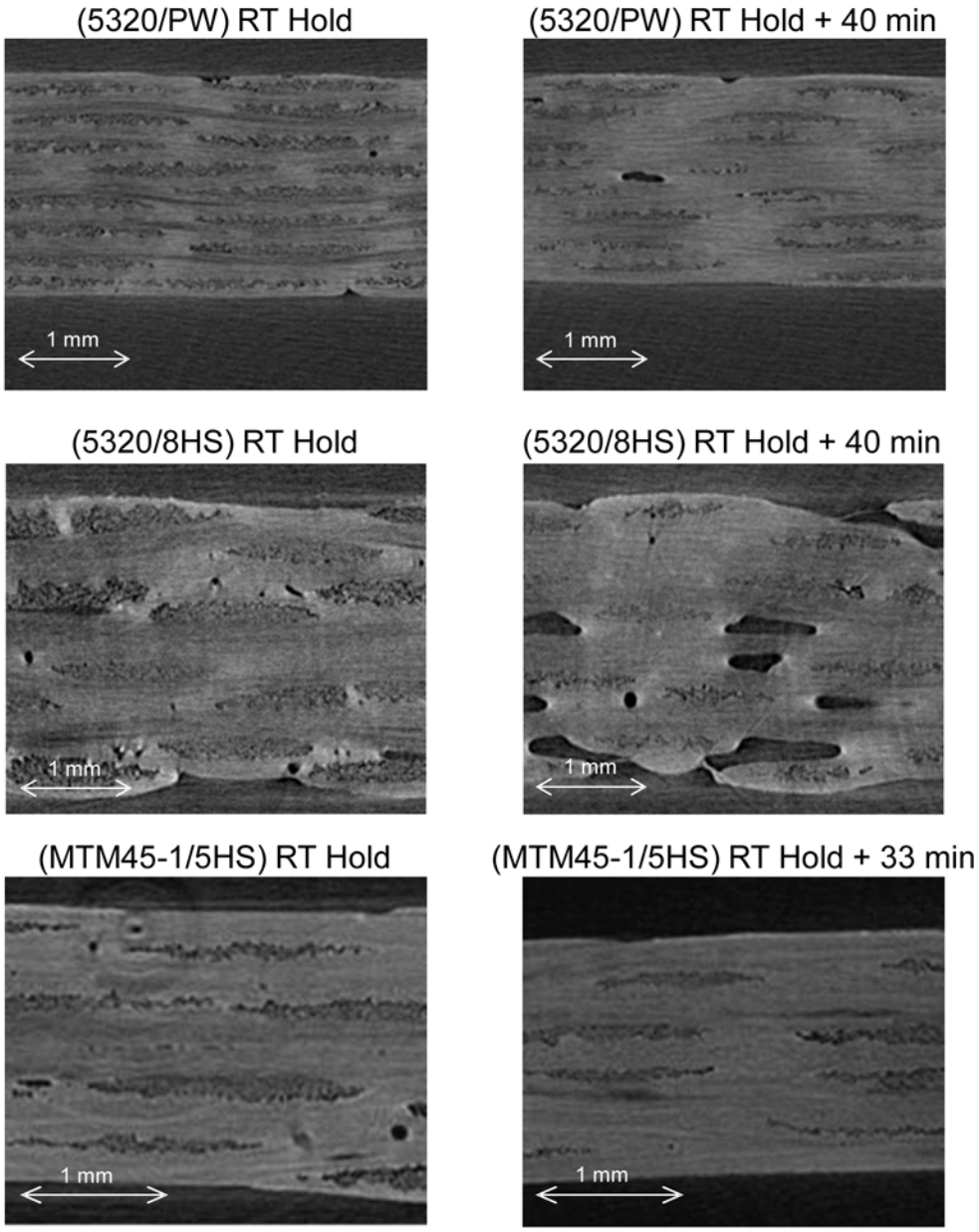

Figure 5–2: X-ray micrographs showing representative prepreg microstructures after the room temperature vacuum hold (RT) (left) and between 30 min and 40 min into elevated temperature processing (right). Brightness and contrast adjusted for visibility.

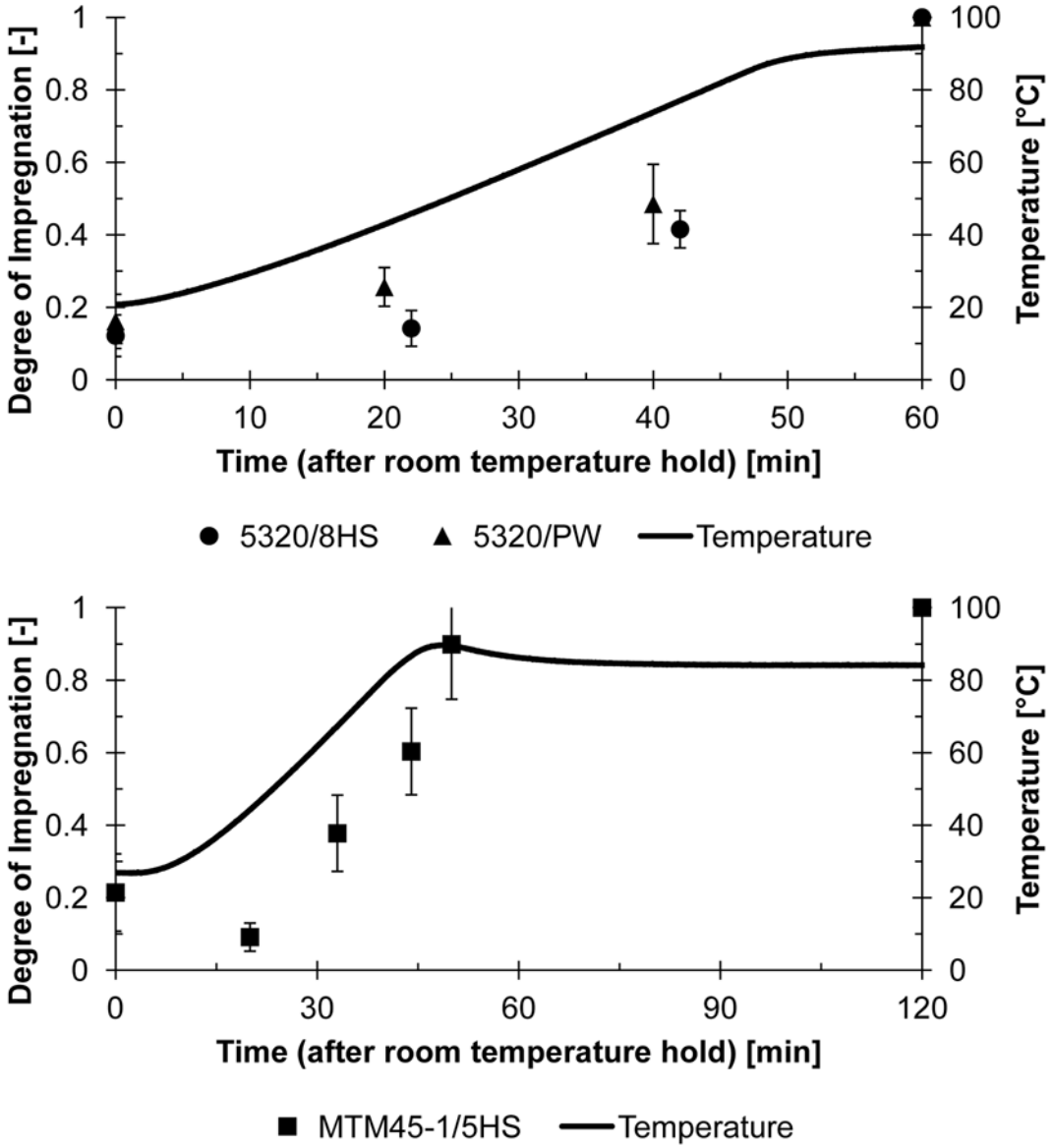

Figure 5–3: Graphs of the evolution of the degree of impregnation of the 5320/PW and 5320/8HS prepregs (top) and of the MTM45-1/5HS prepreg (bottom) for their respective benchmark cure cycles. The error bars show the standard deviation in the measured degrees of impregnation of the 20 tows for each material.

Figure 5–3 shows the evolution of the degree of impregnation (with the standard deviation in the measured degrees of impregnation of the 20 tows for each material) for the benchmark cure cycles and all three prepregs. Between the 5320-based materials, the PW has a slightly higher degree of impregnation following the 16 h room temperature vacuum hold, and impregnates faster once the temperature is increased, likely due to the lower areal weight (and consequently lower fibre volume fraction) of its tows. It may also be seen from the larger deviation bars that the PW shows more variability in β between tows of the same sample. For both materials, the scans at 60 min showed no visible dry fibre areas, indicating full tow impregnation. The MTM45-1/5HS prepreg presents a similar degree of impregnation at the end of the room temperature vacuum hold and, although exhibiting more variability, is found to follow the same impregnation trend over the cure cycle.

5.5 Model Development

In OOA prepregs based on woven fabrics, dry areas are generally found inside the fibre tows while resin-rich areas consist of the macro-pore spaces around tows and between plies. The X-ray micrographs obtained in Chapter 4 indicate that, following room temperature vacuum compaction, these macro-pore spaces are saturated with resin (some isolated macro-voids notwithstanding). Since this resin is not allowed to bleed out of the laminate, large-scale resin flow within the macro-pore network is likely to be negligible. Thus, the key flow phenomenon to be modelled is tow impregnation.

Consider a prepreg layer consisting of dry, micro-porous fibre tows (each made up of thousands of individual fibres) surrounded by resin. Since each tow has characteristic dimensions on the order of millimeters and composite

parts are usually several orders of magnitude larger, each part contains a large number of such tows. Thus, to analyze processing, a single model based on average tow properties is proposed.

During processing, each tow is infiltrated by surrounding resin. This low Reynolds number flow of a viscous fluid within a porous medium can be described by continuity equations for the solid and fluid phases and by Darcy's Law. As first presented in Chapter 2, these equations are, respectively:

$$\frac{\partial V_f}{\partial t} + \nabla \cdot (V_f \bar{v_f}) = 0 \tag{5.2}$$

$$\frac{\partial (1 - V_f) S}{\partial t} + \nabla \cdot ((1 - V_f) S \bar{v_r}) = 0 \tag{5.3}$$

$$(1 - V_f) S (\bar{v_r} - \bar{v_f}) = -\frac{\bar{\bar{K}}}{\mu} \nabla P \tag{5.4}$$

For reference, V_f is the fibre volume fraction; S is the saturation; $\bar{v_f}$ is the fibre velocity; $\bar{v_r}$ is the average local velocity of the resin within the pore volume; $\bar{\bar{K}}$ is the permeability tensor of the medium; μ the dynamic viscosity of the resin, and P is the resin pressure [11].

Several assumptions may be invoked to simplify the above equations and reduce the number of parameters to be determined while remaining suitably representative. First, it is assumed that as a consolidation pressure P_{app} is applied by the vacuum bag, the dry fibre tows are immediately compressed to a fibre volume fraction V_f corresponding to a constant transverse effective stress equal to P_{app}. This assumption is justified by the likely fact that, within dry prepreg areas, the fibre bed carries the applied load. Furthermore, it is also

assumed that the tows remain rigidly compressed at a fibre volume fraction V_f throughout infiltration. This condition implies that, during infiltration, the progressive load-sharing between fibres and resin will not cause a sudden change in fibre volume fraction, and is partly justified by the increasing resin viscosity during cure, which may prevent rapid tow deformation. Furthermore, it is also invoked because any potential fibre bed relaxation is, from a practical standpoint, close to impossible to observe and therefore to validate. Finally, it is assumed that the tow infiltration is saturated, with the pores behind the resin flow front completely filled with resin. In light of these two assumptions, $\bar{v_f} = 0$, V_f remains constant, and $S = 1$ and constant behind the flow front. Thus, the governing equations reduce to:

$$\bar{v_r} = -\frac{\bar{\bar{K}}}{\mu(1 - V_f)}\nabla P \tag{5.5}$$

$$\nabla \cdot \bar{v_r} = 0 \tag{5.6}$$

It is further assumed that the tows are circular (though their elliptical shape will be taken into account further on) and that infiltration is uniform along the tow length and axisymmetric in the radial direction r in the cross-section. The latter assumptions are justified by the fact that, at least in theory and intention, tows are designed to have homogenous properties along their length. Altogether, these simplifications reduce the more complicated problem of tracking a flow front in three dimensions to a one-dimensional situation that retains the key phenomena. With K the transverse tow permeability and v_r the radial resin velocity, Eqs. 5.5 and 5.6 become:

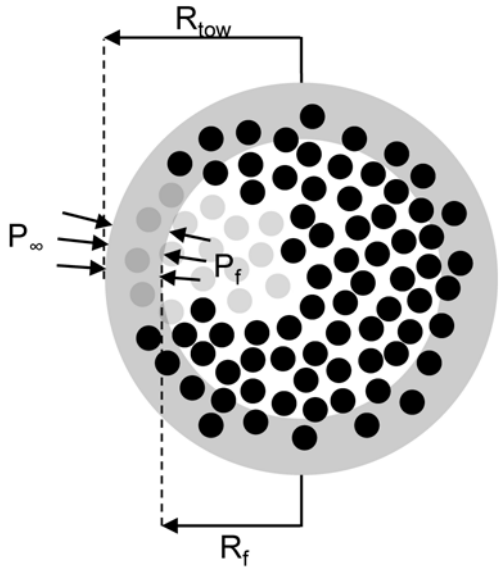

Figure 5–4: Schematic of assumed tow geometry.

$$v_r = -\frac{K}{\mu(1-V_f)}\left(\frac{dP}{dr}\right) \tag{5.7}$$

$$\frac{d(rv_r)}{dr} = 0 \tag{5.8}$$

As shown in Figure 5–4, the circular tow is assumed to have a total radius R_{tow} and an infiltration flow front radius R_f, with corresponding resin boundary pressures P_∞ and P_f (both defined in the upcoming section). Eqs. 5.7 and 5.8 may be combined and integrated (assuming constant parameters over the region of integration) to obtain a pressure field $P(r)$, which may be re-inserted into Darcy's Law and evaluated at $r = R_f$ to obtain the following expression for the resin flow front velocity:

$$v_f = \frac{dR_f}{dt} = -\frac{K}{\mu(1-V_f)}\left(\frac{1}{R_f}\frac{(P_\infty - P_f)}{ln(R_{tow}/R_f)}\right) \tag{5.9}$$

Finally, the previously defined degree of impregnation β may be used to normalize the above expression:

$$\beta = 1 - \sqrt{\frac{A_f}{A_{tow}}} = 1 - \frac{R_f}{R_{tow}} \tag{5.10}$$

$$\frac{d\beta}{dt} = \frac{K}{\mu R_{tow}^2 (1 - V_f)} \left(\frac{P_\infty - P_f}{(1-\beta) ln(1/(1-\beta))} \right) \tag{5.11}$$

Eqs. 5.10 and 5.11 can be used to track the tow impregnation as β increases from 0 to 1 (or as R_f decreases from R_{tow} to 0). They are solved in successive small time steps with the assumption that during each time step, all parameters remain constant. After each solution step, relevant parameters such as the viscosity may be updated as needed. It should be noted that in order to avoid the singularities at $\beta = 0$ and $\beta = 1$ during modelling, a minimum value of $\beta = 0.01$ (unless otherwise specified) is used and a maximum value of $\beta = 1$ is imposed by means of a step function once $\beta = 0.999$ is reached.

5.6 Model Parameter Determination

The parameters required to solve the model defined by Eqs. 5.10 and 5.11 are the fibre bed properties (the tow fibre volume fraction and radius); the resin viscosity; the driving and resisting pressures and the tow permeability.

5.6.1 Fibre Bed Properties

The tow microstructure was analyzed using a modified version of the technique proposed by Hubert and Poursartip [23] to determine prepreg fibre bed compaction curves. An MTS Insight 5 kN electromechanical test frame equipped with flat, well-aligned, heated (99 °C ± 5 °C) platens was used to

compress square laminate samples and hold them at specified thicknesses for approximately 24 h. During the test, the resin matrix was allowed to bleed out (transferring a known load to the fibre bed), gel and vitrify. The resin bleed and load relaxation phases occured within the first two hours of the test, while the resin degree of cure remained below $\alpha = 0.25$ for the 5320 resin and below $\alpha = 0.10$ for the MTM45-1, and several hours before either resin's gelation. The samples were 55 ± 1 mm per side, with layups of $[(0°/90°)_4]_s$ for the 5320/PW and $[(0°/90°)_2]_s$ for the 5320/8HS and MTM45-1/5HS. The platen compression rate was $0.05\,\mathrm{mm\,min^{-1}}$. Ten samples were compressed for the 5320/PW, eleven for the 5320/8HS and nine for the MTM45-1/5HS prepregs to final thicknesses between 1.3 mm and 2 mm. Additional information about this method, including representative graphs, is provided in Appendix C. Once manufactured, each sample was cut, polished and inspected under a Nikon Eclipse L150 optical microscope with attached Clemex digital camera.

Figure 5–5 shows a representative tow micrograph. The fibres, generally assumed to be circular, are in reality slightly eccentric and have irregular boundaries. Furthermore, the fibre arrangement is random and varies considerably, even between regions of the same tow; in Figure 5–5, the solid and dashed regions show quasi-hexagonal and quasi-quadratic arrangements, respectively.

For each sample, the tow volume fraction V_f was obtained using image analysis (grayscale thresholding) from an average of 30 cross-sectional images at 500X magnification. Then, for each material, the measured data was used to fit the analytical model proposed by Gutowski et al. and shown in Eq. 5.12, where V_{f0} and A_s are the zero stress fibre volume fraction and the elastic

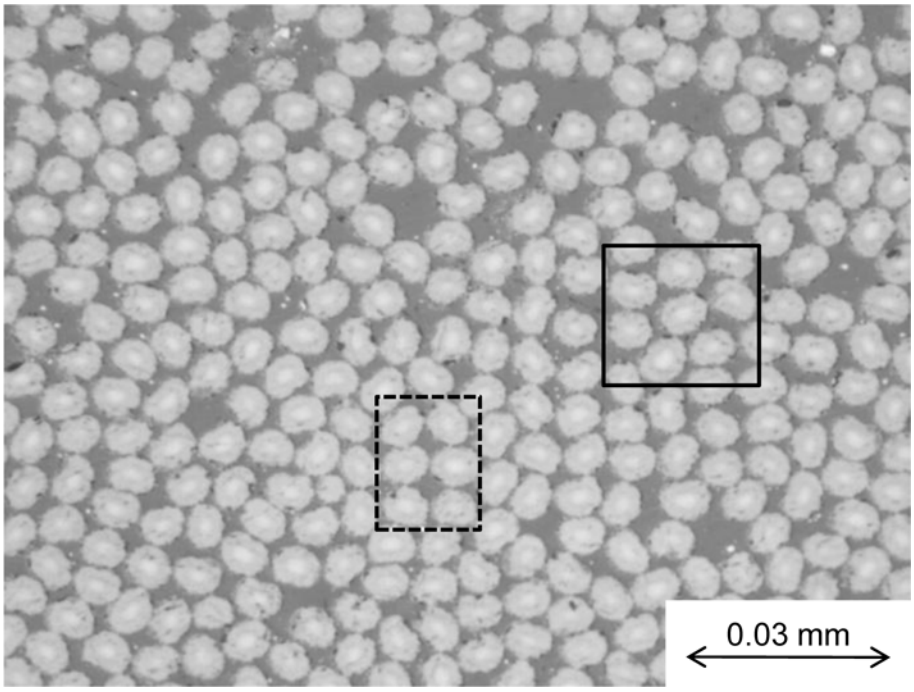

Figure 5–5: Optical micrograph of a representative tow cross-section, showing quasi-hexagonal (solid) and quasi-quadratic (dashed) fibre arrangements.

fitness constant (found by least squares fitting) and V_{fa} is the maximum allowable volume fraction for the highest (hexagonal) packing arrangement:

$$\sigma = A_s \frac{\sqrt{V_f/V_{f0}} - 1}{(\sqrt{V_{fa}/V_f} - 1)^4} \tag{5.12}$$

Figure 5–6 shows the tow compaction curves relating the tow fibre volume fraction to the effective stress (normalized, for intuitive reading, by atmospheric pressure), with experiments as markers and model predictions as solid lines. All three materials display the stiffening behaviour characteristic of such fibre beds. As expected, the 8HS fabric exhibits higher tow volume fractions than the PW for a given effective stress due to its tighter weave. In addition, the 8HS and 5HS fibre beds show very similar compaction curves,

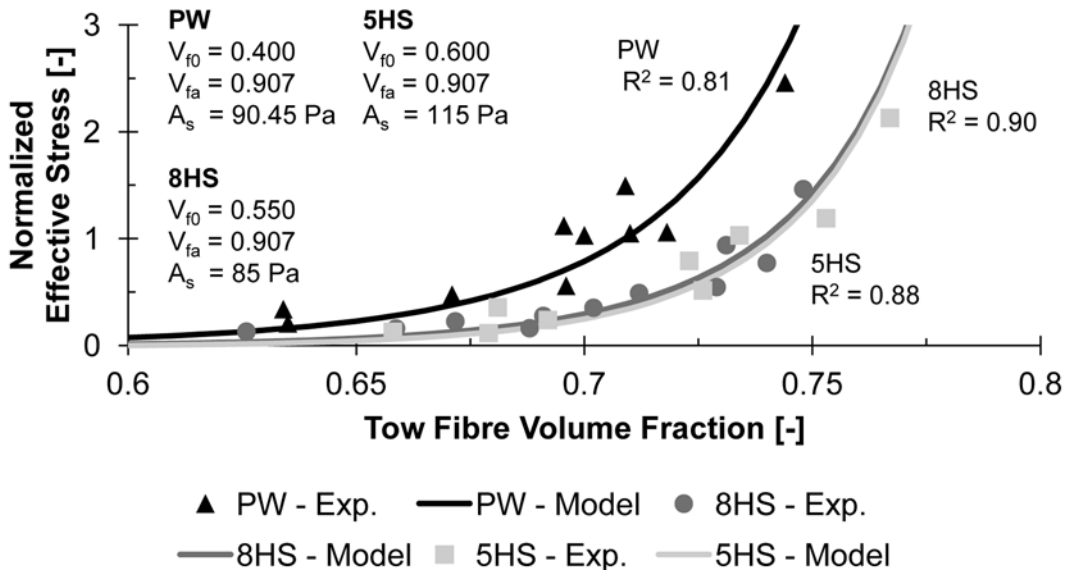

Figure 5–6: Graph of fibre bed compaction curves (with the effective stress normalized by 101 325 Pa). Measurements are shown as markers and model predictions as solid lines. Experimental scatter bars are omitted for clarity, but average standard deviations of 0.04 were observed in the 30 cross-sectional image measurements. The model parameters shown correspond to Eq. 5.12.

likely due to their similar areal weights and weaves. Significant scatter is observed in the experimental data (with average volume fraction standard deviations of 0.04 or 5.6 % of full scale) since the micro-scale distribution of fibres is random; however, the models capture the measured trends and may be used to estimate the tow volume fraction V_f for any imposed effective stress. At an effective stress of 101 325 Pa, V_f = 0.71 for the 5320/PW, V_f = 0.74 for the 5320/8HS and V_f = 0.74 for the MTM45-1/5HS. These values are assumed to remain constant during tow impregnation under constant consolidation pressure.

In addition to the volume fractions, the major and minor axis dimensions of the elliptic tows (denoted $2a_0$ and $2b_0$) were also obtained from an average of 30 tow cross-sections per sample. These values were converted to an equivalent

circular radius R_{tow} by the relation suggested by Van West et al. [117], who investigated the infiltration of circular and elliptic porous domains and found equal times-to-fill for equal hydraulic radii:

$$R_{tow} = \sqrt{2}\frac{a_0 b_0}{\sqrt{a_0^2 + b_0^2}} \tag{5.13}$$

No consistent trends were observed in the data with increasing effective stress within the measured variability, and average values of R_{tow} were assigned to each material. For the 5320/PW samples, $R_{tow} = 0.0917$ mm (with standard deviation in the 30 measured tows of 0.006 mm); for the 5320/8HS, $R_{tow} = 0.118$ mm (with standard deviation in the 30 measured tows of 0.005 mm) and for the MTM45-1/5HS, $R_{tow} = 0.127$ mm (with standard deviation in the 30 measured tows of 0.005 mm). The equivalent radius of the 5320/8HS is higher than that of the 5320/PW due to its thicker tows, which present a longer effective flow path for the infiltrating resin. The equivalent radius of the MTM45-1/5HS is only slightly larger than that of the 5320/8HS because, even though the tows contain twice as many fibres, they are significantly wider but not significantly thicker, and the flow length required for infiltration is similar. It should be noted that higher variability was observed in the 5320/PW than in the 5320/8HS and MTM45-1/5HS, particularly with respect to the scatter in the tow fibre volume fraction data relative to the model predictions. It is speculated that the lower solid density of the 5320/PW allows more room for scatter while, conversely, the denser fabrics constrain randomness.

5.6.2 Resin Viscosity

The dynamic viscosity of each resin is predicted, for any given time-temperature cure cycle, using the resin property models developed by Kratz et al. [36] for the 5320 and MTM45-1 systems and presented in Chapter 2 as Equations 2.12 and 2.14.

5.6.3 Pressure Boundary Conditions

The resin pressure boundary condition P_∞, at the edge of the fibre tow ($r = R_{tow}$), is assumed to be constant and equal to the applied consolidation pressure P_{app}. This assumption is based on the fact that in resin-rich regions, the resin is likely to carry the majority of the applied load. Unless otherwise specified, the atmospheric pressure is taken as 101 325 Pa. Furthermore, since bag pressures below 5 % of atmospheric pressure are achievable and recommended for OOA prepreg processing [85], full vacuum is assumed drawn under the bag, and the resin pressure driving flow is hence, $P_\infty = P_{app} = 101\,325\,\text{Pa}$.

The pressure boundary condition at $r = R_f$ is assumed to consist of the difference between the gas pressure entrapped within the tow and the capillary pressure at the flow front:

$$P_f = P_{gas} - P_c \tag{5.14}$$

Gases present during composites processing may have complex effects on impregnation and void formation phenomena depending on their source, their nature, their distribution within and interaction with the surrounding materials and processing conditions such as temperature and pressure. The developed model is capable of accounting for variations in P_{gas} by updating

it at each time step. However, since an accurate determination of P_{gas} requires considerable experimental characterization and validation, and since the present study is primarily interested in flow dynamics, the remainder of this chapter is confined to cases where the OOA prepreg has been entirely evacuated by means of a sufficiently long room temperature vacuum hold, and $P_{gas} = 0\,\mathrm{Pa}$.

The capillary pressure may be estimated from fibre bed and resin properties. First, the criterion for spontaneous infiltration used by Foley and Gillespie [75] and shown as Eq. 5.15 is used to determine whether spontaneous capillary infiltration takes place. If the criterion is not satisfied, a capillary wetting contribution to infiltration is assumed negligible, and P_c is set to zero. If the criterion is satisfied, an average value for P_c is determined using the relation proposed by Neacsu et al. [118] and shown in Eq. 5.16:

$$V_f \geq V_{f,min} = \frac{\sqrt{3}\pi}{2(\cos\theta + 1)^2} \tag{5.15}$$

$$P_c = \frac{\gamma}{R_{fib}} \frac{\sin(\alpha_{sup} + \theta) - \sin(\alpha_{inf} + \theta)}{(5/6)\pi(1+\xi) - 1 - \sqrt{3}/2} \tag{5.16}$$

In Eqs. 5.15 and 5.16, θ is the contact angle of the resin with the medium ($20°$) while γ is the resin's surface tension ($0.035\,\mathrm{N\,m^{-1}}$), both approximated from values reported in [119, 120]. R_{fib} is the fibre radius and ξ is the ratio of fibre half-spacing to radius, obtained for a given V_f using a geometric relationship for hexagonal fibre arrangements [19]:

$$\xi = R_{fib}\sqrt{\frac{V_a}{V_f}} - 1 \tag{5.17}$$

Finally, the limits of the angular coordinate that tracks the resin front as it flows in the space between two fibres is defined as $\alpha_{sup} = \pi/2 - \theta$ and $\alpha_{inf} = \theta - \pi/2$, as suggested in first approximation by Neacsu et al. [118].

For the assumed contact angle, Eq. 5.15 estimates a minimum volume fraction $V_{f,min} = 0.72$ for spontaneous infiltration. Therefore, the 5320/PW fails the criterion and is assigned $P_c = 0$ Pa while the 5320/8HS and MTM45-1/5HS pass it and are assigned $P_c = 17\,833$ Pa, as per Eq. 5.16.

The use of Eqs. 5.15 and 5.16 and published data derives from the difficulty of accurately quantifying both wetting properties and the capillary contribution to flow in prepregs, in which the constituents are intimately mixed and flow occurs over small, internal distances. The use of such estimates is, however, mitigated by the fact that the capillary pressure is significantly smaller than the flow-driving contribution of the consolidation pressure (P_∞).

5.6.4 Tow Transverse Permeability

As outlined in Chapter 2, the transverse permeability of porous media such as arrays of aligned cylinders may be measured experimentally or estimated by models. Experiments are appropriate when the parameters required to calculate the permeability (such as the sample dimensions, resin viscosity, pressure gradient and flowrate or flow front progression) can be controlled or accurately measured. Such methods are difficult to apply to OOA prepregs, since the latter are already partially impregnated, and tow infiltration occurs internally and over very short distances. Model-wise, permeability may be predicted for a given idealized cylinder radius, volume fraction and packing arrangement by several types of models (including, for example, the Gebart relations shown in Eqs. 2.8 and 2.9). However, actual permeabilities may

differ considerably from predictions due to deviations from the ideal conditions assumed by the models, such as variability in fibre shape and packing and the presence of flow-impeding "bottlenecks" and "dead ends". Randomness has been the subject of several studies, with results generally showing that it decreases permeability relative to the ideal case [30, 31, 121]. For these reasons, in this study, the transverse permeability will be obtained indirectly from experimental data, by correlating model predictions to measured tow impregnation data as described in the next section. By the same token, the predicted trends will be validated.

5.7 Model Correlation with Experimental Data

The benchmark cure cycles used to characterize the micro-flow behaviour of the OOA prepregs in Section 5.4 were used to obtain the tow permeability and validate the trends predicted by the developed model. Figure 5–7 shows the predicted (solid lines) and measured (markers) evolution of the degree of impregnation for the three materials. These predictions were obtained by running the cure kinetics, viscosity and impregnation models over the time-temperature data of the benchmark cure cycles (with an initial β value as measured at the end of the room temperature vacuum hold) and obtaining a best-fit permeability value. The models largely agree with the measured trends. The increased discrepancy of the 5320/PW material is attributed to its higher variability at the fibre bed and prepreg impregnation level, as seen throughout the study. The disagreeing experimental data point at 20 min for the MTM45-1/5HS was identified as a probable outlier in Chapter 4, Section 4.5.2.2.

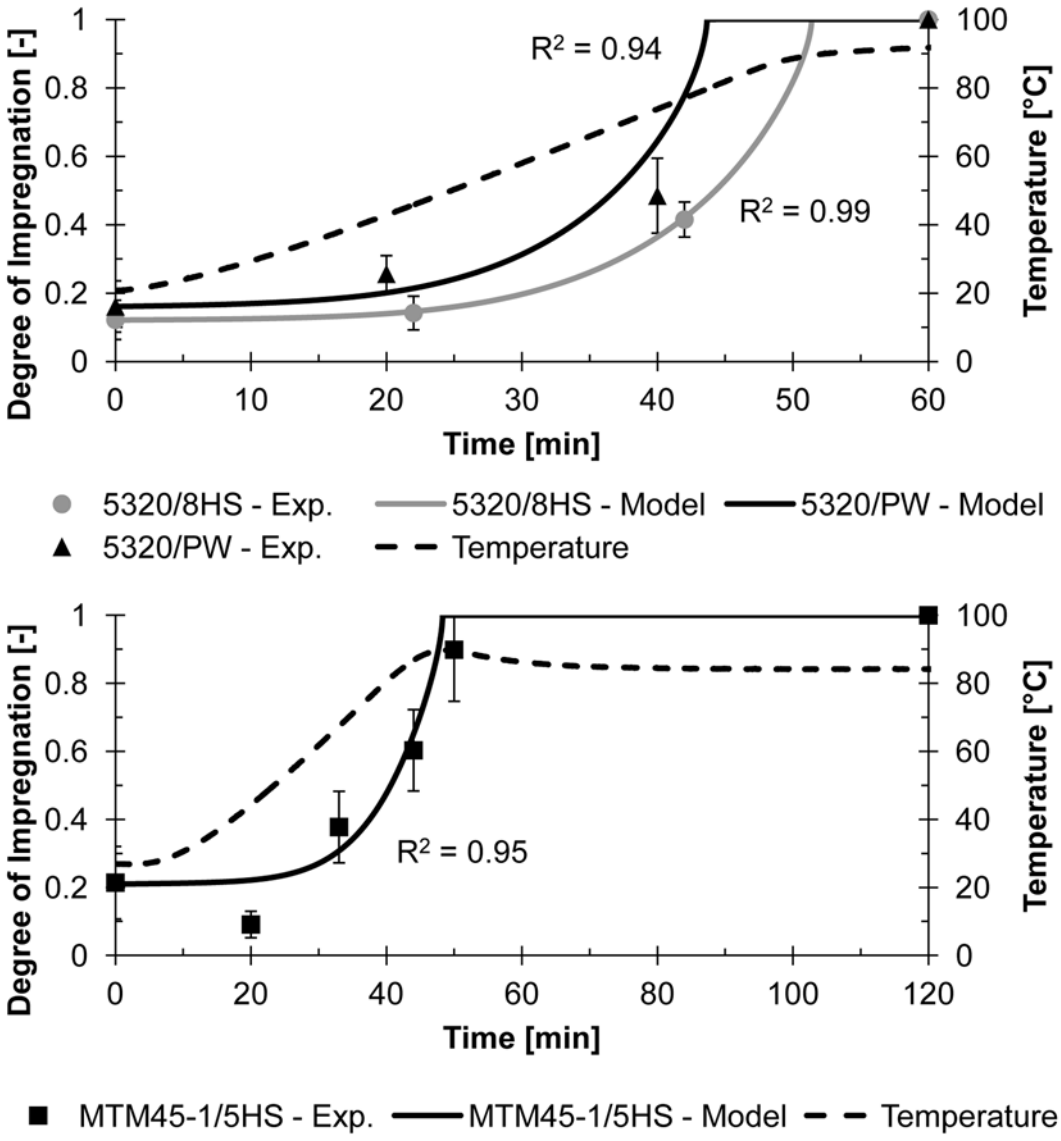

Figure 5–7: Graphs of the evolution of the degree of impregnation as measured by micro-CT (markers) and predicted by the model (solid lines) for the 5320/PW and 5320/8HS prepregs (top) and the MTM45-1/5HS prepreg (bottom).

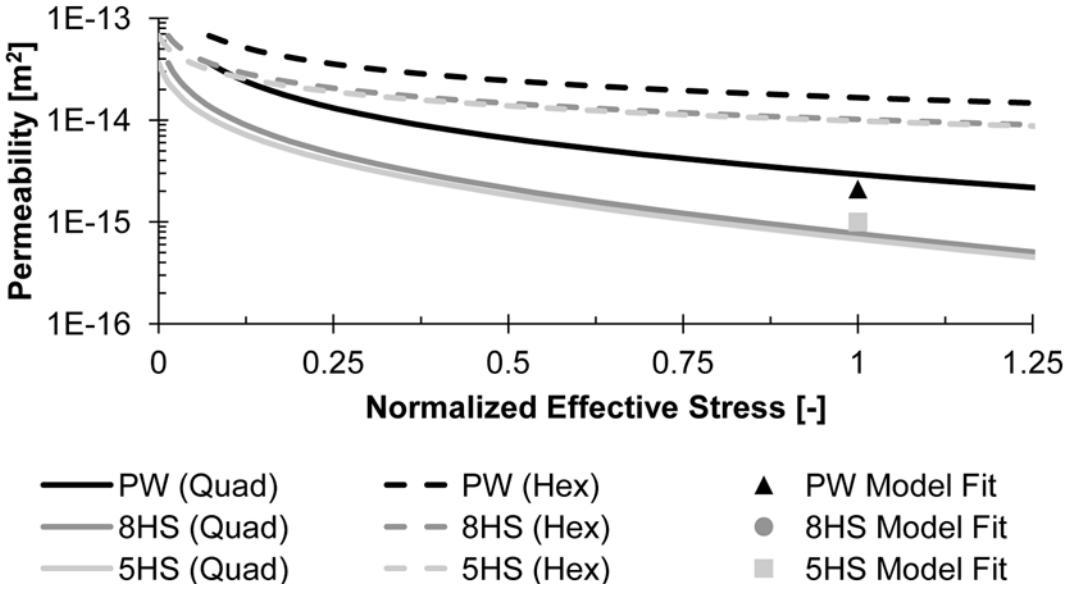

Figure 5–8: Graph of the permeability versus effective stress (normalized by 101 325 Pa), showing best-fit permeability values (markers) and Gebart model predictions (solid lines) for ideal fibre arrangements. The 8HS and 5HS Model Fit markers are overlapping.

Figure 5–8 compares the best-fit transverse tow permeabilities for each material to the Gebart model predictions for hexagonal and quadratic fibre arrangements. As expected, between the 5320/PW and 5320/8HS, the denser 8HS is less permeable. The MTM45-1/5HS permeability is similar to that of the 5320/8HS, which is reasonable in light of their similar tow volume fractions. Because these permeabilities were obtained for different resin systems and benchmark cure cycles, this agreement also supports the model development and parameter determination approach. For all three materials, the best-fit value falls close to the lower-bound permeability predicted for a quadratic fibre arrangement. While Figure 5–5 displays both quasi-hexagonal and quasi-quadratic arrays, they are far from the ideal case assumed by the model. Indeed, variations are seen in fibre diameter, spacing and packing and,

Table 5–2: Summary of determined model parameters for Eq. 5.11 for the 5320/PW, 5320/8HS and MTM45-1/5HS prepregs.

Parameters	**5320/PW**	**5320/8HS**	**MTM45-1/5HS**
V_f	0.71	0.74	0.74
R_{tow}	0.0917 mm	0.118 mm	0.127 mm
μ	Model	Model	Model
P_∞	101 325 Pa	101 325 Pa	101 325 Pa
P_{gas}	0 Pa	0 Pa	0 Pa
P_c	0 Pa	17 833 Pa	17 833 Pa
K	2.1×10^{-15} m^2	9×10^{-16} m^2	1×10^{-15} m^2

as mentioned previously, this randomness is expected to reduce the permeability relative to the ideal case predictions. The results shown in Figure 5–8 are consistent with this expectation but remain within the range and order of magnitude predicted by the models; they are hence considered reasonable . The model parameters for each of the three studied prepregs are summarized in Table 5–2.

5.8 Parametric Study

The models developed above were used in a parametric study to evaluate the importance of several factors on tow impregnation rates, and to identify conditions potentially leading to flow-induced micro-porosity.

5.8.1 Cure Cycle and Resin Initial Degree of Cure

5.8.1.1 Procedure

For a first set of simulations, the factors considered were the cure cycle and the resin initial degree of cure, both of which are known to affect the evolution of the resin viscosity. The specific conditions considered were:

– Cure cycle ramps of 0.5 °C min^{-1}, 1 °C min^{-1}, 2 °C min^{-1} and 3 °C min^{-1};

– Cure cycle dwell temperatures of 93 °C and 121 °C;
– Resin initial degrees of cure α_0 of 0.01, 0.05, 0.10, 0.15, 0.20, 0.25 and 0.30.

The ramp rates broadly correspond to the 1 °F to 5 °F range, and are representative of the resin manufacturers' recommendations. By the same token, they also span the range that, in the author's experience, may be realistically achieved using a traditional convection oven and standard tooling. The dwell temperatures correspond to 200 °F and 250 °F, and are also representative of the ranges recommended by the resin manufacturers. The initial resin states are a first approximation of the viscosity increase due to prepreg room-temperature out-time and resin polymerization.

For each simulation, the selected time-temperature and initial resin degree of cure conditions were used to compute the resin viscosity profile. Then, the impregnation model was run over this profile. For the confines of this study, processing was assumed to occur at sea level under perfect vacuum (so that $P_{app} = 101\,325\,\text{Pa}$). Furthermore, as aforementioned, no entrapped air was assumed to remain within the tow before impregnation due to a sufficiently long room temperature vacuum hold (not simulated).

5.8.1.2 Results

Figure 5–9 shows representative resin property curves for a $1\,^{\circ}\text{C}\,\text{min}^{-1}$ ramp to 93 °C and two initial resin degrees of cure: 0.01 and 0.20; the top graph corresponds to the 5320 resin and the bottom to the MTM45-1. Both graphs show the imposed temperature cycle along with the evolution of degree of cure and viscosity for each α_0, and it may be noted that increasing α_0 results in both a higher overall viscosity and a more rapid rise during the

dwell. Differences may also be noted between the two resin systems, with the MTM45-1 being slightly more viscous at these temperatures and, for an initial degree of cure of 0.20, quicker to gel.

Figure 5–10 shows the corresponding predicted evolution of the degree of impregnation for all three materials. Comparing the 5320-based prepregs, it may be seen that for $\alpha_0 = 0.01$, the PW tows impregnate in approximately 53 min and the 8HS in about 67 min. For $\alpha_0 = 0.20$, the 5320/PW tows impregnate in approximately 73 min. However, the 5320/8HS tows never reach full impregnation. By the minimum viscosity point (at 73 min), the degree of impregnation is only approximately 0.4 and the subsequent exponential increase in viscosity overcomes the impregnation rate, slowing it down to the extent that $\beta = 1$ is never reached. Similar behavior may be observed for the MTM45-1/5HS tows, with the tows impregnating fully in approximately 68 minutes for $\alpha_0 = 0.01$ but reaching only $\beta = 0.43$ for $\alpha_0 = 0.20$. For these fabric architectures, resin systems and cure conditions, these are examples of flow-induced micro-voids.

Similar simulations were run for all parameter combinations and materials. The results are reported in Figure 5–11 in terms of time-to-fill for cases where full impregnation is reached or, conversely, in Figure 5–12 in terms of degree of impregnation at gelation. These process maps provide insights into the principal drivers and material - process - property trends governing tow impregnation.

The initial degree of cure of the resin had the most important effect on tow impregnation times. Figure 5–11 shows that for the 5320/PW, $\alpha_0 > 0.25$ results in incomplete impregnation for all cure cycle combinations. For the

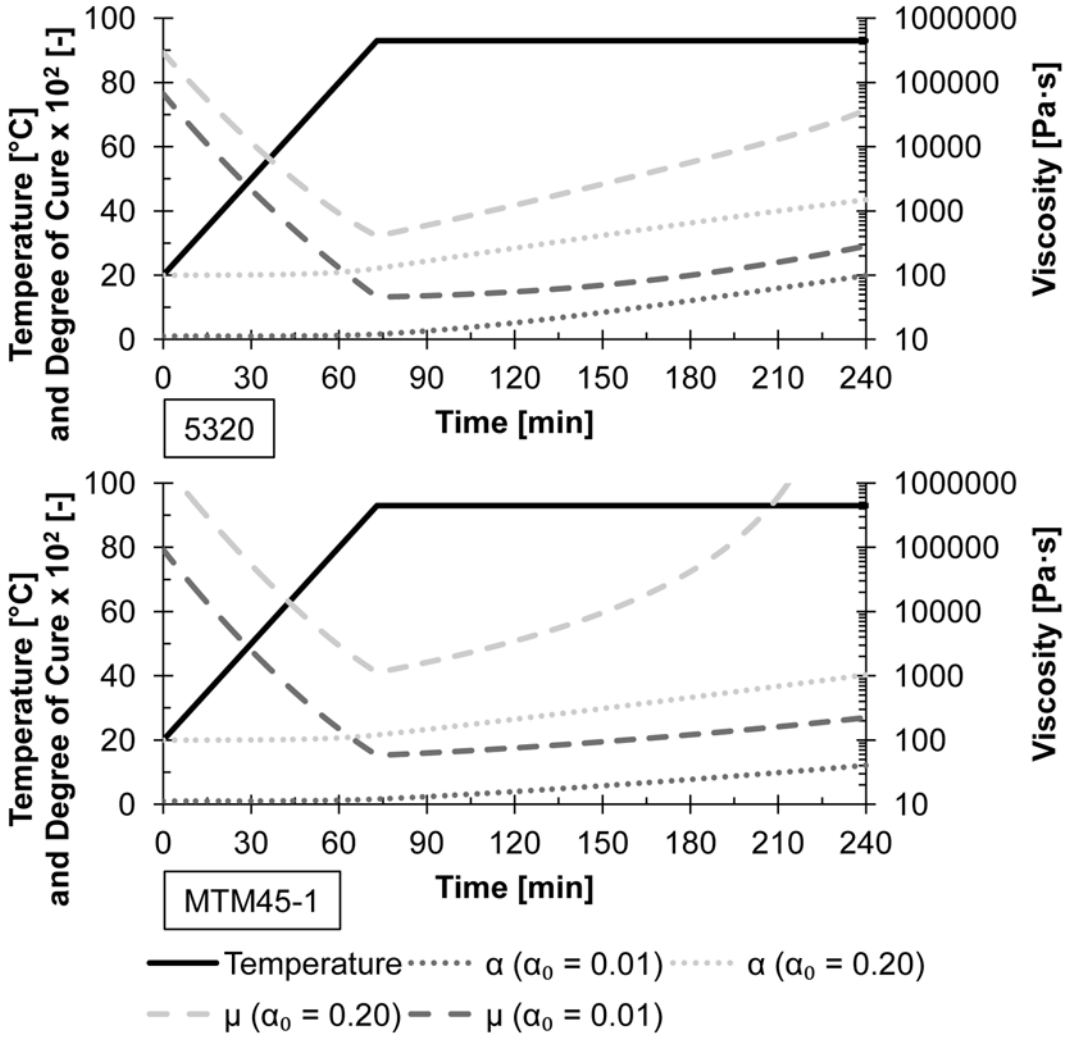

Figure 5–9: Graphs of predicted resin properties for a 1 °C min^{-1} ramp to 93 °C and initial resin degrees of cure of 0.01 and 0.20 for the 5320 resin (top) and the MTM45-1 resin (bottom). The degree of cure data is multiplied by 10^2 for graphing purposes.

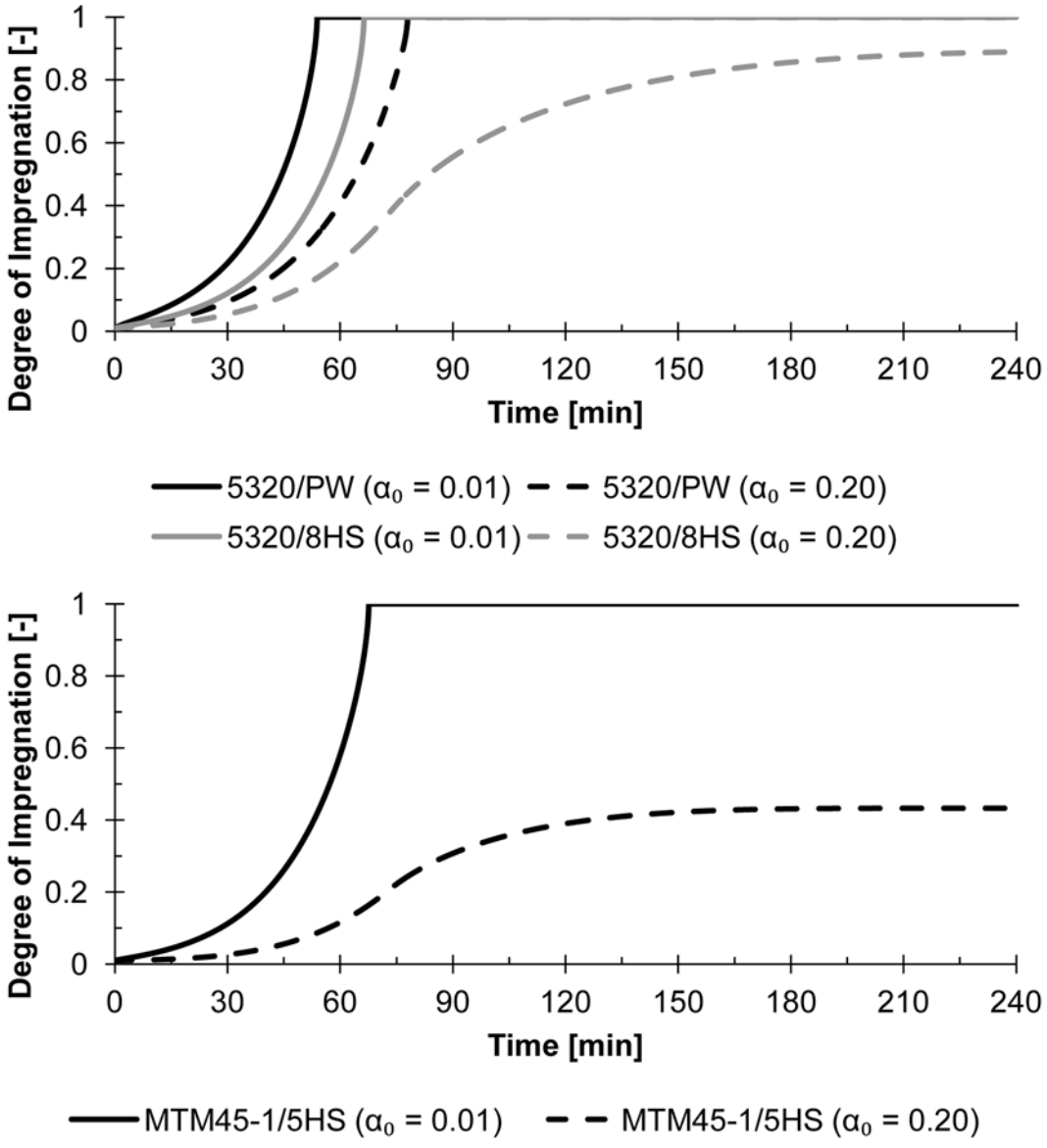

Figure 5–10: Graphs of the predicted evolution of the degree of impregnation for a $1\,^{\circ}\mathrm{C\,min^{-1}}$ ramp to $93\,^{\circ}\mathrm{C}$ and initial resin degrees of cure of 0.01 and 0.20 for the 5320/PW and 5320/8HS prepregs (top) and the MTM45-1/5HS prepreg (bottom).

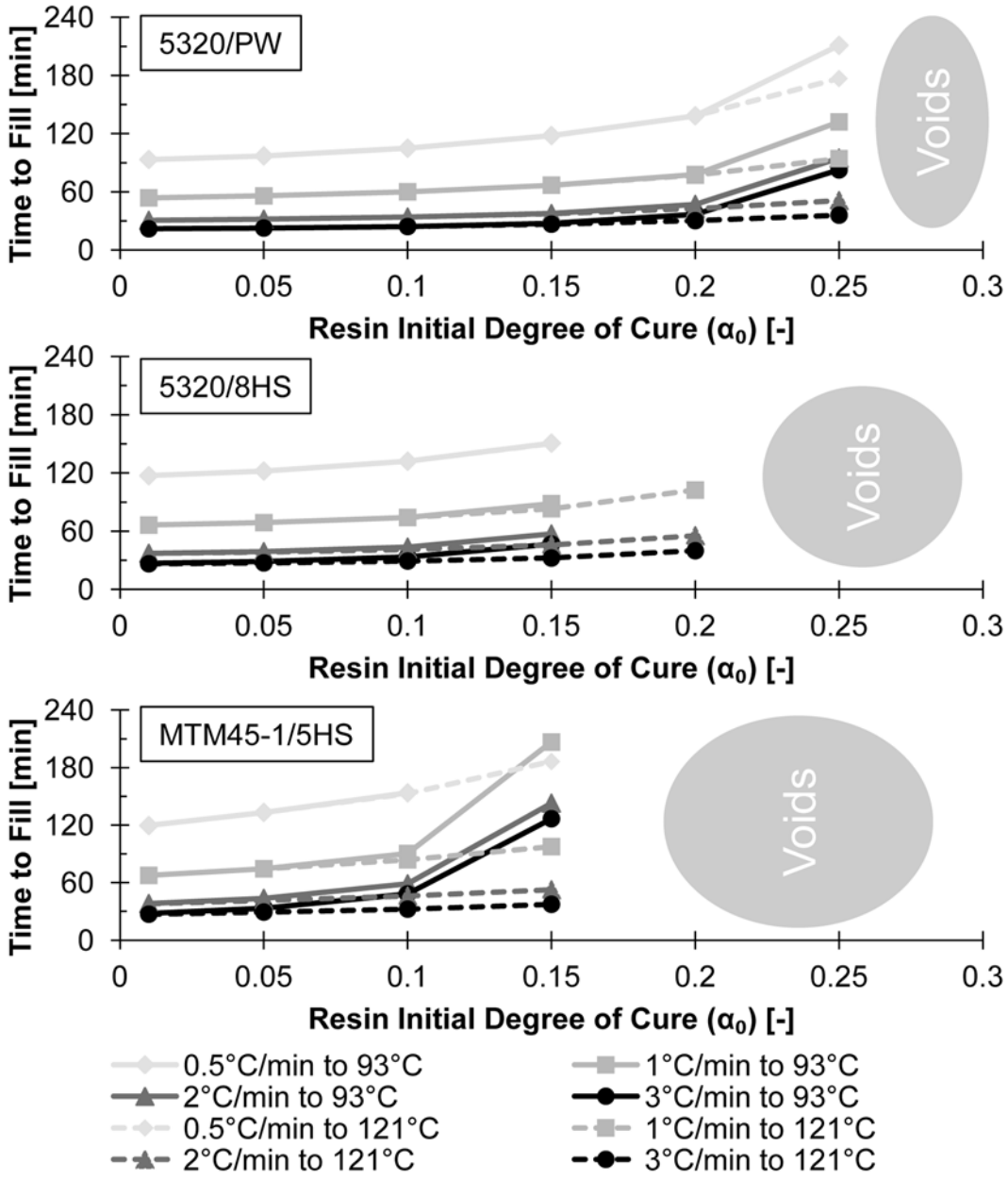

Figure 5–11: Graphs of the predicted time-to-fill versus resin initial degree of cure for 5320/PW (top), 5320/8HS (middle) and MTM45-1/5HS (bottom). Areas labeled "voids" indicate conditions in which $\beta = 1$ is not reached.

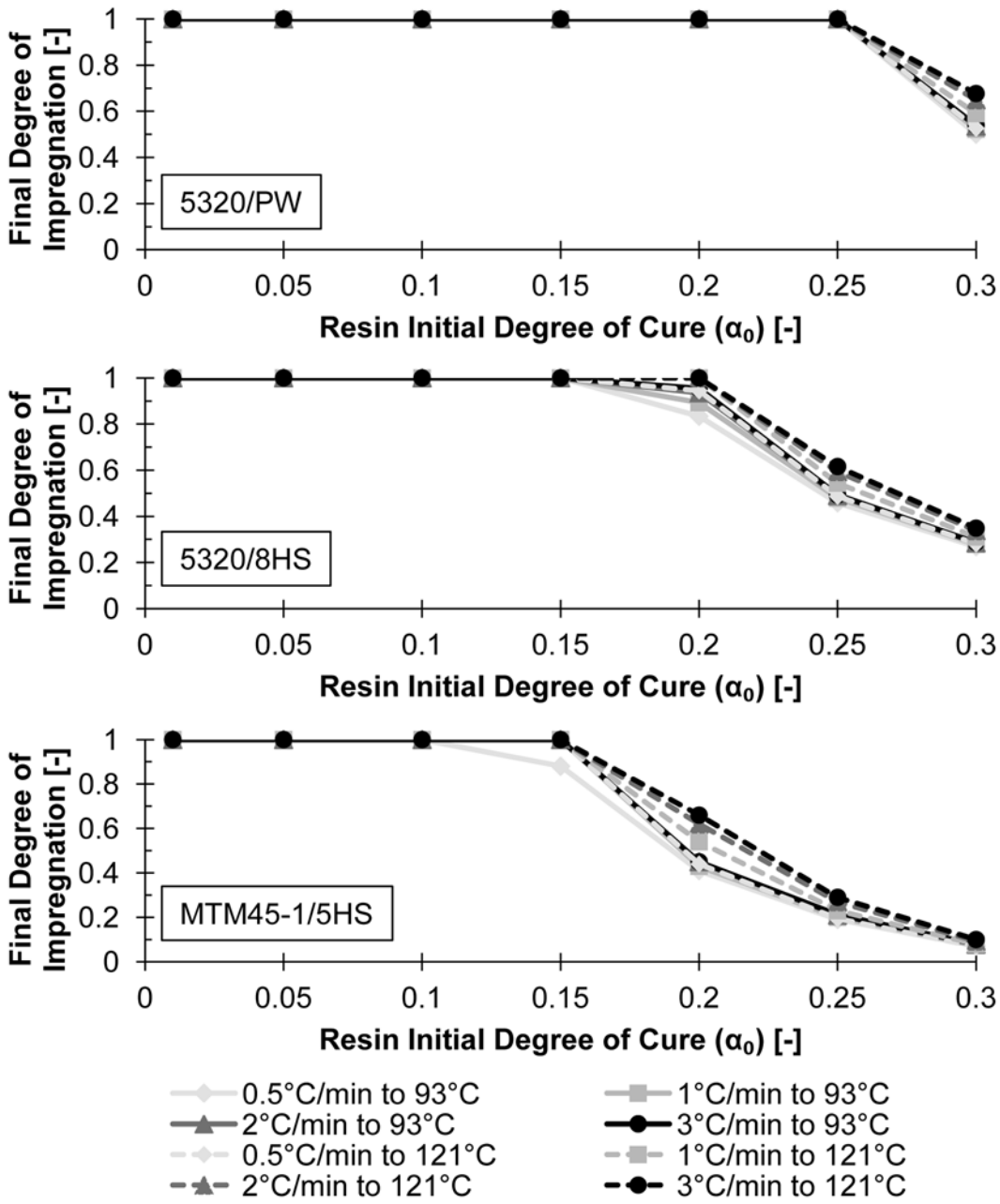

Figure 5–12: Graphs of the predicted final degree of impregnation versus resin initial degree of cure for 5320/PW (top), 5320/8HS (middle) and MTM45-1/5HS (bottom).

5320/8HS, $\alpha_0 > 0.15$ results in incomplete impregnation for all cure cycles except $1\,^{\circ}\mathrm{C\,min^{-1}}$ and higher to 121 °C, for $\alpha_0 = 0.20$. For the MTM45-1/5HS, $\alpha_0 = 0.15$ results in incomplete impregnation for $0.5\,^{\circ}\mathrm{C\,min^{-1}}$ to 93 °C, and $\alpha_0 > 0.15$ for all other cycles. Furthermore, as seen in Figure 5–12, increasing α_0 resulted in significantly lower degrees of impregnation at gelation (and thus larger micro-voids in the final part) for cases with predicted micro-voids.

The temperature ramp rate was also found to have a visible effect on tow impregnation, with higher rates generally resulting in significantly faster impregnation. For example, for the 5320-based prepregs, increasing the rate from $0.5\,^{\circ}\mathrm{C\,min^{-1}}$ to $3\,^{\circ}\mathrm{C\,min^{-1}}$ with all other parameters constant resulted in a decrease of approximately 75 % in the time-to-fill. This trend occurs not only because of the shorter heat-up time, but also because faster ramp rates combine conditions of high temperature and low resin degree of cure, and favor low viscosity flow. Conversely, while slow ramp rates eventually lead to the same dwell temperature, the viscosity during the dwell would be higher due to more extensive resin cure in the course of the ramp.

The dwell temperature was found to have limited effect at low initial resin degrees of cure, since most often full impregnation was reached during the temperature ramp. However, increasing the dwell temperature from 93 °C to 121 °C was quite beneficial at higher degrees of cure, where the largest possible reduction in viscosity is desired. For example, Figure 5–11 shows that for the 5320/8HS, only 121 °C cure cycles resulted in full impregnation at $\alpha_0 = 0.20$, and that for the MTM45-1/5HS, at $\alpha_0 = 0.15$, the 121 °C cycles had considerably faster times to full infiltration. Furthermore, Figure 5–12 shows

that in the case of predicted micro-voids, the final degree of impregnation is higher for cure cycles with 121 °C dwell temperatures.

Finally, by comparing the 5320-based prepregs, the fibre architecture was found to have a significant impact on tow impregnation. The 5320/PW features tows with a lower effective flow length and higher permeability, which impregnate fully in a wider variety of cure cycle and resin conditions; indeed, only very high resin degrees of initial cure ($\alpha_0 > 0.25$) result in micro-void formation. Conversely, the thicker and fibre-denser 5320/8HS tows result in slower flow speeds and are therefore more susceptible to micro-voids in high viscosity conditions brought on by high resin initial degrees of cure and low ramp rates or dwell temperatures. While a direct comparison between the 5320-based prepregs and the MTM45-1 / 5HS must remain qualitative due to the different resins involved, the MTM45-1/5HS does behaves similarly to the 5320/8HS, supporting the above conclusions. This similarity likely occurs because the MTM45-1/5HS and 5320/8HS have similar tow thicknesses and fibre volume fractions, and therefore comparable effective flow lengths and permeabilities.

The above results, while specific to the prepregs under analysis, show consistent trends for multiple material systems, and therefore offer several insights into OOA prepreg processing. For the materials under analysis, tow impregnation times vary considerably with cure cycle and resin initial degree of cure. For the ideal situation of a low initial degree of cure and a fast ramp to a high dwell temperature, full tow impregnation will rapidly occur. However, as processing deviates from the ideal case, the impregnation flow slows down and conditions leading to flow-induced micro-voids may occur.

Such deviations may be expected in a real production environment, since long lay-up times and large metallic tools, which are difficult to heat, are commonplace when processing the large structures for which OOA prepregs have been developed. For such situations, the results nevertheless show that diligent cure cycle selection may mitigate or even eliminate micro-void generation. The results further show that differences in fabric architecture, and therefore in tow geometry, fibre volume fraction and permeability, may significantly change the tow impregnation dynamics. Generally speaking, the data suggests that fabrics whose tows have high fibre volume fractions and large flow lengths (or, in other words, more circular cross-sections) may have a significantly narrower process windows for successful tow impregnation than tows with comparatively lower fibre volume fractions and smaller flow lengths (or thinner, more elongated shapes). This discrepancy may be relevant for components made from multiple architectures; in such cases, the chosen process conditions should ensure no micro-voids within the material with the slowest tow impregnation rate.

5.8.2 Consolidation Pressure (Due to Ambient Pressure)

5.8.2.1 Procedure

A second set of simulations considered variations in consolidation pressure. In OOA processing, the latter is generated by the difference between the ambient pressure outside the bag and the vacuum pressure within; since the current work does not consider non-zero gas pressures within the bag (due to the as-of-yet unclear mechanisms governing OOA gas-induced voids), this study considered variations of $\pm$ 25 % in ambient conditions (or atmospheric pressures of 75 994 Pa, 101 325 Pa and 126 656 Pa). The lower value

is the minimum that may reasonably be expected in a production setting; the standard atmosphere is the benchmark, and the elevated value is offered for comparative purposes. A cure cycle of $0.5\,^{\circ}\mathrm{C\,min^{-1}}$ to $93\,^{\circ}\mathrm{C}$ was selected, being the most likely to result in micro-voids. Furthermore, as before, initial degree of cure conditions ranging from 0.01 to 0.30 were considered.

Consolidation pressure variations affect three model parameters: the resin pressure P_∞, the tow fibre volume fraction V_f and the tow permeability K. A decrease in pressure and, consequently, in fibre volume fraction, reduces the flow velocity (as per Darcy's Law); however, the associated increase in tow permeability increases it.

The resin pressure P_∞ was, as before, assumed equal to applied pressure P_{app}. The tow volume fraction V_f was obtained, for each pressure condition, from the tow compaction curves presented in Figure 5–6. The tow permeability K for the reduced and elevated pressure cases was obtained by assuming that the ratio between the actual permeability and the value predicted by the Gebart model for quadratic fibre arrangement [19] is constant for different applied pressures. First, the ratio between these two values was computed at standard atmospheric conditions. Then, the Gebart quadratic fibre arrangement model [19] was used to predict a theoretical permeability at reduced and elevated pressures using the corresponding fibre volume fraction. Finally, the ratio was used to obtain a corrected K value.

5.8.2.2 Results

Table 5–3 shows the numerical values of the tow fibre volume fraction and transverse permeability for the three material and pressure conditions. For a variation of $\pm$ 25 % in pressure, the changes in V_f are relatively small for

Table 5–3: Tow fibre volume fraction and permeability for reduced pressure conditions.

Parameters	**5320/PW**	**5320/8HS**	**MTM45-1/5HS**
75 994 Pa			
V_f	0.70	0.73	0.73
K	$3.14 \times 10^{-15}\,\mathrm{m}^2$	$1.52 \times 10^{-15}\,\mathrm{m}^2$	$1.50 \times 10^{-15}\,\mathrm{m}^2$
101 325 Pa			
V_f	0.71	0.74	0.74
K	$2.1 \times 10^{-15}\,\mathrm{m}^2$	$9.00 \times 10^{-16}\,\mathrm{m}^2$	$1.00 \times 10^{-15}\,\mathrm{m}^2$
126 656 Pa			
V_f	0.72	0.75	0.75
K	$1.62 \times 10^{-15}\,\mathrm{m}^2$	$6.22 \times 10^{-16}\,\mathrm{m}^2$	$6.04 \times 10^{-16}\,\mathrm{m}^2$

all three materials; however, the associated changes in K are more significant, particularly for the 5320/8HS and MTM45-1/5HS.

Figure 5–13 shows the predicted evolution of the degrees of impregnation for a cycle consisting of a $0.5\,^{\circ}\mathrm{C\,min}^{-1}$ ramp to $93\,^{\circ}\mathrm{C}$, a resin initial degree of cure of $\alpha_0 = 0.01$ and all three pressure conditions, for all materials. These representative results show that the variation in permeability is dominant, with lower consolidation pressures leading to faster infiltration, but that the overall effect is limited at low resin initial degrees of cure. For example, the times-to-fill range from 92.2 min under reduced pressure to 93.8 min under elevated pressure for the 5320/PW, 111.8 min to 120.6 min for the 5320/8HS, and 117.03 min to 126.62 min for the MTM45-1/5HS.

Similar simulations were run for increasing values of resin initial degree of cure, and the results are compiled in Figure 5–14 in terms of time-to-fill and in Figure 5–15 in terms of final degree of impregnation at gelation.

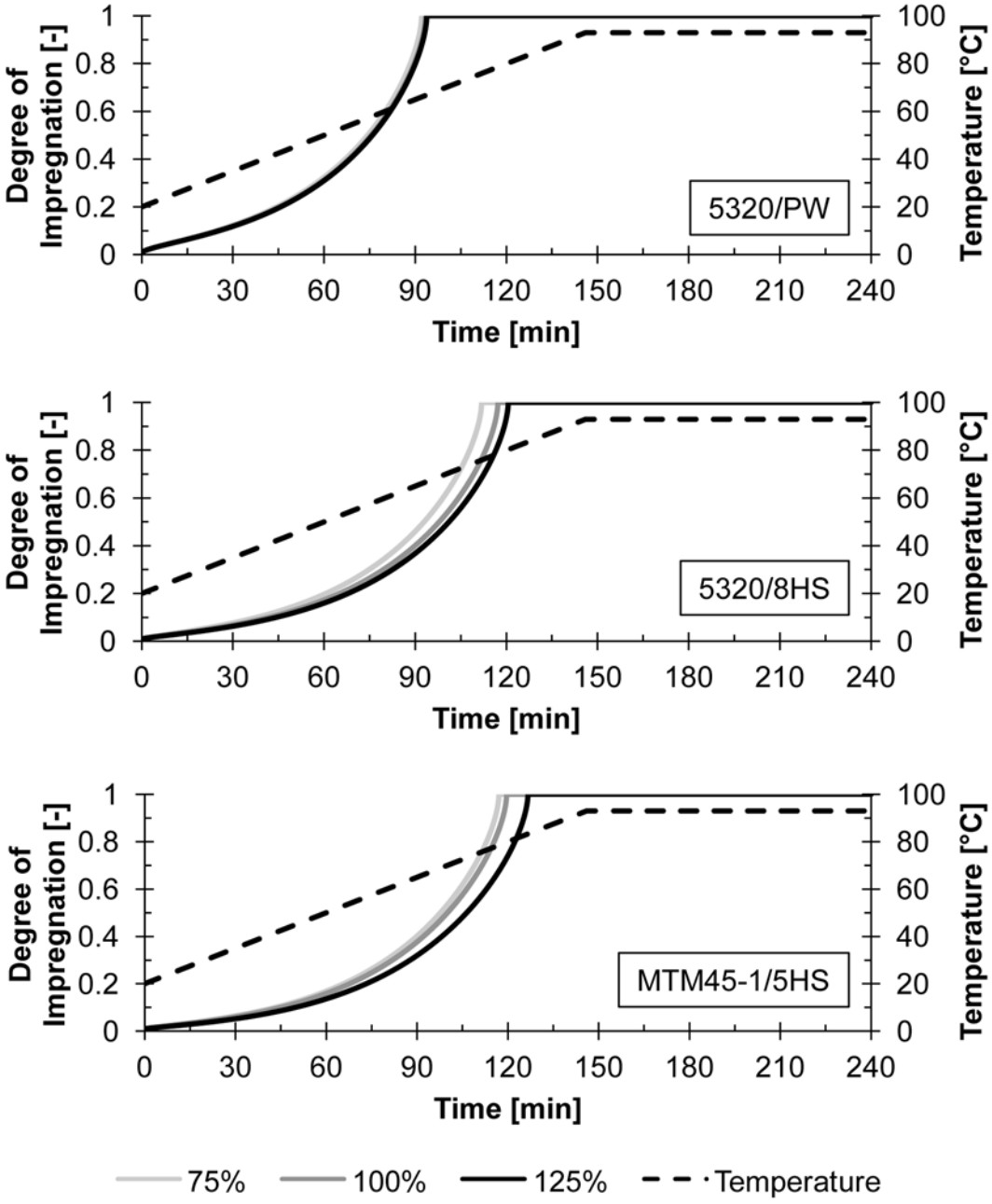

Figure 5–13: Graphs of the predicted degree of tow impregnation versus time for a 0.5 °C min^{-1} ramp to 93 °C, initial resin degree of cure of 0.01 and ambient pressures of 75 %, 100 % and 125 % of atmospheric for 5320/PW (top), 5320/8HS (middle) and MTM45-1/5HS (bottom).

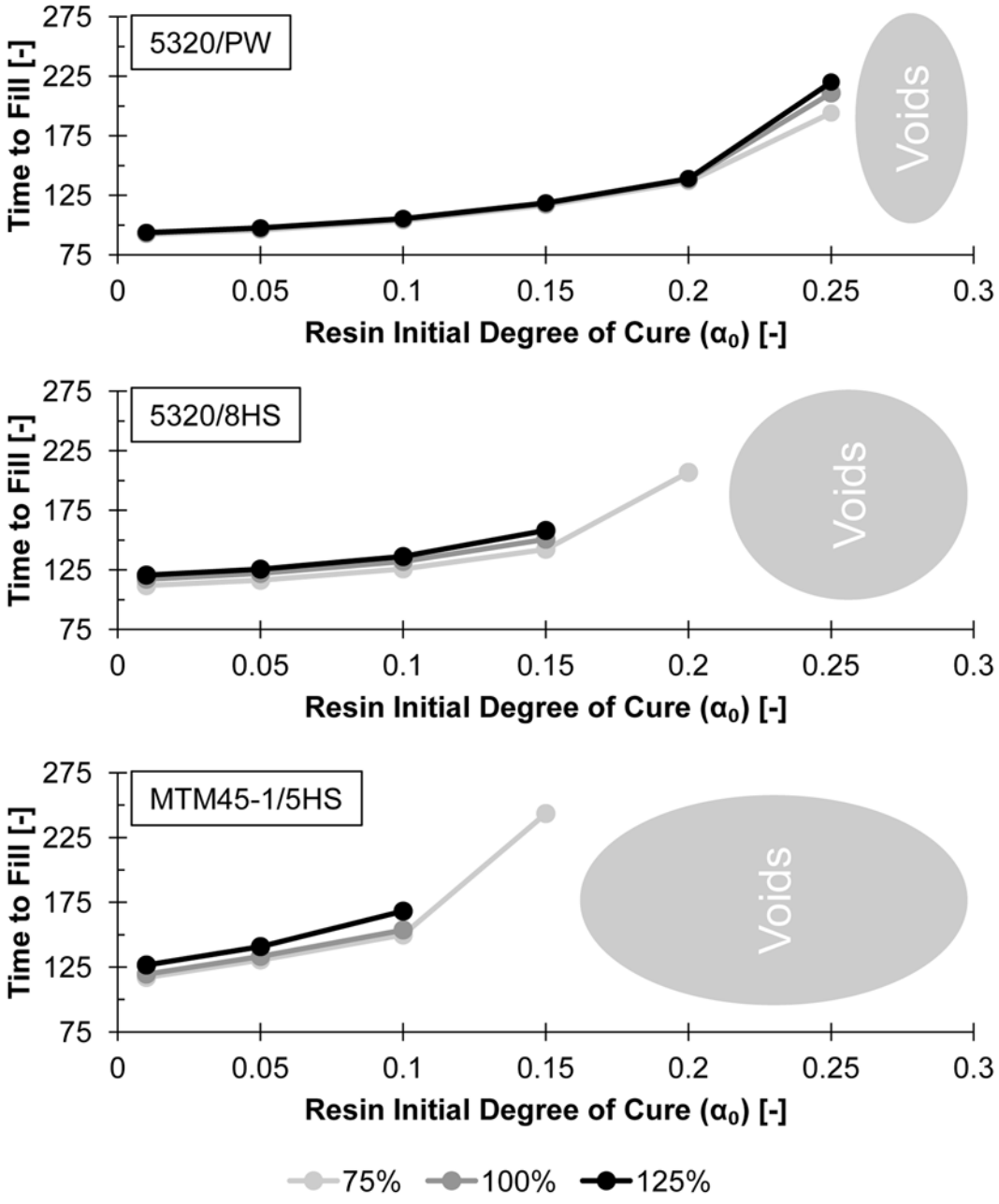

Figure 5–14: Graphs of the predicted time to fill versus resin initial degree of cure for a 0.5 °C min^{-1} ramp to 93 °C and ambient pressures of 75 %, 100 % and 125 % of atmospheric, for 5320/PW (top), 5320/8HS (middle) and MTM45-1/5HS (bottom).

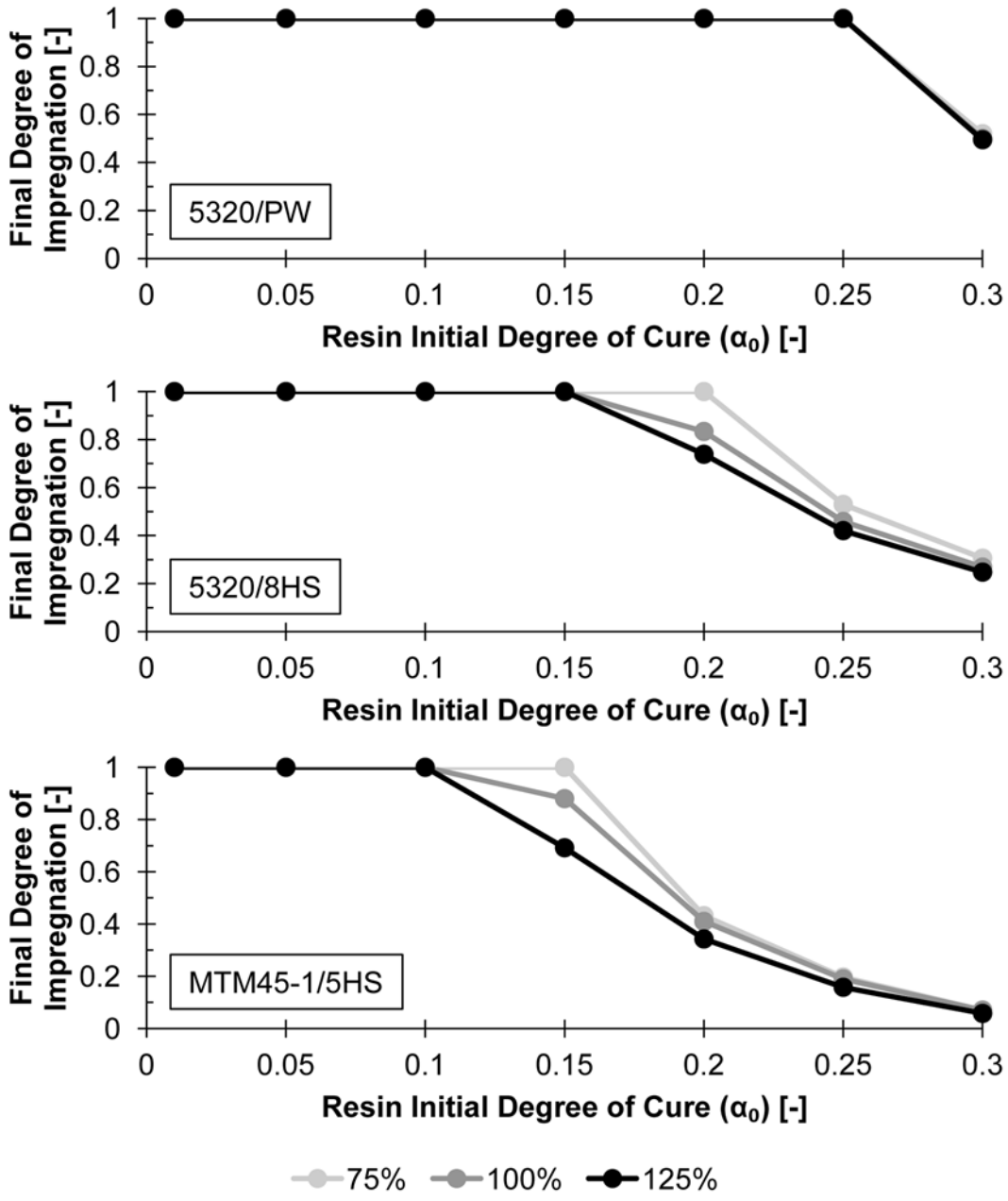

Figure 5–15: Graphs of the predicted final degree of impregnation versus resin initial degree of cure for a 0.5 °C min^{-1} ramp to 93 °C and ambient pressures of 75 %, 100 % and 125 % of atmospheric, for 5320/PW (top), 5320/8HS (middle) and MTM45-1/5HS (bottom).

Figure 5–14 shows that, for all three materials and all resin initial degrees of cure that lead to full tow impregnation, an increase in atmospheric pressure results in a slightly longer impregnation time due to the dominant effect of decreased tow transverse permeability. Similarly, a decrease in atmospheric pressure leads to slightly faster infiltration due to the converse increase in tow permeability.

This effect is, as expected, more beneficial at higher resin initial degree of cure; indeed, for the 5320/8HS and MTM45-1/5HS, the case of 75 % ambient pressure allows predicted full impregnation for this cycle at $\alpha = 0.2$ and $\alpha = 0.15$, respectively. This advantage is also observed in Figure 5–15, which indicates that lower atmospheric pressure may lead to reductions in tow micro-void content for a given material, cure cycle and resin state.

Overall, the effect of varying ambient pressure on tow impregnation dynamics is relatively minor compared to the impact of cure temperature and out-time identified in the previous parametric study, suggesting that the resin viscosity and, hence, the material properties and process parameters affecting it, are the dominant factors controlling resin flow in OOA prepregs. Furthermore, since the ambient pressure is, by and large, not a controlled parameter in industrial environments, and since day-to-day variations are likely to span a few percentage points rather than 25 %, the above results suggest that atmospheric pressure conditions do not have a significant impact on tow impregnation in most relevant cases.

5.9 Limitations

The above study offers a wide variety of insights into the tow impregnation phenomena at the core of OOA prepreg consolidation. However, it

is necessarily limited by the assumptions inherent to the model, which are outlined throughout Sections 5.5 and 5.6.

One major assumption is that of a rigid tow and, consequently, of a constant resin pressure. In reality, during infiltration, the fibre bed may deform, share some of the applied consolidation load, and lead to local variations in fibre volume fraction, permeability and resin pressure. However, even in first approximation, the above study has shown resin viscosity to be the highly dominant factor. Thus, it is assumed that minor variations in the above-listed parameters will not lead to large deviations from the predicted trends.

A second major assumption is that of negligible gas pressure at the resin flow front. In reality, drawing a perfect vacuum under the bag is impossible, and some gas will remain with the tow's micro-pores, further impede impregnation, and likely result in slower tow fill times and larger micro-voids. Thus, the results predicted above may be taken as minimum bounds for their corresponding cure cycle, resin and pressure conditions.

A third, though perhaps more minor assumption, involves the use of predictive models for estimating the capillary pressure contribution and for validating the permeability. While the use of these models was considered necessary and reasonable in light of the difficulty of accurately measuring these parameters, the possible uncertainties in their outputs should be noted.

Two approximations are also implicit in the use of the resin viscosity models at high levels of polymerization. First, in this study, elevated initial degrees of cure were used to estimate, in first approximation, the higher viscosities of resins exposed to room temperature out-time. However, the

chemical transformations occurring at room temperature may not be equivalent to those taking place at the intended process temperatures, particularly for complex systems with multiple simultaneous cure reactions. Thus, the predicted viscosity curves may only be approximate.

Second, the molecular chains and networks that gradually form during cure may cause, in addition to an increase in viscosity, eventual deviations from the assumed behaviour, such as the previously reported non-Newtonian behaviour [20]. Generally, at relatively high levels of cure, these deviations may be expected to decrease the resin's capacity to flow within the porous medium of the tow. The present study assumes that flow remains that of a Newtonian fluid, and continues until the resin viscosity model reaches a mathematical singularity; however, it is acknowledged that it may stop before that point. Thus, as above, the predicted defect levels may be taken as minimum bounds for their corresponding cure cycle, resin and pressure conditions.

5.10 Conclusions

The present chapter considered the effects of material and process parameters on tow impregnation for three commercially-available OOA prepregs. First, a representative model for tow impregnation was developed. Then, the relevant material parameters were determined and the models were correlated and validated with tow impregnation data measured by micro-CT for benchmark cure cycles. Finally, the developed models were used for a parametric study to determine the impact of fibre architecture, resin initial degree of cure, cure cycle temperature and atmospheric pressure on tow impregnation. The study contributes to the knowledge on OOA prepreg processing through the following conclusions.

1. **Tow impregnation may be achieved for a wide variety of conditions if material properties and process parameters remain close to the ideal.** This wide cure cycle window highlights the versatility and flexibility of OOA prepregs, and offers optimization opportunities by allowing the selection of fast ramp rates, high dwell temperatures, and thus short process times. The relative resilience of tow impregnation to deviations in atmospheric pressure also suggests a material and process robustness with respect to consolidation pressure.
2. **Flow-induced micro-voids may occur if material properties and process parameters deviate to the detriment of resin viscosity, but may also be avoided.** In particular, conditions of high initial resin degree of cure and low cure temperatures were shown to lead to micro-porosity in fibre-dense tows. In cases of extreme initial cure, such micro-voids may be unavoidable; however, in many other cases, careful cure cycle selection of fast ramp rates and high dwell temperatures may allow the mitigation of such defects.

CHAPTER 6
An Experimental Study of the Effect of Cure Cycle and Out-Time in Out-of-Autoclave Prepreg Processing

6.1 Introduction

Manufacturing low porosity OOA prepreg parts requires the evacuation of the air entrapped between or within the prepreg plies through the dry zones of an incompletely impregnated ply microstructure. In Chapter 4, these dry zones were identified as the fibre tow cores, and their infiltration at elevated temperature was shown to be the key consolidation phenomenon. Then, in Chapter 5, a tow impregnation model was used to suggest that the resin infiltration dynamics are highly dependent on the resin viscosity, and thus on the material and process conditions that affect it.

The viscosity of OOA prepreg resins can change by several orders of magnitude during processing due to the cure cycle temperature profile and the rate of polymerization [36]. Furthermore, thermosetting resins may also undergo room-temperature polymerization due to room temperature out-time prior to processing [101, 102]. Out-time has already been shown to induce porosity and degrade mechanical performance of OOA prepreg laminates manufactured using a manufacturer-recommended cure cycle [102]. However, the previous chapter suggested that changes in cure cycle may mitigate or even eliminate flow-induced micro-defects in certain cases. Thus, a closer experimental investigation of the interactions between cure cycle, out-time and part quality is desirable.

6.2 Objectives and Structure

The objectives of the present study were to experimentally investigate the effects of cure cycle and out-time on tow impregnation and, more broadly, on OOA laminate consolidation so as to clarify the relationship between material properties, processing phenomena and final part quality.

The study considered two prepregs made from different fabric architectures, and was divided into four parts. First, prepreg and neat resin were exposed to three different levels of out-time. Second, changes to the resin viscosity and prepreg microstructure were investigated by parallel plate rheometry and micro-CT to identify the potential root causes for the effects of out-time on consolidation. Third, laminates were manufactured using four different cure cycles in an instrumented fixture capable of tracking laminate thickness in-situ. Finally, the microstructural quality of the laminates was determined using optical microscopy, interpreted in the context of the previous results, and compared to model estimates.

6.3 Materials

The two OOA prepregs chosen for this study were the previously used 5320/PW and 5320/8HS prepregs, whose properties are summarized in Table 6–1. They are manufactured by Cytec Engineered Materials from Cycom 5320 epoxy resin and two different carbon fabrics: T650-35 PW, a relatively lightweight plain weave, and T650-35 8HS, a thicker, heavier eight harness satin. As shown in the previous chapter, despite having the same tow fibre count, the 8HS tows are less elliptically eccentric, thicker and fibre-denser than those of the PW.

Table 6–1: Properties of the 5320/PW and 5320/8HS prepregs.

Parameters	**5320/PW**	**5320/8HS**
Resin	5320	5320
Resin content	36 %	36 %
Out-life	21 days	21 days
Fabric	T650-3K PW	T650-3K 8HS
Areal weight	$195\,\mathrm{g\,cm^{-3}}$	$370\,\mathrm{g\,cm^{-3}}$
Tow count	3k	3k

The 5320 resin has a manufacturer-stated out-life of 21 days [85]. The baseline out-time of the quantity of materials used for this study was estimated at four days (by accounting for the shipping time of the prepreg rolls before their arrival, and by tracking their out-time during subsequent operations).

It should be noted that while the present prepregs are ostensibly the same as those used in the previous chapter, they originate from a different batch, and (as seen further on) present some differences.

6.4 Procedures

6.4.1 Resin and Prepreg Aging

Neat resin film and prepreg were stored in sealed plastic bags at ambient conditions (temperatures of 22 °C ± 2 °C and relative humidities of 22.5 % ± 1.5 % RH, measured using a wall-mounted environmental sensor). Three different levels of out-time were reached: the 4 day baseline; 21 days, the manufacturer-specified out-life; and 28 days, an extreme level intended to induce potential defects. Once aged, the samples were stored in a freezer until further use.

Table 6–2: Cure cycles for the study of the effects of cure cycle and out-time on OOA prepreg consolidaton.

Cycle	Vacuum Hold Time	Ramp Rate	Dwell Temp.	Dwell Time
1	4 h	$0.56\,^{\circ}\mathrm{C\,min^{-1}}$	93 °C	8 h
2	4 h	$2.77\,^{\circ}\mathrm{C\,min^{-1}}$	93 °C	8 h
3	4 h	$0.56\,^{\circ}\mathrm{C\,min^{-1}}$	121 °C	4 h
4	4 h	$2.77\,^{\circ}\mathrm{C\,min^{-1}}$	121 °C	4 h

6.4.2 Cure Cycles

Four cure cycles were chosen based on two ramp rates ($0.56\,^{\circ}\mathrm{C\,min^{-1}}$ and $2.77\,^{\circ}\mathrm{C\,min^{-1}}$, or 1 °F $\mathrm{min^{-1}}$ and 5 °F $\mathrm{min^{-1}}$) and two dwell temperatures (93 °C and 121 °C, or 200 °F and 250 °F). As in Chapter 5, these selections capture the upper and lower bounds recommended by the material manufacturer as well as conditions that may be typical during industrial oven cure. The four cure cycles are summarized in Table 6–2. For both dwell temperatures, the chosen dwell times meet or exceed the manufacturer recommendations; they ensure sample gelation and vitrification, but have no inherent influence for this study. For laminate manufacture, each cycle included an initial room temperature vacuum hold of four hours (± 20 min), chosen based on prepreg manufacturer recommendations and intended to ensure that air was adequately extracted from the laminate.

6.4.3 Resin and Prepreg Characterization

The evolution of the resin viscosity was determined, as part of a joint study, by Kratz [122]. Resin samples exposed to all three levels of out-time were tested in controlled oscillatory strain mode (0.25 % strain, 1 Hz) in a

TA Instruments AR2000 rheometer, between 25 mm parallel plates, at conditions corresponding to all four chosen cure cycles. The temperature profiles were imposed so as to simulate the thermal history measured during laminate manufacture (and described below). The same experimental method is further discussed by Kratz et al. in [36].

Furthermore, prepreg samples were analyzed using micro-CT to investigate possible changes in initial microstructure due to out-time. The samples, which measured approximately 18 mm per side, with layups of $[(0°/90°)_4]_s$ for the 5320/PW and $[(0°/90°)_2]_s$ for the 5320/8HS, were sectioned from material at all three levels of out-time. Then, they were mounted and scanned using a Skyscan 1172 High Resolution Micro-CT. The scan procedure and parameters were identical to those previously described in Section 4.4.3 with one exception: due to insufficient tack, the 21 and 28 day samples were unable to remain laminated within the the micro-CT sample holder and were wrapped in one layer of masking tape. No changes to the results of interest were expected or observed.

The resultant X-ray micrographs were first used to inspect the prepreg microstructure qualitatively. Then, to obtain a more precise metric of impregnation, the average percent unsaturated tow area was calculated by measuring the average visible dry fibre tow area of 20 randomly chosen tows (using the approach previously described in Section 4.5.2.2) and dividing it by the average nominal tow cross-sectional area (namely, $0.170\,\mathrm{mm}^2$ for 5320/PW and $0.151\,\mathrm{mm}^2$ for 5320/8HS).

6.4.4 Laminate Manufacture

6.4.4.1 Cure Cycle, Dimensions and Layup

Laminates were manufactured from both prepregs and all three levels of out-time using all four cure cycles, for a total of 24 parts. All manufactured laminates measured 101.6 mm by 152.4 mm ± 5 mm (or 4 in by 6 in ± 0.2 in). The 5320/PW laminates had a layup of $[(0°/90°)_8]_s$, while the 5320/8HS layup was $[(0°/90°)_4]_s$, for a nominal expected laminate thickness of approximately 3 mm. Since each laminate contained a large number of tows, and since out-time was expected to mainly affect tow impregnation, only one laminate was manufactured for a given combination of material, cure cycle and out-time. The full set of conditions is summarized in Table 6–3.

Laminates were manufactured using a standard OOA vacuum bag arrangement consisting of individual layers of non-perforated release film below and above the laminate; edge breathing dams made of sealant tape wrapped in fibreglass boat cloth; one layer of breather and the vacuum bag film.

6.4.4.2 Consolidation Fixture

The consolidation fixture used to manufacture the laminates, shown schematically in Figure 6–1 and in a photograph in Figure 6–2, is made up of two components: a tool plate and a sensor support. The tool plate consists of flat aluminum surfaces, and the vacuum bag assembly described above was placed in its center, over two integrated vacuum ports. One port was connected to a vacuum line and used to reduce the bag pressure, while the other was connected to a WIKA A-10 pressure sensor with a 0 Pa to 202 650 Pa (absolute) range. Two OMEGA type-K thermocouples (TT-K-30-SLE (ROHS)) were used to measure the laminate temperatures at the tool and vacuum bag

Table 6–3: Laminates manufactured to investigate the effect of cure cycle and out-time.

#	Material	Ramp Rate	Dwell Temp.	Out-Time
1	5320/PW	$0.56\,^{\circ}\mathrm{C\,min^{-1}}$	$93\,^{\circ}\mathrm{C}$	4 days
2	5320/PW	$0.56\,^{\circ}\mathrm{C\,min^{-1}}$	$93\,^{\circ}\mathrm{C}$	21 days
3	5320/PW	$0.56\,^{\circ}\mathrm{C\,min^{-1}}$	$93\,^{\circ}\mathrm{C}$	28 days
4	5320/PW	$0.56\,^{\circ}\mathrm{C\,min^{-1}}$	$121\,^{\circ}\mathrm{C}$	4 days
5	5320/PW	$0.56\,^{\circ}\mathrm{C\,min^{-1}}$	$121\,^{\circ}\mathrm{C}$	21 days
6	5320/PW	$0.56\,^{\circ}\mathrm{C\,min^{-1}}$	$121\,^{\circ}\mathrm{C}$	28 days
7	5320/PW	$2.77\,^{\circ}\mathrm{C\,min^{-1}}$	$93\,^{\circ}\mathrm{C}$	4 days
8	5320/PW	$2.77\,^{\circ}\mathrm{C\,min^{-1}}$	$93\,^{\circ}\mathrm{C}$	21 days
9	5320/PW	$2.77\,^{\circ}\mathrm{C\,min^{-1}}$	$93\,^{\circ}\mathrm{C}$	28 days
10	5320/PW	$2.77\,^{\circ}\mathrm{C\,min^{-1}}$	$121\,^{\circ}\mathrm{C}$	4 days
11	5320/PW	$2.77\,^{\circ}\mathrm{C\,min^{-1}}$	$121\,^{\circ}\mathrm{C}$	21 days
12	5320/PW	$2.77\,^{\circ}\mathrm{C\,min^{-1}}$	$121\,^{\circ}\mathrm{C}$	28 days
13	5320/8HS	$0.56\,^{\circ}\mathrm{C\,min^{-1}}$	$93\,^{\circ}\mathrm{C}$	4 days
14	5320/8HS	$0.56\,^{\circ}\mathrm{C\,min^{-1}}$	$93\,^{\circ}\mathrm{C}$	21 days
15	5320/8HS	$0.56\,^{\circ}\mathrm{C\,min^{-1}}$	$93\,^{\circ}\mathrm{C}$	28 days
16	5320/8HS	$0.56\,^{\circ}\mathrm{C\,min^{-1}}$	$121\,^{\circ}\mathrm{C}$	4 days
17	5320/8HS	$0.56\,^{\circ}\mathrm{C\,min^{-1}}$	$121\,^{\circ}\mathrm{C}$	21 days
18	5320/8HS	$0.56\,^{\circ}\mathrm{C\,min^{-1}}$	$121\,^{\circ}\mathrm{C}$	28 days
19	5320/8HS	$2.77\,^{\circ}\mathrm{C\,min^{-1}}$	$93\,^{\circ}\mathrm{C}$	4 days
20	5320/8HS	$2.77\,^{\circ}\mathrm{C\,min^{-1}}$	$93\,^{\circ}\mathrm{C}$	21 days
21	5320/8HS	$2.77\,^{\circ}\mathrm{C\,min^{-1}}$	$93\,^{\circ}\mathrm{C}$	28 days
22	5320/8HS	$2.77\,^{\circ}\mathrm{C\,min^{-1}}$	$121\,^{\circ}\mathrm{C}$	4 days
23	5320/8HS	$2.77\,^{\circ}\mathrm{C\,min^{-1}}$	$121\,^{\circ}\mathrm{C}$	21 days
24	5320/8HS	$2.77\,^{\circ}\mathrm{C\,min^{-1}}$	$121\,^{\circ}\mathrm{C}$	28 days

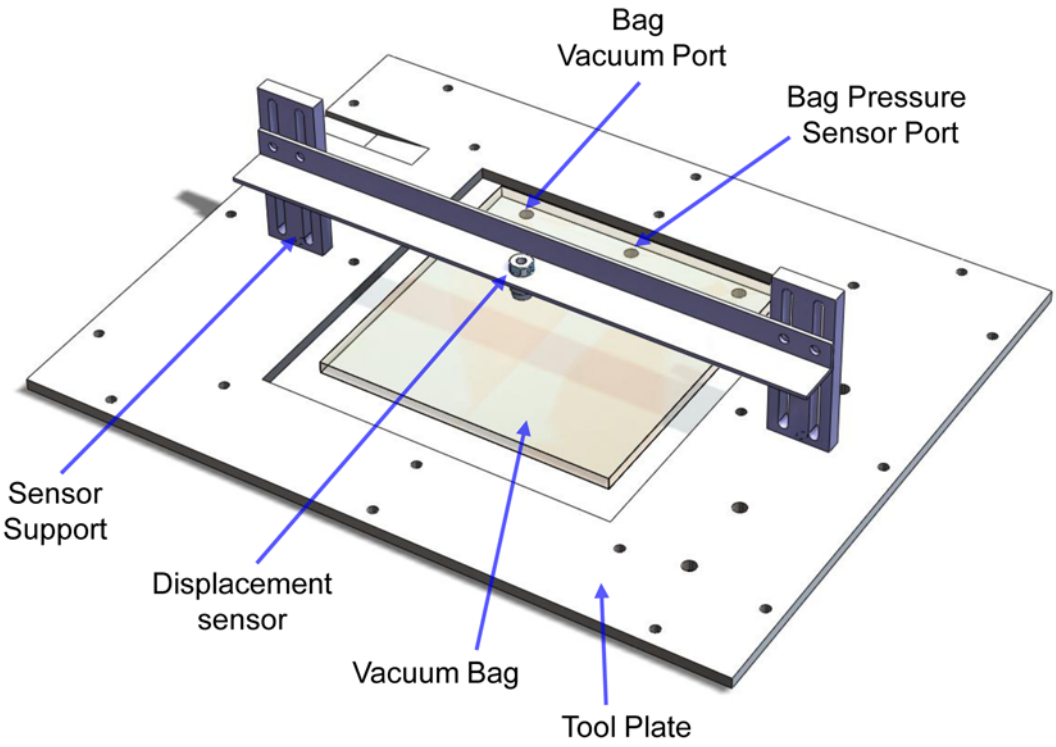

Figure 6–1: Schematic of the custom-designed, instrumented consolidation fixture used for laminate manufacture.

interfaces, and thus to quantify the maximum thermal gradient present in the part.

The sensor support held a Micro-Epsilon eddyNCDT 3010 / U6 non-contact eddy current sensor, which detected the displacement of a 75 mm by 75 mm by 2 mm steel target placed directly underneath on the laminate, between the release film and the breather. The sensor has a range of 6 mm, a maximum resolution of 0.3 µm and a maximum working temperature of 150 °C, which allowed it to measure laminate thickness changes in-situ, in OOA prepreg processing conditions. These displacement readings were corrected for sensor temperature drift and support structure thermal expansion

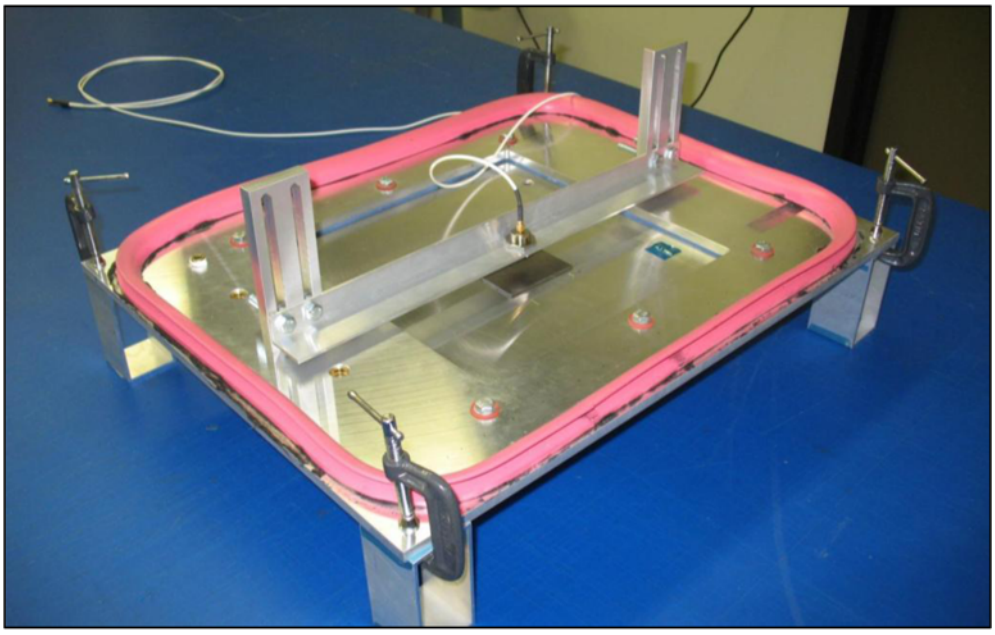

Figure 6–2: Photograph of the custom-designed, instrumented consolidation fixture used for laminate manufacture.

using a third thermocouple adjacent to the sensor; the calibration and correction procedure is explained in Appendix D.

During laminate processing, the fixture was placed within a Thermal Product Solutions Blue M convection oven. The oven set-points during heat-up were chosen to ensure that the laminate temperature followed the desired ramp rates. A thermocouple was placed within the oven to measure the oven air temperature. Vacuum was drawn using either wall-mounted Busch vacuum pumps or a stand-alone Edwards xDS 5 vacuum pump, run continuously to ensure uniform and maximal vacuum quality.

A more detailed description of the consolidation fixture, along with the results of the pressure and displacement sensor calibrations, are offered in Appendix D.

6.4.5 Laminate Quality Analysis

The quality of each manufactured laminate was determined through external observation and microstructural analysis. For external observation, the laminate surfaces, edges and adjacent consumables were visually inspected for any unusual features, and laminate thickness measurements were performed in six locations using a Mitutoyo 0 - 25.4 mm micrometer (model 293-765-30).

Microstructural analysis consisted of sample preparation, optical microscopy and image analysis. Samples were prepared by sectioning two pieces (approximately 50 mm long and 25.4 mm wide) from the area under the displacement sensor's steel target, mounting them on honeycomb core using two-part epoxy for easy manipulation and wet-polishing one of their edges with up to 1200 grit sandpaper using a Buehler MetaServ2000 grinder/polisher. Optical micrographs were acquired using a Nikon Eclipse L150 optical microscope with attached Clemex Captiva digital camera. Image analysis was performed using the ImageJ software to determine two quality metrics: the average percent unsaturated tow area and the macro-void content of the sample.

For these manufactured laminates, the average percent unsaturated tow area $(A_f/A_{tow})_{ave}$ was defined as a weighted average:

$$\left(\frac{A_f}{A_{tow}}\right)_{ave} = \left(\frac{A_f}{A_{tow}}\right)_{porous,20} \left(\frac{n_{porous}}{n_{total}}\right) + \left(\frac{A_f}{A_{tow}}\right)_{sat} \left(1 - \frac{n_{porous}}{n_{total}}\right) \quad (6.1)$$

$(A_f/A_{tow})_{porous,20}$ is the average percent unsaturated area in the cross-section of twenty random porous tows, obtained by measuring the visible dry fibre tow area A_f and dividing by the total cross-sectional area A_{tow}; n_{porous} is the number of incompletely impregnated tows in the sample cross-section;

n_{total} is the total number of tows in the cross-section; and $(A_f/A_{tow})_{sat}$ is the average unsaturated area in a fully saturated tow, and equal to zero. While the total micro-void content may also be expressed as the ratio of the total micro-void area to the total cross-sectional area, it is prohibitively lengthy to calculate for a sample with pervasive tow micro-porosity. Furthermore, the average percent unsaturated tow area directly acknowledges the process of tow impregnation and is easily compared to the degree of impregnation β obtained from modelling:

$$\left(\frac{A_f}{A_{tow}}\right)_{ave} = (1-\beta)^2 \tag{6.2}$$

The macro-void content of each sample was obtained by measuring the total macro-void area in the cross-section using ImageJ, and dividing it by the total cross-sectional area.

6.4.6 Comparison to Model Estimates

The average percent unsaturated tow areas measured above were compared to model predictions for the same materials and cure cycles. The change in resin viscosity induced by out-time was taken into account in two ways.

The first approach consisted of simply using the experimentally measured viscosity as a model input. However, while direct, this method may not always be suitable or practical, since measured data may not be available for all materials, cure cycles and resin states.

The second approach thus relied on the 5320 resin cure kinetics and viscosity models. First, the 21 and 28 day out-times considered in this study were associated to corresponding resin glass transition temperatures using

data obtained for the 5320 resin using MDSC by Grunenfelder and Nutt [101, 102, 123]. Then, these T_g values were input into the 5320 glass transition temperature model developed by Kratz et al. [36] to obtain associated resin degree of cure α values:

$$\frac{T_g - T_{g0}}{T_{g\infty} - T_{g0}} = \frac{\lambda\alpha}{1 - (1 - \lambda)\,\alpha} \tag{6.3}$$

As explained in Chapter 2, T_g is the glass transition temperature corresponding to a degree of cure α; T_{g0} and $T_{g\infty}$ are the glass transition temperatures of the uncured and fully cured resin, respectively, and λ is used as a fitting constant; the values of all constants are offered in [36].

Finally, the resin degree of cure values thus obtained were set as initial α_0 values in the cure kinetics model and used, along with the time-temperature cycles used to manufacture the laminates, to obtain resin viscosity and tow impregnation profiles and predict tow micro-porosity.

6.5 Results and Discussion

6.5.1 Resin and Prepreg Aging

Several changes were observed in the neat resin and prepregs after aging. A significant loss of tack (or surface adhesiveness) was noted with increasing out-time, with the materials being optimally tacky at the four-day baseline, significantly less tacky at 21 days and having no tack at 28. Both resin and prepregs were also seen to become considerably less compliant with out-time, being soft and pliable at four days and stiff or brittle after 28. Plies from both prepregs were also seen to undergo slight warpage with increasing out-time. Such observations are in line with previous reports [79, 102].

The differences in tack and compliance are attributed to changes in resin thermomechanical properties due to room temperature cure: as the degree of cure increases at constant ambient conditions, the resin evolves towards a solid state. Furthermore, if the increasing glass transition temperature exceeds room temperature prior to gelation, vitrification may bring about a glassy, stiff consistency. The onset of warpage may be explained by the above changes in resin properties coupled with a possible slight through-thickness asymmetry of the prepreg.

6.5.2 Resin and Prepreg Characterization

The measured evolution of the resin viscosity is shown in Figure 6–3 for the 93 °C dwell temperature cure cycles and in Figure 6–4 for the 121 °C dwell temperature cure cycles. Two major trends are visible. First, the entire viscosity profile is shifted upwards with increasing out-time, indicating an increase in viscosity at each time-temperature point. These increases are significant: for example, for the 0.56 °C min^{-1} to 93 °C cycle, the minimum viscosity increases from 42 Pa s at four days to 273 Pa s at 28 days. Second, since high viscosities are reached more rapidly at higher out-times, the gel point (defined as reaching a storage modulus G' of 100 000 Pa) is shifted to the left. This change is also significant: for the same 0.56 °C min^{-1} to 93 °C cycle, the gel time is reduced from approximately 400 min to 288 min. Both changes are likely to impede tow impregnation, higher viscosities leading to slower resin flow (as per Darcy's Law) and earlier gelation reducing the overall flow time.

Representative X-ray micrographs at each of the three levels of out-time are shown in Figure 6–5 for 5320/PW and in Figure 6–6 for 5320/8HS, while

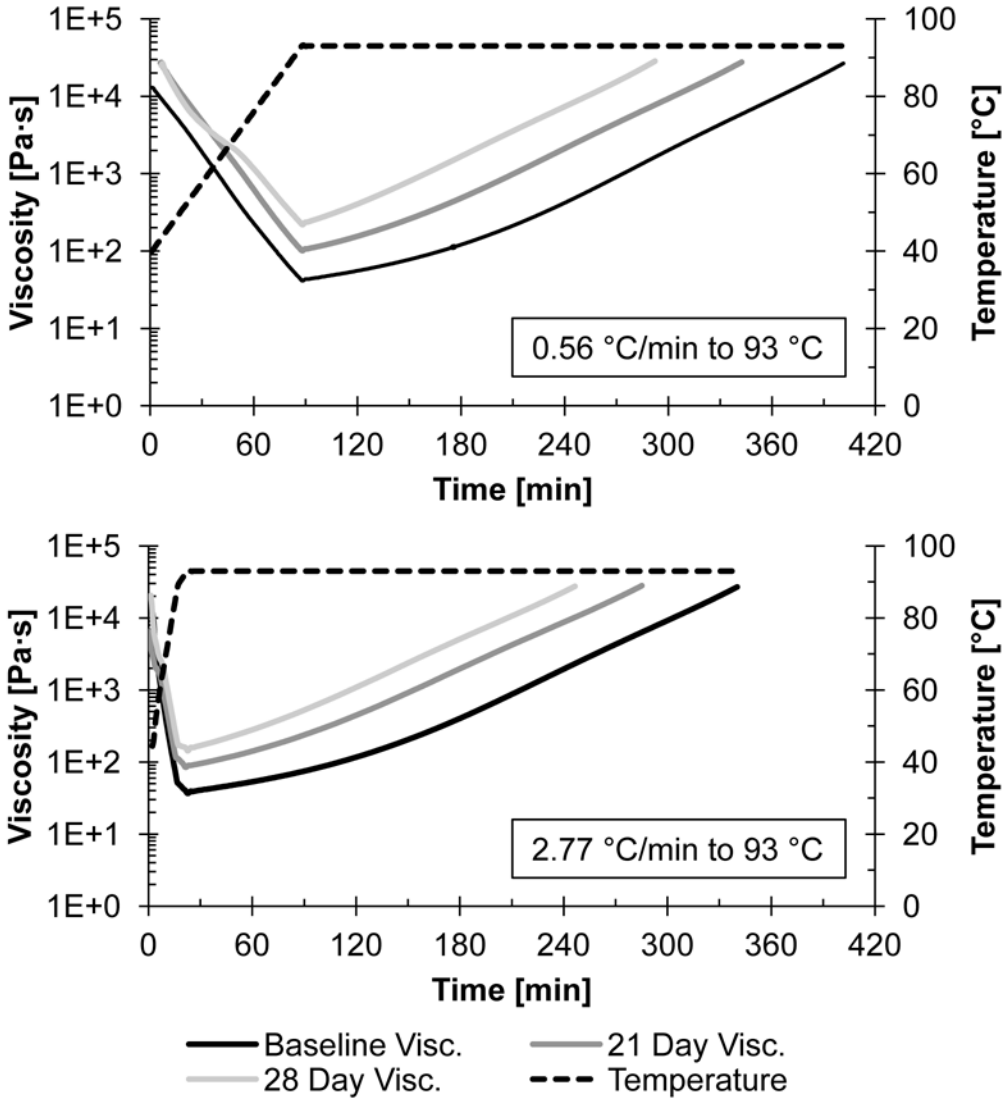

Figure 6–3: Graphs of the resin viscosity for baseline, 21 day and 28 day outtimes and two cure cycles: 0.56 °C min^{-1} to 93 °C (top) and 2.77 °C min^{-1} to 93 °C (bottom).

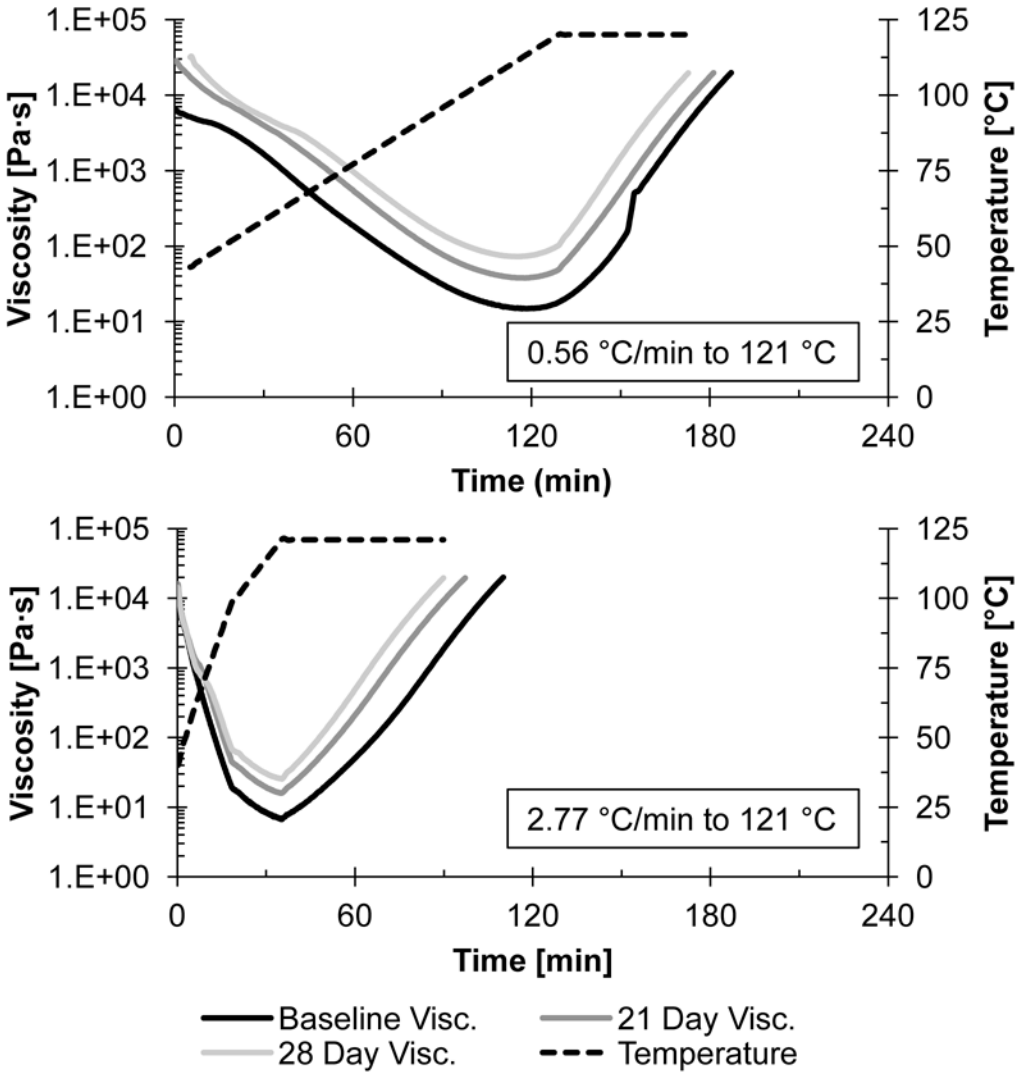

Figure 6–4: Graphs of the resin viscosity for baseline, 21 day and 28 day outtimes and two cure cycles: $0.56\,^{\circ}\mathrm{C\,min^{-1}}$ to 121 °C (top) and $2.77\,^{\circ}\mathrm{C\,min^{-1}}$ to 121 °C (bottom).

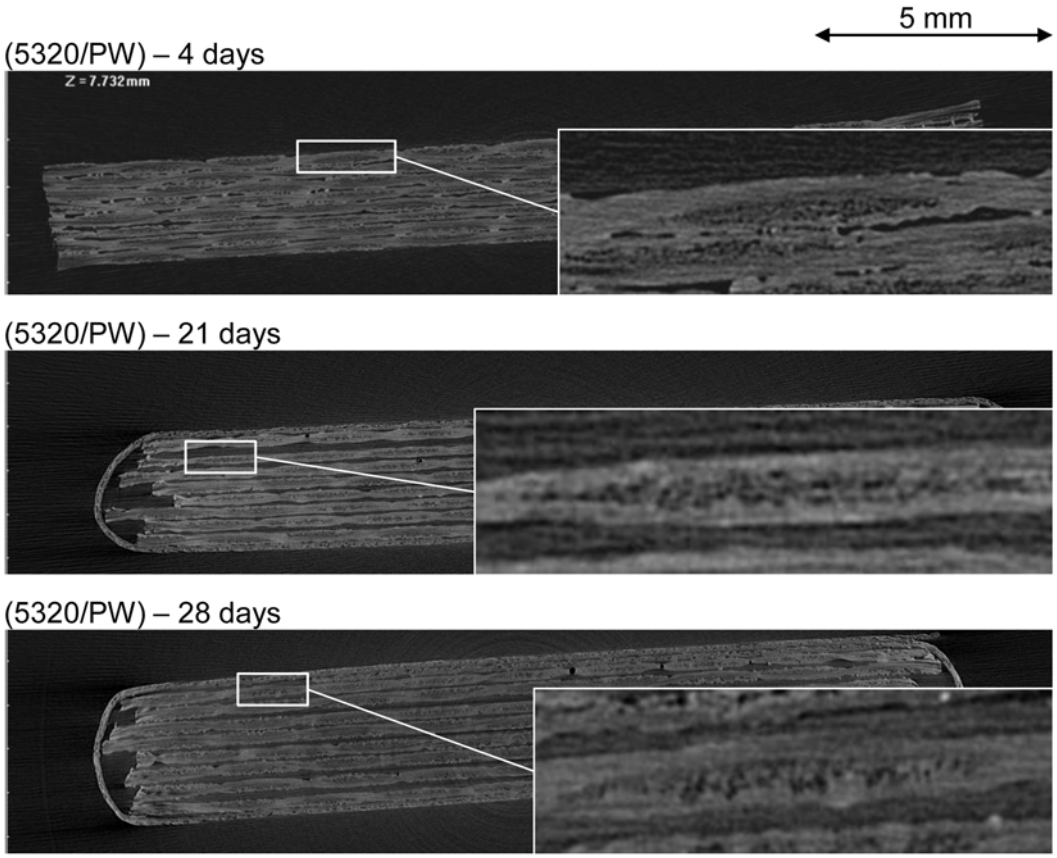

Figure 6–5: X-ray micrographs of representative microstructures for baseline, 21 and 28 day out-times and the 5320/PW. The scale bar applies to the large micrographs; the scale of the insets varies

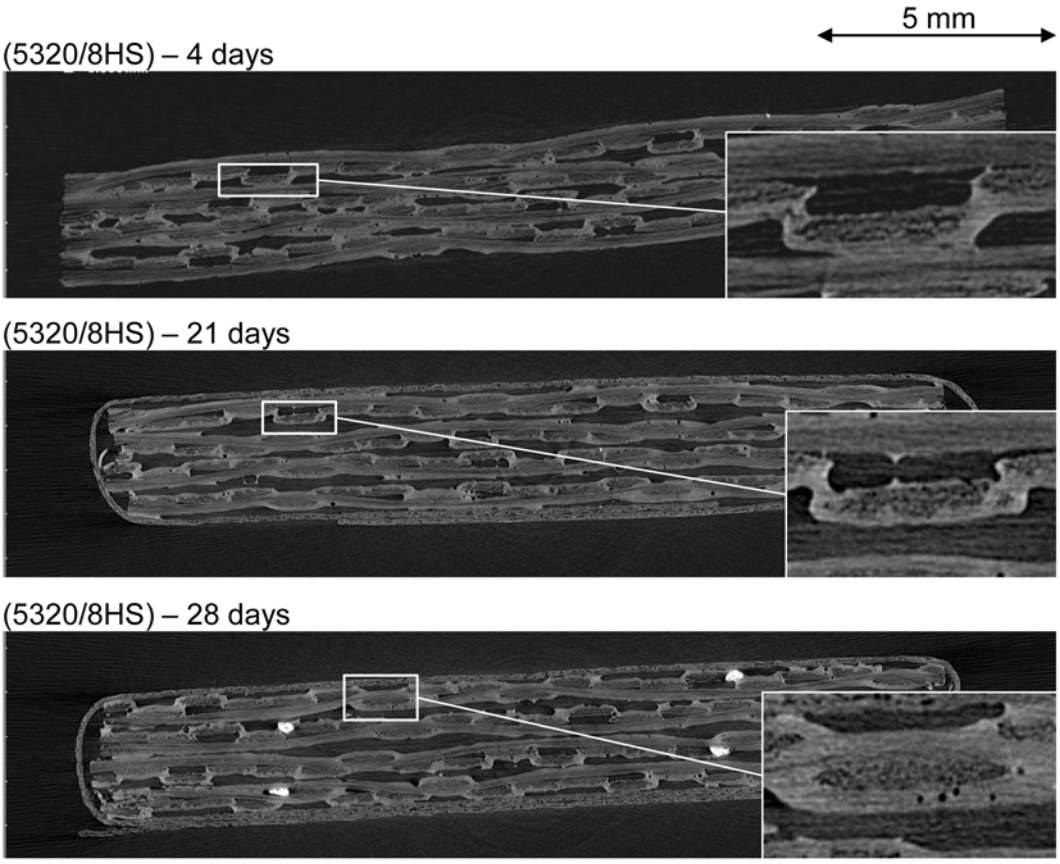

Figure 6–6: X-ray micrographs of representative microstructures for baseline, 21 and 28 day out-times and the 5320/8HS. The scale bar applies to the large micrographs; the scale of the insets varies. The bright areas are nylon tracers embedded during the prepregging process.

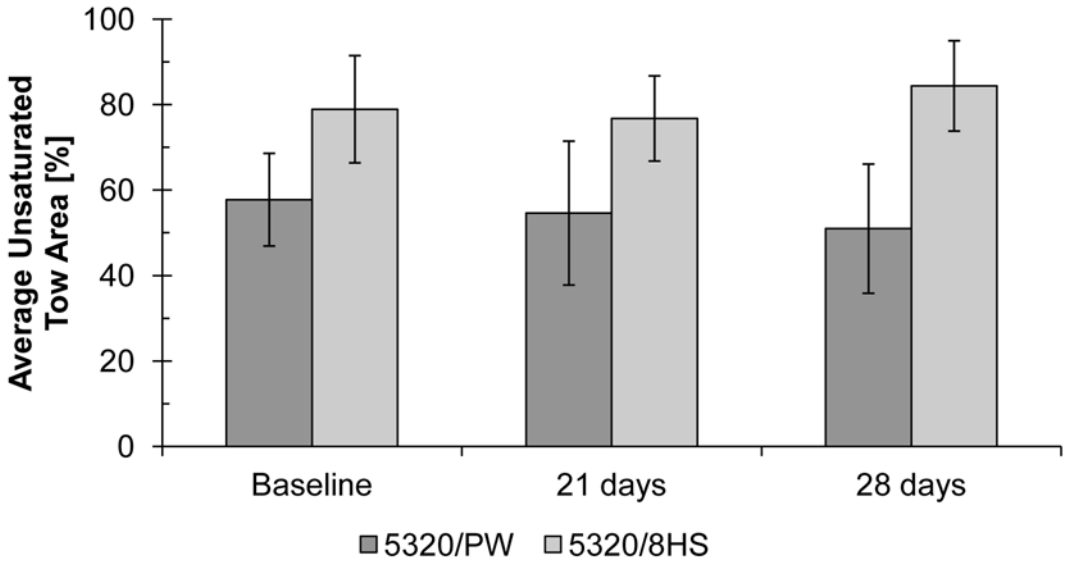

Figure 6–7: Chart of the average unsaturated tow area versus out-time for 5320/PW and 5320/8HS prepregs. The error bars show one standard deviation in the twenty tow measurements.

the average percent unsaturated tow area data is compiled in Figure 6–7. The micrographs show similar partially impregnated prepreg microstructure at four, 21 and 28 days of out-time, and the measured values confirm that, within the inherent material variability, there are no significant changes to the unsaturated tow area at room temperature. Thus, the effect of out-time on the initial prepreg structure is found to be negligible.

Interestingly, the above results also show that the batch of 5320/PW used for this study was significantly more impregnated than the 5320/8HS, and indeed than the batch of 5320/PW used in Chapter 5. This difference is attributed to changes in the manufacturing of the actual prepreg, and highlights both the importance of regular batch inspection and control for such commercially-available engineered materials.

6.5.3 Laminate Manufacture

6.5.3.1 Temperature and Pressure

Representative graphs showing thermocouple and bag pressure sensor readings during laminate manufacture are shown in Figures 6–8 to 6–11.

The oven temperature (and, consequently, the sensor temperature) are seen to have exceeded the target laminate dwell temperature at the end of the heat-up ramp; this intentional over-set was used to ensure that the laminate heated at the desired rate. In some cycles, the oven temperature also varied around the dwell temperature as a result of the oven controller maintaining the correct laminate temperature. No major thermal gradients occurred, with the largest instantaneous difference between the top and bottom of a laminate being approximately 3.3 °C during heat-up.

The pressure readings show that the bag pressure quickly descended below 5 % of atmospheric pressure once vacuum was applied at the beginning of the cycle. Then, it experienced mild fluctuations during processing, likely due to the behaviour of the vacuum bag sealant tape under vacuum compression and elevated temperature. Such issues are part of the inherent variability of the manufacturing process, and the vacuum quality achieved during all cure cycles respected the material manufacturer's recommendations.

Overall, the thermocouple and bag pressure sensor readings showed that all laminates were manufactured under the intended process parameters.

6.5.3.2 Laminate Thickness

The data acquired from the in-situ displacement sensor measurements offers several insights into the consolidation phenomena that occurred during processing. Representative results are shown for the $0.56\,^{\circ}\mathrm{C\,min^{-1}}$ to 93 °C

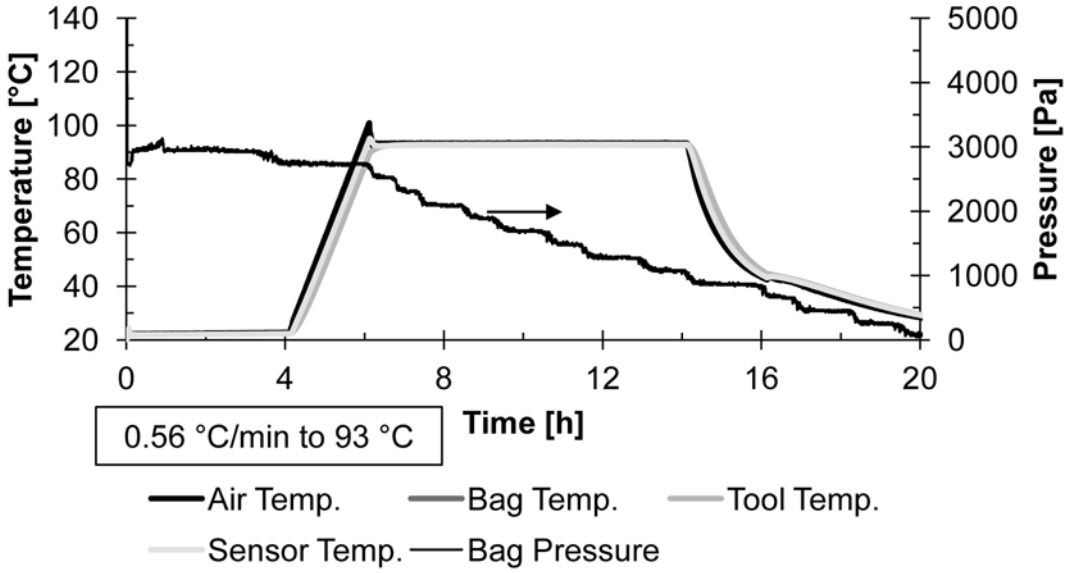

Figure 6–8: Graphs of temperature and bag pressure for the $0.56\,^{\circ}\mathrm{C\,min^{-1}}$ to $93\,^{\circ}\mathrm{C}$ manufacture of the 4-day 5320/PW laminate.

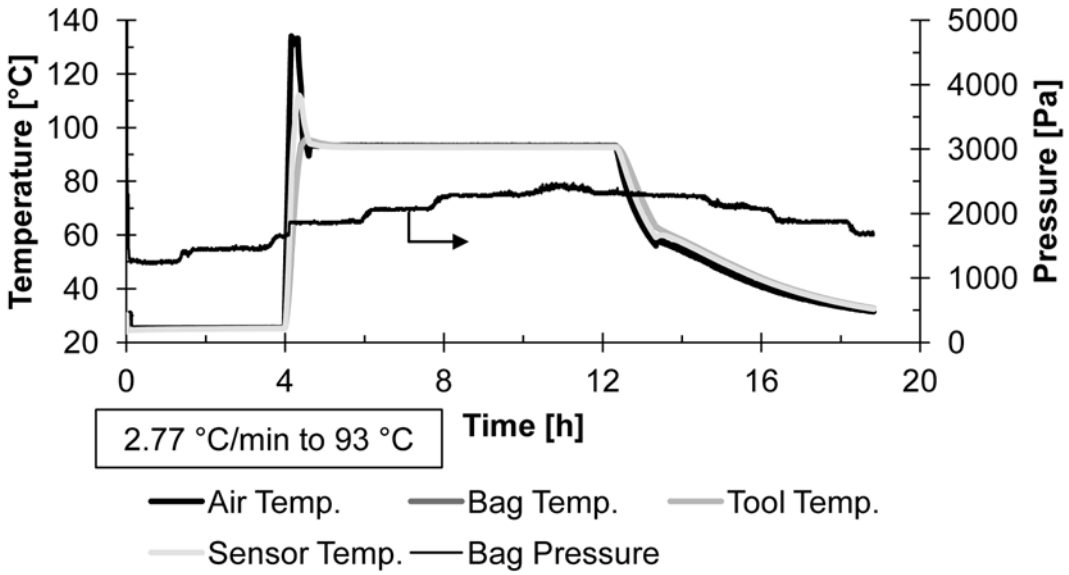

Figure 6–9: Graphs of temperature and bag pressure for the $2.77\,^{\circ}\mathrm{C\,min^{-1}}$ to $93\,^{\circ}\mathrm{C}$ manufacture of the 4-day 5320/PW laminate.

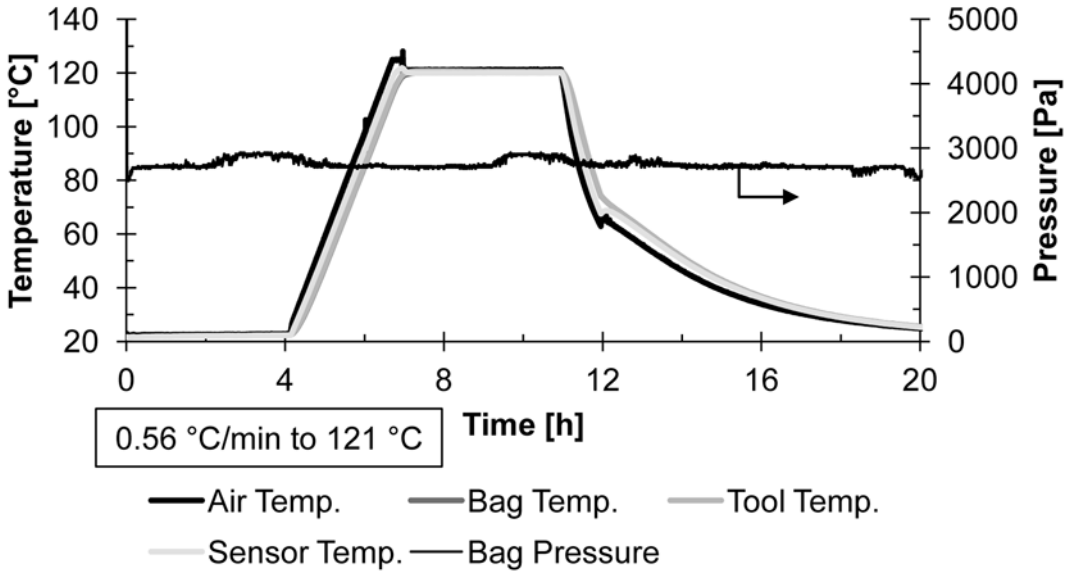

Figure 6–10: Graphs of temperature and bag pressure for the $0.56\,^{\circ}\mathrm{C\,min^{-1}}$ to 121 °C manufacture of the 4-day 5320/PW laminate.

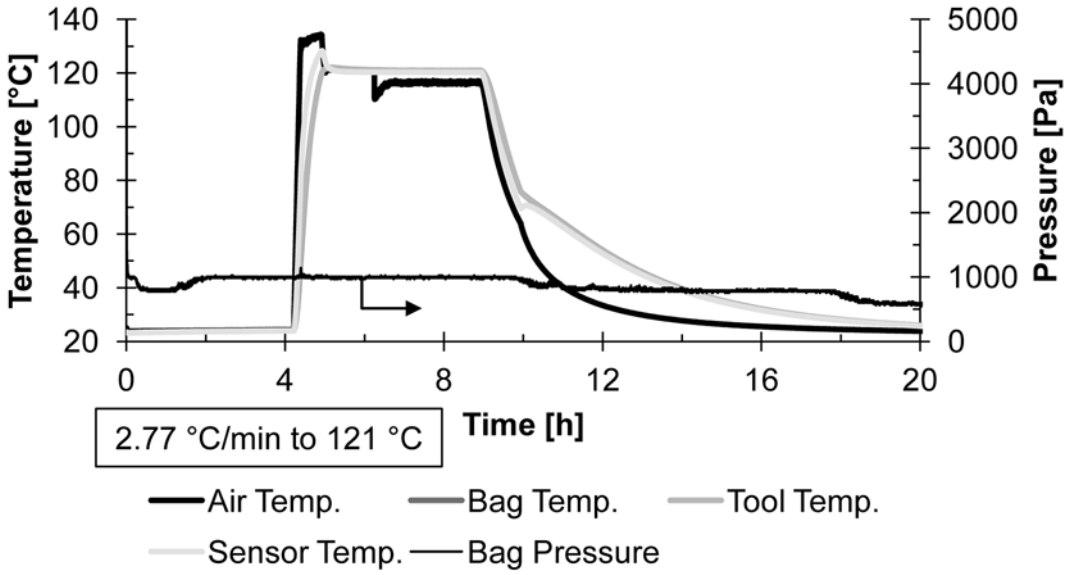

Figure 6–11: Graphs of temperature and bag pressure for the $2.77\,^{\circ}\mathrm{C\,min^{-1}}$ to 121 °C manufacture of the 4-day 5320/PW laminate.

cure cycles in Figures 6–12 and 6–13, and the complete set of graphs for all cure cycles is available in Appendix E. The laminate thickness curves were obtained by combining the change in distance to target measured by the displacement sensor with the final thickness of each laminate, and anchored on the time axis such that for all curves, heating begins precisely at the four hour mark. For each figure, the top graph shows the data for the entire manufacturing cycle, while the bottom graph magnifies the heat-up ramp.

Two significant laminate thickness changes took place. The first began once vacuum was drawn, and is referred to as the "initial compaction phase". The second occurred as the temperature began to increase, and is broadly denoted as the "flow phase". Both show the effects of out-time.

The initial laminate thickness prior to vacuum application increased with out-time, a trend attributed to the warpage and lack of tack observed in aged prepreg, which inhibited intimate ply contact before compaction. Then, during initial compaction and the vacuum hold, the laminate thickness remained higher for aged samples. The likely cause is the stiffer, less compliant consistency of the resin, which prevented adjacent layers from conforming to each others' morphology, or nesting.

These differences in ply-level interaction are significant because they may have impacted gas evacuation. Indeed, assuming incompressible individual fibres and resin, an increase in laminate thickness necessarily implies a larger pore volume between the plies. This pore volume may, in turn, increase the laminate permeability and thus favor gas evacuation. Such effects, which have previously been suggested [102], will be clarified through the cured laminate quality.

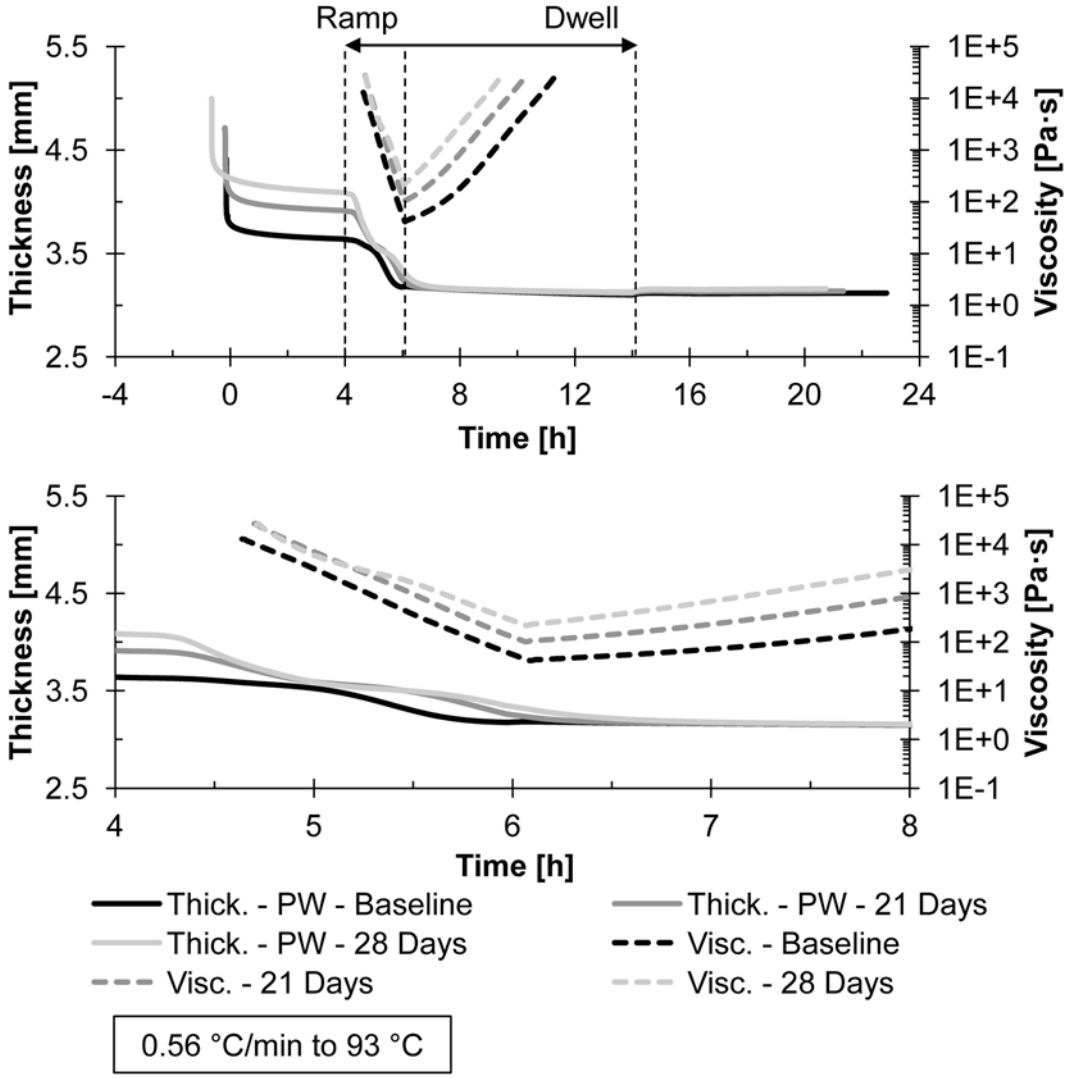

Figure 6–12: Graphs of measured laminate thickness and resin viscosity for the $0.56\,^{\circ}\mathrm{C\,min^{-1}}$ to $93\,^{\circ}\mathrm{C}$ manufacture of the 5320/PW laminates. The top graph shows the data curves for the entire cure cycle, while the bottom graph magnifies the period between hours four and eight.

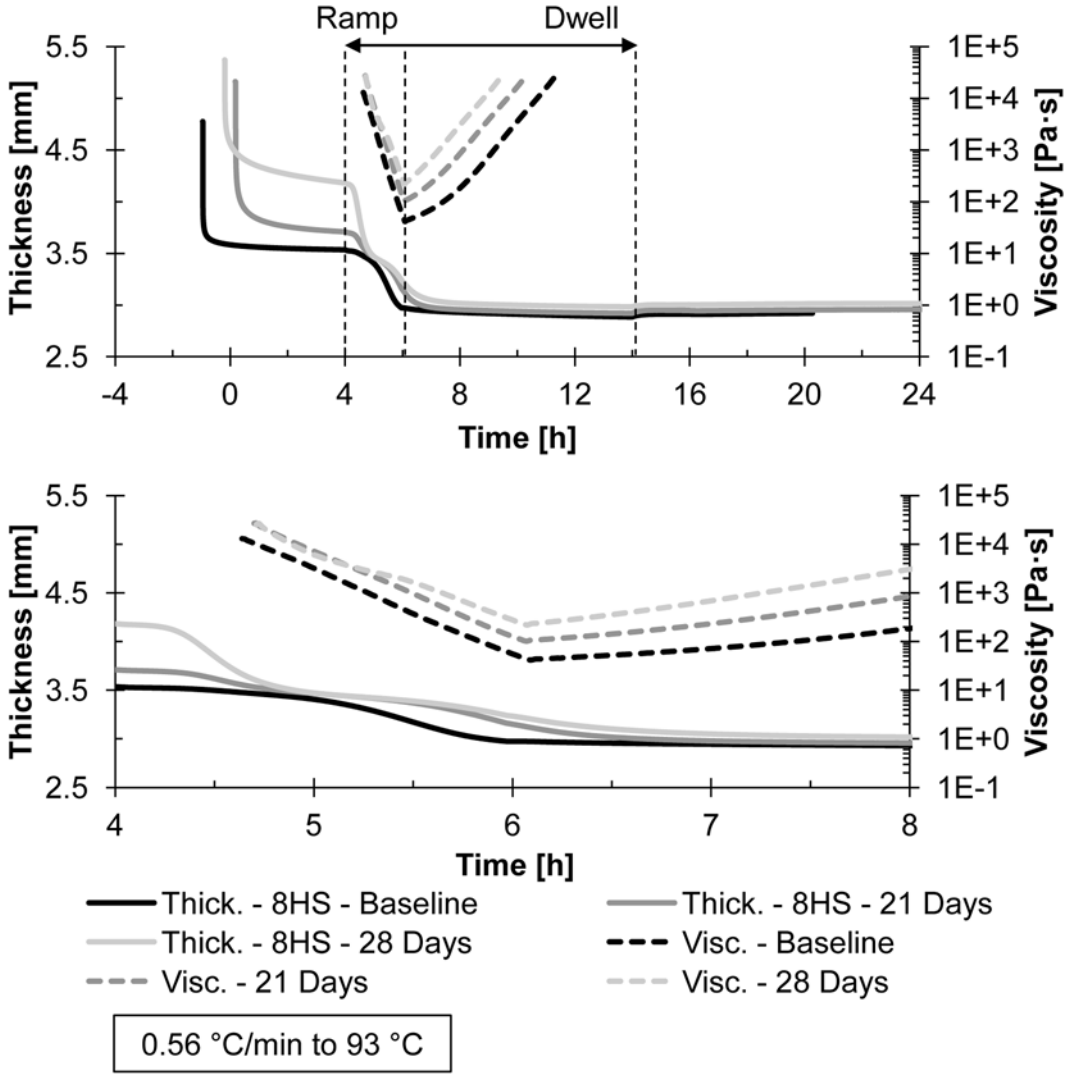

Figure 6–13: Graphs of measured laminate thickness and resin viscosity for the $0.56\,^{\circ}\mathrm{C\,min^{-1}}$ to $93\,^{\circ}\mathrm{C}$ manufacture of the 5320/8HS laminates. The top graph shows the data curves for the entire cure cycle, while the bottom graph magnifies the period between hours four and eight.

During the flow phase, a single decrease in laminate thickness was observed for the baseline laminates, beginning approximately 4.75 h into the cycle in Figures 6–12 and 6–13. In light of the results and conclusions of Chapters 4 and 5, it likely includes the reduction in pore space due to tow impregnation; however, it is important to note that other phenomena (such as fibre bed relaxation, ply interaction and cure shrinkage) may also be involved.

In contrast to the baseline, a two-step thickness change was observed in laminates exposed to higher levels of out-time. The first, comparatively rapid, occured approximately 4.25 h into the cycle in Figures 6–12 and 6–13 and brought the aged laminates to the level of the baselines. It was likely caused by additional ply nesting, brought on by decreasing resin viscosity and increasing ply compliance. The second took place at approximately 4.75 h, as with the baselines, and likely marked the onset of actual flow. With increasing out-time, this change occurred at a slower rate and over a longer period of time, and led to thicker laminates.

The results also highlight the effect of dwell temperature: laminates cured at 93 °C generally continued undergoing thickness changes during the dwell, well past the end of the heat-up ramp, while those cured at 121 °C generally consolidated faster, reaching their final thickness close to the minimum viscosity point. This difference is due to the significantly lower viscosity offered by the 121 °C dwell temperature, and the consequent increase in infiltration rate. Conversely, no clearly observable differences were noted between 0.56 °C min^{-1} and 2.77 °C min^{-1}.

For comparison purposes, a "flow time" may be defined as the period between the four hour mark and the moment the rate of thickness change

decreased below the nominal value of $-1 \times 10^{-5}\,\mathrm{mm\,s^{-1}}$. Flow times for all laminates are shown in Figure 6–14. These values are, naturally, influenced by the ramp rate and dwell temperature. However, the trends therein, and the general out-time-induced changes in consolidation behaviour (which may also be observed in the graphs of the remaining cure cycles in Appendix E) have significant potential implications.

The observed increases in flow time with out-time imply reduced rates of thickness change, and thus of resin flow. In extremis, such conditions may result in incomplete tow impregnation and pervasive flow-induced micro-porosity. However, the results also show that out-time induced changes in flow time are significantly smaller for the cycle with the highest ramp rate and dwell temperature, suggesting the same interplay between cure cycle and out-time that was previously predicted by the tow impregnation model.

Finally, the 5320/8HS flow times were longer than those of the 5320/PW for the same cure cycle and out-time conditions. Furthermore, slightly more significant differences were seen between 93 °C and 121 °C flow times for the 5320/8HS, suggesting that an increase in dwell temperature may be more influential for this prepreg.

6.5.4 Laminate Quality Analysis

6.5.4.1 Qualitative Inspection

An external inspection determined that the laminates featured excellent surface finish and no notable visible defects. A single difference was correlated to the processing conditions: the edge breathing dams used in the 121 °C cure cycles were more difficult to detach from the laminate edges than those used in

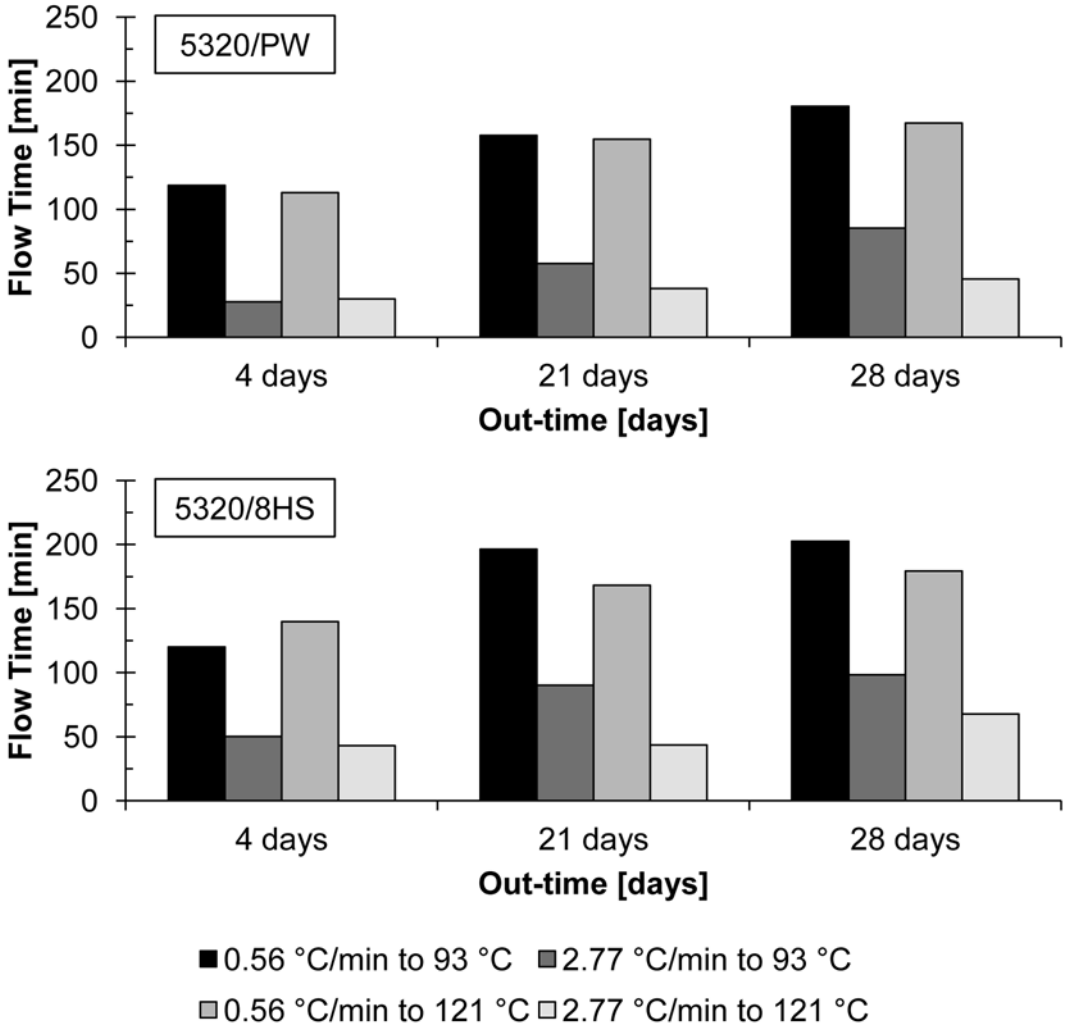

Figure 6–14: Charts of flow time versus out-time for the 5320/PW (top) and 5320/8HS (bottom) laminates.

the 93 °C cycles, suggesting that a larger (though still very limited) quantity of resin may have migrated from the laminate into the dry fibreglass.

6.5.4.2 Thickness

The laminate thickness results are presented in Figure 6–15. For all cases but one (2.77 °C min^{-1} to 121 °C), out-time led to increased thickness and, hence, decreased consolidation quality. This increase may be due to a combination of reduced ply nesting and higher porosity. For any given out-time, the effects of cure cycle are also visible, with faster ramps and higher dwells generally leading to thinner, better-consolidated laminates. Such changes are attributed to the increased capacity for resin flow and fibre bed mobility offered by lower resin viscosities; this hypothesis is also in agreement with the higher resin content observed in the edge breathing dams for the 121 °C dwell laminates. The relative importance of dwell temperature and ramp rate is difficult to discern. However, the effects of both were most pronounced and consistent at 28 days, suggesting that changes in process temperatures may most affect the final microstructure of aged (rather than "fresh") laminates. Overall, however, the changes in thickness are comparable to the standard deviation of the thickness measurements, and a more detailed microstructural analysis is desirable.

6.5.4.3 Tow Micro-Porosity

Figures 6–16 and 6–17 show representative examples of observed tow micro-porosity, while Figure 6–18 provides the average percent unsaturated tow areas. The micrographs confirm that micro-voids are generally found in the center of the tow, and maintain a shape similar to that of the tow. The unsaturated area size is also strongly associated with out-time, increasing

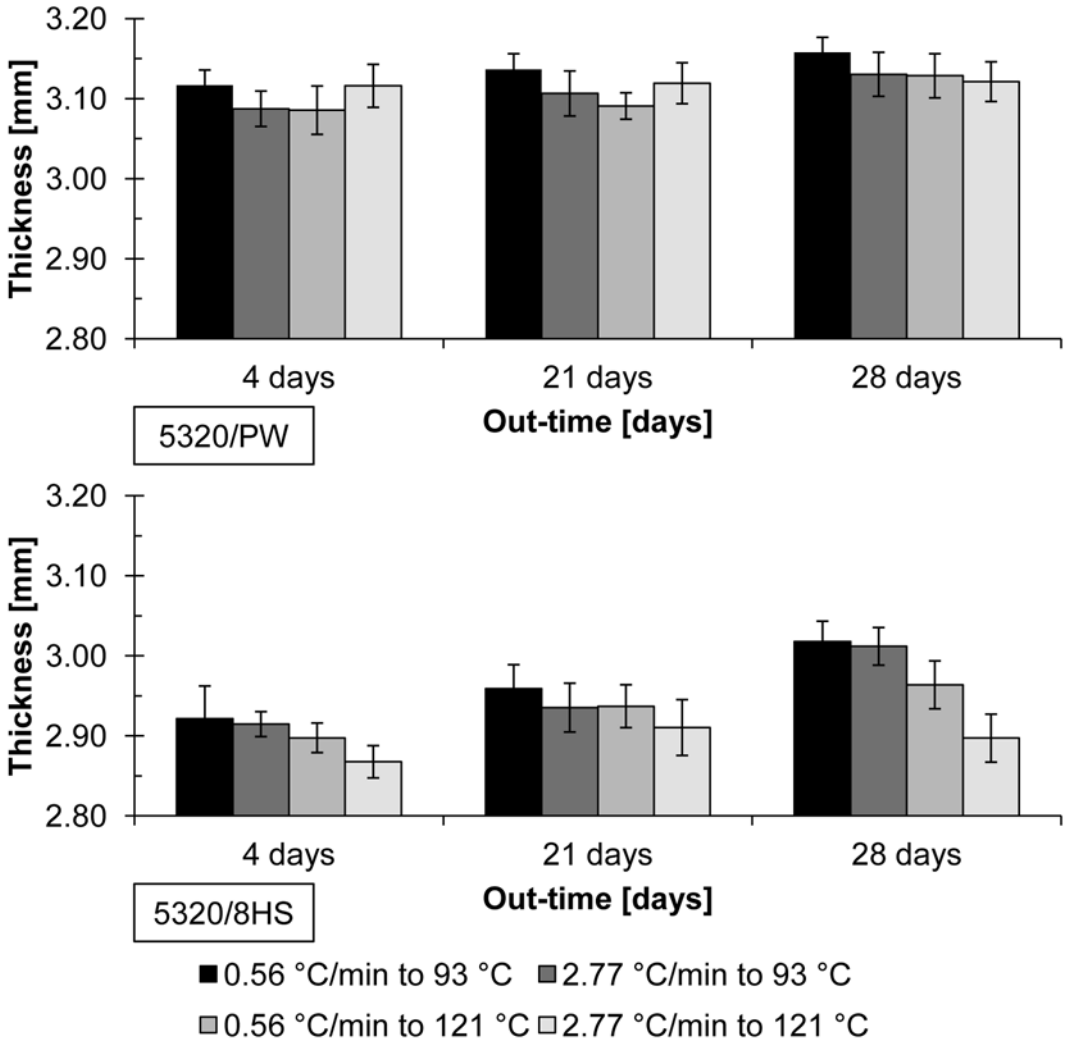

Figure 6–15: Charts of laminate thickness versus out-time and cure cycle for the 5320/PW laminates (top) and the 5320/8HS laminates (bottom). The error bars show one standard deviation in the six micrometer measurements.

Figure 6–16: Optical micrograph of representative tow micro-porosity observed in 5320/PW laminates at elevated out-times.

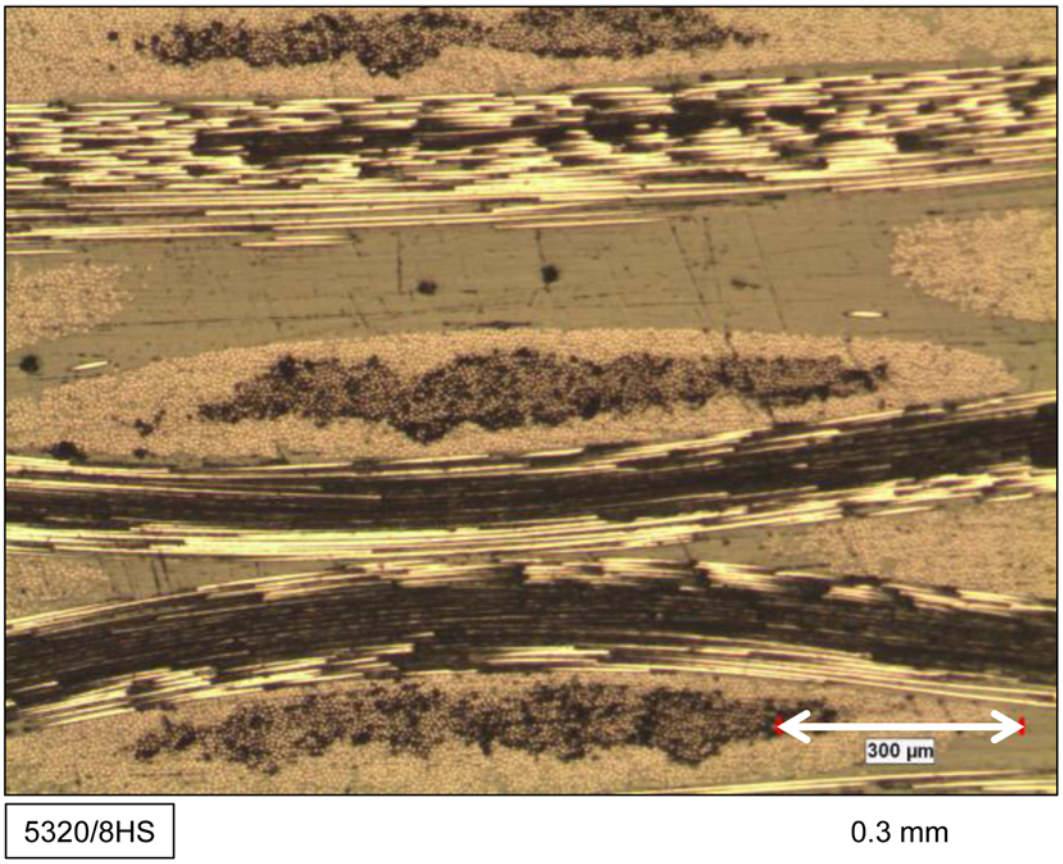

Figure 6–17: Optical micrograph of representative tow micro-porosity observed in 5320/8HS laminates at elevated out-times.

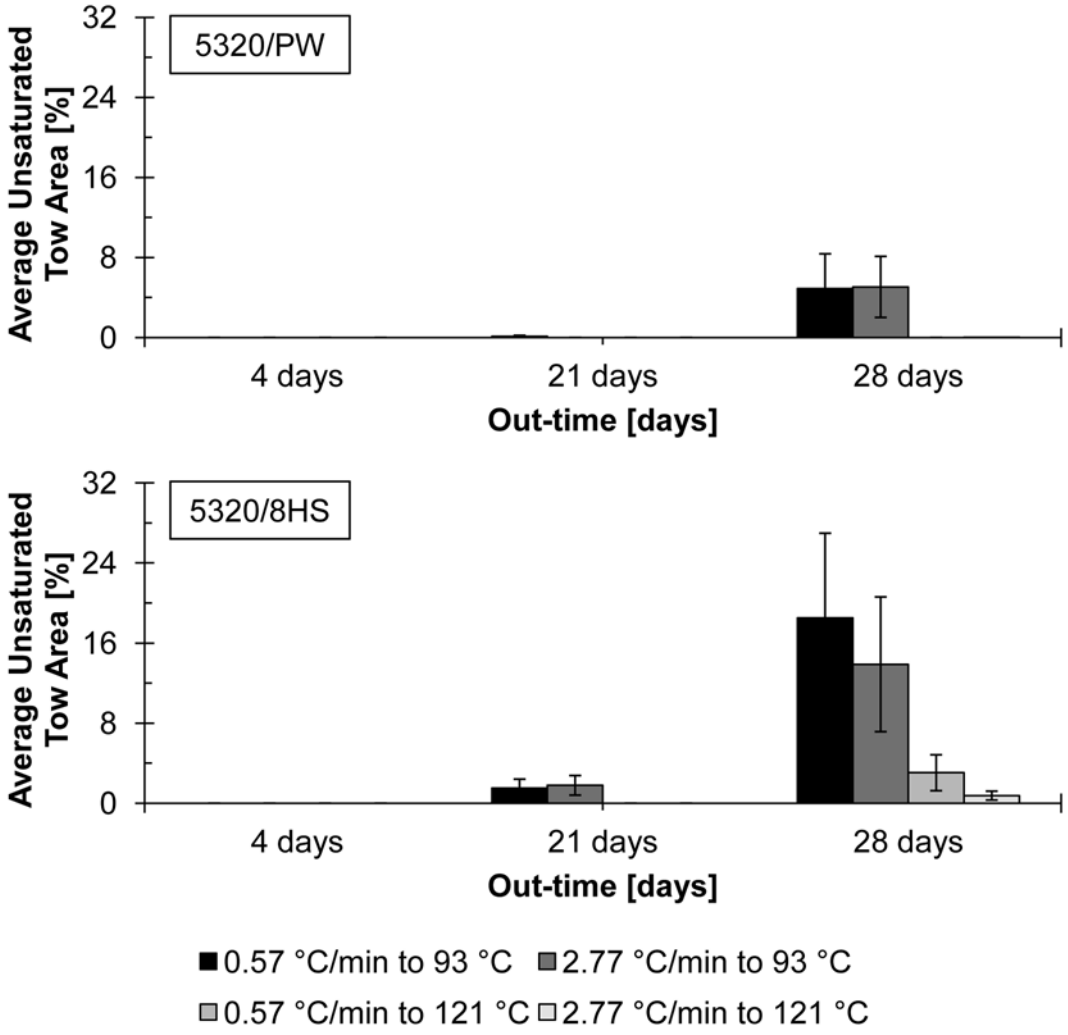

Figure 6–18: Charts of average percent unsaturated tow area versus out-time and cure cycle for the 5320/PW laminates (top) and the 5320/8HS laminates (bottom). The error bars show one standard deviation in the average values of the two samples.

from none at four days to close to 20 % (in some conditions) at 28 days. It is also predominantly associated with laminates cured at 93 °C; indeed, the 121 °C dwell was found to reduce or even eliminate porosity even for the 28 day out-time, which exceeds the material's specified out-life. The effect of ramp rate remained difficult to discern, with higher ramp rates benefitting the 28 day 5320/8HS laminates but not others. Finally, the influence of fabric architecture was found to be significant, with the 5320/8HS and its less-impregnated, thicker and fibre-denser tows being much more prone to micro-porosity than the comparatively thinner, more permeable and initially more impregnated 5320/PW.

Overall, these results show that the tows of partially impregnated OOA prepregs may not be completely impregnated in cases of high resin viscosity (or, in other words, low temperature and extended out-time) and present significant, pervasive micro-porosity. However, they also confirm that judicious cure cycle selection can effectively control these defects for some materials and process conditions.

6.5.4.4 Macro-Porosity

Finally, Figure 6–19 displays the percent macro-void contents of each manufactured laminate. These values, found to be consistently below 1 %, indicate excellent laminate quality (in terms of macro-voids) for all materials, out-times and cure cycles, and suggest that the four hour room temperature vacuum hold was sufficient for gas evacuation. However, some further distinctions may be made.

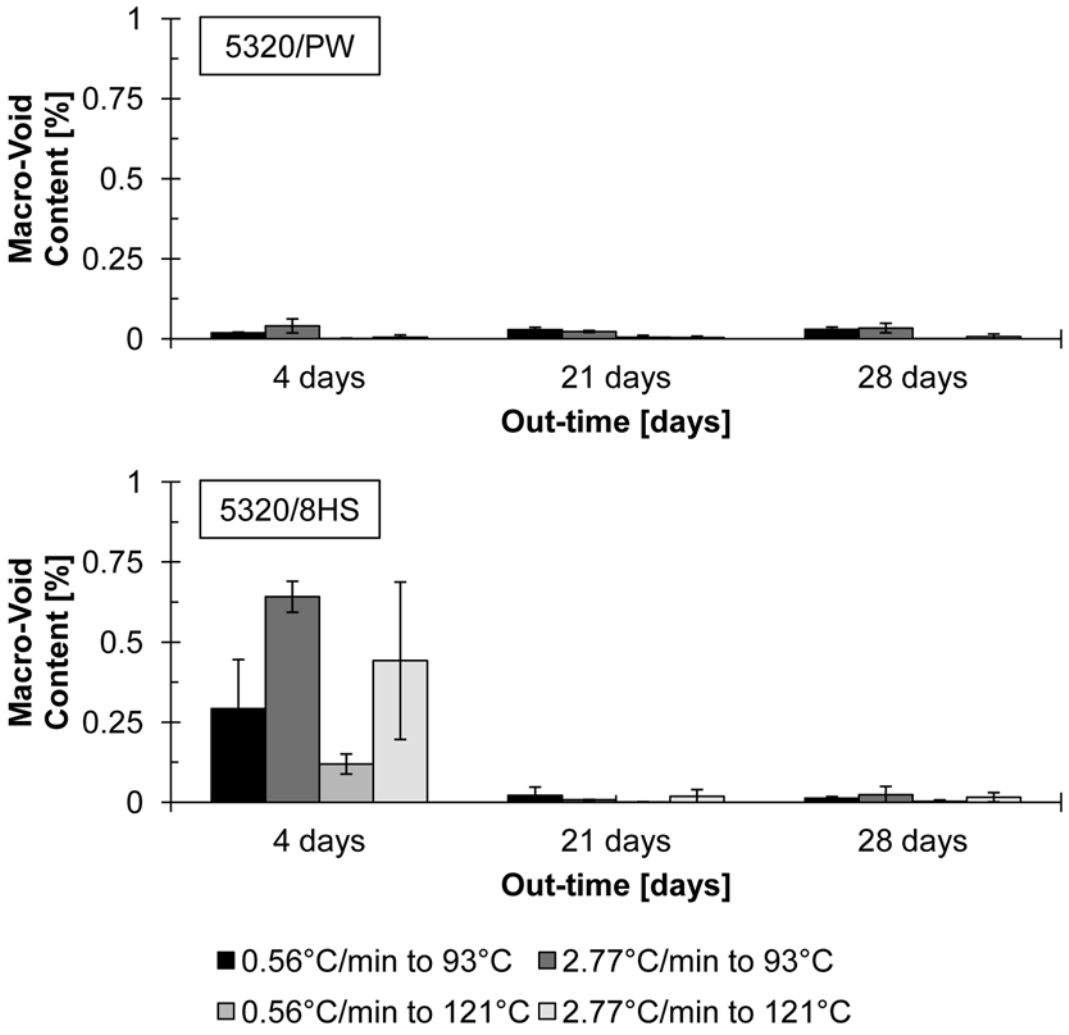

Figure 6–19: Charts of the average percent macro-void content versus out-time and cure cycle for the 5320/PW laminates (top) and 5320/8HS (bottom). The error bars show one standard deviation in the average values of the two samples.

The effect of prepreg age may be clearly observed for the 5320/8HS laminates: as out-time increases from four to 21 days, the macro-void content becomes negligible, and remains negligible for 28 days. This seemingly peculiar increase in quality with out-time may be explained by the reduced tack and increased thickness (under vacuum compaction) of high out-time laminates. As previously speculated, such changes likely led to higher in-plane permeability, increased gas evacuation and, overall, a lower potential for macro-void formation.

For the 5320/PW laminates, the macro-void content is initially negligible at four days, and the presence of this effect is thus not discernible. While the data is limited to four laminates, these results nevertheless suggest that the PW fabric is either less prone to entrapping air during layup or more capable of evacuating it in the early stages of processing; in light of the lower fabric areal weight and looser weave, the latter hypothesis is speculated to be more likely.

Overall, however, these results confirm that while cure cycle and out-time are dominant factors influencing resin flow and tow impregnation, they have at most a weak effect on macro-void formation or collapse provided proper air evacuation can be achieved.

6.5.5 Comparison with Model Estimates

As explained in Section 6.4.6, two methods were used to relate out-time to viscosity and simulate tow impregnation. The first used the measured viscosity data as a direct input in the tow impregnation model; the second related out-time to glass transition temperature and resin degree of cure, and

Table 6–4: Resin out-time, glass transition temperature and degree of cure.

Out-Time	Glass Transition Temp.	Degree of Cure
4 days	5.2 °C	0.089
21 days	17.43 °C	0.168
28 days	23.06 °C	0.202

then used the latter values as initial conditions for the 5320 resin cure kinetics and viscosity models.

Table 6–4 shows the corresponding resin out-times, glass transition temperatures and degree of cure obtained for the second approach. These values show that by the 28 day mark, significant room temperature cure has taken place: the glass transition temperature is in the vicinity of the ambient, and the degree of cure is nearly halfway to the degree of cure at gelation, $\alpha_{gel} = 0.48$ [36].

Figure 6–20 shows representative resin property and tow impregnation curves for a 0.57 °C min^{-1} to 93 °C cycle at 28 days of out-time. A discrepancy exists between the measured and predicted viscosities, with the values predicted by the α_0 method being higher than those measured using a rheometer. The difference was found to be minimal at low initial resin degrees of cure (as expected, since the model constants were determined based on these curves); however, it was found to grow with increasing initial degree of cure.

This discrepancy also translated to the flow dynamics. For the 0.57 °C min^{-1} to 93 °C, 28 day example shown in Figure 6–20, the simulations based on measured values predicted full impregnation (and thus no tow micro-porosity) for both materials; however, those based on the resin property models predicted incomplete impregnation and flow-induced micro-porosity for the 5320/8HS.

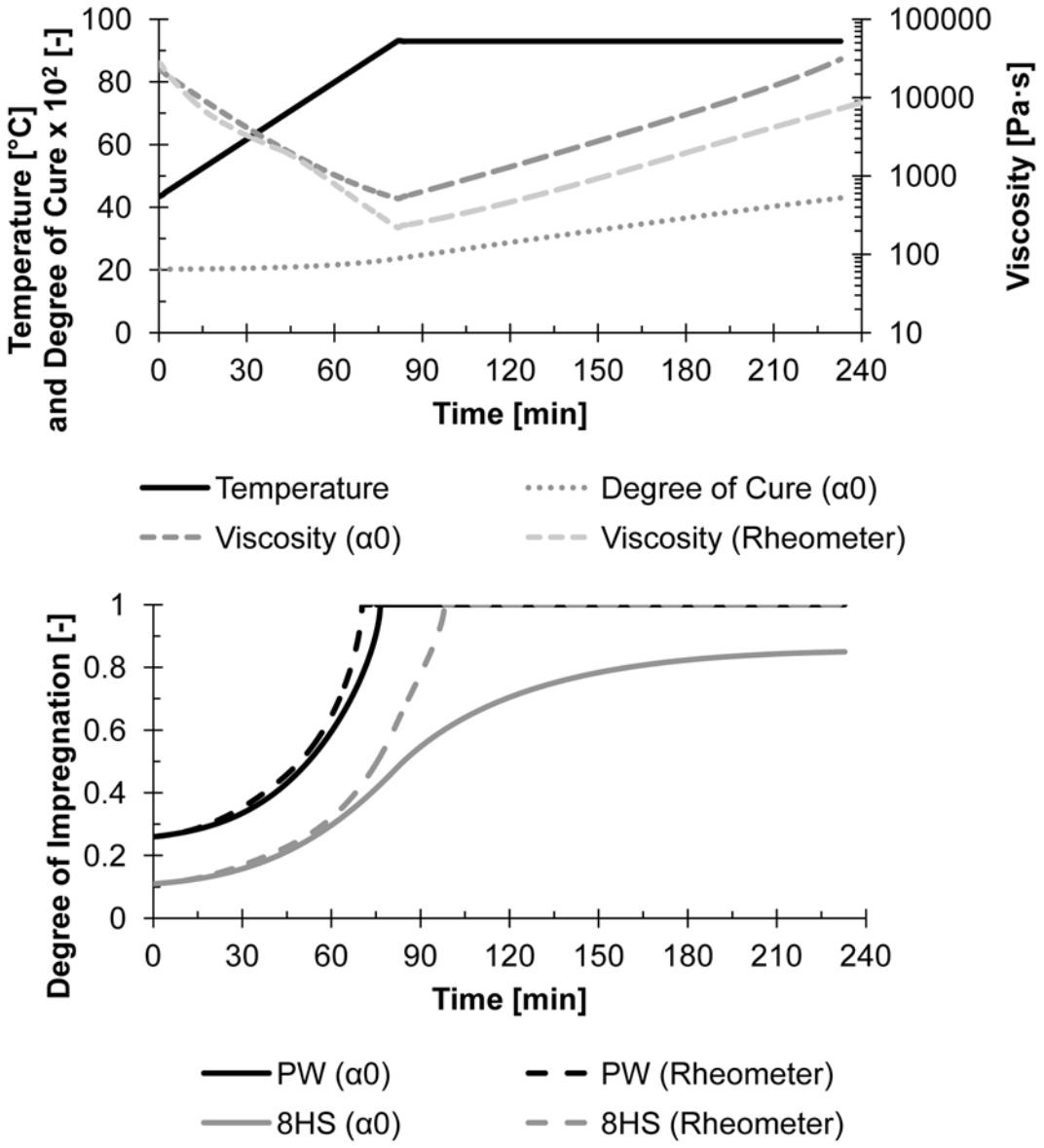

Figure 6–20: Graphs of temperature, predicted degree of cure, and viscosity (α_0- and rheometer-based) (top) and tow impregnation (bottom), shown for the example of a 0.57 °C min^{-1} to 93 °C cycle at 28 days of out-time.

The average percent unsaturated areas predicted by the model based on both rheometer and α_0-based viscosities are shown along with the measured (and previously presented) results in Figures 6–21 and 6–22.

The comparison shows that both modelling approaches correctly predict the general absence of micro-voids at 4 days and 21 days of out-time, and capture the trend that at 28 days, micro-porosity occurs predominantly in the 5320/8HS material and for low ramp rate, low dwell temperature cure cycles. However, both modelling approaches under-estimate the magnitude of micro-voids at 28 days. For the 5320/PW, no micro-voids were predicted for any cure cycle or out-time, whereas some were observed for the 93 °C dwell temperature at 28 days. For the 5320/8HS, micro-porosity was simulated to occur for the two 93 °C dwell temperature cycles and 28 days of out-time. Among these, a maximum of about 4 % was predicted for the $0.57\,^{\circ}\mathrm{C\,min^{-1}}$ ramp rate, whereas the measured average is close to 20 %. Surprisingly, the comparison also shows that the modelling approach based on obtaining predicted viscosity curves using the relation between out-time and glass transition temperature is more representative of the actual defect levels than the one based on the measured viscosity of aged resins.

These discrepancies may be partly attributed to out-time induced changes to the resin viscosity and flow behaviour. As mentioned in Chapter 5, the model assumes that the resin flows according to Darcy's Law until full impregnation or gelation occur. At low out-times, this assumption is valid, since flow takes place before significant polymerization. Conversely, aged resin has a high initial degree of polymerization at the beginning of processing; furthermore, this polymerization may differ from that which occurs during high

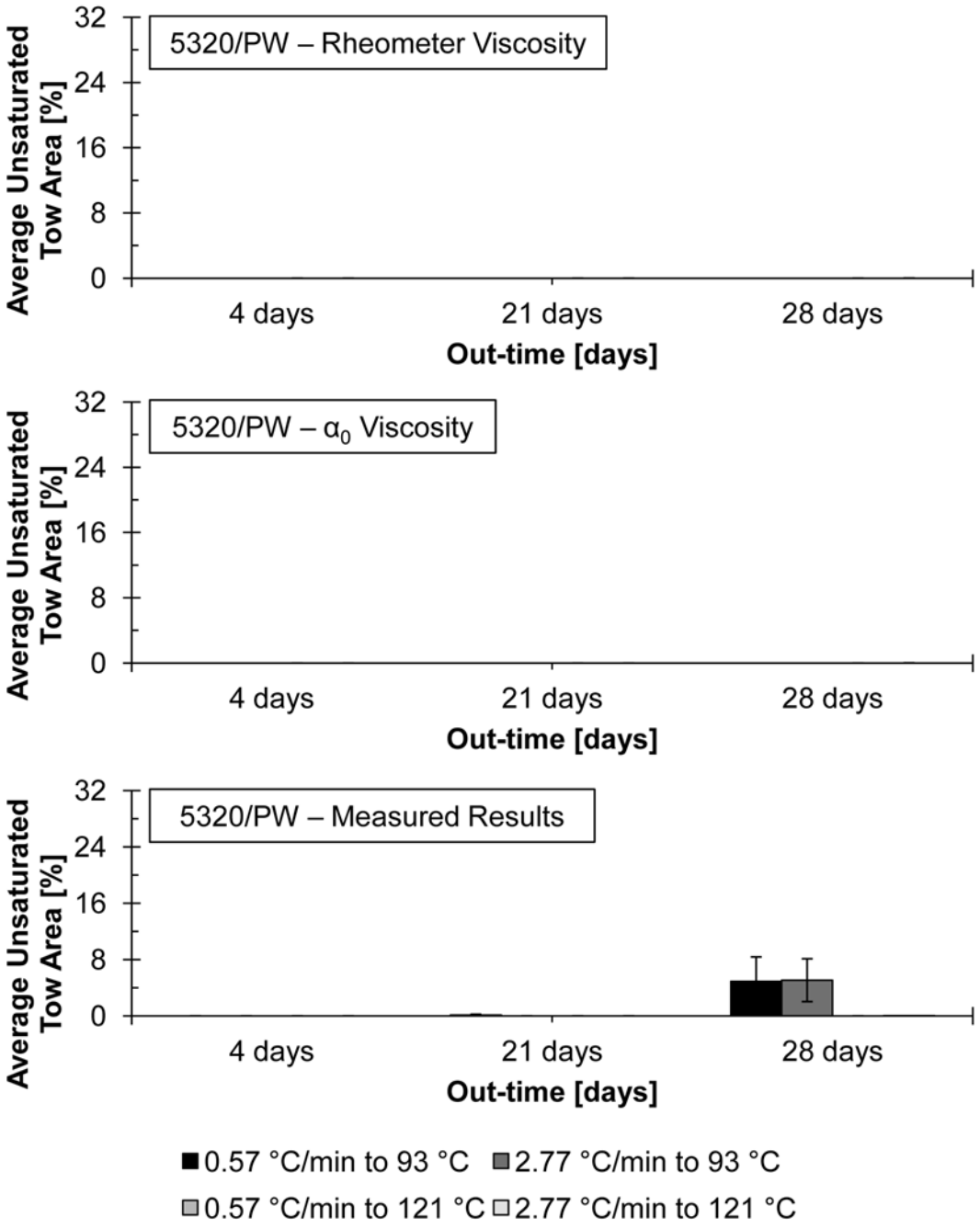

Figure 6–21: Charts of the average percent unsaturated tow area versus out-time and cure cycle for the 5320/PW prepreg based on model simulations using (top) rheometer viscosity and (middle) α_0-based viscosity; and (bottom) measured results.

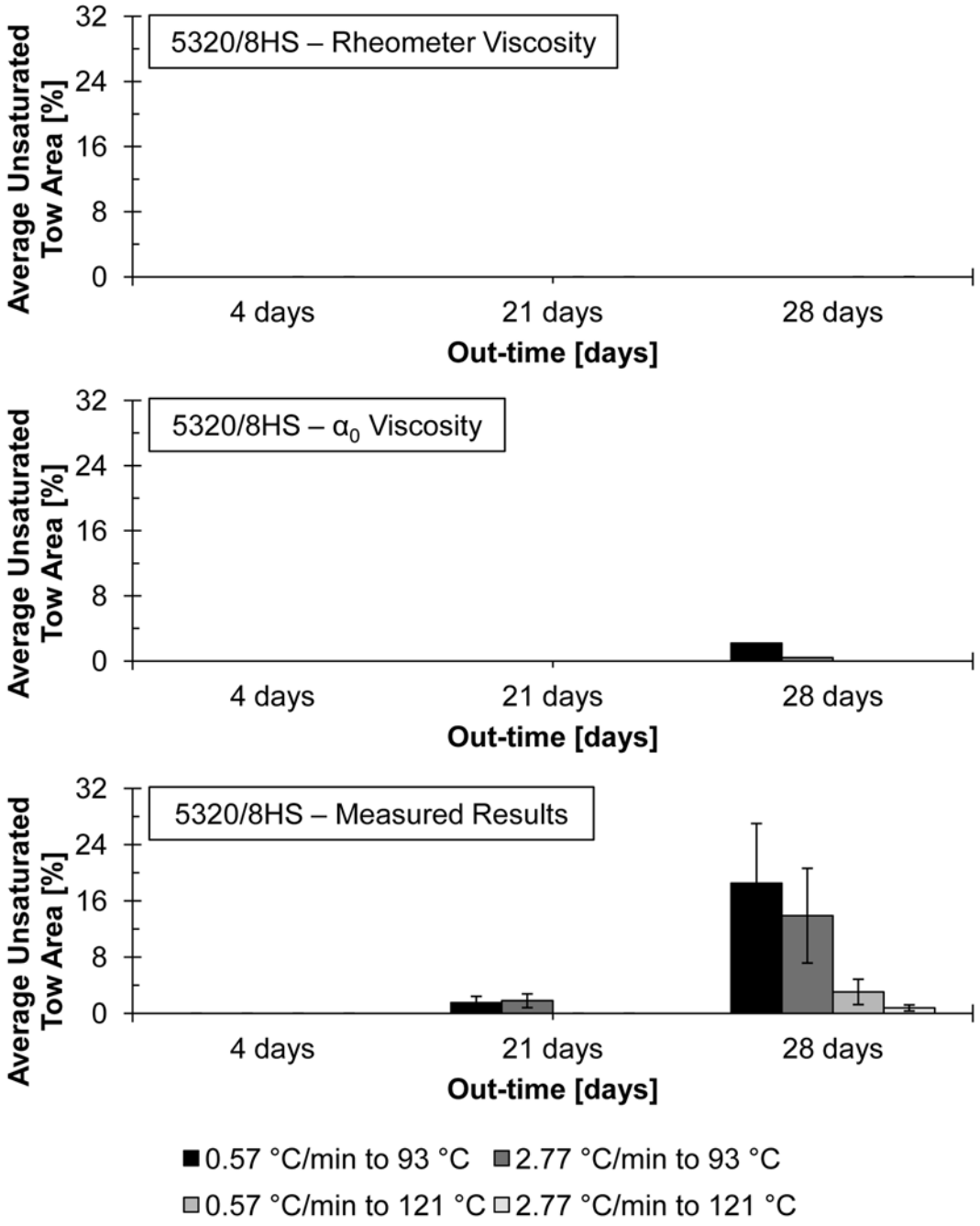

Figure 6–22: Charts of the average percent unsaturated tow area versus out-time and cure cycle for the 5320/8HS prepreg based on model simulations using (top) rheometer viscosity and (middle) α_0-based viscosity; and (bottom) measured results.

temperature processing. Thus, the resin may no longer strictly behave like a simple, Newtonian viscous fluid, and its capacity to flow may be lower than that predicted by Darcy's Law.

This hypothesis may also relate to the difference between the rheometer and α_0 approaches. During the rheometer tests, the viscosity was obtained by imposing an oscillatory shear displacement on the resin samples using parallel plates, measuring the resultant force response, and converting this data into viscosity values using a set of equations. These equations, however, are based on the assumption that the sample is a Newtonian fluid. Thus, while the measured aged resin viscosity data may be correct (in the sense that experimental errors are believed to have been minor), it may not be an accurate representation of the resin's capacity to flow. Conversely, the results in Figures 6–21 and 6–22 suggest that the higher viscosity values predicted using the cure kinetics and viscosity models based on measured glass transition temperature data may compensate for this change in behaviour and lead to a better approximation of the infiltration rate of the resin.

The under-predicted tow micro-porosity levels may also arise due to other model assumptions discussed in Chapter 5, including those of perfect vacuum within the bag, a constant resin pressure equal to 101 325 Pa, and the absence of any other environmental factors (such as moisture absorption by the resin).

6.6 Conclusions

The present chapter investigated the effects of out-time and cure cycle on OOA prepreg consolidation by examining changes in material properties, consolidation phenomena and final part quality. Two prepregs (5320/PW and 5320/8HS), three out-times (four, 21 and 28 days) and four cure cycles

(with ramp rates of $0.56\,^{\circ}\mathrm{C\,min^{-1}}$ and $2.77\,^{\circ}\mathrm{C\,min^{-1}}$, and dwells of 93 °C and 121 °C) were considered. Finally, tow impregnation model predictions were compared to measured micro-porosity values. The results lead to several significant insights into the importance of cure cycle and out-time factors in OOA prepreg processing.

1. **Out-time affects resin properties, prepreg properties, and all phases of processing.** Out-time increases the resin viscosity and decreases its gel time, reducing the window for full tow impregnation. Out-time also decreases prepreg tack and compliance, making ply collation difficult (if not impossible) for thick or complex-shaped parts and rendering laminate consolidation more difficult by inhibiting ply nesting. Both effects have consequences on defect formation phenomena: a significant reduction in tow impregnation rates can lead to pervasive micro-porosity, and incomplete ply nesting favors gas evacuation and reduces macro-porosity formation.
2. **Cure cycle changes may mitigate or even eliminate micro-porosity induced by out-time.** As suggested by the process maps generated in Chapter 5, an increase in viscosity brought on by room-temperature polymerization may be counteracted by resorting to fast ramp rates and high dwell temperatures, which favor low viscosity conditions in the early stages of processing. Indeed, as shown experimentally, judicious cure cycle selection may even allow some OOA prepregs (such as the 5320/PW) to exceed their manufacturer-specified out-life.
3. **OOA processing requires feasibility studies and judicious material and process parameter selection, particularly for large**

parts. Small parts generally consist of a single prepreg type, and can be laid up without significant out-time. Therefore, any combination of ramp rate and dwell temperature may be used to obtain a well-consolidated part, and cure cycle selection may be guided by other considerations, including oven capability, tooling geometry and material, and minimal process time. Conversely, the processing of the large, integrated parts for which OOA prepregs are ostensibly suited may involve weeks of ply collation, large and difficult-to-heat tools and multiple fibre bed architectures. Thus, in the potential presence of out-time and different impregnation dynamics, the cure cycle window is significantly narrower, with only fast ramp rates and high dwell temperatures leading to parts with acceptably low micro-porosity. Hence, as a final conclusion, the present study suggests that significant thought and detailed assessment are required to ensure that the process parameters required for successful tow impregnation and part consolidation are feasible.

CHAPTER 7
An Experimental Study of the Effect of Deficient Consolidation Pressure Conditions in Out-of-Autoclave Prepreg Processing

7.1 Introduction

OOA prepreg processing relies on the application of temperature and pressure to consolidate a stack of prepreg plies into a laminate and form a defect-free part. The importance of cure cycle has been highlighted in Chapters 5 and 6, which demonstrated, through modelling and experiments, that judicious selection of ramp rates and dwell temperature may lead to process optimization in terms of manufacturing time and final part quality. However, other than the inclusion of atmospheric pressure in Chapter 5's parametric study, the effect of consolidation pressure conditions on ply- and laminate-level phenomena and defect formation mechanisms has not been considered.

7.1.1 Background

Generally speaking, three gas pressures are of interest during OOA processing: the ambient pressure within the oven, the bag pressure (or vacuum), and the pressure of gases remaining within the laminate. Initially, all three are equal to the ambient. Then, once the bag pressure is reduced by means of a vacuum pump, gas evacuation occurs through the prepreg's dry tow network and edge breathing. Thus, the pressure of gases within the laminate decreases, and the differential thus generated contributes to local void collapse and laminate consolidation. In the ideal case, the ambient and bag

pressures are 101 325 Pa and 0 Pa, respectively, and the laminate gas pressure decreases until it is equal to the bag pressure.

7.1.2 Deficient Pressure Conditions

While such optimum process conditions may be approached in a tightly controlled laboratory setting, the manufacturing of large or complex composites in a production-oriented facility may bring about several deviations from the ideal case.

Thick or sharply contoured parts may require debulking, or the short-term application of vacuum between ply collation, to eliminate wrinkles and ply bridging. Unfortunately, debulking may also pre-consolidate an OOA prepreg, reducing the size and permeability of the dry tow cores and thus potentially impeding gas evacuation and increasing the likelihood of void formation.

The ambient pressure may be change from the standard atmosphere, mainly due to geographic location but also due to weather variations. A lower pressure may decrease the consolidation pressure, and thus reduce the laminate compaction, flow driving potential and void suppression capacity.

The vacuum quality may also be lower than assumed due to an inadequate vacuum system or leaks brought on by poor bagging. A higher bag pressure would also decrease the consolidation pressure; furthermore, it would also allow gases to remain within the bag and laminate.

Finally, in-plane gas extraction from the laminate may be restricted by improper edge breathing, insufficient vacuum hold times for a given prepreg

material and part geometry, or by other flow-impeding features (such as inserts). Thus, air present in the laminate during layup may become entrapped and generate voids.

The capacity of OOA prepreg processing to resist such deviations, or its robustness, is critical. Thus, a clear understanding of their effect on processing phenomena and an assessment of their impact on part quality are necessary.

7.2 Objectives and Structure

The following study investigated the link between deficient consolidation pressure conditions, physical phenomena occurring during consolidation and final part quality for two OOA prepregs with different fibre bed architectures. The four above-mentioned conditions were considered: debulking; reduced ambient pressure; reduced vacuum and restricted gas evacuation.

First, laminates were manufactured under traditional as well as deficient conditions in an instrumented fixture, and data measured in-situ was used to gain a better understanding of the physical phenomena involved. Then, the laminate quality was assessed. The desired outcomes are an increased understanding of the causes and magnitude of such deficiencies' effects for different prepregs and, overall, an evaluation of the robustness of OOA processing.

7.3 Materials

The properties of the two OOA prepregs chosen for this study are summarized in Table 7–1. They were manufactured by CYTEC Engineered Materials from CYCOM 5320 epoxy resin and two carbon fibre beds: an 8HS fabric and unidirectional tape (UD). The 5320/8HS, previously used, features

Table 7–1: Properties of the 5320/8HS and 5320/UD prepregs.

Parameters	5320/8HS	5320/UD
Resin	5320	5320
Resin content	36 %	33 %
Out-life	21 days	21 days
Fabric	T650-3K 8HS	T40/800B UD
Areal weight	$370\,\mathrm{g\,cm^{-3}}$	$145\,\mathrm{g\,cm^{-3}}$
Tow count	3k	6k

a relatively heavy fabric and a high bulk factor; the 5320/UD tape is comparatively thin and compact. The out-time of both materials prior to processing was estimated at four days.

The 5320/8HS prepreg was shown to be partially impregnated in previous chapters. The similar nature of the 5320/UD was confirmed using micro-CT, in the same manner as the scans described in Chapters 4, 5 and 6. A representative X-ray micrograph of a $[(0°/90°)_2]_s$ laminate is shown in Figure 7–1; it indicates that the microstructure is indeed partially impregnated but that, in contrast to fabric-based prepregs, it consists of planar, alternating dry and resin-rich regions.

7.4 Procedures

7.4.1 Laminate Manufacture

7.4.1.1 Cure Cycle, Dimensions and Layup

The cure cycle used for all tests consisted of a four hour room temperature vacuum hold; a ramp of approximately $1\,°\mathrm{C\,min^{-1}}$ to 93 °C and an eight hour hold at 93 °C. The room temperature hold allows appropriate air extraction; the heat-up rate is both within the manufacturer's recommendations

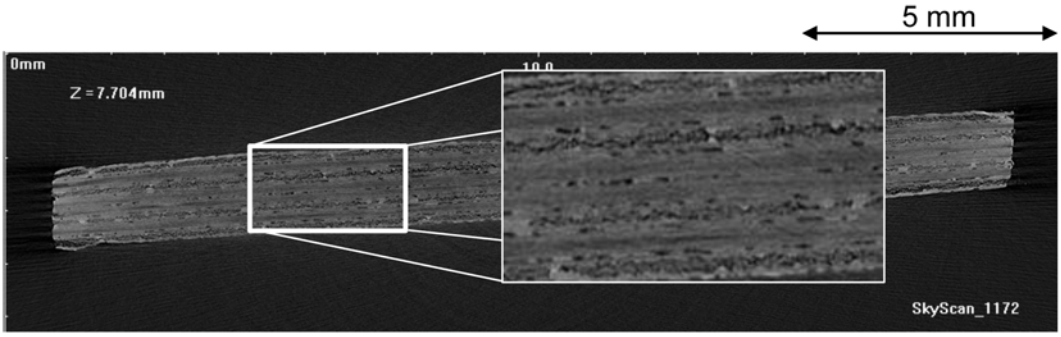

Figure 7–1: X-ray micrograph of a representative 5320/UD microstructure, showing alternating planar dry and resin-rich regions. The scale bar applies to the large image.

and achievable given the experimental set-up described below, and the dwell ensures the necessary laminate gelation and vitrification.

All manufactured laminates measured 101.6 mm by 152.4 mm ± 5 mm (or 4 in by 6 in ± 0.2 in). The layup of the 5320/8HS laminates was $[(0°/90°)_4]_s$, while that of the 5320/UD laminates was $[(0°)_{11}]_s$. The expected cured laminate thickness for both materials under normal processing conditions was approximately 3 mm.

The consumables consisted of layers of non-perforated release film below and above the laminate; edge breathing dams made of sealant tape wrapped in fiberglass cloth (unless otherwise specified); one layer of breather and the vacuum bag.

7.4.1.2 Consolidation Fixture

The instrumented consolidation fixture used to manufacture the laminates is shown schematically in Figure 7–2, and in photographs in Figure 7–3. As described in the previous chapter, it contains a tool plate and a sensor support; for this chapter, a sealed lid was also used.

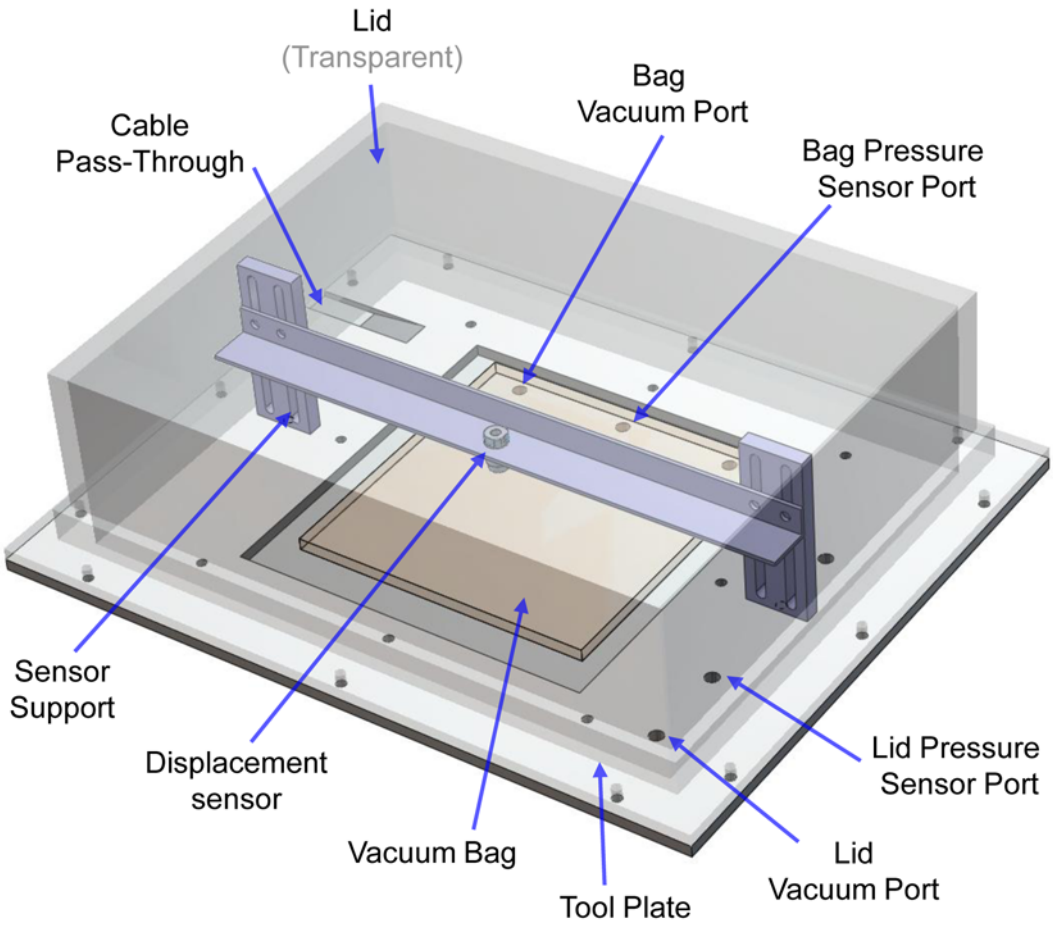

Figure 7–2: Schematic of the instrumented consolidation fixture, with the lid partially transparent for clarity.

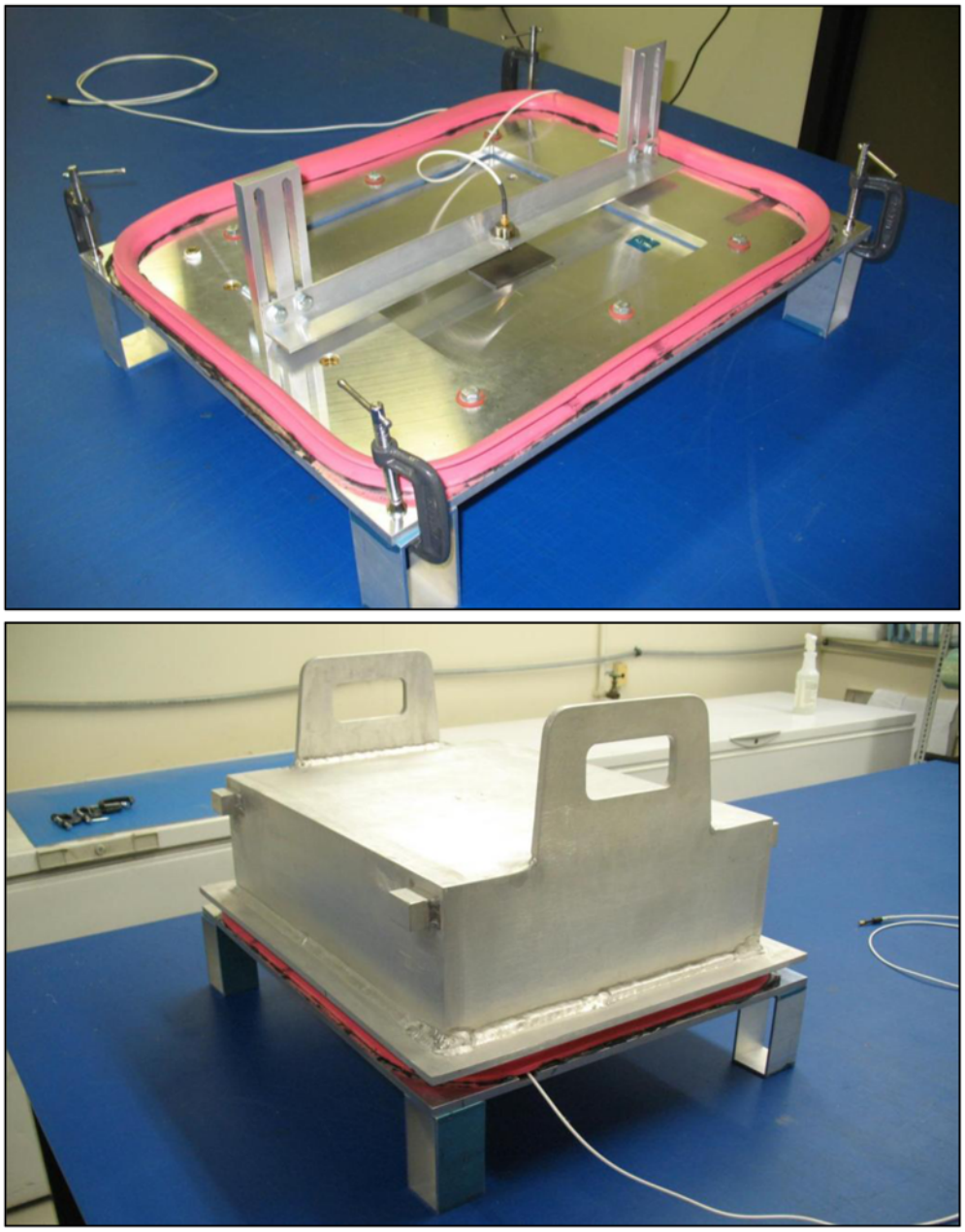

Figure 7–3: Photographs of the instrumented consolidation fixture without the lid (top) and with the lid (bottom).

The tool consists of flat aluminum surfaces with two sets of integrated vacuum ports. The vacuum bag assembly described above was placed in the center of the tool, over the first set of vacuum ports. One such port was connected to a regulated vacuum line used to control the bag pressure, while the other was connected to a WIKA A-10 pressure sensor with a 0 Pa to 202 650 Pa (absolute) range. Two OMEGA TT-K-30-SLE (ROHS) type-K thermocouples were used to measure the temperature at the tool-laminate and laminate-bag interfaces.

The sensor support held a Micro-Epsilon eddyNCDT 3010 / U6 non-contact eddy current sensor, which detected the displacement of a 75 mm by 75 mm by 2 mm steel target placed on the laminate, between the release film and the breather. The sensor has a range of 6 mm, a maximum resolution of 0.3 µm and a working temperature of up to 150 °C, which allowed it to measure laminate thickness changes at OOA processing conditions. These displacement readings were compensated for sensor temperature drift and support structure thermal expansion using a third thermocouple adjacent to the sensor, as explained in Appendix D.

The lid, also aluminum, was placed on top of the tool and sensor support, over silicone vacuum seals, above the other set of integrated vacuum ports. One such port was connected to a second regulated vacuum line and used to decrease the pressure within the lid (or, from the vacuum bag's perspective, the ambient pressure); the other was connected to a second vacuum pressure sensor.

Data from the thermocouples, pressure sensors and displacement sensor was recorded using a digital acquisition system (DAQ). During laminate

processing, the fixture was placed within a Thermal Product Solutions Blue M convection oven. A thermocouple was placed within the oven to measure the oven air temperature. Although not strictly required for every considered process condition, the fixture's lid was maintained on the tool during each laminate manufacture to ensure consistent heat transfer. Vacuum was drawn using either wall-mounted Busch vacuum pumps or a stand-alone Edwards xDS 5 vacuum pump, run continuously to ensure uniform and maximal vacuum quality.

A more detailed description of the consolidation fixture, along with the pressure and displacement sensor calibrations, is offered in Appendix D.

7.4.1.3 Processing Conditions

Two laminates were manufactured for each deficient pressure condition since, in some of these configurations, variability in the air behaviour may occur. The complete set of laminates manufactured for this study is summarized in Table 7–2.

The baseline laminates were manufactured using the traditional OOA method detailed in the above sections: the lid cavity pressure was maintained as atmospheric, and maximal vacuum was drawn under the bag.

The repeated debulk laminates differed from the baselines by being subjected, before the room temperature hold, to ten compression-relaxation cycles consisting of five minutes of bag vacuum and two minutes of venting.

The reduced ambient pressure conditions consisted of decreasing the lid cavity pressure to nominal target values of 77.5 % and 55 % of ambient (or approximately 78 527 Pa and 55 729 Pa). The 77.5 % condition is, broadly, the lowest that may be reasonably expected for an actual OOA cure; the

Table 7–2: Laminates manufactured to investigate the effect of deficient consolidation pressure conditions. Bag and lid pressures are nominal targets, and expressed in percent of atmospheric.

#	Material	Bag Pressure	Lid Pressure	Other
1	5320/8HS	0 %	100 %	
2	5320/8HS	0 %	100 %	
3	5320/8HS	0 %	100 %	Ten debulk steps
4	5320/8HS	0 %	100 %	Ten debulk steps
5	5320/8HS	0 %	77.5 %	
6	5320/8HS	0 %	77.5 %	
7	5320/8HS	0 %	55 %	
8	5320/8HS	0 %	55 %	
9	5320/8HS	22.5 %	100 %	
10	5320/8HS	22.5 %	100 %	
11	5320/8HS	45 %	100 %	
12	5320/8HS	45 %	100 %	
13	5320/8HS	0 %	100 %	Sealed edges
14	5320/8HS	0 %	100 %	Sealed edges
15	5320/UD	0 %	100 %	
16	5320/UD	0 %	100 %	
17	5320/UD	0 %	100 %	Ten debulk steps
18	5320/UD	0 %	100 %	Ten debulk steps
19	5320/UD	0 %	77.5 %	
20	5320/UD	0 %	77.5 %	
21	5320/UD	0 %	55 %	
22	5320/UD	0 %	55 %	
23	5320/UD	22.5 %	100 %	
24	5320/UD	22.5 %	100 %	
25	5320/UD	45 %	100 %	
26	5320/UD	45 %	100 %	
27	5320/UD	0 %	100 %	Sealed edges
28	5320/UD	0 %	100 %	Sealed edges

55 % case is an extreme condition intended to emphasize any effects. In each case, following laminate layup and bagging, the pressure in the bag was first reduced to the target ambient pressure. Then, the lid pressure was regulated to the same level, and the bag pressure was finally lowered to full vacuum. The above procedure ensured that the laminate was never consolidated by more than the target reduced ambient pressure. At this point, it may be noted that a case of increased ambient pressure, while not deficient, would have been of interest, and would have complemented the parametric study in Chapter 5. However, in its current state, the experimental set-up did not allow above-ambient conditions.

The reduced vacuum laminates saw, following layup and bagging, the bag pressure regulated to nominal target values of 22.5 % and 45 % of atmospheric pressure (or approximately 22 798 Pa and 45 596 Pa) while the lid pressure was maintained ambient. These bag pressure values reflect the above cases of reduced ambient pressure, since they generate the same consolidation pressures (77.5 % and 55 % of atmospheric pressure, respectively); however, in the case of reduced vacuum, air remained present in the bag.

The final deficient condition, restricted air evacuation, was imposed by replacing the traditional edge breathing dams made of sealant tape wrapped in dry fibreglass boat cloth with dams consisting solely from sealant tape, which overlapped and thus sealed the laminate edges.

7.4.2 Laminate Quality Analysis

As in the previous chapter, laminate quality was assessed by external visual inspection and microstructural analysis. For external observation, the laminate surfaces, edges and adjacent consumables were visually inspected for

any unusual features, and laminate thickness measurements were performed in six locations using a Mitutoyo 0 - 25.4 mm micrometer (model 293-765-30).

Microstructural analysis consisted of sample preparation, optical microscopy and image analysis. For each laminate, samples were prepared by sectioning two pieces (approximately 50 mm long and 25.4 mm wide) from the area under the displacement sensor's steel target, mounting them on honeycomb core using two-part epoxy for easy manipulation and wet-polishing one of their edges with up to 1200 grit sandpaper using a Buehler MetaServ2000 grinder/polisher. Optical micrographs were acquired using a Nikon Eclipse L150 optical microscope with attached Clemex Captiva digital camera. Image analysis was performed using the ImageJ software to determine two quality metrics: the average micro-void and macro-void contents of the sample. The macro-void content relates to porosity found in the resin regions around tows and between plies; the micro-void content relates to porosity found within the tows. Both were obtained by measuring the respective total micro- or macro-void areas and dividing them by the total cross-sectional area of the sample. For this study, the total micro-void content metric was chosen over the average percent unsaturated area because the latter is difficult to define for the 5320/UD prepreg, whose layers doe not contain clearly defined tows.

7.5 Results and Discussion

7.5.1 General

The laminate thickness just after layup was measured using a micrometer for every laminate. Averages of 4.75 mm $\pm$ 0.15 mm for the 5320/8HS and 3.70 mm $\pm$ 0.15 mm for the 5320/UD were obtained. Thus, for comparable final part dimensions, the 5320/8HS laminates had a higher bulk factor

Table 7–3: Average consolidation pressures for laminates manufactured to investigate consolidation pressure deficiencies, expressed in percent of atmospheric.

	Consolidation Pressure			
	5320/8HS		**5320/UD**	
	Repeat I	**Repeat II**	**Repeat I**	**Repeat II**
Baseline	99.1 %	97.1 %	97.8 %	97.5 %
Repeated Debulks	97.9 %	95.4 %	98.7 %	97.1 %
Reduced Amb. (77.5 %)	73.7 %	74.2 %	74.5 %	75.1 %
Reduced Amb. (55 %)	55.1 %	53.4 %	54.8 %	52.0 %
Reduced Vac. (22.5 %)	78.6 %	78.2 %	78.4 %	78.4 %
Reduced Vac. (45 %)	53.1 %	52.8 %	53.3 %	53.3 %
Restricted Air Evac.	98.6 %	97.0 %	99.0 %	97.9 %

than the 5320/UD, and therefore contained significantly more air-filled pore volume prior to processing. This difference may be explained by the fabric morphology. Tape plies, composed of straight, aligned tows, are likely to nest tightly in a unidirectional layup, leaving few macro-spaces between them. In contrast, fabric plies feature bi-directional, crimped, overlapping fibres. Tight nesting is less likely to occur, and isolated macro-spaces may exist around tows and between plies.

7.5.2 Laminate Manufacture

The data collected in-situ during processing offers several insights into the consolidation phenomena. The average consolidation pressure between bag and ambient is given in Table 7–3, while representative temperature and displacement sensor readings are provided in Figure 7–4.

Table 7–3 shows that the actual consolidation pressures were generally close to the nominal targets, with the largest measured deviation being 4.6 percentage points. Generally, the consolidation pressure targets for reduced

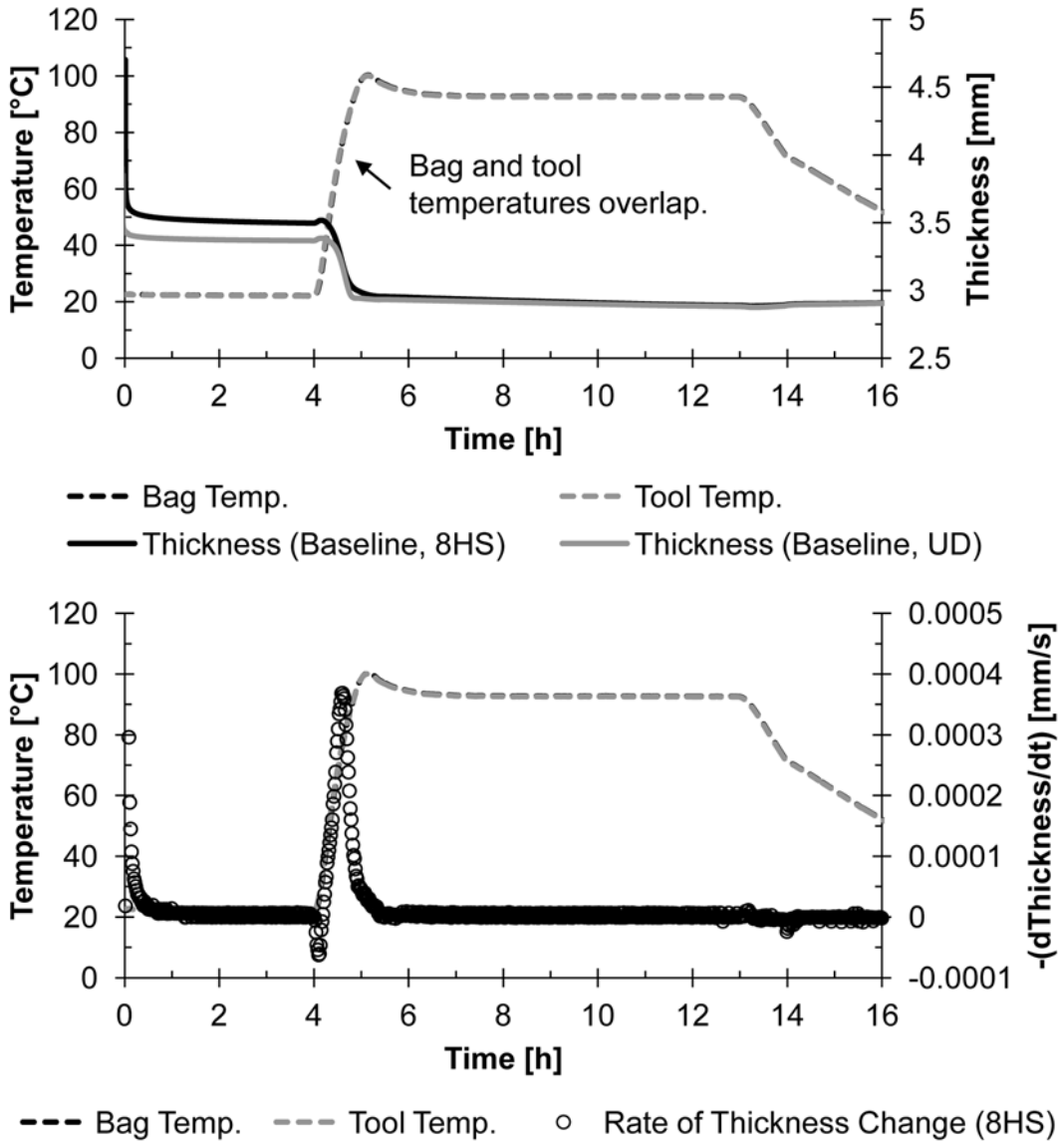

Figure 7–4: Graphs of bag and tool temperature along with laminate thickness for 5320/8HS and 5320/UD baselines cures (top), or along with the rate of change of the thickness for the 5320/8HS laminate (bottom). The bag and tool temperature curves overlap.

ambient pressure cases were most challenging to achieve, due to the difficulty of predicting the exact bag pressure; in the other cases, variations in atmospheric pressure also contributed to the slight discrepancies.

The bag and tool temperatures and the laminate thicknesses correspond to baseline cycles for the 5320/8HS and 5320/UD, but are common to all manufactured parts. Their maximum difference was only 2.15 °C, confirming that cure occured without significant through-thickness thermal gradients. According to the 5320 resin property models, the minimum resin viscosity attained was 28 Pa s and gelation occurred 7 h into the heated portion of the cycle.

The thickness curves in the top graph of Figure 7–4 were obtained by combining the displacement sensor data (corrected for thermal drift and support thermal expansion, as per Appendix D) with the measured final thickness of the laminate. As in Chapter 6, both initial compaction and flow phases were observed. First, once vacuum was drawn, the laminates quickly compressed due to fibre bed compaction and ply nesting. Then, during heating, resin flowed into unsaturated areas, further reducing the laminate volume.

The heated portion of manufacturing is likely to encompass defect formation phenomena, and to therefore be the more influential for part quality. Thus, the following sections will focus on the effect of deficient consolidation conditions on the thickness change during the flow period. However, these effects were most clearly observed by plotting the rate of change of thickness with time (averaged over 60 s intervals) rather than the thickness or flow time, as in the previous chapter. A representative example of a rate of change plot is shown in the bottom graph of Figure 7–4 for the 5320/8HS.

7.5.2.1 Baseline

Figure 7–5 shows the rate of change of thickness during the flow period for the two 5320/8HS baseline laminates (top) and the two 5320/UD baseline laminates (bottom), along with the temperature profile. Both sets of curves have the same general shape: an increase in the rate of change of thickness during the first half of the ramp; a maximum rate attained after approximately 35 minutes and a subsequent decrease. The increase begins as the resin viscosity decreases with temperature, but peaks before the minimum viscosity point is reached at the end of the ramp; all phenomena occur several hours before resin gelation. Good agreement may be seen between the two repeats for both materials.

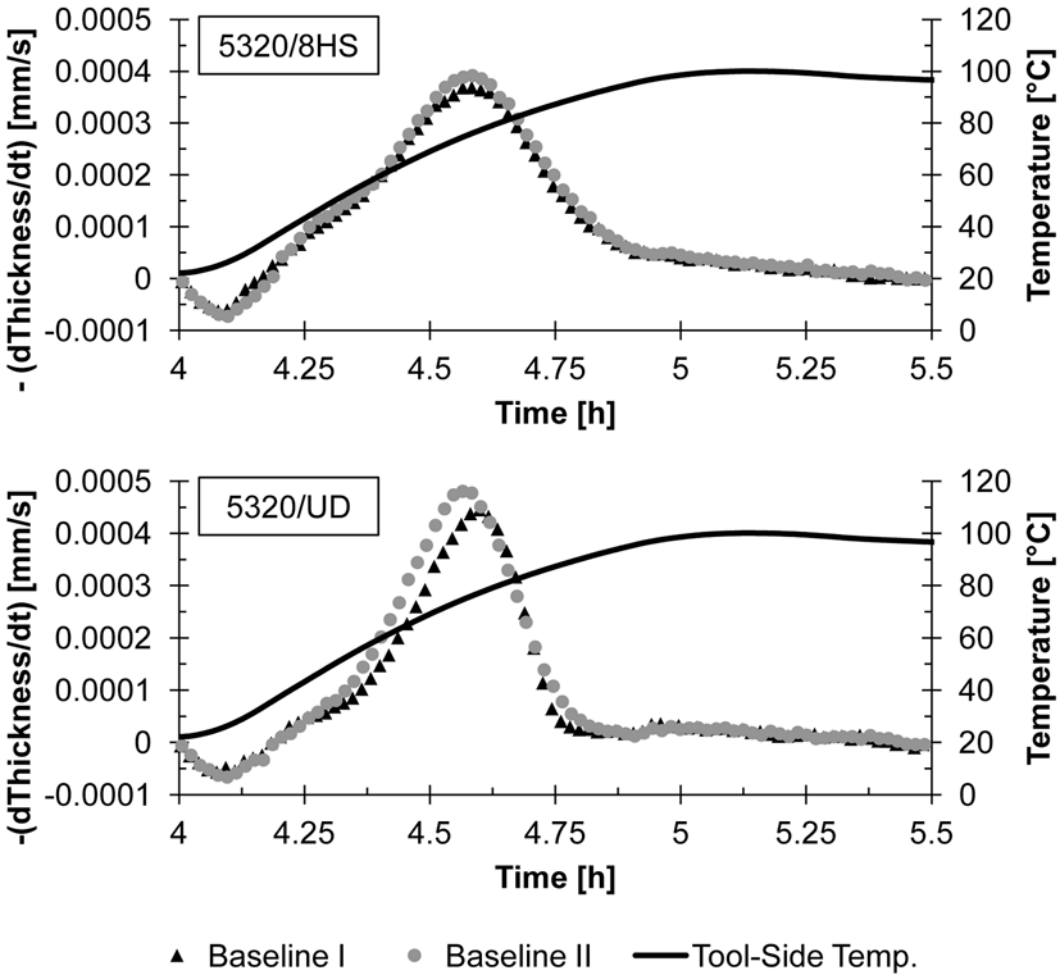

Figure 7–5: Graphs of the rate of change of thickness and cure cycle temperature for the baseline 5320/8HS (top) and 5320/UD (bottom) laminates.

7.5.2.2 Repeated Debulks

Figure 7–6 shows the consolidation curves during the flow period for the 5320/8HS and 5320/UD laminates manufactured with repeated debulks as well as the baselines, for reference. For the 5320/8HS, the repeated debulk curves overlap the baselines almost perfectly. For the 5320/UD, laminate I shows a slight delay (rightward shift) in the onset of consolidation and a slightly lower rate of consolidation, while laminate II closely conformed to the baseline. The changes for laminate I may be due to the increased compaction (and consequently, decreased permeability) of the fibre bed after repeated debulking. However, in both cases, the bell shape of the curve remains the same, suggesting that repeated debulks did not fundamentally change the physical phenomena taking place during processing.

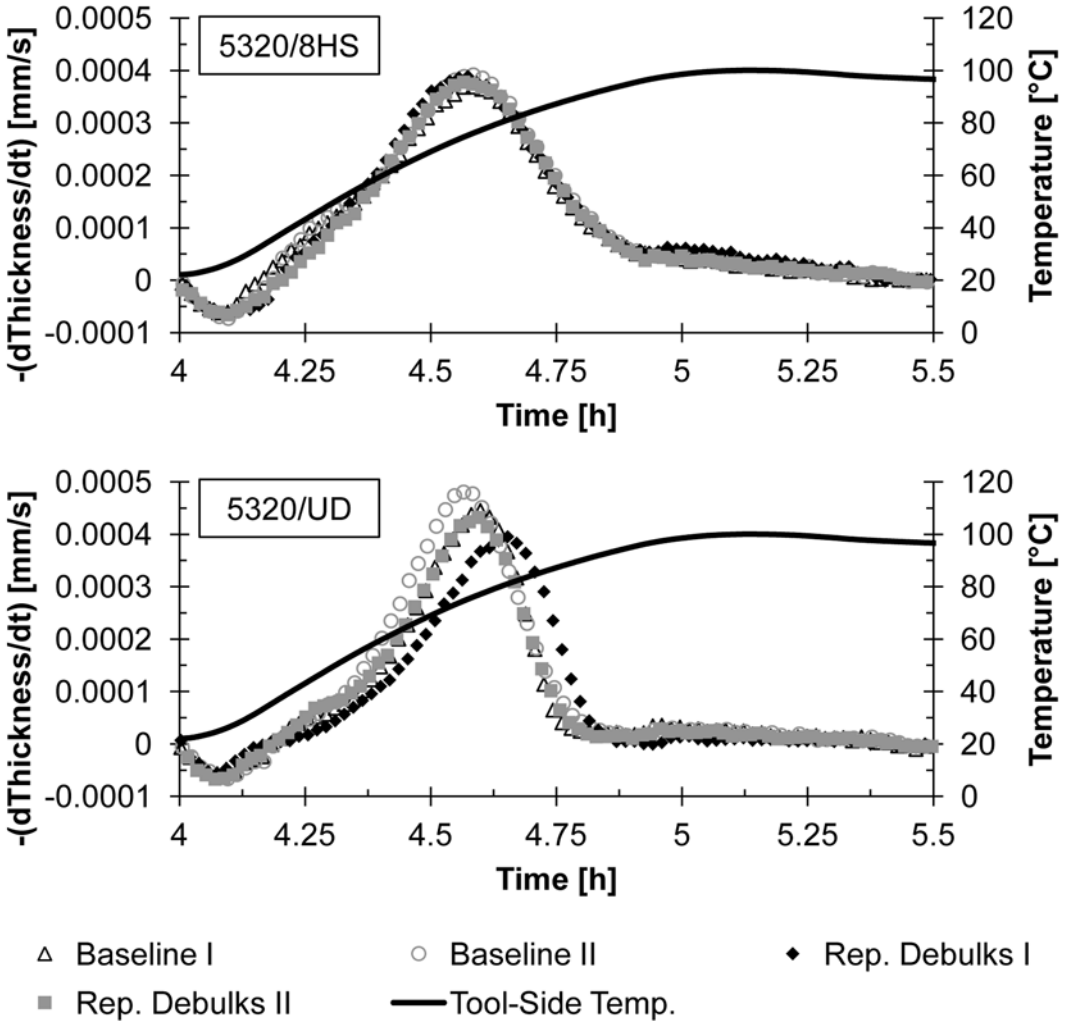

Figure 7–6: Graphs of the rate of change of thickness and cure cycle temperature for the repeated debulk 5320/8HS (top) and 5320/UD (bottom) laminates.

7.5.2.3 Reduced Ambient Pressure

Figures 7–8 and 7–7 show the rate of change of thickness during the flow period for laminates manufactured under reduced ambient pressure.

For the 5320/8HS, several differences with the baseline are noticeable at 55 % of ambient pressure. During the early portions of the ramp, the rate of change of thickness was higher and increased faster, possibly due to the reduced compaction and increased permeability of the fibre bed. Then, between 55 °C and 65 °C, a significant deviation from the bell shape occurred in the form of a sharp drop in consolidation rate. This event may relate to a suggestion by Ridgard [5] that the pressure of air within OOA prepregs during cure corresponds to a water boiling point of approximately 70 °C. In this light, the measurements imply that once the moisture present in entrapped air began to vaporize, the void pressure rose relative to the resin pressure (in this case, reduced to a maximum of 55 % of ambient) and slowed down consolidation. A similar but much less pronounced deviation from the baseline may be observed for the case of 77.5 % of ambient pressure.

For the UD, the curves also show an increased consolidation rate, again attributed to reduced fibre volume fraction and increased permeability. However, no significant dip is visible, suggesting that overall, any gas present within the unidirectional laminate did not significantly impede consolidation.

Finally, it is worth noting that reducing the ambient pressure did not result in a significantly longer flow period, suggesting that the reduction in driving pressure differential is counteracted by an increase in permeability, and supporting the results of the model parametric study (presented in Chapter 5).

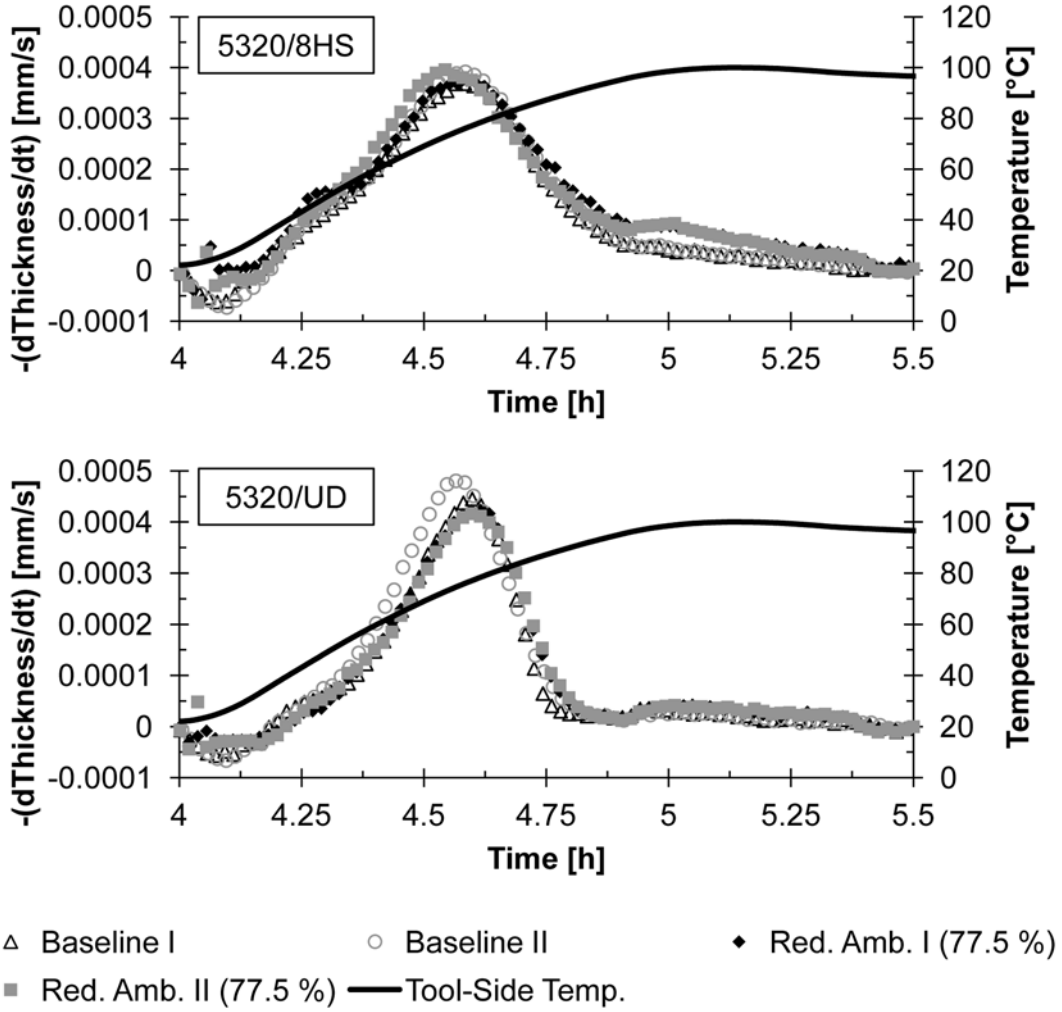

Figure 7–7: Graphs of the rate of change of thickness and cure cycle temperature for the reduced ambient pressure (77.5 % of atmospheric) 5320/8HS (top) and 5320/UD (bottom) laminates.

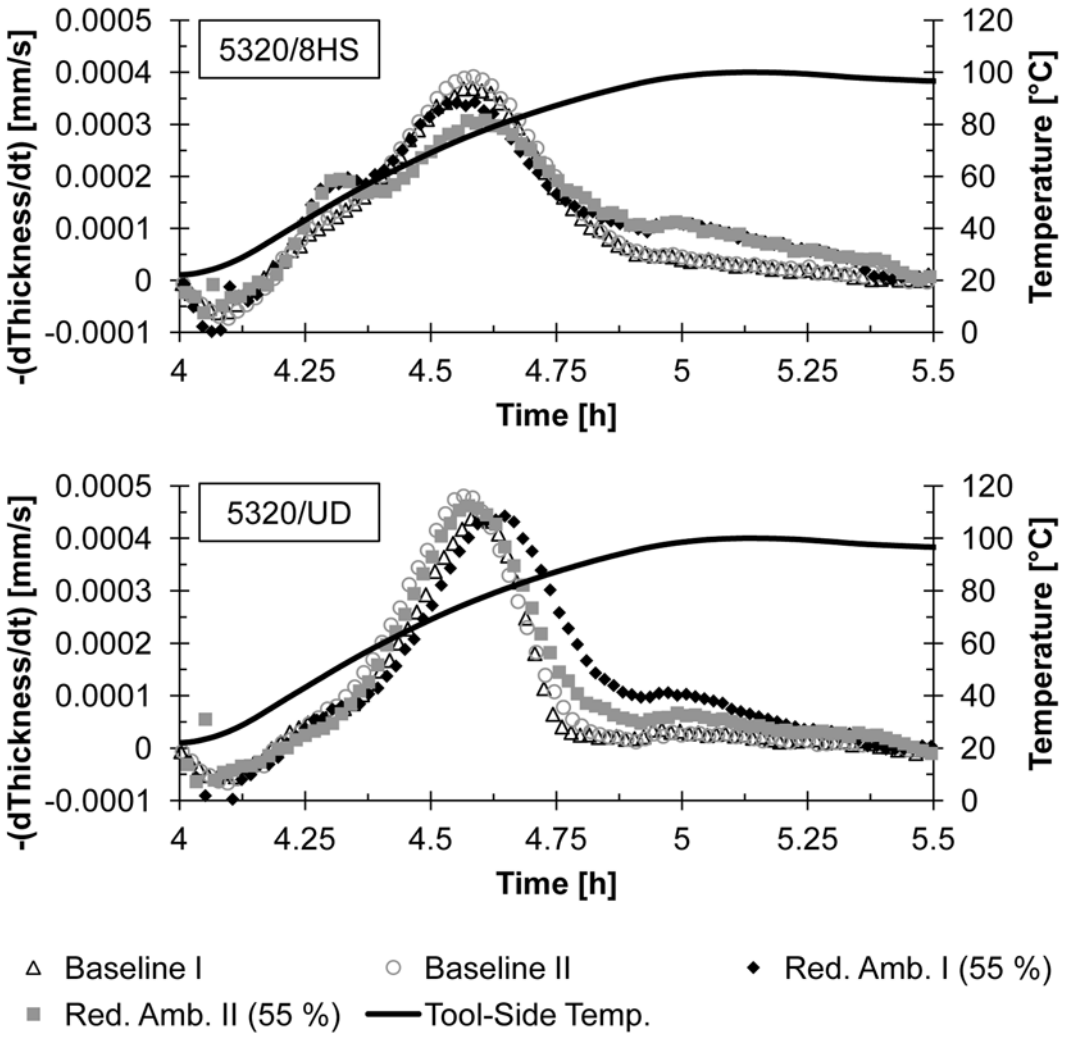

Figure 7–8: Graphs of the rate of change of thickness and cure cycle temperature for the reduced ambient pressure (55 % of atmospheric) 5320/8HS (top) and 5320/UD (bottom) laminates.

7.5.2.4 Reduced Vacuum

Figures 7–10 and 7–9 show the rate of change of thickness for the laminates cured under reduced vacuum.

The results are similar to those obtained for the case of reduced ambient pressure, with the major impact of reduced vacuum being a sharp drop in thickness rate of change between 55 °C and 65 °C for the 55 % case and the 5320/8HS material.

This similarity is, at first thought, somewhat surprising: even if the consolidation pressure differential is the same, reduced vacuum implies the presence of air within the bag and laminate. However, air present within a laminate may escape until the tows are sufficiently impregnated to become sealed, and may therefore not undergo significant pressurization for most of the flow period. Therefore, the majority of the air likely to pressurize and offer significant resistance to consolidation is that which is trapped within isolated pores. Since the process of pore entrapment and void growth is likely to occur in a similar manner for reduced ambient pressure and reduced vacuum, the rate of change of consolidation may also be expected to remain similar.

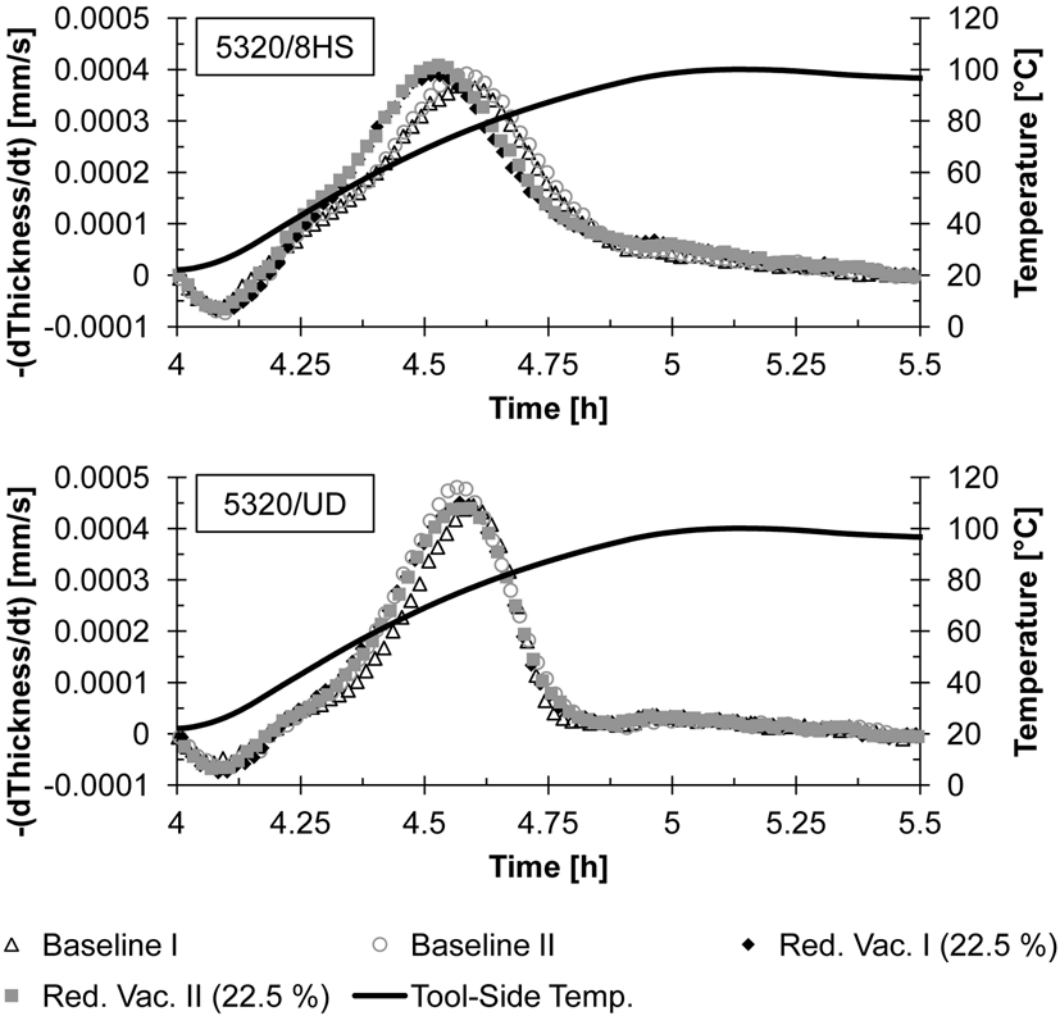

Figure 7–9: Graphs of the rate of change of thickness and cure cycle temperature for the reduced vacuum (22.5 % of atmospheric) 5320/8HS (top) and 5320/UD (bottom) laminates.

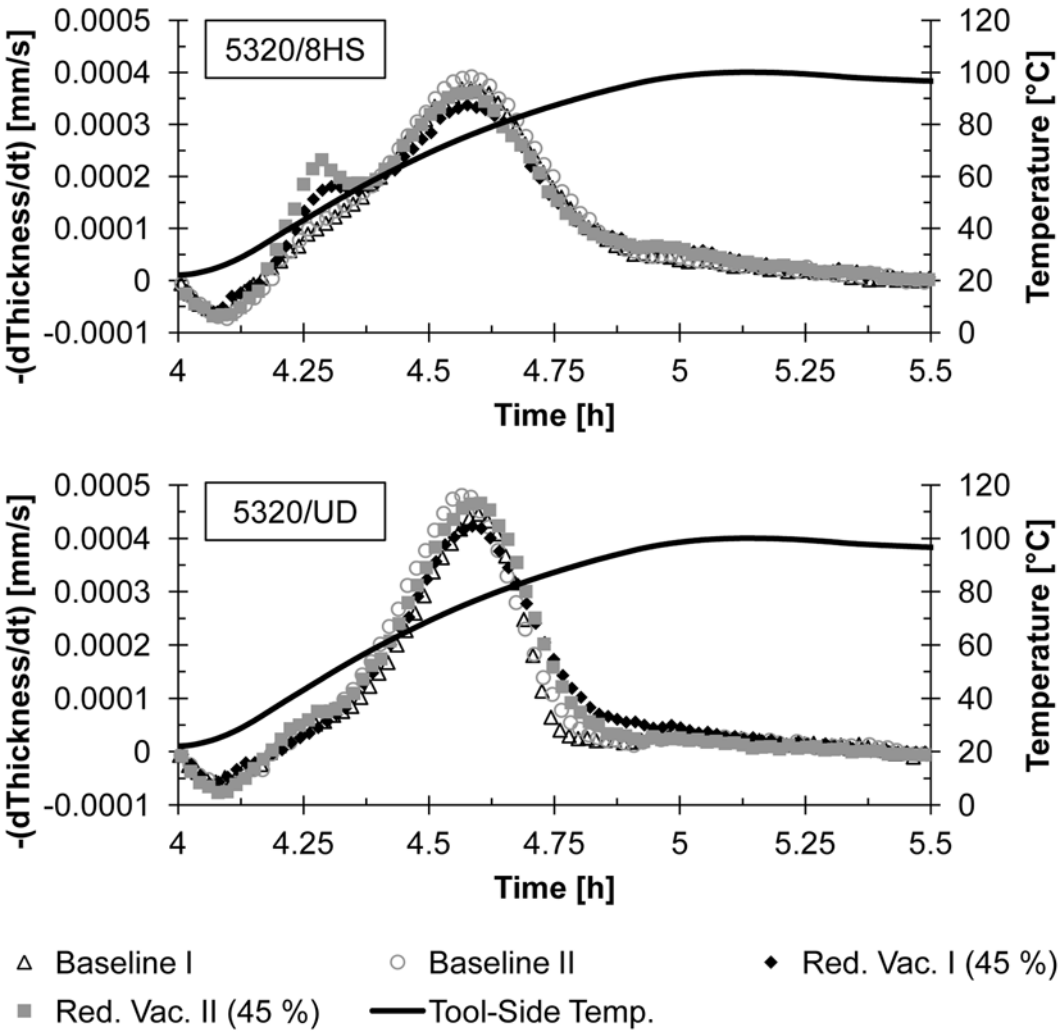

Figure 7–10: Graphs of the rate of change of thickness and cure cycle temperature for the reduced vacuum (45 % of atmospheric) 5320/8HS (top) and 5320/UD (bottom) laminates.

7.5.2.5 Restricted Air Evacuation

Figure 7–11 shows the consolidation curves for the laminates cured with restricted air evacuation.

For the 5320/8HS, consolidation started off in a similar manner to the baseline. Then, as the temperature crossed approximately 60 °C, the rate of change of thickness decreased substantially. As with the cases of reduced ambient pressure and reduced vacuum, this drop likely occurred because the average gas pressure of entrapped air became comparable to the resin pressure that drives consolidation. However, in this case, due to the amount of entrapped air, the impact was much more significant: in both repeats, the rate momentarily reduced to nearly zero. Some variability can be observed in the rate profile between the two repeats. However, it is not unexpected, since the initial amount and distribution of entrapped air may have been different; furthermore, the total thickness decrease during the period (or the area under the curves) is comparable for both cases.

For the 5320/UD, the results show that the rates of thickness change were uniformly lower than the baseline and, in the case of the first laminate, somewhat delayed. This slow-down occured because the air present inside the tows was entrapped, pressurizing, and therefore resisting tow impregnation. However, as with the case of reduced ambient pressure or vacuum, the results differ from the 5320/8HS by not exhibiting any sudden or significant "dips". This comparatively muted response is attributed to the reduced bulk factor of the 5320/UD laminates and the likely intra-tow nature of its porosity.

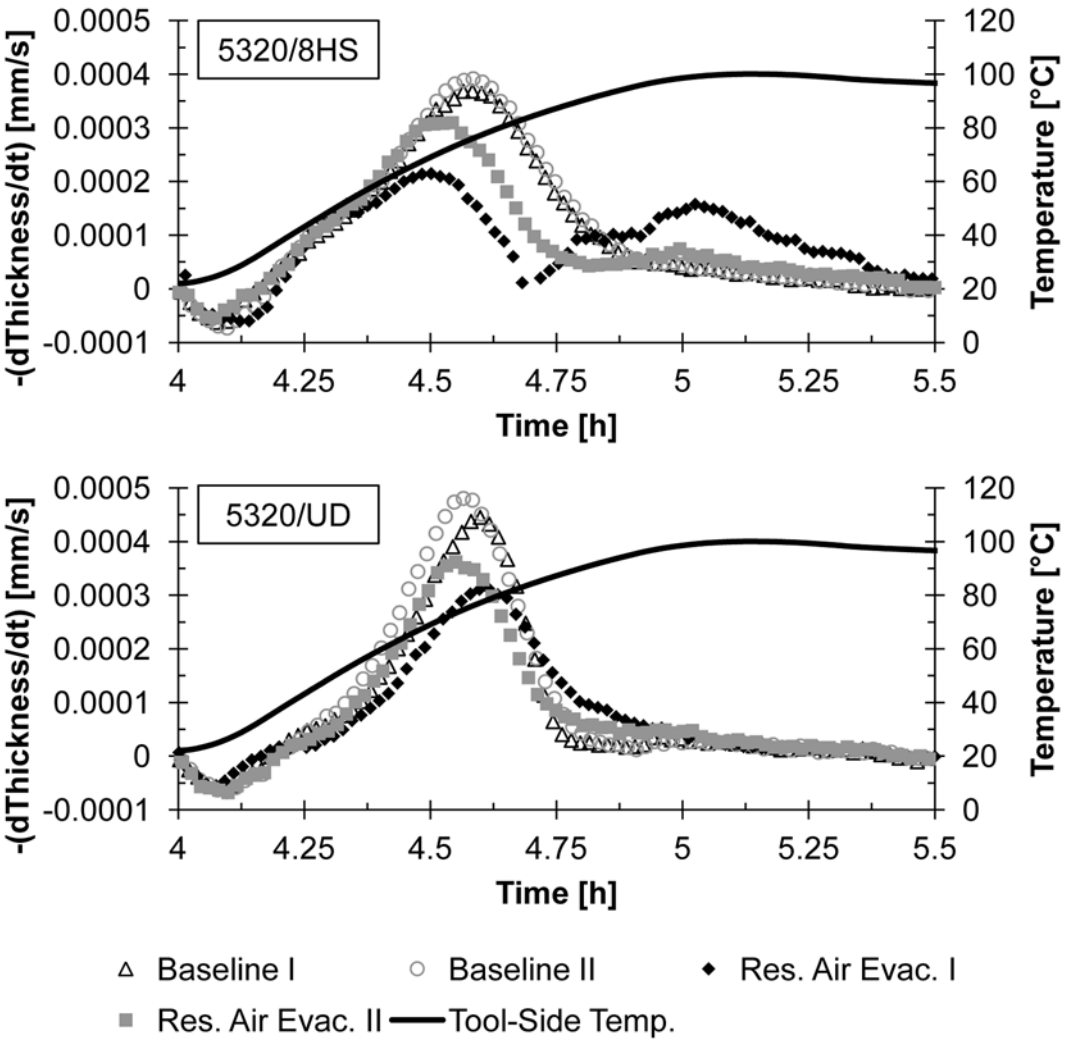

Figure 7–11: Graphs of the rate of change of thickness and cure cycle temperature for the restricted air evacuation 5320/8HS (top) and 5320/UD (bottom) laminates.

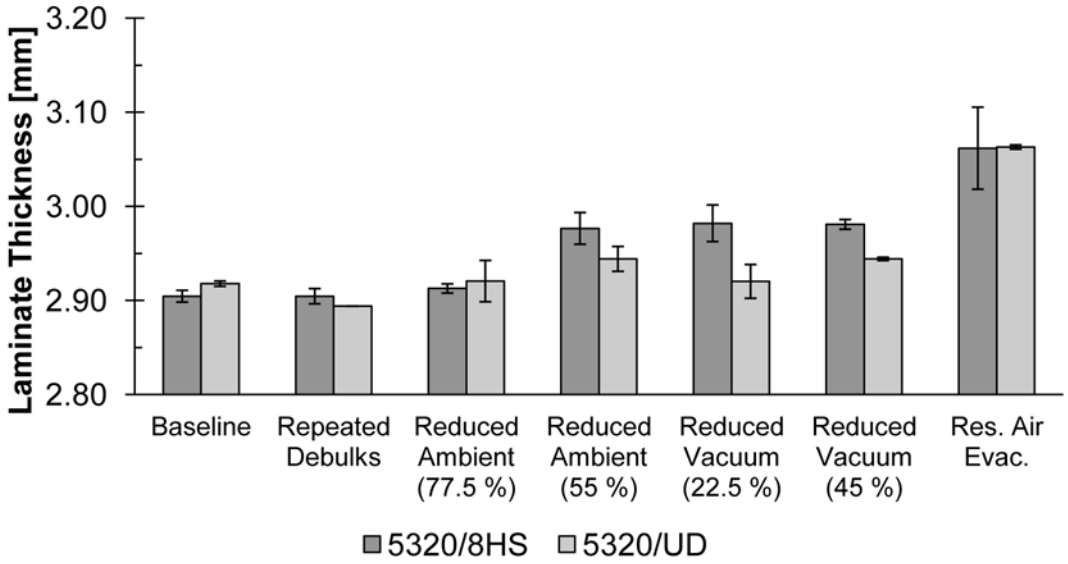

Figure 7–12: Chart of the laminate thickness versus deficient process condition and material. The error bars show one standard deviation in the six thickness measurements.

7.5.3 Laminate Quality

The average laminate thickness (with standard deviation) versus deficiency and material is shown in Figure 7–12. The baseline laminates were approximately 2.9 mm thick, as expected. The laminates subjected to repeated debulks were equally thick in the case of the 8HS and marginally (1 %) thinner for the UD. Therefore, repeated debulking had a negligible effect on final thickness for both materials. The laminates manufactured under reduced ambient pressure were thicker for both materials; as expected, the reduction in applied pressure resulted in lower consolidation. Interestingly, in all but one case, similar thickness values were measured for the laminates manufactured with the same consolidation pressure but under reduced vacuum. Thus, for the thickness, the magnitude of the consolidation pressure may be a more important factor than the manner in which it is attained.

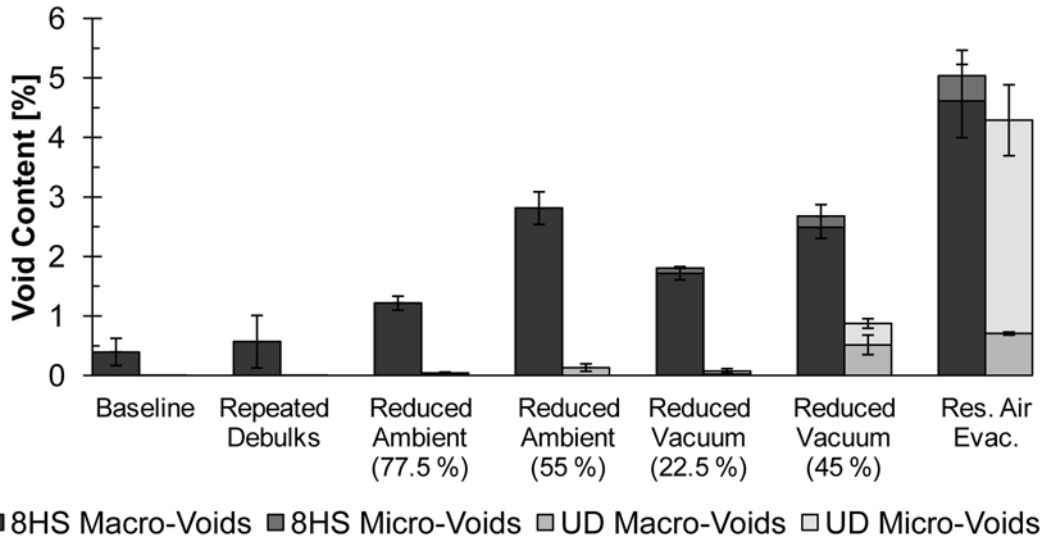

Figure 7–13: Chart of the laminate void content versus deficient process condition and material. The error bars show one standard deviation in the average macro- or micro-void values of the two laminates used for analysis.

Finally, for both materials, the laminates manufactured with restricted air evacuation exhibited the highest deviation from the baseline, indicating that the presence of entrapped air within the laminate has the most detrimental effect on consolidation quality.

Figure 7–13 provides the average macro- and micro-void contents (with standard deviation) versus process deficiency and material, while Figures 7–14 and 7–15 show optical micrographs with examples of representative void morphologies. For both materials, the overall trends echo the in-situ data: the repeated debulks show little difference to the baseline; reduced ambient pressure and reduced vacuum conditions noticeably increase defect levels and restricted air evacuation has the strongest detrimental effect on quality. However, on closer analysis, Figure 7–13 offers several additional insights.

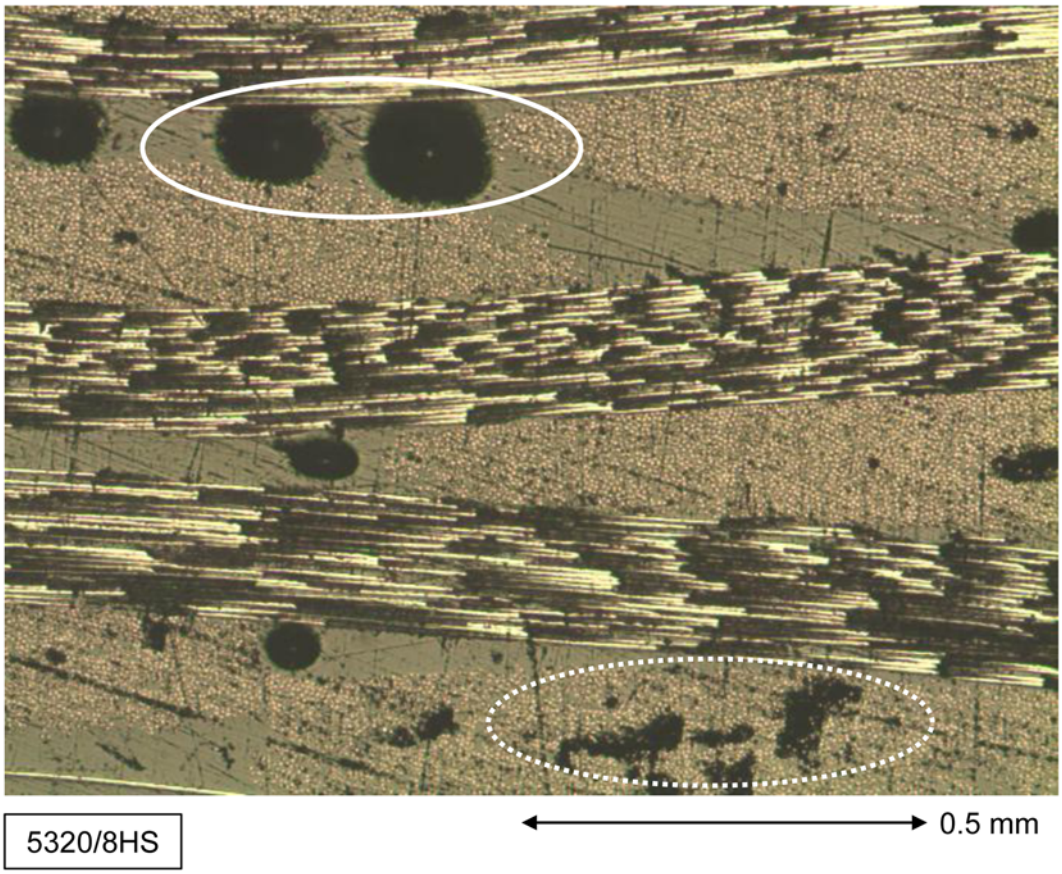

Figure 7–14: Optical micrograph of representative macro- and micro-void morphologies (solid and dashed line areas, respectively) in a high defect 5320/8HS laminate.

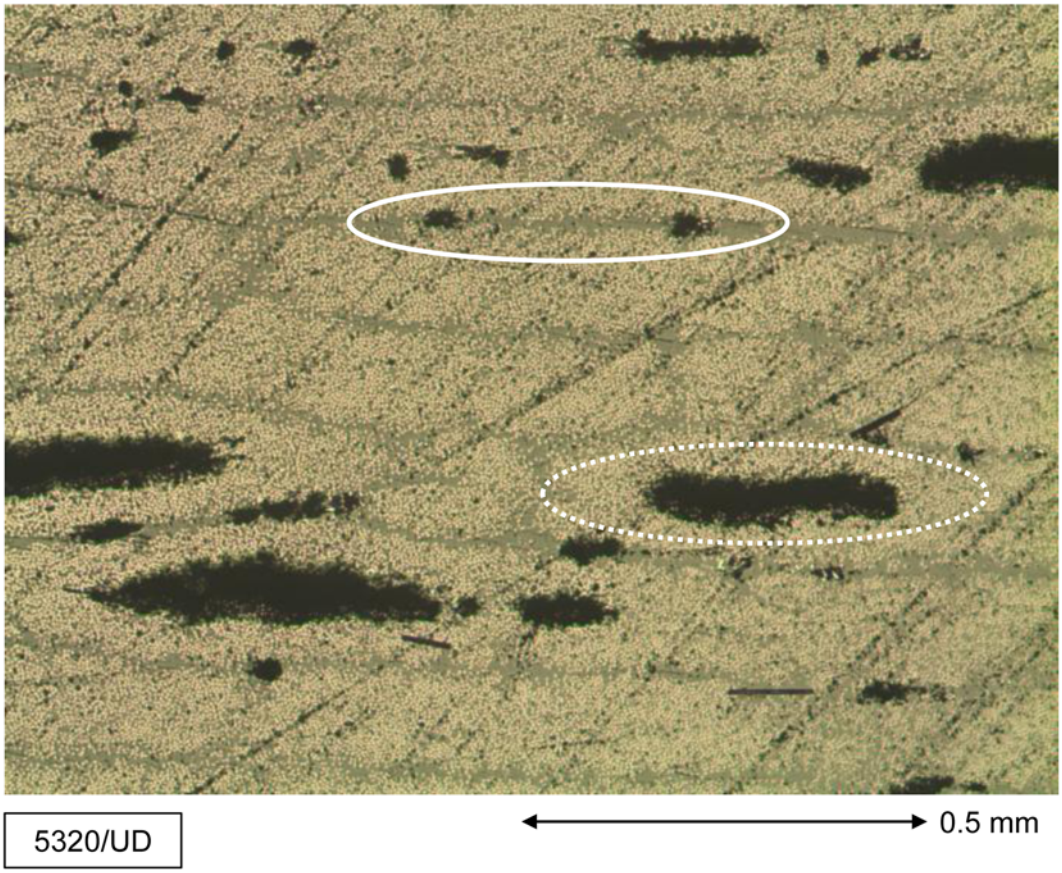

Figure 7–15: Optical micrograph of representative macro- and micro-void morphologies (solid and dashed line areas, respectively) in a high defect 5320/UD laminate.

The first pertains to the occurrence of micro-voids, which are only observed in conditions of reduced vacuum and restricted air evacuation. Such conditions involve the presence of air within the dry tow cores during processing, either because of non-zero bag pressure or an inability to escape; the results therefore suggests that it is this air, rather than conditions of decreased permeability or driving pressure, that primarily impede tow impregnation and generate micro-porosity in these laminates.

The second concerns the difference between the two fibre bed architectures. For the 5320/8HS, only the baseline and repeated debulk laminates are safely below the 1 - 2 % void content threshold band relevant to aerospace applications. In contrast, the UD void content values do not exceed 2 % until the worst-case condition of incomplete air evacuation. This difference may be attributed to macro-voids. As previously mentioned, 5320/8HS laminates have a relatively large bulk factor, containing closed spaces around tows and between plies that are likely sites for air entrapment and void formation. In contrast, 5320/UD laminates, with their aligned, straight, well-nested fibre bed architecture, do not feature many such spaces and hence contain less air. In essence, the ply morphology and layup of the 5320/UD limit air entrapment and hence result in much smaller macro-void levels. This theory is supported by the large macro-voids in the 5320/8HS micrographs and the much smaller ones in the 5320/UD (Figures 7–14 and 7–15), and by the fact that displacement sensor data deviations were mostly observed for the 5320/8HS.

A further point of interest is the relation between consolidation pressure and porosity, which is isolated in Figure 7–16. As the consolidation pressure is decreased due to either reduced ambient pressure or reduced vacuum, the

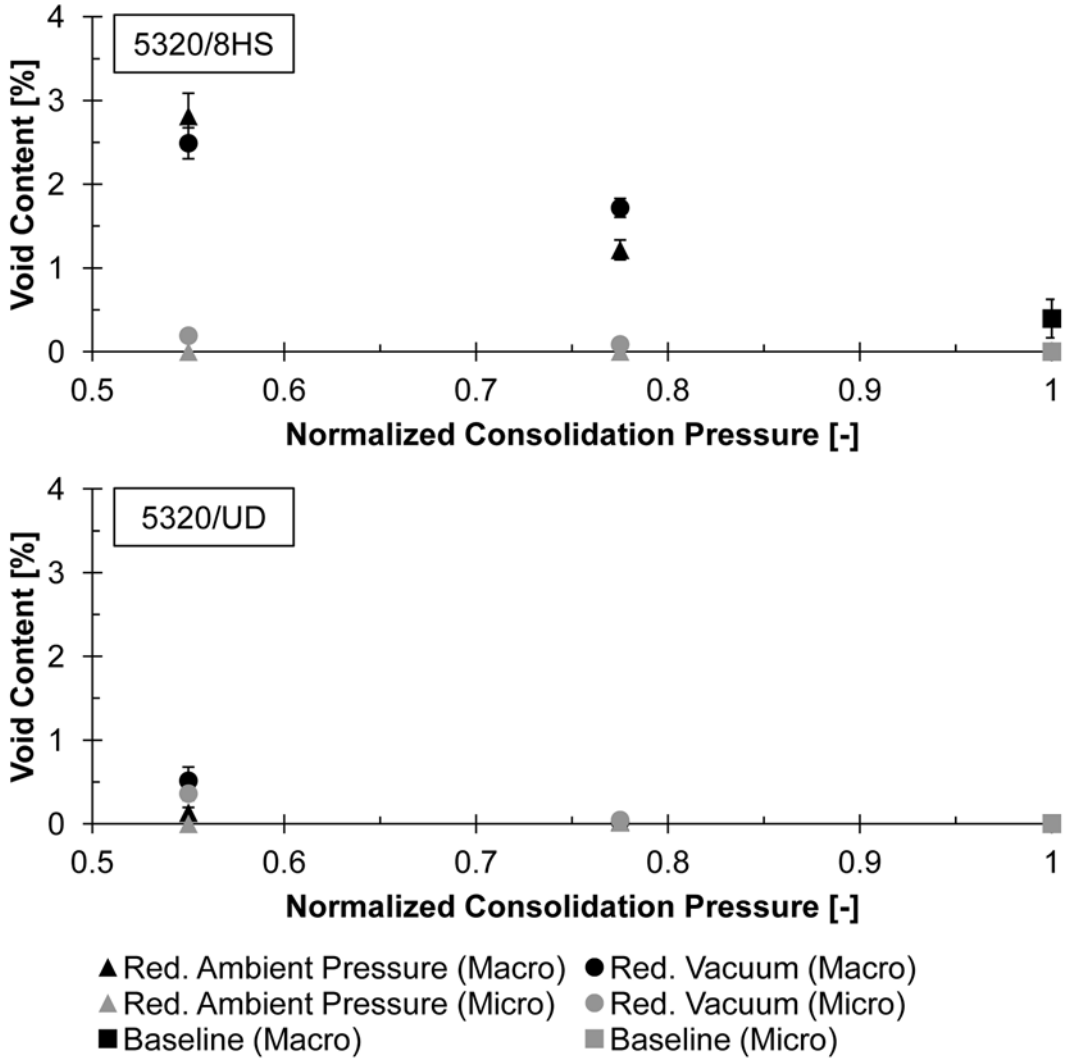

Figure 7–16: Graphs of the void content versus consolidation pressure for the cases of reduced ambient pressure, reduced vacuum and baseline, for the 5320/8HS laminates (top) and 5320/UD laminates (bottom)

macro-void content increases in an approximately linear manner. While this increase is much more pronounced for the 5320/8HS than the 5320/UD, it may be observed for both materials. Furthermore, for the case of reduced vacuum, the micro-void content increase with decreasing consolidation pressure is similarly consistent. This predictability, which spans the range of consolidation pressures that may reasonably be encountered in OOA prepreg processing, is helpful. Indeed, it allows a first estimation of defect levels based on process conditions, and thus serves as a useful tool for quickly assessing the success or failure of a given OOA cure.

Finally, it is also interesting to note that, for the restricted evacuation case, while the 5320/8HS porosity consists mainly of macro-voids and that of the 5320/UD is dominated by micro-voids content, both materials exhibit comparable void contents. The results thus suggest that an inability for air to escape leads to unacceptable porosity levels regardless of fabric architectures.

7.6 Conclusions

The present study investigated the link between four pressure-related potential consolidation deficiencies (repeated debulks, reduced ambient pressure, reduced vacuum and restricted air evacuation), the physical phenomena that take place during processing and microstructural quality for two OOA prepregs (5320/8HS and 5320/UD). The results lead to several conclusions.

1. **The consolidation of fabric-based OOA prepregs is sensitive to process deficiencies that decrease their void suppression capacity.** Laminates made up of fabric plies contain interstitial spaces that entrap air during layup. In the ideal case, the combination of resin pressure and gas evacuation under room temperature vacuum holding

is sufficient to ensure low final part porosity. However, if the consolidation pressure is reduced due to deficient atmospheric or vacuum conditions, or if air evacuation is restricted, the VBO method is unable to prevent any remaining air from growing into voids that quickly exceed the acceptable threshold for high quality parts. In contrast, since unidirectional tape prepregs have a significantly lower propensity for air entrapment, they are more robust, and only fail to achieve the required quality if air is prevented from evacuating.

2. **Process deficiencies are associated with specific void contents, distributions and morphologies.** Macro-voids occur in all cases, but their amount and size increases predictably with decreasing consolidation pressure. Micro-voids only occur when air remains within the dry tow cores due to insufficient vacuum or an inability to evacuate. Both types of porosity occur in extreme quantities when air is severely restricted from exiting the laminate. A clear understanding of the formation causes of specific void types thus allows the "forensic" analysis of manufactured parts, and the identification of process deficiencies.
3. **Void formation may be observed through the rate of thickness change during cure.** Indeed, laminates with significant macroporosity were associated with a decrease in the rate of thickness change during heat-up, at around 60 °C. These results thus point out the stage of the manufacturing process at which porosity may begin to form, and offer data that may be used for a more comprehensive analysis of void growth mechanisms in OOA processing.

4. **Successful OOA manufacturing requires stringent process control.** The results of the present study emphasize the importance of maximizing the consolidation pressure, both by ensuring adequate ambient conditions and by drawing a sufficient vacuum under the bag, particularly for high bulk factor prepregs. Furthermore, they indicate that laminate air evacuation is the most critical factor in achieving high quality, and highlight the importance of appropriate layup and bagging arrangements (such as edge breathing) and of sufficiently long room temperature vacuum hold times for the large, complex parts that may most benefit from OOA prepreg processing.

CHAPTER 8
Conclusions

8.1 Contributions

The work presented in this thesis, and the conclusions derived from it, have led to several contributions to the knowledge and literature on OOA prepreg processing. They are presented here in chronological order.

1. **A new method for analyzing process-induced microstructural changes in OOA prepregs was demonstrated.** Micro-CT, or X-ray computed microtomography, was used to investigate the initial and evolving microstructure of several OOA prepregs. Laminates were partially processed to different stages of a given cure cycle, sectioned, and imaged using an appropriate set of scan parameters. The resultant X-ray micrographs detected both macro- and micro-scale features within the laminate cross-sections, and allowed both two- and three-dimensional analysis. This micro-CT approach can serve as a useful complement to existing microstructural analysis methods, offering higher spatial resolution than, for example, published examples of ultrasound or MRI while avoiding the need for extensive, time-consuming and potentially disruptive sample preparation. Furthermore, it is also applicable to other manufacturing processes provided that they can be precisely interrupted.

2. **The key consolidation phenomena occurring during OOA prepreg processing were identified.** The micro-CT analysis results showed that the initial microstructure of OOA prepreg laminates consists of dry, micro-porous fibre tow cores surrounded by resin rich areas containing macro-pores of air entrapped during layup. During processing, two phenomena were seen to occur: the progressive disappearance of macro-voids following vacuum application due to gas extraction through the dry tows, and the gradual infiltration of the dry tows themselves at elevated temperature. Together, these conclusions offer the necessary basis for further study of OOA prepreg consolidation.
3. **A model describing OOA prepreg tow impregnation was developed.** The model, which consists of a simple but representative application of Darcy's Law, relies on several carefully chosen and reasonably realistic material properties and process parameters. It was found to match micro-CT flow measurements for several fibre bed architectures and resin systems under traditional material and process conditions. It was also found to qualitatively capture micro-porosity formation trends for conditions of elevated out-time. Overall, it is the first instance of a flow model linking material properties, process parameters and final part quality for OOA prepregs, and may be used to both gain a better understanding of the effect of various factors and as the foundation for a means of predicting part quality.
4. **The effects of several selectable material properties and process parameters on tow impregnation were quantitatively evaluated using experiments and modelling, and potential process**

optimizations were proposed. The fibre bed architecture was found to influence consolidation, with thicker, fibre-denser materials being more prone to air entrapment during layup (due to a higher bulk factor) and slower to impregnate during processing. The cure cycle was found to have a similarly significant impact, with tow infiltration occurring much quicker for cycles which maximize the time spent at low viscosity conditions. However, both fibre bed and cure cycle selection were found to be non-critical in the absence of other deviations from ideal conditions, with a wide range of materials, ramp rates and dwell temperatures leading to complete tow impregnation. In these ideal conditions, cure cycle selection was found to offer the potential for process optimization, with faster ramp rates and higher dwell temperatures dramatically reducing the time required for full tow impregnation, resin gelation, and thus part manufacture.

5. **The effects of key potential deviations from ideal material properties and process parameters on consolidation were quantitatively assessed using experiments and modelling, and the process robustness was clarified.** These deviations, which included the prepreg out-time (or, analogously, the resin initial degree of cure) and pressure-related issues such as repeated debulks, reduced ambient pressure, reduced vacuum and restricted air evacuation, were also investigated using a combination of modelling and experiments. Out-time was found to influence both the initial compaction and flow phases of consolidation, and to potentially lead to pervasive tow micro-porosity.

However, its influence was found to be coupled with that of the process temperature, and cure cycle modifications that mitigate or even eliminate its defects were identified. Repeated debulking was not found to be detrimental to laminate manufacture, supporting its use in the manufacturing of thick or complex parts. Reduced ambient pressure and reduced vacuum were linked with higher macro-void contents due to lower consolidation pressure. In addition, reduced vacuum was also seen to generate micro-porosity due to the presence of air within the bag and tows. Restricted air evacuation was found to cause extensive macro- and micro-porosity, suggesting that the inability to extract air from a laminate is the single most detrimental factor in OOA processing. Finally, the fibre architecture was found to be highly important, with fibre-dense, high bulk factor materials being more sensitive to process deviations. These results combine to offer a clearer understanding of the allowable process windows and are essential to determining whether a proposed OOA prepreg cure is viable.

The above-listed contributions directly resulted in scholarly literature on OOA prepreg processing, in the form of journal articles [124–126] and conference papers [127–131]. In addition, the micro-CT approach was used to analyze OOA prepreg microstructures in two aforementioned studies [95, 96].

8.2 Implications for Industrial Applications

Within each chapter, results with particular industrial relevance have been highlighted and discussed. However, a concise summary of the industrial implications of this work may be useful.

The results presented in Chapters 4 through 7 emphasize that high quality parts (with a void content below 1 %) may be produced using a wide variety of materials and process parameters, provided several conditions remain within the ideal ranges recommended by the prepreg manufacturers. However, the results also emphasize that OOA processing is sensitive, and that if these conditions deviate from these ideals, large decreases in quality may occur. Three key deviations were identified.

The first is out-time, an issue of particular importance since OOA prepregs are, at first thought, ideally suited for very large parts. Out-time was found to lead to pervasive micro-porosity due to incomplete tow impregnation, and was thus highly detrimental to quality. Its effects were mitigated by cure cycle and fibre architecture changes. However, since such changes may not be feasible in an industrial context (due to constraints such as oven and tool thermal capacity, part structural design and performance, material supply, and certification considerations), out-time should be considered a significant concern and actively avoided.

The second deviation is reduced consolidation pressure, which may come about through either reduced ambient pressure (due to geographic location or atmospheric variations) or reduced vacuum (due to an inadequate vacuum bag). Reduced consolidation pressure was found to significantly increase macro-porosity in laminates manufactured from prepregs with high bulk factors, which entrap significant air and therefore contain more potential void nucleation and growth sites. This problem was considerably less important in low bulk factor prepregs (such as a unidirectional tape), which entrap less air and are therefore simply less prone to macro-voids. However, as with the

issue of out-time, it is acknowledged that changing materials may not be feasible in many conditions. Therefore, it is recommended that the consolidation pressure be maximized by choosing a location with adequate ambient pressure, using an adequate vacuum system, and ensuring that the vacuum bag assembly is leak-free.

The third, and final, deviation is restricted air evacuation, which may be considered an extreme case of inadequate in-plane laminate breathing or insufficient room temperature vacuum evacuation in very large parts. Restricting air evacuation was found to lead to catastrophic porosity in all manufactured laminates, emphasizing that if air is impeded from exiting an OOA prepreg laminate, both macro- and micro-void contents will remain unacceptably high. No meaningful solution may exist to this issue. Thus, the proper and near-complete evacuation of air from a part, no matter the method or time required, is considered an essential step in successful OOA prepreg cure.

The above guidelines form a larger modus operandi by emphasizing that successful OOA prepreg processing requires comprehensive and detailed considerations of the part geometry, materials, layup, and process conditions. Indeed, in a given case, constraints on the part size may dictate the materials and process conditions that can be used. Conversely, in a different case, cure cycle limitations may constrain the allowable out-time, and thus the part size, or the material. Therefore, overall, only a systemic understanding of the process may truly lead to successful, robust and efficient part manufacture.

8.3 Future Work

The results presented within this thesis offers several opportunities for further study, the main lines of which are discussed below.

1. **The tow impregnation model may be extended to account for other phenomena relevant to OOA processing.** The addition of a module that accounts for the gas pressure within the tow as a function of such parameters as bag pressure, room temperature gas evacuation time and moisture off-gassing is particularly desirable, as it would allow the simulation of the complete OOA manufacturing process and the more accurate prediction of defect levels. Furthermore, the integration of the current model within a larger framework that accounts for part geometry and spatial distributions of temperature and pressure would be highly advantageous and a natural next step.
2. **The effect of coupled process deficiencies may be studied.** Within this thesis, most process deficiencies (such as reduced out-time, ambient pressure and vacuum) were studied independently, in order to clearly understand their fundamental effects. However, during the manufacture of large or complex parts, these deficiencies are likely to interact and influence each other. A detailed understanding of these interactions and their combined effect on part quality, and the development of more complex process maps to guide part manufacture in such conditions would be a significant contribution.
3. **The effect of industrially relevant structural features on OOA prepreg consolidation may be considered** The work presented in this thesis is applicable to monolithic, quasi-planar laminates, which are commonly found in aerospace applications such as wing skins and fuselage sections with large curvatures. However, many other applications involve additional structural features, such as tight radii, inserts

of various shapes and sizes, and sandwich cores such as honeycomb. Such features may impact consolidation locally or globally, and produce deviations from the behaviours identified in the present studies.

4. **The effect of out-time on resin viscosity may be studied in greater detail.** The present study showed that the viscosity of resins exposed to high levels of out-time may deviate from that predicted by resin cure kinetics and viscosity models for the same measured α_0, and lead to differences between predicted and measured defect levels in manufactured laminates. A more detailed experimental study of the viscosity and flow capacity of representative resins, and the development of improved models to describe these, would be of considerable interest.
5. **The influence of variability and the issue of repeatability within OOA prepreg processing may be studied in detail.** Several results in this thesis suggest that the properties of OOA prepregs and of their constituent materials may feature considerable variability. In the present work, average values of such properties have been reported (along with common measures of dispersion such as the standard deviation or minima/maxima) and used to determine overall trends. Furthermore, experiments have been repeated whenever reasonable (or possible), given material and time constraints. However, the specific question of how variability affects the process has not been addressed. Thus, a focused and detailed investigation of the influence and importance of variability in OOA prepreg processing would be beneficial. Two issues would be of particular interest: the sensitivity of specific consolidation

phenomena to variations (or uncertainties) in material properties, and the overall repeatability of OOA prepreg processing.

APPENDIX A
Nomenclature

A.1 List of Symbols

a_0	Ellipse major half-axis
A_f	Visible dry fibre tow (unsaturated) area
A_{tow}	Tow cross-sectional area
A_i	Cure kinetics model parameter
$A_{\mu i}$	Viscosity model parameter
A_s	Gutowski compaction model fibre bed stiffness constant
b_0	Ellipse minor half-axis
B	Viscosity model parameter
C	Viscosity model parameter
CTE	Coefficient of thermal expansion
d	Sensor height in consolidation fixture
d_p	Reynolds number characteristic length
D	Cure kinetics model parameter
E_{ai}	Cure kinetics model parameter
$E_{\mu i}$	Viscosity model parameter
G'	Storage modulus
H	Heat of reaction released during resin cure
H_{tot}	Total heat of reaction released during resin cure
I	Beam intensity of X-rays

I_0	Beam intensity of unattenuated X-rays
K	Transverse tow permeability
K_i	Cure kinetics model Arrhenius function
$K_{\perp,quad}$	Gebart model transverse permeability, quadratic arrangement
$K_{\perp,hex}$	Gebart model transverse permeability, hexagonal arrangement
$\bar{\bar{K}}$	Permeability tensor
m_i	Cure kinetics model parameter
n	Gutowski compaction model fitting constant
n_i	Cure kinetics model parameter
n_{porous}	Number of incompletely impregnated tows in cross-section
n_{total}	Total number of tows in cross-section
P	Pressure
P_{app}	Consolidation pressure
P_∞	Resin pressure at external tow boundary
P_c	Capillary pressure at flow front
P_f	Resin pressure at flow front
P_{gas}	Gas pressure at flow front
P_{void}	Void gas pressure
r	Radial coordinate
R	Universal gas constant
R_f	Resin infiltration front radius
R_{fib}	Fibre radius
R_{tow}	Equivalent circular tow radius
Re	Reynolds number

s	Line segment
S	Saturation
t	Time
T	Temperature
T_{amb}	Ambient temperature
T_g	Glass transition temperature
T_{g0}	Glass transition temperature model parameter
$T_{g\infty}$	Glass transition temperature model parameter
$\bar{v_f}$	Fibre bed velocity
$\bar{v_r}$	Average local resin velocity
v_r	Radial resin velocity
V_f	Fibre volume fraction
V_{f0}	Zero stress volume fraction
V_{fa}	Maximum allowable volume fraction
$V_{f,min}$	Minimum fibre volume fraction for spontaneous infiltration
α	Degree of cure
α_0	Initial degree of cure
α_{C0}	Cure kinetics model parameter
α_{CT}	Cure kinetics model parameter
α_{gel}	Resin degree of cure at gelation
α_{sup}	Capillary pressure model angular coordinate
α_{inf}	Capillary pressure model angular coordinate
β	Degree of impregnation

δ	Sensor height, after thermal expansion, in consolidation fixture.
$\eta_{att,ave}$	X-ray linear attenuation coefficient
γ	Surface tension
λ	Glass transition temperature model parameter
μ	Viscosity
ρ	Density
θ	Contact angle
σ	Fibre bed effective stress (through-thickness)
$\bar{\bar{\sigma}}$	Fibre bed effective stress tensor
ξ	Ratio of fibre half-spacing to radius

A.2 List of Acronyms

FDEMS	Frequency dependent electromagnetic sensing
FOV	Field of view
LCM	Liquid composite moulding
MRI	Magnetic resonance imaging
OOA	Out-of-autoclave
RFI	Resin film infusion
RT	Room temperature
RTM	Resin transfer moulding
VBO	Vacuum bag-only

APPENDIX B
Micro-CT Scan and Reconstruction Procedures

B.1 Experimental Apparatus

As shown in Figure B–1, the Skyscan 1172 High Resolution Micro-CT consists of the actual X-ray microtomograph and a control computer. The former houses the sample test chamber and all other hardware; the latter contains the control software used to run the tests and the reconstruction software used for data analysis.

B.2 Procedures

B.2.1 Calibration

The micro-CT was not explicitly calibrated by the author. Rather, being highly specialized equipment, its operation was managed by the McGill Institute for Advanced Materials and it underwent regular maintenance by a Skyscan service agent. To the best of the author's knowledge, this maintenance included the alignment of the X-ray generator and detector and the adjustment of the generator itself for optimal control of the X-ray current and voltage. Two facts mitigate this procedural limitation. First, the consequences of any deviation in X-ray generator or detector response will likely have been reduced by the flat field correction described below. Second, for the work presented in this thesis, the ability to compare different scans and to distinguish between solid (or fluid-saturated) and void areas is more important than the inherent "accuracy" of the micro-CT (defined as, for example,

Figure B–1: Photograph of the Skyscan 1172 High Resolution Micro-CT [110].

its ability to produce the same grayscale response in an X-ray micrograph of a given sample as a benchmark system).

B.2.2 Scan

The following steps were used to scan prepreg samples using the Skyscan 1172 High Resolution Micro-CT. They are based on information found in the user manual, [110], the additional method notes [132] and the scan flowchart [133], as well as on user experience.

1. The micro-CT was powered on, and the "Skyscan 1172" desktop software was opened on the control computer.
2. The X-ray generator was activated, and allowed to go through the fifteen minute pre-heating step,

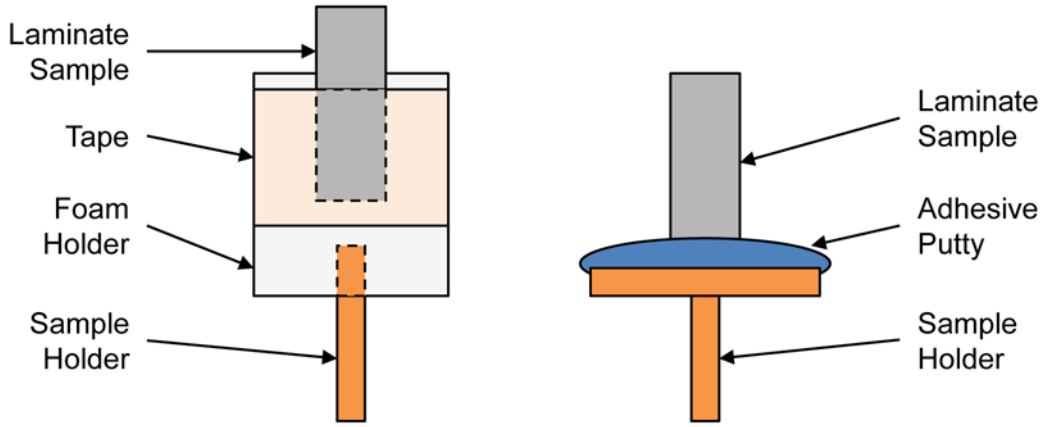

Figure B–2: Schematic of prepreg mounting configurations for micro-CT scanning: in foam holder (left) or in adhesive putty (right).

3. The prepreg sample was mounted on a sample holder in one of two configurations (Figure B–2): embedded in a foam block with a notch cut out of it and wrapped in masking tape, or held in place with blue adhesive putty. Both approaches were found to be equivalent in terms of scan quality, but the latter was eventually favored due to easier handling.
4. The mounted sample was inserted into the micro-CT scan chamber (Figure B–3) and fastened to the rotating stage; care was ensured to turn the screw mechanism finger-tight in order to prevent any relative motion between the sample holder and the rotating stage. Then, the scan chamber was closed.
5. The Skyscan 1172 control software was used to set-up the scan.
   5.1 The sample stage was moved up (or down) to center the sample within the X-ray detector's field of view (FOV).
   5.2 The filter setting was moved to "No Filter".
   5.3 The image size of 4000 x 2096 pixels was selected.

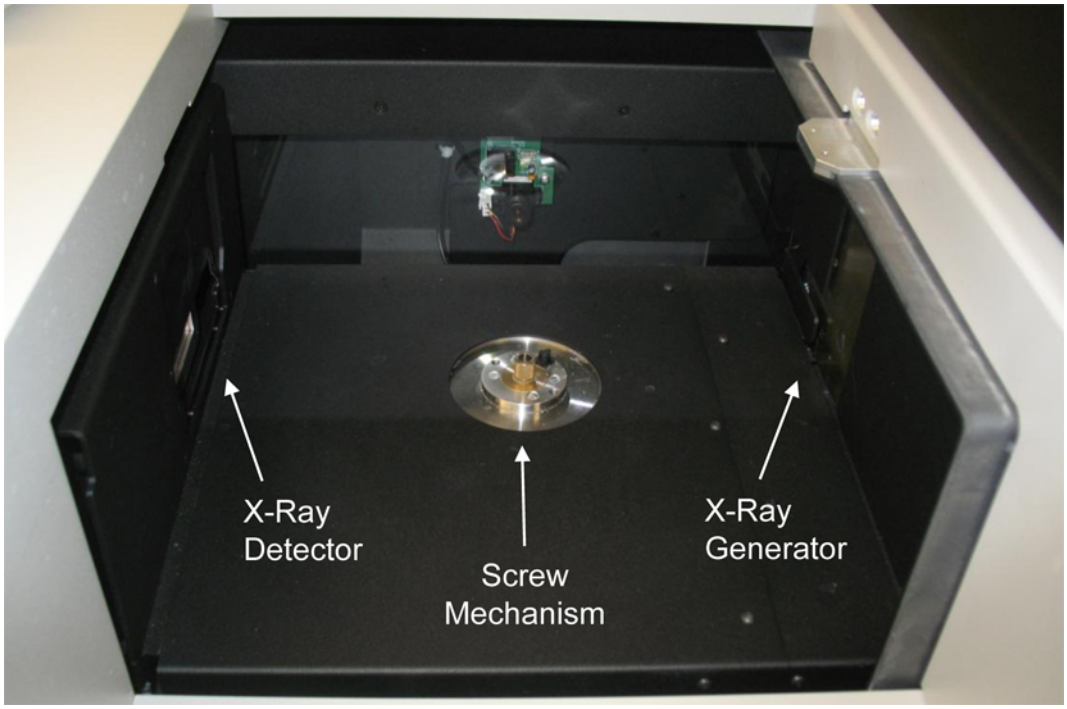

Figure B–3: Photograph of the micro-CT scan chamber.

5.4 The desired scan resolution (pixel size) was chosen, with care taken to ensure the entire sample fit within the FOV. For the work presented in this thesis, the scan resolutions were either 7 µm/pixel or 2 µm/pixel.

5.5 The flat field correction option was activated (if inactive). The flat field is the signal detected by the X-ray detector at the desired scan parameters, with no sample in the FOV. Being a baseline measure of background radiation, it is subtracted from the data taken during the actual scan.

5.6 The X-ray voltage and intensity were adjusted to obtain optimal contrast. For the work presented in this thesis, the voltage and intensity were 64 kV and 154 µA, respectively.

5.7 The sample was removed from the field of view by lowering it, and the flat field correction option was turned off. Then, the average uncorrected detector signal brightness was inspected to ensure it fell between 40 % and 60 %. For the scans presented in this thesis, this was indeed the case; in the opposite case, the exposure time may be adjusted as needed.

5.8 The flat field correction data was updated at the current scan settings.

5.9 The flat field correction option was turned back on, the sample was brought back into the FOV, and the contrast was re-verified in light of the updated flat field correction data.

5.10 Steps 5.5 to 5.8 were repeated as necessary to ensure optimal contrast (as shown in [132]). For the work presented in this thesis, only one iteration was generally necessary.

6. The scan dialog window was opened, and the options were verified to ensure they remained at their default settings (a rotation step of 0.28°, a frame averaging value of 3, a random movement value of 10, and no 360° rotation).
7. The scan was started and allowed to complete. Scans generally lasted between 1h and 2 h and produced shadow projection datasets between 1 Gb and 3 Gb in size.

B.2.3 Reconstruction

1. The "NReconServer" and "NRecon" applications were opened on the control computer.

2. In NRecon, the scanned dataset was opened and the reconstruction options were set.
   2.1 The vertical region of interest was set by selecting the top-most and bottom-most X-ray micrographs to be reconstructed.
   2.2 A slice was previewed at the default reconstruction settings (in terms of misalignment compensation, ring artifact reduction and beam hardening reduction) to verify reconstruction quality. Generally, these settings were kept at their default values; in cases where they required adjustment, NRecon's fine-tuning option was used to obtain adequate setting values as instructed in the software's manual.
   2.3 In the Output dialog, the region of interest enclosing the sample was selected, and the upper and lower histogram values were set to -0.01 and 0.085, respectively, in order to ensure consistent comparison between different scans.
3. The reconstruction was started and allowed to complete. Reconstruction times were generally on the order of 5 h, and produced X-ray micrograph datasets on the order of 5 Gb.

APPENDIX C
Fibre Bed Compaction Characterization

This addendum to the details provided in Chapter 5 offers additional information about the experimental procedures used to perform the fibre bed compaction, and the data analysis used to extract the load carried by the fibre bed.

C.1 Experimental Apparatus

The compaction fixture used to characterize the fibre bed compaction behaviour of the prepregs considered in Chapter 5 is shown in Figure C–1. It consists of an MTS Insight 5 kN electromechanical test frame with a 5 kN load cell (connected to a computer with control and digital acquisition capabilities) and a compaction platen system. The latter consists of a two-part, stainless steel, rectangular channel mould attached to copper plates with integrated cartridge heaters and ceramic thermal insulator blocks. The female part of the channel, on the bottom platen, measures approximately 55 mm by 100 mm, and can accomodate samples up to 10 mm thick. It remains fixed during operation. The male or top part of the channel may be moved vertically using the test frame's control computer and software. The eight cartridge heaters are activated by setting the desired temperature on two external controllers. Overall, the position of the top platen and the load carried by the attached load cell may be recorded.

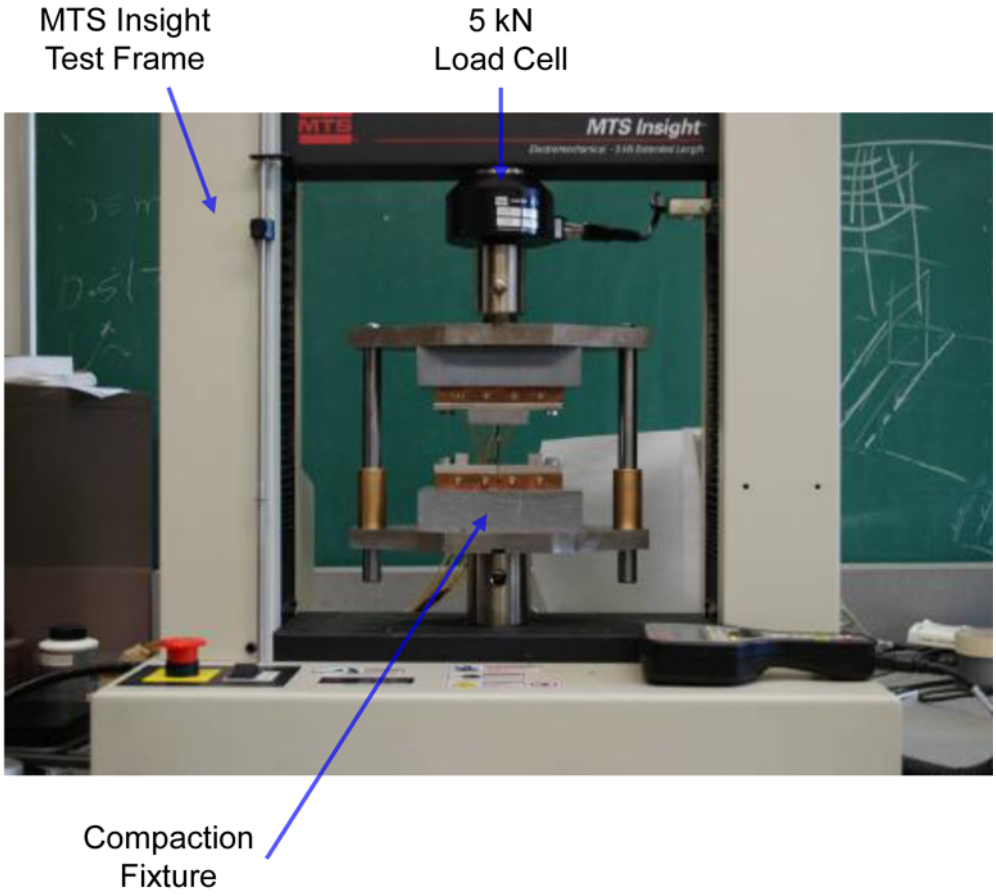

Figure C–1: Photograph of the fibre bed compaction fixture [134].

C.2 Procedures

C.2.1 Experimental

C.2.1.1 Compaction Fixture Preparation

Prior to any series of tests, the compaction platens were installed within the test frame and aligned to ensure optimal fit between male and female parts as well as parallelism. Then, the heater temperature set-points were set and the heaters were activated at least 12 h prior to any test in order to allow the temperature of the platens to reach 99 °C ± 5 °C, the temperature of the test frame to equilibrate, and any thermal expansion to occur. Finally, once the fixture and test frame were properly heated, the load cell and cross-head readings were tared.

C.2.1.2 Sample Preparation

Prepreg plies approximately 55 mm by 55 mm were cut and laid up to form a laminate sample; layups were $[(0°/90°)_4]_s$ for the 5320/PW and $[(0°/90°)_2]_s$ for the 5320/8HS and MTM45-1/5HS. Then, the sample was pre-consolidated in a vacuum bag using a 45 min room temperature vacuum hold; this practice has been previously shown to reduce variability during compaction testing [134]. Finally, the sample was removed from vacuum, measured and wrapped in non-perforated FEP release film (of total thickness equal to 80 µm ± 5 µm) in order to avoid bonding the resin matrix to the compaction fixture platens. This wrapping, however, only sealed the two sample edges adjacent to the compression platen's side walls, allowing resin to bleed out through the remaining two edges.

C.2.1.3 Compaction Test

Each compaction test consisted of placing the sample within the bottom (female) compaction platen, bringing the top platen into contact, and executing the test procedure on the MTS test frame's control computer.

The test procedure consisted of a $0.05\,\mathrm{mm\,min^{-1}}$ decrease in cross-head (or sample compression) down to a desired thickness (generally between 1.3 mm and 2 mm), and a hold at that thickness for 24 h. During the compression and hold steps, the resin was allowed to bleed out of two of the sample's edges, decreasing the overall applied load while transferring it to the fibre bed, and then gel and vitrify, resulting in a solid, cured part. Cross-head and load data were recorded by the test frame's digital acquisition system.

Once the test was complete, the sample was removed from the platens, and the compliance of the compaction fixture was tested by compressing the empty platens at the same $0.05\,\mathrm{mm\,min^{-1}}$ rate down to a maximum compressive load of 2000 N. This compliance data was used to verify the consistency of the compaction fixture's mechanical response.

C.2.2 Results and Data Analysis

The load-displacement data recorded by the MTS software was analyzed in order to determine the fibre bed compaction load associated with the thickness of the cured laminate (measured at nine points directly on the sample using a Mitutoyo 0 - 25.4 mm micrometer, model 293-765-30, and averaged).

A set of representative cross-head and load curves, obtained from a 5320/PW sample compressed to 1.56 mm, are shown in Figure C–2; the data after the 12 h mark is omitted for clarity. While the load measure accurately represents the force applied on the sample, the cross-head value

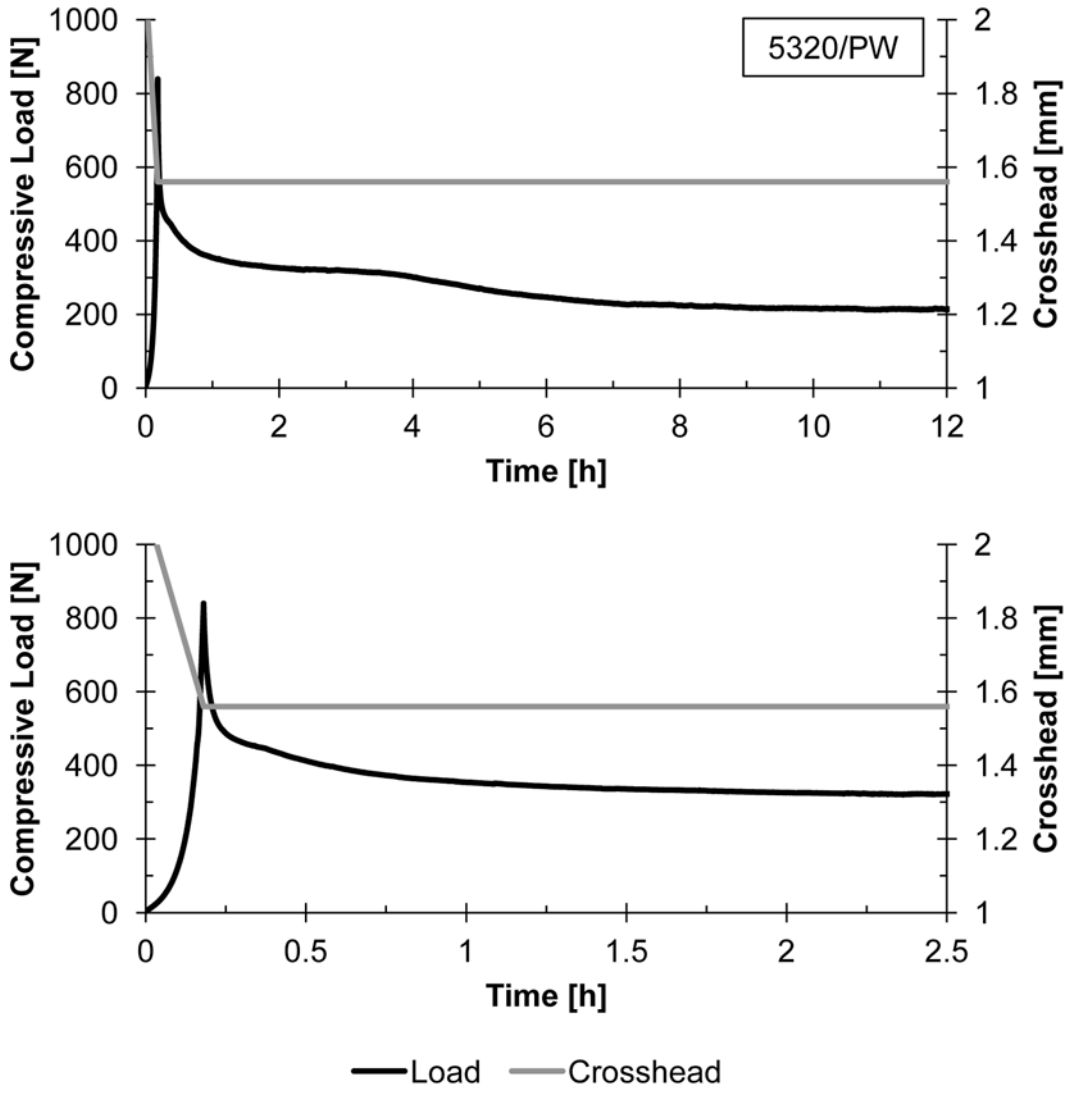

Figure C–2: Graphs of the cross-head and load histories of a representative 5320/PW sample, with time between zero and twelve hours (top) and magnified between zero and 2.5 h (bottom). The data after 12 h is omitted for clarity.

does not account for the compliance of the fixture itself; however, since all thickness values in this study were obtained by directly measuring the cured sample thickness, the cross-head data showed in the graph data is used for qualitative purposes only.

The results show that, as the laminate is compressed, the load increases to a maximum, but begins to decrease as soon as constant thickness is reached. At constant thickness, the load tends towards a constant value, corresponding to the stress carried solely by the fibre bed at this thickness. For the purposes of this study, the load value at 2.5 h was assumed to have reached equilibrium, and was divided by the sample's surface area to obtain the effective stress data shown in Figure 5–6.

The results also show that a second, less significant decrease in load occurs, for this material, between hours four and seven. This decrease is attributed to a combination of resin gelation, which is predicted by the 5320 resin cure kinetics and viscosity models to occur around the 6.5 h - 7 h mark, and cure shrinkage. Indeed, as the epoxy matrix solidifies and shrinks, it may be expected to begin carrying some of the fibre bed loads, and thus reduce the load measured by the load cell. However, since the resin bleed and gelation periods are seen to be relatively separate, this phenomenon is not believed to have influenced the test results.

APPENDIX D
Consolidation Fixture

A full description of the fixture, including detailed design notes and engineering drawings, may be found in the thesis by Chew [135]. However, a summary of its main components and of the instrumentation relevant to this thesis is offered in the following sections.

D.1 Components

The consolidation fixture is shown schematically in Figure D–1. As explained in Chapters 6 and 7, it is made up of three main components: a tool plate; a sensor support and a lid (used only in Chapter 7).

The tool plate consists of two aluminum pieces which, fastened together, form a flat area that may be used to support a vacuum bag assembly and manufacture laminates. The tool plate features two pairs of vacuum ports: one is located on the inner piece, within the area dedicated to the vacuum bag, while another may be found within the outer piece, outside the vacuum bag.

The sensor support is composed of two parallel vertical posts and a horizontal beam. The vertical posts feature slots that allow the horizontal beam to be raised or lowered; the latter holds and locates the non-contact displacement sensor above the laminate to be manufactured.

The lid is a large, hollow aluminum block that covers both other components. At the mating interface with the tool plate, airtight contact is ensured

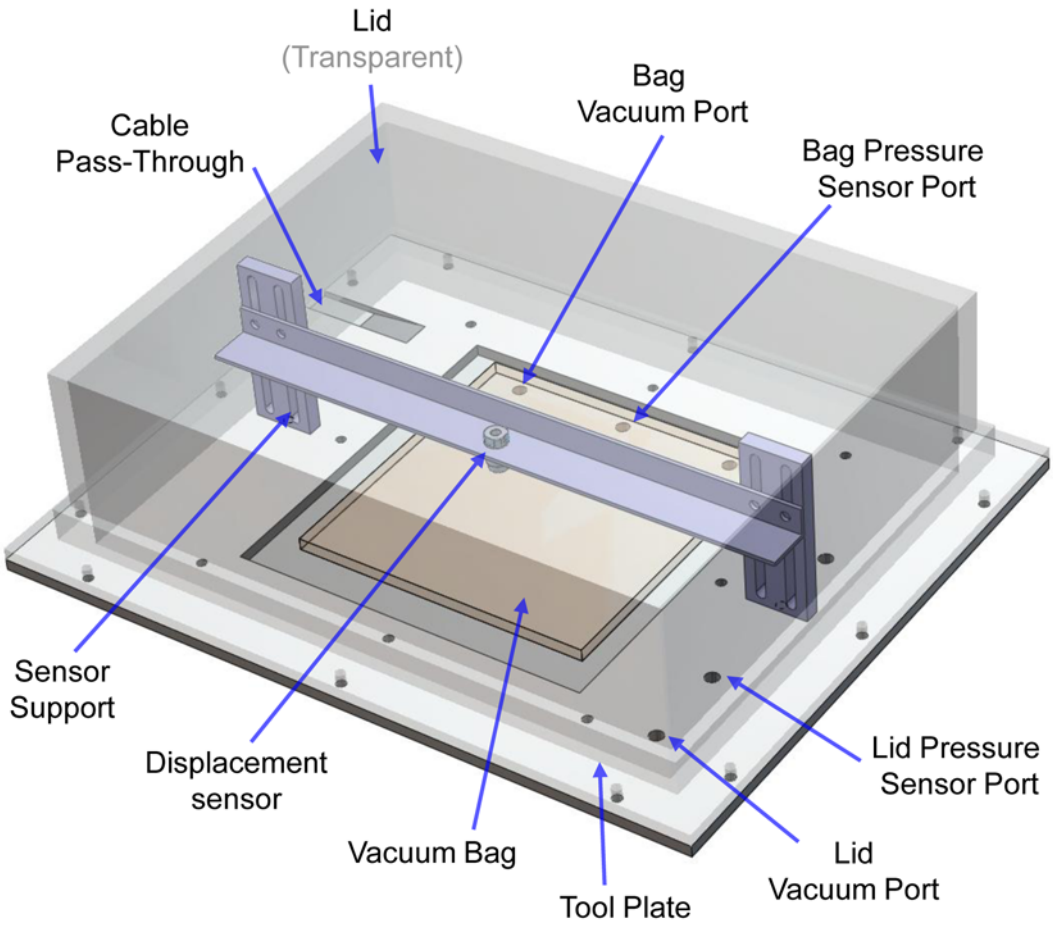

Figure D–1: Schematic of the custom-designed, instrumented consolidation fixture.

by temperature-resistant silicone vacuum seals; a machined and silicone-sealed cable pass-through channel is also present. The lid allows the air pressure within the lid cavity (but outside the vacuum bag) to be regulated between ambient and vacuum in order to simulate reduced atmospheric pressure conditions.

The entire consolidation fixture is approximately 0.6 m wide by 0.48 m deep by 0.16 m high, is manufactured from aluminum (6061-T6), and is thus suitable for the instrumented manufacture of lab-scale laminates using OOA oven cure techniques.

D.2 Instrumentation

The fixture is instrumented to measure temperature, pressure and laminate thickness in-situ.

Temperature is measured by means of OMEGA type-K thermocouples (part number TT-K-30-SLE (ROHS), with a specified drift of $\leq 0.05\,^{\circ}\mathrm{C}$ at $200\,^{\circ}\mathrm{C}$).

Pressure is measured by means of two WIKA A-10 pressure sensors, connected to their respective vacuum ports via vacuum fittings. The sensors have an absolute pressure range of 0 Pa to 202 650 Pa. Their calibration is described in the upcoming Section D.2.1.

Laminate thickness is measured by means of a non-contact eddy current sensor, Micro-Epsilon eddyNCDT 3010 / U6, which detects the distance between its tip and a 75 mm by 75 mm by 2 mm steel (AISI 4130) target located on the laminate, between the bag-side release film and the breather. The sensor has a range of 6 mm, a non-linearity of ≤ 0.25 % of full scale below half-range, a resolution of 0.3 µm, a static repeatability of 0.6 µm and

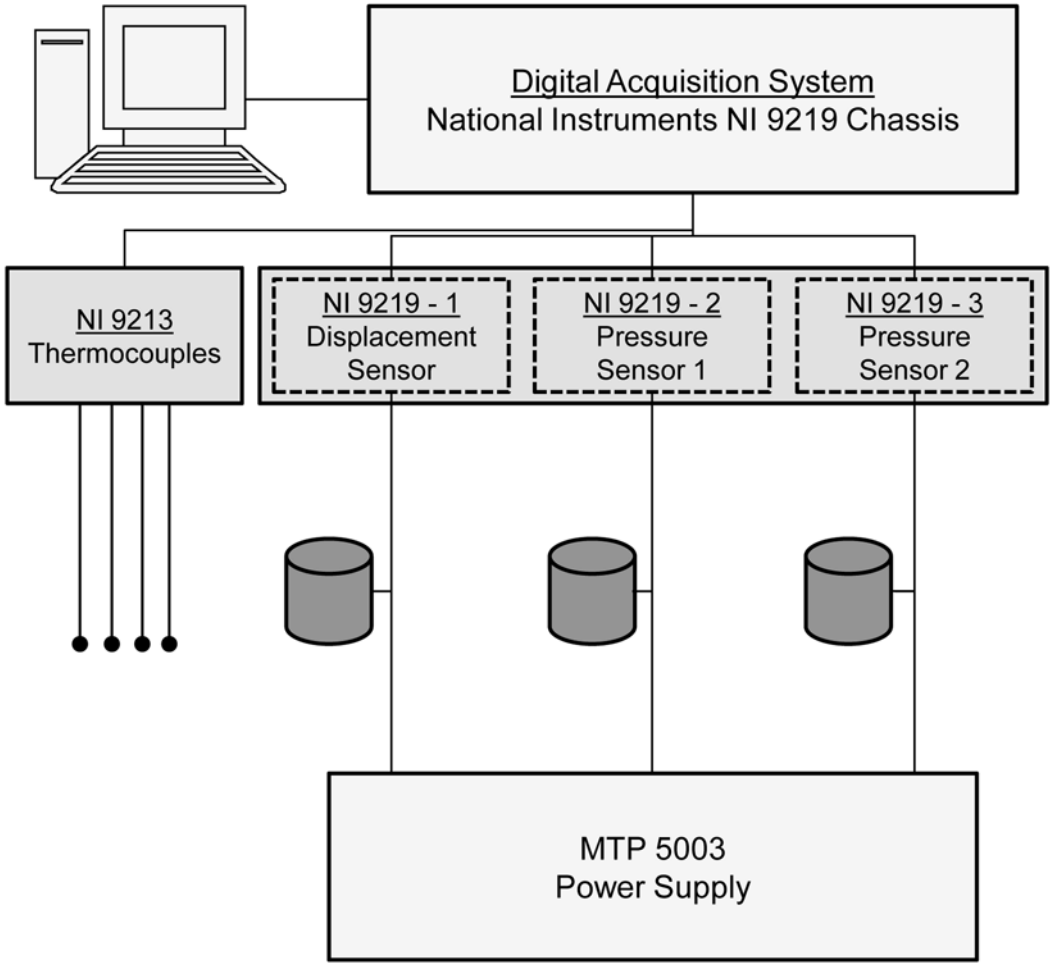

Figure D–2: Schematic of the digital acquisition system.

a maximum operating temperature of up to 150 °C. The displacement sensor was calibrated and compensated for temperature drift as described in the upcoming Section D.2.2.

The thermocouple, pressure and displacement measurements were acquired using a digital acquisition system consisting of a Toshiba Tecra M9 laptop connected to a National Instruments cDAQ-9174 acquisition chassis. The digital acquisition system configuration is shown schematically, in simplified form, in Figure D–2. The chassis contained a National Instruments

9213 cartridge (for temperature measurement) and a National Instruments 9219 cartridge (for the 4 mA - 20 mA current output of the pressure and displacement sensors). Where needed, power was provided by a MTP 5003 DC power supply.

D.2.1 Pressure Sensor Calibration

The WIKA A-10 sensors were calibrated using the set-up shown in Figure D–3, which consisted of a sealed test chamber connected to a regulated vacuum line, the WIKA sensor and an OMEGA DPG7010-VAC digital test gauge (with certified calibration documentation). The vacuum pump and regulator were used to decrease the pressure in the sealed chamber from ambient towards vacuum in six decrements; at each step, the pressure measured by the OMEGA digital test gauge was recorded and correlated to the WIKA sensor output (in mA). The calibration curves thus obtained are shown in Figure D–4 (top) for Sensor 1, connected to the consolidation fixture vacuum bag and used in Chapters 6 and 7, and (bottom) for Sensor 2, connected to the consolidation fixture lid cavity and used in Chapter 7. Both sensors show very similar behaviour and exhibit excellent linearity over the range of interest (vacuum to ambient). Hence, the linear equations displayed on the graphs were used to convert the sensor current output to absolute pressure data.

D.2.2 Displacement Sensor Calibration

The eddyNCDT 3010 / U6 displacement sensor was calibrated within the fixture, in its operating position and conditions, using the following procedure.

1. The sensor was mounted on its support within the fixture.

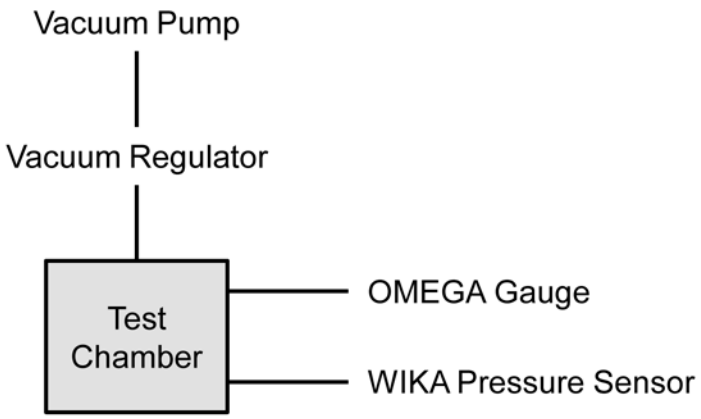

Figure D–3: Schematic of the setup used to calibrate the WIKA pressure sensors.

2. The horizontal support beam was fixed at a height that was kept constant for all experiments presented in this thesis.
3. The steel sensor target was placed beneath the sensor head, on the aluminum tool plate.
4. A set of Starrett EDP50314 stainless steel thickness gauges was used to set the gap between the sensor target and sensor head tip to a known value close to the minimum measurable range (of 0 mm plus a 0.6 mm "dead zone" near the sensor tip). Then, the sensor head was lowered by means of its own threaded nuts until it just touched the thickness gauges, and the latter were removed.
5. The current output of the sensor corresponding to this known sensor - target gap was recorded.
6. The fixture was placed in the oven, and the oven set-point was increased to 45 °C. Once the oven temperature reached the set-point, the fixture was allowed to dwell at that temperature for several hours, in

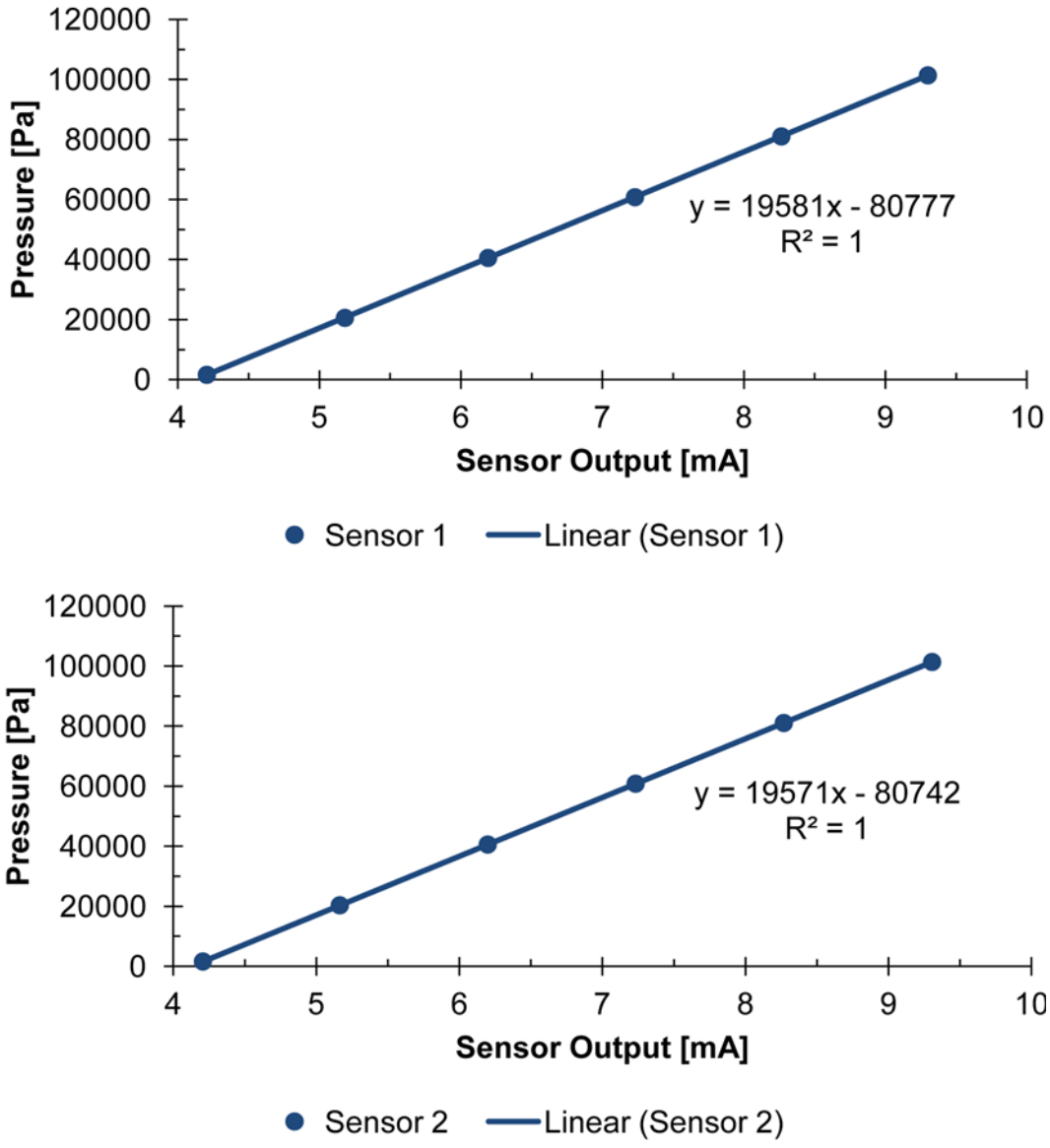

Figure D–4: Graphs of the pressure versus current calibration curves for WIKA pressure sensor 1 (top) and 2 (bottom).

order to allow proper heat-up and thermal equilibration to occur. During this time, the sensor current output was seen to drift towards a new, temperature-affected equilibrium value corresponding to the initial (room temperature) gap between target and sensor head plus the thermal expansion of the support pillars, δ, which was obtained from the following equation:

$$\delta = CTE(T - T_{amb})d \tag{D.1}$$

CTE is the thermal expansion coefficient of aluminum ($23.6 \times 10^{-6}\,^{\circ}\mathrm{C}^{-1}$ [136]), T is the temperature, T_{amb} is the ambient temperature (approximately 25 °C) and d is the distance, at room temperature, between the base of the sensor support pillars and the horizontal support beam (22 mm). Once stabilized, the current output, corrected gap and corresponding temperature were recorded.

7. The previous step was repeated three more times at temperatures of 70 °C, 95 °C and 120 °C.
8. Steps 1 through 7 were repeated with the gap between the steel target and the sensor head set to values close to quarter-range, half-range and three-quarter-range (or approximately 1.5 mm, 3 mm and 4.5 mm).

A representative set of sensor output drift curves (at mid-range) is shown in Figure D–5. The drift in sensor current is well correlated with the change in temperature, and the sensor current is fully stabilized at the end of each temperature dwell. Furthermore, the sensor current returns to its original

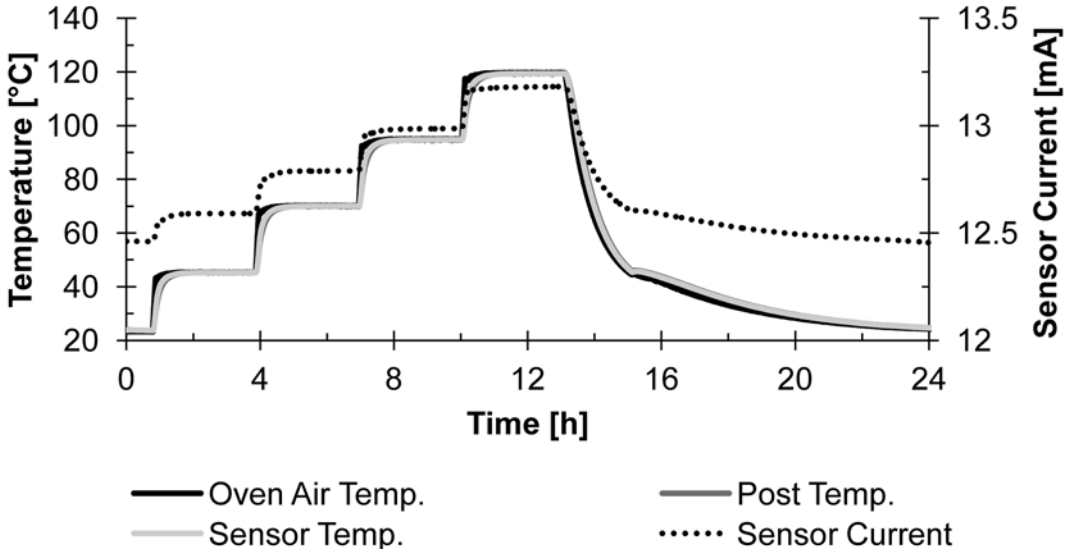

Figure D–5: Graph of the displacement sensor current output drift versus temperature at mid-range.

value following cool-down, indicating that the sensor drift is consistent and repeatable.

The above procedure resulted in a twenty-point calibration map relating four sets of current (with thermal drift) and distance (with thermal expansion) to five temperatures. This map is shown in Figure D–6 along with third-order polynomial fitting functions for each temperature, and indicates that, for a given gap between sensor head and target, an increase in temperature leads to an increase in sensor current output. This increase is relatively small in the lower half of the sensor range (0 mm to 3 mm) but becomes significantly more important above half-range. For this reason, for all experiments in this thesis, the lower half of the sensor range was favored. The calibration map and polynomial functions allows the determination of the actual distance between sensor and target: the current sensor output provided by the DAQ system fixes the x-axis coordinate, and the measured sensor temperature is used to

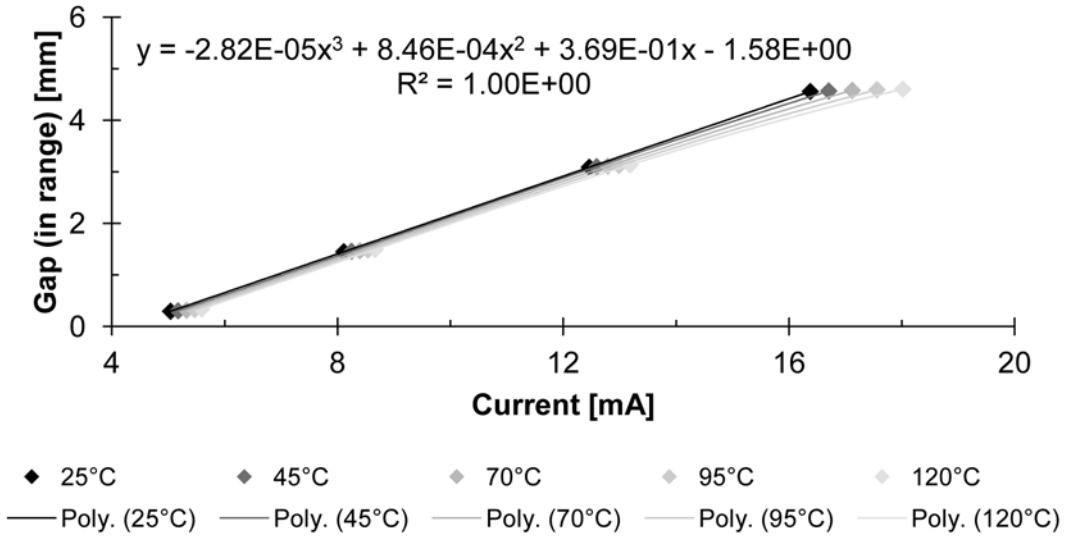

Figure D–6: Graph of the displacement sensor calibration curves along with the polynomial fitting function for the 25 °C curve (other equations omitted for clarity).

interpolate between the two nearest polynomial fitting functions to obtain the y-axis coordinate, or the gap.

APPENDIX E
Additional Data for Chapter 6

E.1 Displacement Sensor Data

The following graphs show the complete displacement sensor data for both the 5320/PW and 5320/8HS prepregs, for all cure cycles and out-times.

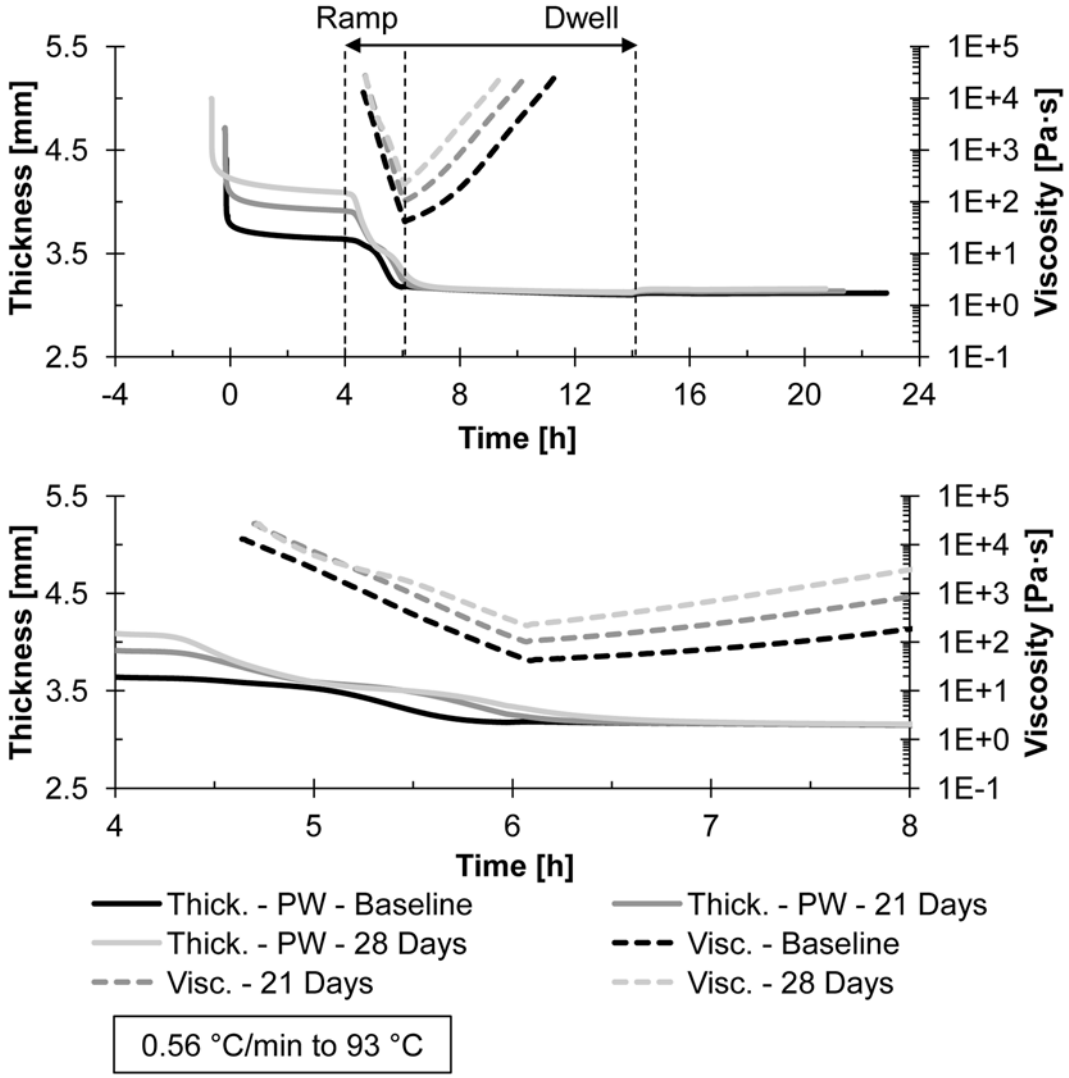

Figure E–1: Graphs of measured laminate thickness and resin viscosity for the $0.56\,^{\circ}\mathrm{C\,min^{-1}}$ to $93\,^{\circ}\mathrm{C}$ manufacture of the 5320/PW laminates. The top graph shows the data curves for the entire cure cycle, while the bottom graph magnifies the period between hours four and eight.

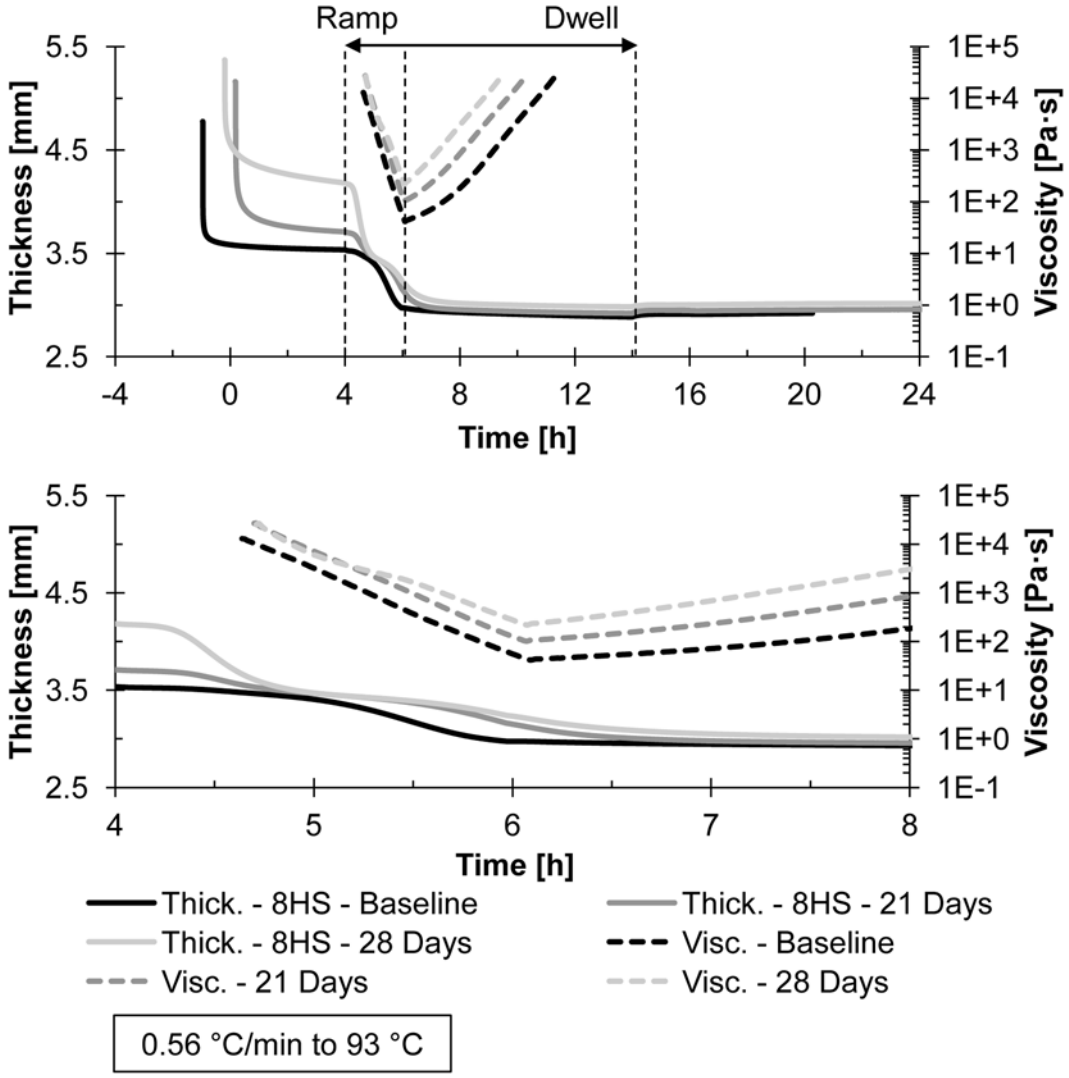

Figure E–2: Graphs of measured laminate thickness and resin viscosity for the $0.56\,^{\circ}\mathrm{C\,min^{-1}}$ to $93\,^{\circ}\mathrm{C}$ manufacture of the 5320/8HS laminates. The top graph shows the data curves for the entire cure cycle, while the bottom graph magnifies the period between hours four and eight.

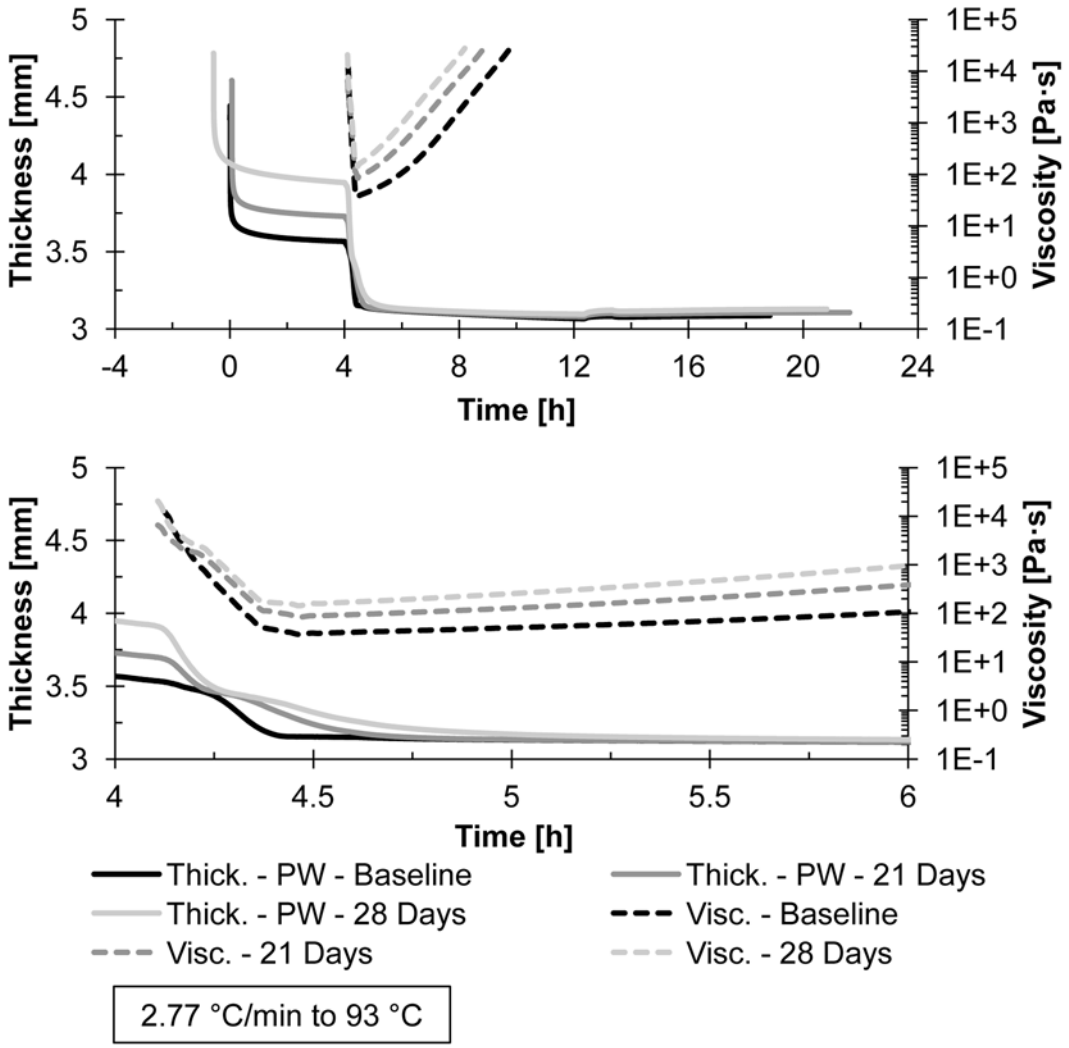

Figure E–3: Graphs of measured laminate thickness and resin viscosity for the 2.77 °C min^{-1} to 93 °C manufacture of the 5320/PW laminates. The top graph shows the data curves for the entire cure cycle, while the bottom graph magnifies the period between hours four and eight.

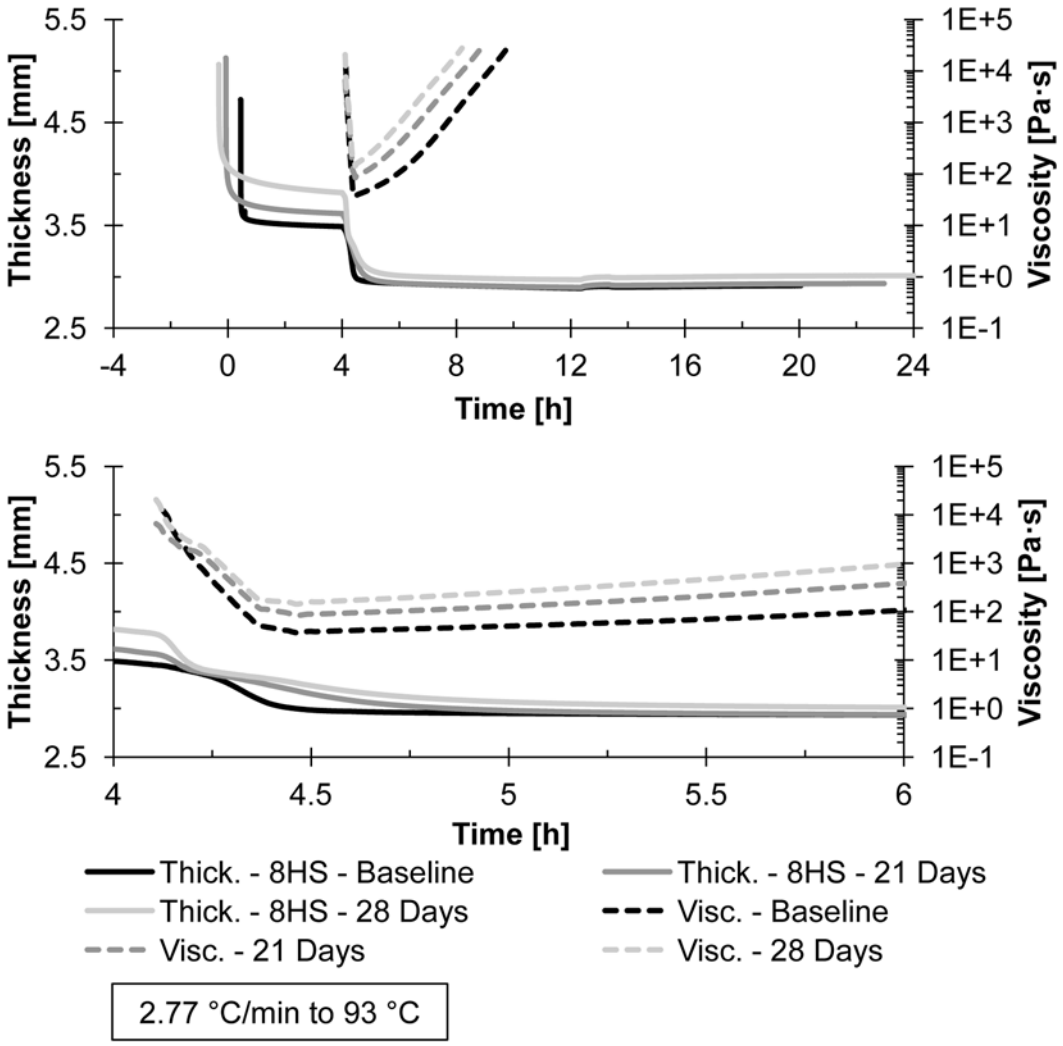

Figure E–4: Graphs of measured laminate thickness and resin viscosity for the $2.77\,^{\circ}\mathrm{C\,min^{-1}}$ to $93\,^{\circ}\mathrm{C}$ manufacture of the 5320/8HS laminates. The top graph shows the data curves for the entire cure cycle, while the bottom graph magnifies the period between hours four and eight.

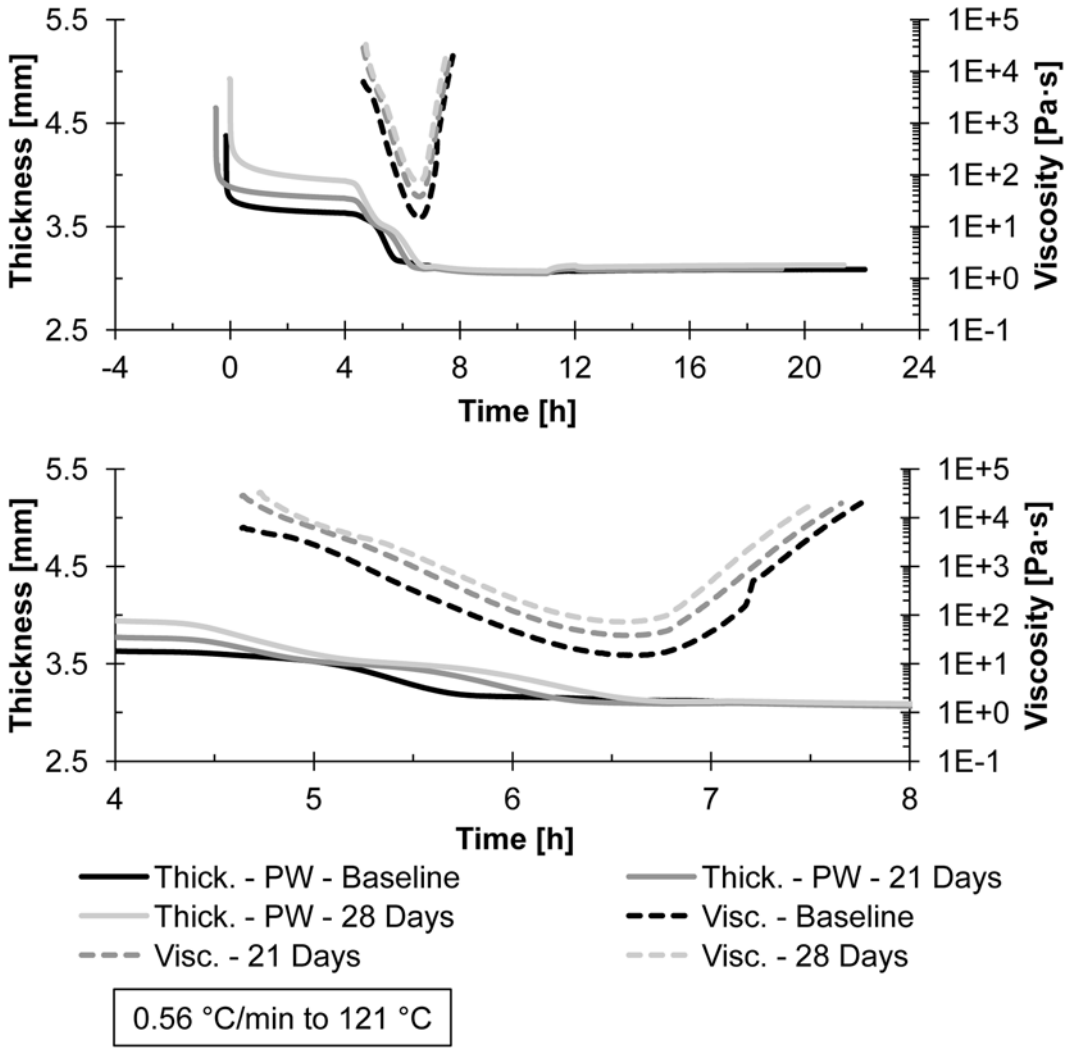

Figure E–5: Graphs of measured laminate thickness and resin viscosity for the $0.56\,^{\circ}\mathrm{C\,min^{-1}}$ to $121\,^{\circ}\mathrm{C}$ manufacture of the 5320/PW laminates. The top graph shows the data curves for the entire cure cycle, while the bottom graph magnifies the period between hours four and eight.

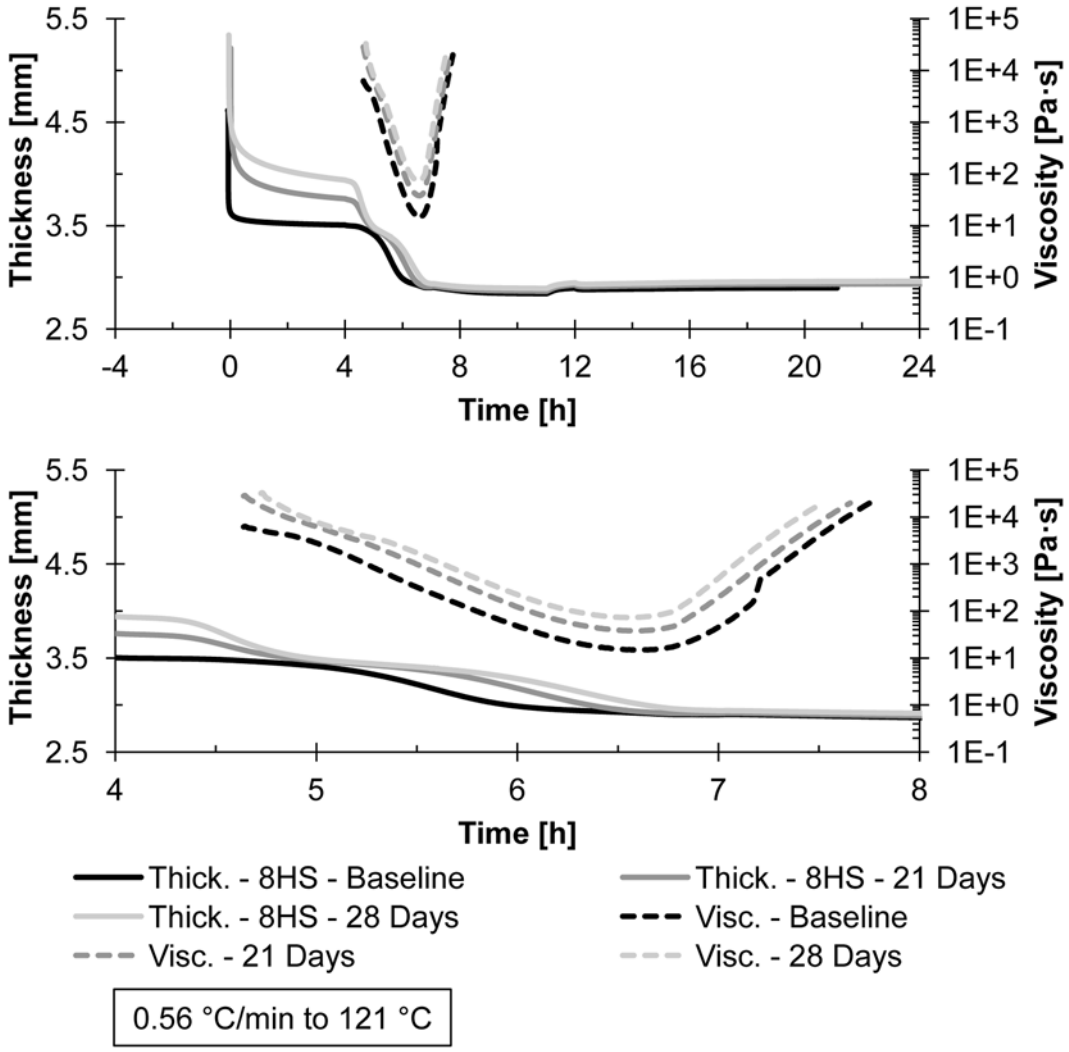

Figure E–6: Graphs of measured laminate thickness and resin viscosity for the $0.56\,^{\circ}\mathrm{C\,min^{-1}}$ to $121\,^{\circ}\mathrm{C}$ manufacture of the 5320/8HS laminates. The top graph shows the data curves for the entire cure cycle, while the bottom graph magnifies the period between hours four and eight.

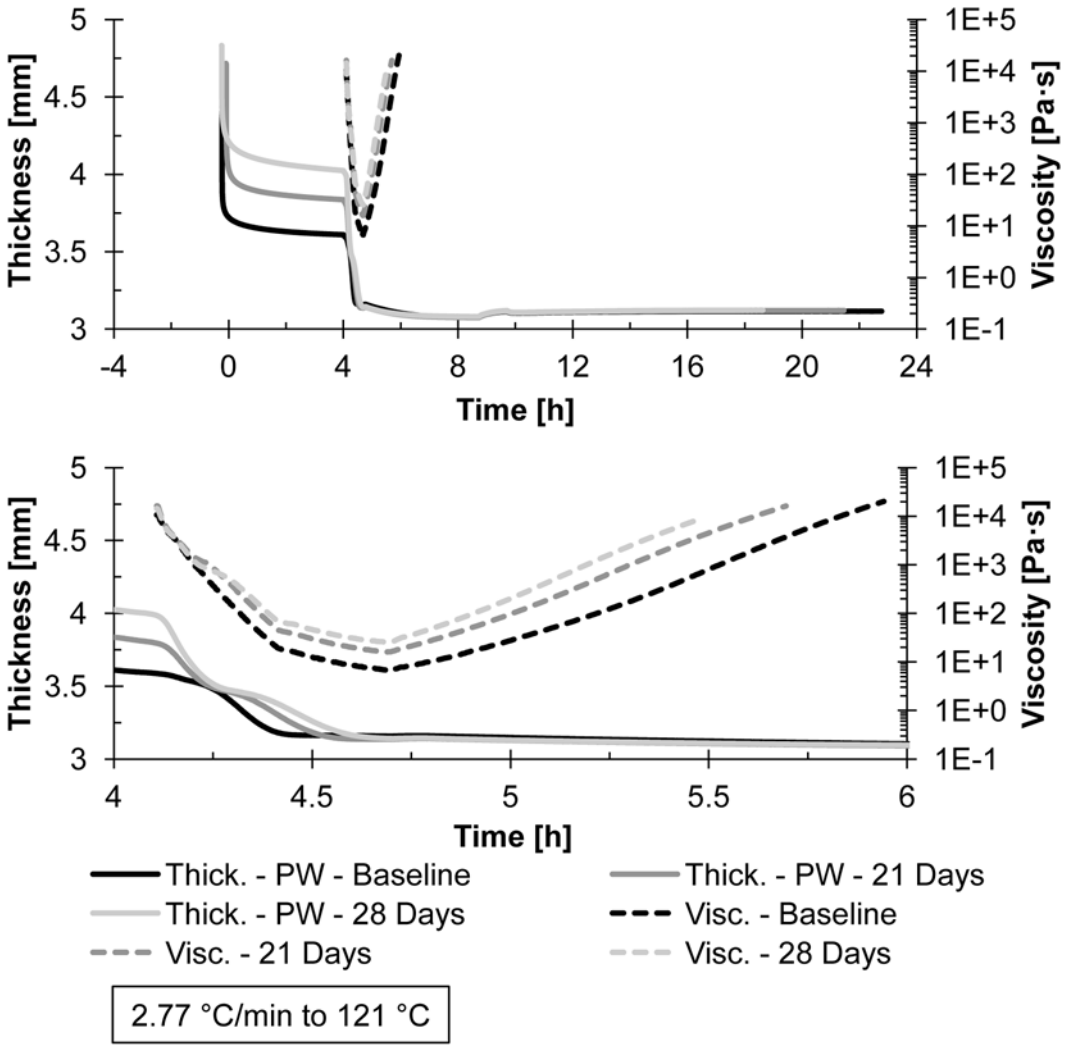

Figure E–7: Graphs of measured laminate thickness and resin viscosity for the $2.77\,^{\circ}\mathrm{C\,min^{-1}}$ to $121\,^{\circ}\mathrm{C}$ manufacture of the 5320/PW laminates. The top graph shows the data curves for the entire cure cycle, while the bottom graph magnifies the period between hours four and eight.

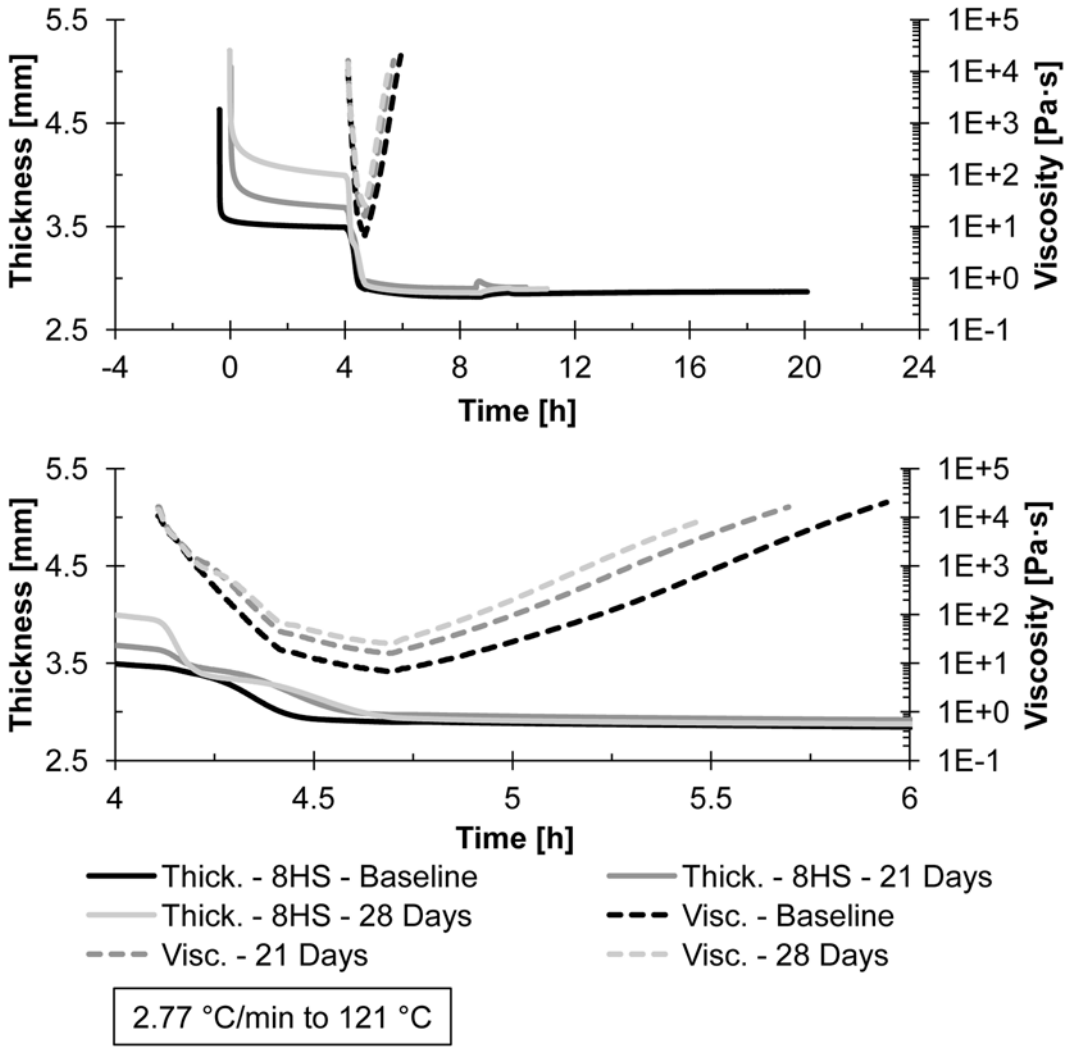

Figure E–8: Graphs of measured laminate thickness and resin viscosity for the $2.77\,^{\circ}\mathrm{C\,min^{-1}}$ to $121\,^{\circ}\mathrm{C}$ manufacture of the 5320/8HS laminates. The top graph shows the data curves for the entire cure cycle, while the bottom graph magnifies the period between hours four and eight.

References

[1] F.C. Campbell. *Manufacturing Technology for Aerospace Structural Materials*. Elsevier, London, U.K., 2006.

[2] W.G. Roeseler, B. Sarh, and M.U. Kismarton. Composite structures: The first 100 years. In *Proceedings of the 16th International Conference on Composite Materials*, Kyoto, Japan, 2007.

[3] P. Hubert. *Aspects of Flow and Compaction of Laminated Composite Shapes During Cure*. PhD thesis, University of British Columbia, 1996.

[4] L. Repecka and J. Boyd. Vacuum-bag-only-curable prepregs that produce void-free parts. In *Proceedings of the SAMPE 2002 Conference of the Society for the Advancement of Materials and Process Engineering*, Long Beach, CA, United States, 2002.

[5] C. Ridgard. Out of autoclave composite technology for aerospace, defense and space structures. In *Proceedings of the SAMPE 2009 Conference of the Society for the Advancement of Materials and Process Engineering*, Baltimore, MD, United States, 2009.

[6] B. Thorfinnson and T. Biermann. Production of void free composite parts without debulking. In *Proceedings of the 31st International SAMPE Symposium*, Las Vegas, NV, United States, 1986.

[7] B. Thorfinnson and T. Biermann. Degree of impregnation of prepregs - effects on porosity. In *Proceedings of the 32nd International SAMPE Symposium*, Anaheim, CA, United States, 1987.

[8] J.C. Seferis, R.W. Hillermeier, and F.U. Buehler. Prepregging and autoclaving of thermoset composites. In A. Kelly and C. Zweben, editors, *Comprehensive Composite Materials*, chapter 2.20. Elsevier, 2000.

[9] S.G. Advani and E.M. Sozer. Liquid moulding of thermoset composites. In A. Kelly and C. Zweben, editors, *Comprehensive Composite Materials*, chapter 2.23. Elsevier, 2000.

[10] S.G. Advani and E. Murat Sozer. *Process Modeling in Composites Manufacturing*. CRC Press (Taylor and Francis Group), Boca Raton, FL, United States, 2011.

[11] V. Michaud and A. Mortensen. Infiltration processing of fibre reinforced composites: governing phenomena. *Composites Part A: Applied Science and Manufacturing*, 32(8):981–996, 2001.

[12] S. Whitaker. *The method of volume averaging*. Kluwer Academic, Boston, MA, United States, 1999.

[13] M. Quintard and S. Whitaker. Theoretical analysis of transport in porous media. In K. Vafai, editor, *Handbook of Porous Media*, chapter 1. Marcel Dekker, New York, NY, United States, 2000.

[14] D.A. Nield and A. Bejan. *Convection in Porous Media (4th Ed.)*. Springer, New York, NY, United States, 2013.

[15] H. Darcy. Les fontaines publiques de la ville de dijon. Technical report, Dalmont, Paris, 1856.

[16] C.L. Tucker III and R.B. Dessenberger. Governing equations for flow and heat transfer in stationary fibre beds. In S.G. Advani, editor, *Flow and Rheology in Polymer Composites Manufacturing*, chapter 8. Elsevier, Amsterdam, The Netherlands, 1994.

[17] M.A. Biot. General theory of three-dimensional consolidation. *Journal of Applied Physics*, 12:155–164, 1941.

[18] K. Terzaghi. *Theoretical Soil Mechanics*. John Wiley and Sons, New York, United States, 1943.

[19] B.R. Gebart. Permeability of unidirectional reinforcements for rtm. *Journal of Composite Materials*, 26(8):1100–1133, 1992.

[20] P. Hubert and A. Poursartip. Review of flow and compaction modelling relevant to thermoset matrix laminate processing. *Journal of Reinforced Plastics and Composites*, 17(4):286–318, 1998.

[21] T.G. Gutowski, Z. Cai, S. Bauer, D. Boucher, J. Kingery, and S. Wineman. Consolidation experiments for laminate composites. *Journal of Composite Materials*, 21(7):650–669, 1987.

[22] J-H. Byun and T-W. Chou. Mechanics of textile composites. In A. Kelly and C. Zweben, editors, *Comprehensive Composite Materials*, chapter 1.23. Elsevier, 2000.

[23] P. Hubert and A. Poursartip. A method for the direct measurement of the fibre bed compaction curve of composite prepregs. *Composites Part A: Applied Science and Manufacturing*, 32(2):179–187, 2001.

[24] Z. Cai and T. Gutowski. The 3d deformation behavior of a lubricated fibre bundle. *Journal of Composite Materials*, 26(8):1207–1237, 1992.

[25] F. Robitaille and R. Gauvin. Compaction of textile reinforcements for composites manufacturing. i: Review of experimental results. *Polymer Composites*, 19(2):198–216, 1998.

[26] S. Sharma and D.A. Siginer. Permeability measurement methods in porous media of fiber reinforced composites. *Applied Mechanics Reviews*, 63(2), 2010.

[27] R. Arbter et al. Experimental determination of the permeability of textiles: A benchmark exercise. *Composites Part A: Applied Science and Manufacturing*, 42(9):1157–1168, 2011.

[28] S.G. Advani, M.V. Bruschke, and R.S. Parnas. Resin transfer molding flow phenomena in polymeric composites. In S.G. Advani, editor, *Flow and Rheology in Polymer Composites Manufacturing*, chapter 12. Elsevier, Amsterdam, The Netherlands, 1994.

[29] M.V. Bruschke and S.G. Advani. Flow of generalized newtonian fluids across a periodic array of cylinders. *Journal of Rheology*, 37(3):479–498, 1993.

[30] G. Bechtold and L. Ye. Influence of fibre distribution on the transverse flow permeability in fibre bundles. *Composites Science and Technology*, 63(14):2069–2079, 2003.

[31] X. Chen and T. Papathanasiou. The transverse permeability of disordered fiber arrays: a statistical correlation in terms of the mean nearest interfiber spacing. *Transport in Porous Media*, 71(2):233–251, 2008.

[32] A. Yousefi and G. Lafleur. Kinetic studies of thermoset cure reactions: A review. *Polymer Composites*, 18(2):157–168, 1997.

[33] M.R. Kamal and S. Sourour. Kinetics and thermal characterization of thermoset cure. *Polymer Engineering and Science*, 13(1):59–64, 1973.

[34] K.C. Cole, J.J. Hechler, and D. Noel. New approach to modeling the cure kinetics of epoxy amine thermosetting resins. 2. application to a typical system based on bis[4-(diglycidylamino)phenyl]methane and bis(4-aminophenyl) sulfone. *Macromolecules*, 24(11):3098–3110, 1991.

[35] L.K. Khoun, T. Centea, and P. Hubert. Characterization methodology of thermoset resins for the processing of composite materials - case study: Cycom 890rtm epoxy resin. *Journal of Composite Materials*, 44(11):1397–1415, 2009.

[36] J. Kratz, K. Hsiao, G. Fernlund, and P. Hubert. Thermal models for mtm45-1 and cycom 5320 out-of-autoclave prepreg resins. *Journal of Composite Materials*, 2011. doi: 10.1177/0021998312440131.

[37] C.J. Bartlett. Use of the parallel plate plastometer to characterize glass-reinforced resins: I. flow model. *Journal of Elastomers and Plastics*, 10:369–376, 1978.

[38] J.M. Castro and C.W. Macosko. Kinetics and rheology of typical polyurethane reaction injection molding systems. In *Society of Plastics Engineers Technical Papers*, volume 26, pages 434–438, 1980.

[39] A.R.A. Arafath, G. Fernlund, and A. Poursartip. Gas transport in prepregs: Model and permeability experiments. In *Proceedings of the 17th International Conference on Composite Materials*, Edinburgh, Scotland, 2009.

[40] J.L. Kardos, M.P. Dudukovic, and R. Dave. Void growth and resin transport during processing of thermosetting-matrix composites. *Advances in Polymer Science*, 80:101–123, 1986.

[41] H.H. Lin, S. Ranganathan, and S.G. Advani. Consolidation of continuous-fiber systems. In S.G. Advani, editor, *Flow and Rheology in Polymer Composites Manufacturing*, chapter 9. Elsevier, Amsterdam, The Netherlands, 1994.

[42] Hexcel. *Prepreg Technology (Publication Number FGU 017b)*, March 2005.

[43] D.E. Kranbuehl, P. Kingsley, S. Hart, G. Hasko, B. Dexter, and A.C. Loos. In situ sensor monitoring and intelligent control of the resin transfer molding process. *Polymer Composites*, 15(4):299–305, 1994.

[44] F.C. Campbell, A.R. Mallow, and C.E. Browning. Porosity in carbon fiber composites: An overview of causes. *Journal of Advanced Materials*, 26(4):18–33, 1995.

[45] K. Lynch, P. Hubert, and A. Poursartip. Use of a simple, inexpensive pressure sensor to measure hydrostatic resin pressure during processing of composite laminates. *Polymer Composites*, 20(4):581–593, 1999.

[46] Y. Gu et al. Resin pressure and resin flow inside tapered laminates during zero-bleeding and bleeding processes. *Journal of Reinforced Plastics and Composites*, 31(4):205–214, 2012.

[47] C.D. Williams, S.M. Grove, and J. Summerscales. The compression response of fibre-reinforced plastic plates during manufacture by the resin infusion under flexible tooling method. *Composites Part A: Applied Science and Manufacturing*, 29(1-2):111–114, 1998.

[48] H.M. Andersson, T.S. Lundstrom, B.R. Gebart, and P. Synnergren. Application of digital speckle photography to measure thickness variations in the vacuum infusion process. *Polymer Composites*, 24(3):448–455, 2003.

[49] Q. Govignon, S. Bickerton, J. Morris, and P.A. Kelly. Full field monitoring of the resin flow and laminate properties during the resin infusion process. *Composites Part A: Applied Science and Manufacturing*, 39(9):1412–1426, 2008.

[50] N. Kuentzer, P. Simacek, S.G. Advani, and S. Walsh. Permeability characterization of dual scale fibrous porous media. *Composites Part A: Applied Science and Manufacturing*, 37(11):2057–2068, 2006.

[51] M. Louis and U. Huber. Investigation of shearing effects on the permeability of woven fabrics and implementation into lcm simulation. *Composites Science and Technology*, 63(14):2081–2088, 2003.

[52] X. Wu, J. Li, and R.A. Shenoi. Measurement of braided preform permeability. *Composites Science and Technology*, 66(15):3064–3069, 2006.

[53] E. Rodriguez, F. Giacomelli, and A. Vasquez. Permeability-porosity relationship in rtm for different fiberglass and natural reinforcements. *Journal of Composite Materials*, 38(3):259–268, 2004.

[54] A. Poursartip, G. Riahi, L. Frederick, and X. Lin. A method to determine resin flow during curing of composite laminates. *Polymer Composites*, 13(1):58–65, 1992.

[55] V. Neacsu, A. Abu Obaid, and S.G. Advani. Spontaneous radial capillary impregnation across a bank of aligned micro-cylinders. part ii: Experimental investigations. *International Journal of Multiphase Flow*, 32(6):677–691, 2006.

[56] V. Neacsu, J. Leisen, H. Beckham, and S.G. Advani. Use of magnetic resonance imaging to visualize impregnation across aligned cylinders due to capillary forces. *Experiments in Fluids*, 42(3):425–440, 2007.

[57] A. Endruweit, P. Glover, K. Head, and A.C. Long. Mapping of the fluid distribution in impregnated reinforcement textiles using magnetic resonance imaging: Methods and issues. *Composites Part A: Applied Science and Manufacturing*, 42(3):265–273, 2011.

[58] A. Endruweit, P. Glover, K. Head, and A.C. Long. Mapping of the fluid distribution in impregnated reinforcement textiles using magnetic resonance imaging: Application and discussion. *Composites Part A: Applied Science and Manufacturing*, 42(10):1369–1379, 2011.

[59] S. Thomas, C. Bongiovanni, and S.R. Nutt. In situ estimation of through-thickness resin flow using ultrasound. *Composites Science and Technology*, 68(15-16):3093–3098, 2008.

[60] S. Thomas and S.R. Nutt. Temperature dependence of resin flow in a resin film infusion (rfi) process by ultrasound imaging. *Applied Composite Materials*, 16(3):183–196, 2009.

[61] G.S. Springer. Resin flow during the cure of fiber reinforced composites. *Journal of Composite Materials*, 16(5):400–410, 1982.

[62] A.C. Loos and G.S. Springer. Curing of epoxy matrix composites. *Journal of Composite Materials*, 17(2):135–169, 1983.

[63] T.G. Gutowski, T. Morigaki, and Z. Cai. Consolidation of laminated composites. *Journal of Composite Materials*, 21(2):172–188, 1987.

[64] R. Dave, J.L. Kardos, and M.P. Dudukovic. A model for resin flow during composite processing: Part 1–general mathematical development. *Polymer Composites*, 8(1):29–38, 1987.

[65] R. Dave, J.L. Kardos, and M.P. Dudukovic. A model for resin flow during composite processing: Part 2–numerical analysis for unidirectional graphite/epoxy laminates. *Polymer Composites*, 8(2):123–132, 1987.

[66] R. Dave. A unified approach to modeling resin flow during composite processing. *Journal of Composite Materials*, 24(1):22–41, 1990.

[67] M.P. Dudukovic, J.L. Kardos, S. Yoon, and Y.B. Yang. Autoclave processing of long fiber thermoplastic composites. *Chemical Engineering and Science*, 45(8):2519–2526, 1990.

[68] G.D. Smith and A. Poursartip. Comparison of two resin flow models for laminate processing. *Composite Materials*, 27(17):1695–1711, 1993.

[69] W.-B. Young. Resin flow analysis in the consolidation of multi-directional laminated composites. *Polymer Composites*, 16(3):250–257, 1995.

[70] P. Hubert, R. Vaziri, and A. Poursartip. A two-dimensional flow model for the process simulation of complex shape composite laminates. *International Journal for Numerical Methods in Engineering*, 44(1):1–26, 1999.

[71] M. Li and C.L. Tucker III. Modeling and simulation of two-dimensional consolidation for thermoset matrix composites. *Composites Part A: Applied Science and Manufacturing*, 33(6):877–892, 2002.

[72] K.M. Pillai. Modeling the unsaturated flow in liquid composite molding processes: A review and some thoughts. *Journal of Composite Materials*, 38(23):2097–2118, 2004.

[73] A.W. Chan and R.J. Morgan. Tow impregnation during resin transfer molding of bi-directional nonwoven fabrics. *Polymer Composites*, 14(4):335–340, 1993.

[74] T.A.K. Sadiq, S.G. Advani, and R.S. Parnas. Experimental investigation of transverse flow through aligned cylinders. *International Journal of Multiphase Flow*, 21(5):755–774, 1995.

[75] M.E. Foley and J.W. Gillespie Jr. Modeling the effect of fiber diameter and fiber bundle count on tow impregnation during liquid molding processes. *Journal of Composite Materials*, 39(12):1045–1065, 2005.

[76] G.G. Bond and J. Luner. Design of experiments evaluation of processing parameters for non-autoclave composite prepreg. In *Proceedings of the SAMPE 2009 Conference of the Society for the Advancement of Materials and Process Engineering*, Baltimore, MD, United States, 2009.

[77] S. Mortimer and M.J. Smith. Product development for out-of-autoclave (o.o.a.) manufacture of aerospace structure. In *Proceedings of the SAMPE 2010 Conference of the Society for the Advancement of Materials and Process Engineering*, Seattle, WA, United States, 2010.

[78] C. Ridgard. Next generation out of autoclave systems. In *Proceedings of the SAMPE 2010 Conference of the Society for the Advancement of Materials and Process Engineering*, Seattle, WA, United States, 2010.

[79] S. Lucas, S. Howard, and J. Senger. Vaccum bag only processing: Improving prepreg out-time and porosity for large composite structure. In *Proceedings of the SAMPE 2010 Conference of the Society for the Advancement of Materials and Process Engineering*, Seattle, WA, United States, 2010.

[80] G. Bond, G.L. Hahn, J.A. Thomas, L.J. Cohen, J. Stavana, and K. Houseal. Non-autoclave manufacturing technology: Drape formed spars. In *Proceedings of the SAMPE 2011 Conference of the Society for the Advancement of Materials and Process Engineering*, Long Beach, CA, United States, 2011.

[81] G.L. Hahn, G. Bond, and J.H. Fogarty. Non-autoclave (prepreg) manufacturing technology: Part scale-up with cycom 5320-1 prepregs. In *Proceedings of the SAMPE 2011 Conference of the Society for the Advancement of Materials and Process Engineering*, Long Beach, CA, United States, 2011.

[82] C.J. Wade and J.R. Savage. The development and application of an out-of-autoclave prepreg solution for airbus a350xwb wing fixed trailing edge. In *Proceedings of the SAMPE 2011 Conference of the Society for the Advancement of Materials and Process Engineering*, Long Beach, CA, United States, 2011.

[83] M. Steele, T. Corden, and A. Gibbs. The development of out-of-autoclave composite prepreg technology for aerospace applications. In *Proceedings of the SAMPE 2011 Conference of the Society for the Advancement of Materials and Process Engineering*, Long Beach, CA, United States, 2011.

[84] Advanced Composites Group. *ACG MTM 45-1 Matrix Resin*.

[85] Cytec Engineered Materials. *CYCOM 5320 Information Sheet*.

[86] A.T. DiBenedetto. Prediction of the glass transition temperature of polymers: A model based on the principle of corresponding states. *Journal of Polymer Science Part B: Polymer Physics*, 25(9):1949–1969, 1987.

[87] K. Hsiao B.M. Louis and G. Fernlund. Gas permeability measurements of out of autoclave prepreg mtm45-1/cf2426a. In *Proceedings of the SAMPE 2010 Conference of the Society for the Advancement of Materials and Process Engineering*, Seattle, WA, United States, 2010.

[88] L. Fahrang and G. Fernlund. Void evolution and gas transport during cure in out-of-autoclave prepreg laminates. In *Proceedings of the SAMPE 2011 Conference of the Society for the Advancement of Materials and Process Engineering*, Long Beach, CA, United States, 2011.

[89] S. Sequeira Tavares, V. Michaud, and J.A.E. Manson. Through thickness air permeability of prepregs during cure. *Composites Part A: Applied Science and Manufacturing*, 40(10):1587–1596, 2009.

[90] S. Sequeira Tavares, V. Michaud, and J.A.E. Manson. Assessment of semi-impregnated fabrics in honeycomb sandwich structures. *Composites Part A: Applied Science and Manufacturing*, 41(1):8–15, 2010.

[91] S. Sequeira Tavares, N. Caillet-Bois, V. Michaud, and J.A.E. Manson. Vacuum-bag processing of sandwich structures: Role of honeycomb pressure level on skincore adhesion and skin quality. *Composites Science and Technology*, 70(5):797–803, 2010.

[92] S. Sequeira Tavares, N. Caillet-Bois, V. Michaud, and J.A.E. Manson. Non-autoclave processing of honeycomb sandwich structures: Skin through thickness air permeability during cure. *Composites Part A: Applied Science and Manufacturing*, 41(5):646–652, 2010.

[93] S. Sequeira Tavares, Y. Roulin, V. Michaud, and J.A.E. Manson. Hybrid processing of thick skins for honeycomb sandwich structures. *Composites Science and Technology*, 71(2):183–189, 2011.

[94] J. Kratz and P. Hubert. Processing out-of-autoclave honeycomb structures: Internal core pressure measurements. *Composites Part A: Applied Science and Manufacturing*, 42(8):1060–1065, 2011.

[95] J. Kratz, T. Centea, and P. Hubert. Manufacturing considerations for out-of-autoclave honeycomb structures. In *Proceedings of the 58th Aeronautics Conference and AGM of the Canadian Aeronautics and Space Institute*, Montreal, QC, Canada, 2011.

[96] J. Kratz, T. Centea, and P. Hubert. Air permeability of out-of-autoclave honeycomb structures during processing. In *Proceedings of the 26th Annual Technical Conference of the American Society for Composites / The 2nd Joint US-Canada Conference on Composites*, Montreal, QC, Canada, 2011.

[97] J. Kratz and P. Hubert. In-situ monitoring of honeycomb pressure using embedded sensors. In *Proceedings of the SAMPE 2011 Conference of the Society for the Advancement of Materials and Process Engineering*, Long Beach, CA, United States, 2011.

[98] K. Hsiao, J. Kay, and G. Fernlund. Gas transport and water evaporation in out-of-autoclave prepregs. In *Proceedings of the 26th Annual Technical Conference of the American Society for Composites / The 2nd Joint US-Canada Conference on Composites*, Montreal, QC, Canada, 2011.

[99] J. Kay and G. Fernlund. Processing conditions and voids in out of autoclave prepregs. In *Proceedings of the SAMPE 2012 Conference of the Society for the Advancement of Materials and Process Engineering*, Baltimore, MD, United States, 2012.

[100] L.K. Grunenfelder and S.R. Nutt. Void formation in composite prepregs - effect of dissolved moisture. *Composites Science and Technology*, 70(16):2304–2309, 2010.

[101] L.K. Grunenfelder and S.R. Nutt. Prepreg age monitoring via differential scanning calorimetry. *Journal of Reinforced Plastics and Composites*, 31(5):295–302, 2012.

[102] L.K. Grunenfelder and S.R. Nutt. Out time effects on vbo prepreg and laminate properties. In *Proceedings of the SAMPE 2011 Conference of*

the Society for the Advancement of Materials and Process Engineering, Long Beach, CA, United States, 2011.

[103] M. Brillant. Out-of-autoclave manufacturing of complex shape composite laminates. Master's thesis, McGill University, 2010.

[104] M. Brillant and P. Hubert. Out-of-autoclave processing of complex shape laminates. In *Proceedings of the SAMPE 2010 Conference of the Society for the Advancement of Materials and Process Engineering*, Seattle, WA, United States, 2010.

[105] J. Cauberghs and P. Hubert. Effect of tight corners and ply terminations on quality in out-of-autoclave parts. In *Proceedings of the SAMPE 2011 Conference of the Society for the Advancement of Materials and Process Engineering*, Long Beach, CA, United States, 2011.

[106] M. Wyscoki, R. Larsson, and S. Toll. Modelling the consolidation of partially impregnated prepregs. In *Proceedings of the 17th International Conference on Composite Materials*, Edinburgh, Scotland, 2009.

[107] T.A. Cender, A. Abu Obaid, P. Simacek, and S.G. Advani. Experimental characterization of a partially pre-impregnated fabric for out-of-autoclave processing. In *Proceedings of the SAMPE 2011 Conference of the Society for the Advancement of Materials and Process Engineering*, Long Beach, CA, United States, 2011.

[108] J.J. Gangloff Jr., S. Sinha, and S.G. Advani. A model for tow impregnation and consolidation for partially impregnated thermoset prepregs. In *Proceedings of the SAMPE 2011 Conference of the Society for the Advancement of Materials and Process Engineering*, Long Beach, CA, United States, 2011.

[109] S.R. Stock. X-ray microtomography of materials. *International Materials Reviews*, 44(4):141–164, 1999.

[110] Skyscan. *Skyscan 1172 Desktop X-Ray Microtomograph*, 2005.

[111] F. Desplentere, S.V. Lomov, D.L. Woerdeman, I. Verpoest, M. Wevers, and A. Bogdanovich. Micro-ct characterization of variability in 3d textile architecture. *Composites Science and Technology*, 65(13):1920–1930, 2005.

[112] J.S.U. Schell, M. Renggli, G.H. van Lenthe, R. Muller, and P. Ermanni. Micro-computed tomography determination of glass fibre reinforced polymer meso-structure. *Composites Science and Technology*, 66(13):2016–2022, 2006.

[113] P. Badel, E. Vidal-Salle, E. Marie, and P. Boisse. Simulation and tomography analysis of textile composite reinforcement deformation at the mesoscopic scale. *Composites Science and Technology*, 68(12):2433–2440, 2008.

[114] L.P. Djukic, I. Herszberg, W.R. Walsh, G.A. Schoeppner, and B. Gangadhara Prusty. Contrast enhancement in visualisation of woven composite architecture using a microct scanner. part 2: Tow and preform coatings. *Composites Science and Technology*, 40(12):1870–1879, 2009.

[115] P.J. Schilling, B.R. Karedla, A.K. Tatiparthi, M.A. Verges, and P.D. Herrington. X-ray computed microtomography of internal damage in fiber reinforced polymer matrix composites. *Composites Science and Technology*, 65(14):2071–2078, 2005.

[116] Imagej. http://rsb.info.nih.gov/ij/index.html. Web site accessed 4 March 2013.

[117] B.P. Van West, R. B. Pipes, and S.G. Advani. The consolidation of commingled thermoplastic fabrics. *Polymer Composites*, 12(6):417–427, 1991.

[118] V. Neacsu, A. Abu Obaid, and S.G. Advani. Spontaneous radial capillary impregnation across a bank of aligned micro-cylinders. part i: Theory and model development. *International Journal of Multiphase Flow*, 32(6):661–676, 2006.

[119] J.D.H. Hughes. The carbon fibre/epoxy interface – a review. *Composites Science and Technology*, 41(1):13–45, 1991.

[120] S.A. Page, J.C. Berg, and J.-A.E. Manson. Characterization of epoxy resin surface energetics. *Journal of Adhesion Science and Technology*, 15:153–170, 2001.

[121] T.S. Lundstrom and B.R. Gebart. Effect of perturbation of fibre architecture on permeability inside fibre tows. *Journal of Composite Materials*, 29(4):424–443, 1995.

[122] J. Kratz. Resin viscosity tests on cycom 5320 epoxy resin, 2012.

[123] L.K. Grunenfelder. Personal communication, 2012.

[124] T. Centea and P. Hubert. Measuring the impregnation of an out-of-autoclave prepreg by micro-ct. *Composites Science and Technology*, 71(5):593–599, 2011.

[125] T. Centea and P. Hubert. Modelling the effect of material properties and process parameters on tow impregnation in out-of-autoclave prepregs. *Composites Part A: Applied Science and Manufacturing*, 43(9):1505–1513, 2012.

[126] L.K. Grunenfelder, T. Centea, P. Hubert, and S.R. Nutt. Effect of room-temperature out-time on tow impregnation in an out-of-autoclave prepreg. *Composites Part A: Applied Science and Manufacturing*, 2012.

[127] T. Centea and P. Hubert. Experimental observation and analytical modelling of the flow inside an out-of-autoclave prepreg. In *Proceedings of the 10th International Conference on Flow Processes in Composite Materials*, Monte Verita, Switzerland, 2010.

[128] T. Centea and P. Hubert. The effect of material and process parameters on tow impregnation and micro-void formation in out-of-autoclave prepregs. In *Proceedings of the 26th Annual Technical Conference of the American Society for Composites / The 2nd Joint US-Canada Conference on Composites*, Montreal, QC, Canada, 2011.

[129] T. Centea, S.-M. Hughes, S. Payette, J. Kratz, and P. Hubert. Scaling challenges encountered with out-of-autoclave prepregs. In *Proceedings of the 53rd AIAA/ASME/ASCE/AHS/ASC Structures, Structural Dynamics and Materials Conference*, Honolulu, Hawaii, 2012.

[130] T. Centea and P. Hubert. Effect of process deficiencies on out-of-autoclave prepreg consolidation. In *Proceedings of the SAMPE 2012 Conference of the Society for the Advancement of Materials and Process Engineering*, Baltimore, MD, United States, 2012.

[131] T. Centea, J. Kratz, and P. Hubert. The effect of out-time and cure cycle on the consolidation of out-of-autoclave prepregs. In *Proceedings of the 11th International Conference on Flow Processes in Composite Materials*, Auckland, New Zealand, 2012.

[132] Skyscan. *Method Notes, SkyScan 1172 Micro-CT: Scanner Operation*, 2008.

[133] Skyscan. *SkyScan 1172 Micro-CT Scan Set-Up Flowchart*, 2008.

[134] X. Gagne-Brulotte. Compaction behaviour of out-of-autoclave pre-impregnate composite materials (honours thesis). Technical report, McGill University, 2008.

[135] T. Chew. Design, manufacture and validation of an out-of-autoclave composite processing fixture (honours thesis). Technical report, McGill University, 2011.

[136] A.P. Boresi. *Advanced Mechanics of Materials*. Wiley, 2002.